Technische Universität München
TUM School of Engineering and Design

Numerical and Physical Modeling of Compressible Multi-component Flows Including Surface Tension, Cavitation, Turbulence, and Real-Fluid Effects

Yu Jiao

Vollständiger Abdruck der von der TUM School of Engineering and Design der Technischen Universität München zur Erlangung eines

Doktors der Ingenieurwissenschaften (Dr.-Ing.)

genehmigten Dissertation.

Vorsitz: Prof. Dr. Dongsheng Wen

Prüfende der Dissertation:

1. Prof. Dr.-Ing. Nikolaus A. Adams
2. Prof. Dr. Manolis Gavaises

Die Dissertation wurde am 11.09.2024 bei der Technischen Universität München eingereicht und durch die TUM School of Engineering and Design am 05.02.2025 angenommen.

© Yu Jiao, 2024

yu.jiao@tum.de

Typesetting LaTeX

Acknowledgement

Abstract

This thesis studies the numerical and physical modeling of compressible multi-component flows taking into account surface tension, cavitation, turbulence and real-fluid effects. It shows the recent development of the CAvitation Technical University of Munich (CATUM) solver. The underlying physical phenomena, such as turbulent jet flow and shock-fuel droplet interaction characteristics, are relevant to low-speed internal combustion engine systems, such as cargo ships, trucks, and tractors, as well as high-speed propulsion systems such as ramjets and scramjets. This application-driven work is carried out at the Institute of Aerodynamics and Fluid Mechanics at the Technical University of Munich. The results of the numerical investigations are presented in three first-author research papers published in international peer-reviewed journals.

Firstly, in the context of internal combustion engines, there are complex multi-component turbulent flows. However, it is difficult to avoid the tendency for interface smearing in the original CATUM solver and surface tension is not included. These limitations result in dissipation for the fuel-gas interfaces. This motivates the development of a robust numerical method that does not require a change to the four-stencil compact scheme of CATUM and is highly efficient. An algebraic-based interface sharpening method, Tangent of Hyperbola for INterface Capturing (THINC), is applied in conjunction with Thermodynamic-Dependent Update (TDU), which enables the sharpening of both liquid-gas and liquid-vapour interfaces. The interface-related modules of CATUM have been enhanced, including the treatment of cavitation, turbulence and surface tension. In order to facilitate the sub-grid turbulence modeling, a fourth-order central scheme has been incorporated into the switching process, along with a modified discontinuity sensor. Furthermore, surface tension effects have been accounted for by utilizing a Continuum Surface Force (CSF) model. To reduce spurious oscillations at interfaces, the computation of the interface curvature has been decoupled from the computation of the gradient of the Heaviside function. The proposed method is applied to a number of cases, including bubble oscillation/advection/deformation, shock-bubble interaction, a vapour/gas bubble collapse and a multi-component shear flow. The results of a near-critical shock-droplet interaction case demonstrate superior performance compared to those obtained by the WENO3 and OWENO3 schemes. This confirms that the proposed methodology is effective in various thermodynamic relations, including the Peng-Robinson equation of state (PR-EOS). Finally, the approach is applied to simulate the three-dimensional primary breakup of a turbulent diesel jet in a nitrogen/methane mixture, under typical dual-fuel conditions. The results obtained demonstrate that the methodology enables robust and accurate simulations of compressible multi-phase/multi-component flows on compact computational stencils without excessive spurious oscillations or significant numerical diffusion/dissipation. The results are published in Computers & Fluids.

Secondly, having studied turbulent jet flow, it is evident that observing the detailed evolution of fuel-gas interfaces is a worthwhile endeavour. It is therefore natural to study the evolution of a single fuel droplet. In high-speed propulsion, it is crucial to consider the effects of real-fluid and shock, which represent a natural transition from normal thermodynamic conditions under incompressible or weakly compressible flow to critical thermodynamic con-

ditions under higher compressible flow. Subsequently, a new research effort is proposed with the aim of implementing a hybrid scheme to address transcritical thermodynamic conditions and to study the shock fuel cylinder/droplet interaction under such conditions. This work represents the first three-dimensional simulation of a cavity-embedded droplet subjected to a normal shock wave at near-critical conditions. Various phenomena are analysed in detail, including the evolution of wave patterns, jet formation, sheet formation, hole appearance, the formation of petal-like structures/lobes, ligament formation, shear-induced entrainment, internal cavity (bubble) rupture, and so on. The results can inform experimental design as, no experiments can currently be performed under such conditions. The results are published in Physical Review Fluids.

Finally, it is natural to consider the effect of gas cavity size and eccentricity on the interaction of shock waves with a cavity-embedded fuel-liquid cylinder under near-critical conditions. A number of scenarios involving both eccentric and concentric cavities, varying cavity radii (0-0.875R), eccentricity angles (0-180°) and distances (0R-0.45R) are analysed. Different phenomena at different stages of evolution are studied, including wave pattern evolution, jet formation, cavity breakup, baroclinic vorticity distribution, and circulation histories. Following these extensive studies, it is postulated that a physically based theoretical model or prediction fit could be developed, with the potential to provide key parameters used in the experiments. A new analytical model for the deposited circulation is then proposed, obtained by appropriately combining the YKZ and ZZ models, which agrees well with numerical results for cases involving smaller cavities. Four predictive fits for the centre-of-mass position of the shocked cylinder under near-critical conditions are also presented. These fits, which are tailored for cases involving cavities of different sizes, eccentricity angles and distances, are as follows: the Time-Size Polynomial Prediction Fit (TS-PPF), the Time-Eccentricity Polynomial Prediction Fit (TE-PPF), the Time-Eccentricity Distance Polynomial Prediction Fit (TED-PPF) and the Connecting Rod Prediction Fit (CRPF). The aforementioned fits demonstrate satisfactory predictive performance and provide valuable insights into the mixing behaviour of liquid fuel sprays in a variety of near-critical environments and high-speed propulsion systems. This leads to the third paper published in Physics of Fluids.

Zusammenfassung

Diese Dissertation untersucht die numerische und physikalische Modellierung kompressibler Mehrkomponentenströmungen unter Berücksichtigung von Oberflächenspannung, Kavitation, Turbulenz und Realfluid-Effekten. Sie zeigt die neuesten Entwicklungen des Cavitation-Solvers an der Technischen Universität München (CATUM). Die zugrunde liegenden physikalischen Phänomene, wie turbulente Strahlströmungen und die Wechselwirkung zwischen Stoßwellen und Treibstofftropfen, sind sowohl für langsam laufende Verbrennungsmotoren, wie Frachtschiffe, Lastwagen und Traktoren, als auch für Hochgeschwindigkeitsantriebssysteme, wie Ramjets und Scramjets, von Bedeutung. Diese anwendungsorientierte Arbeit wurde am Institut für Aerodynamik und Strömungsmechanik der Technischen Universität München durchgeführt. Die Ergebnisse der numerischen Untersuchungen wurden in drei Erstautor-Forschungsartikeln veröffentlicht, die in internationalen, begutachteten Fachzeitschriften erschienen sind.

Zunächst treten im Kontext von Verbrennungsmotoren komplexe, mehrkomponentige, turbulente Strömungen auf. Allerdings neigt der ursprüngliche CATUM-Solver zur Verwischung von Phasengrenzen, und die Oberflächenspannung wird nicht berücksichtigt. Diese Einschränkungen führen zu Dissipation an den Treibstoff-Gas-Grenzflächen. Dies motiviert die Entwicklung einer robusten numerischen Methode, die keine Änderung des Vier-Punkt-Kompaktschemas von CATUM erfordert und gleichzeitig hocheffizient ist. Eine algebraische Methode zur Schärfung von Phasengrenzen, Tangent of Hyperbola for INterface Capturing (THINC), wird in Verbindung mit dem Thermodynamic-Dependent Update (TDU) angewendet, das die Schärfung sowohl von Flüssig-Gas- als auch von Flüssig-Dampf-Grenzflächen ermöglicht. Die mit den Phasengrenzen verbundenen Module von CATUM wurden erweitert, einschließlich der Berücksichtigung von Kavitation, Turbulenz und Oberflächenspannung. Um die Sub-Gitter-Turbulenzmodellierung zu verbessern, wurde ein zentrales Schema vierter Ordnung in den Umschaltprozess integriert, zusammen mit einem modifizierten Diskontinuitätssensor. Darüber hinaus wurden die Effekte der Oberflächenspannung durch ein Continuum Surface Force (CSF)-Modell berücksichtigt. Um störende Oszillationen an den Phasengrenzen zu reduzieren, wurde die Berechnung der Krümmung der Phasengrenze von der Berechnung des Gradienten der Heaviside-Funktion entkoppelt. Die vorgeschlagene Methode wurde auf eine Vielzahl von Fällen angewendet, darunter Blasenoszillation, -advektion, -deformation, Stoß-Blasen-Wechselwirkung, Kollaps einer Dampf-/Gasblase und eine Mehrkomponenten-Schubströmung. Die Ergebnisse eines Falls zur Wechselwirkung zwischen einer Stoßwelle und einem Treibstofftropfen nahe kritischer Bedingungen zeigen eine überlegene Leistung im Vergleich zu den WENO3- und OWENO3-Schemata. Dies bestätigt, dass die vorgeschlagene Methodik in verschiedenen thermodynamischen Zusammenhängen, einschließlich der Peng-Robinson-Zustandsgleichung (PR-EOS), effektiv ist. Schließlich wurde der Ansatz zur Simulation des dreidimensionalen primären Zerfalls eines turbulenten Dieselstrahls in einem Stickstoff/Methan-Gemisch unter typischen Bedingungen eines Dual-Fuel-Systems angewendet. Die erzielten Ergebnisse zeigen, dass die Methodik robuste und präzise Simulationen kompressibler Mehrphasen-/Mehrkomponentenströmungen auf kompakten Rechenstencils ermöglicht, ohne übermäßige störende Oszillationen oder

signifikante numerische Diffusion/Dissipation. Die Ergebnisse wurden in Computers & Fluids veröffentlicht.

Zweitens wurde nach der Untersuchung turbulenter Strahlströmungen deutlich, dass eine detaillierte Analyse der Entwicklung von Treibstoff-Gas-Grenzflächen von großem Interesse ist. Daher liegt es nahe, die Entwicklung eines einzelnen Treibstofftropfens zu untersuchen. Im Hochgeschwindigkeitsantrieb ist es entscheidend, die Effekte von Realfluiden und Stoßwellen zu berücksichtigen, da sie einen natürlichen Übergang von normalen thermodynamischen Bedingungen bei inkompressiblen oder schwach kompressiblen Strömungen zu kritischen thermodynamischen Bedingungen bei stärker kompressiblen Strömungen darstellen. Anschließend wurde ein neues Forschungsvorhaben vorgeschlagen, das die Implementierung eines hybriden Schemas zur Bewältigung transkritischer thermodynamischer Bedingungen sowie die Untersuchung der Wechselwirkung zwischen Stoßwellen und Treibstoffzylindern/-tropfen unter solchen Bedingungen zum Ziel hat. Diese Arbeit stellt die erste dreidimensionale Simulation eines in einer Kavität eingebetteten Tropfens dar, der einer normalen Stoßwelle unter nahezu kritischen Bedingungen ausgesetzt ist. Verschiedene Phänomene werden im Detail analysiert, darunter die Entwicklung von Wellenmustern, Strahlbildung, Blattbildung, das Auftreten von Löchern, die Bildung von blütenblattähnlichen Strukturen/Lappen, die Entstehung von Filamenten, scherspannungsinduzierte Vermischung und die Ruptur der inneren Kavität (Blase). Die Ergebnisse können zur Gestaltung von Experimenten herangezogen werden, da derzeit keine Experimente unter solchen Bedingungen durchgeführt werden können. Die Ergebnisse wurden in Physical Review Fluids veröffentlicht.

Schließlich wird der Einfluss der Gasblasen-Größe und Exzentrizität auf die Wechselwirkung von Stoßwellen mit einem in einer Kavität eingebetteten Treibstoffflüssigkeitszylinder unter nahezu kritischen Bedingungen untersucht. Es werden verschiedene Szenarien analysiert, darunter exzentrische und konzentrische Kavitäten, unterschiedliche Kavitätsradien (0-0.875R), Exzentrizitätswinkel (0-180°) und Abstände (0R-0.45R). Verschiedene Phänomene in unterschiedlichen Entwicklungsstadien werden untersucht, darunter die Entwicklung von Wellenmustern, Strahlbildung, Kavitätszerfall, baroklines Wirbelmuster und Zirkulationsverläufe. Nach diesen umfangreichen Studien wird postuliert, dass ein physikalisch basiertes theoretisches Modell oder eine prädiktive Anpassung entwickelt werden könnte, um wichtige Parameter für Experimente bereitzustellen. Ein neues analytisches Modell zur Berechnung der induzierten Zirkulation wird vorgeschlagen, das durch eine geeignete Kombination der YKZ- und ZZ-Modelle gewonnen wurde und gut mit den numerischen Ergebnissen für Fälle mit kleineren Kavitäten übereinstimmt. Zudem werden vier prädiktive Anpassungen für die Schwerpunktposition eines durch eine Stoßwelle belasteten Zylinders unter nahezu kritischen Bedingungen vorgestellt. Diese Anpassungen, die für Kavitäten unterschiedlicher Größe, Exzentrizitätswinkel und Abstände maßgeschneidert sind, umfassen: die Time-Size Polynomial Prediction Fit (TS-PPF), die Time-Eccentricity Polynomial Prediction Fit (TE-PPF), die Time-Eccentricity Distance Polynomial Prediction Fit (TED-PPF) und die Connecting Rod Prediction Fit (CRPF). Die genannten Anpassungen zeigen zufriedenstellende Vorhersageleistungen und liefern wertvolle Einblicke in das Vermischungsverhalten von flüssigen Treibstoffsprays in einer Vielzahl von nahezu kritischen Umgebungen und Hochgeschwindigkeitsantriebssystemen. Dies führt zum dritten Artikel, der in Physics of Fluids veröffentlicht wurde.

Contents

Chapter 1

Introduction

1.1 Background and Motivation

The quality of fuel and ambient gas mixing plays a significant role in the efficiency of modern fuel injection systems, which are commonly used in cargo ships, trucks, and tractors, as well as high-speed propulsion systems such as ramjets and scramjets. In order to optimise the fuel-gas mixing in propulsion systems with a view to reducing greenhouse gas emissions and achieving sustainability, it is essential to study the characteristics of fuel jet flow, shock-fuel interaction and transcritical flows [30, 31, 46, 129]. These phenomena exert a considerable influence on the efficiency of the combustion process, which in turn has a marked impact on fuel economy and emissions ratings. An understanding of these interactions and the ability to improve them can facilitate significant advancements in propulsion technology, thereby contributing to the development of more sustainable and environmentally friendly transportation solutions.

In order to address the physical characteristics of compressible multi-component flows embedded in the above problems, such as interfacial phenomena, it is necessary to consider the effects of surface tension, cavitation, turbulence and real-fluid effects in numerical and physical modeling with sharpened interfaces. The CAvitation Technical University of Munich (CATUM) solver has demonstrated expertise in addressing cavitation-related problems [45, 158, 184, 185]. However, it has not fully incorporated the aforementioned effects into its framework. One motivation of this thesis is to develop CATUM to address more physics-based industry problems, beyond those related to cavitation, with the use of robust numerical schemes and reduced numerical dissipation.

In the context of jet flow in dual-fuel engines, there are complex multi-component turbulent flows. Nevertheless, it is difficult to avoid the tendency for interface smearing in the original CATUM solver, and surface tension is not included. These limitations result in significant dissipation for the fuel-gas interfaces, making the detailed interface deformation difficult to observe. This has motivated the development of a robust numerical method that does not necessitate a change to the four-stencil compact scheme of CATUM [45, 158, 184, 185] and is highly efficient. An algebraic-based interface sharpening method has been considered, and significant effort has been invested in enhancing the entire interface-related module of CATUM, including the treatment of cavitation, turbulence (implicit large eddy simulation), and surface tension.

Following an investigation into the jet flow, it is evident that observing the detailed evolution of fuel-gas interfaces is a worthwhile endeavour. It is therefore natural to study the evolution of a single fuel droplet [17]. Furthermore, it is imperative to consider the effects of gas cavity, real-fluid and shock, which represent a natural transition from normal thermodynamic conditions under weakly compressible flow to transcritical thermodynamic conditions under higher compressible flow. It is currently challenging to conduct experiments under such conditions. Consequently, the second motivation for undertaking this thesis is to imple-

ment a hybrid scheme to address transcritical thermodynamic conditions and investigate the shock interaction with a cavity-embedded cylinder/droplet at near-critical conditions. This could inform the design of future experiments.

A further motivation for this study is to conduct extensive research on the impact of cavities on the evolution of fuel under transcritical thermodynamic conditions. The objective is to develop physical-based theoretical models and prediction fits, which would enable the acquisition of key parameters (such as deposition circulation, centre-of-mass parameters) used in the experiments. This would be of significant value to the industry.

1.2 Numerical and Physical Modeling of Compressible Multi-component Flows

The simulation of flow processes in propulsion systems typically entails the study of compressible two-phase flows with multi-component fluids. These encompass phenomena such as the deformation of material interfaces, interactions with shock waves, and evaporation and condensation. Two-phase jet flows and droplet breakup in propulsion systems represent practical applications. The discussion on the background and motivation has identified two key issues that will be examined in detail in the subsequent section. The first issue is the reduction of dispassion near the fuel-gas interfaces, while the second is the management of transcritical thermodynamic conditions.

1.2.1 Compressible Multi-component Flows with Interface Sharpening Methods

In essence, two numerical methodologies are typically employed for dealing with interfacial problems encountered in multi-component flows: those that assume sharp interfaces and those that rely on mixture assumptions. Given that the flow field and material properties are typically discontinuous across the interface between different phases or components, the treatment of material boundaries represents a pivotal challenge.

The achievement of sharp interfaces is typically accomplished through the utilisation of various techniques, including front-tracking (FT) [26, 186], level-set methods (LS) [136, 160, 174], and geometric interface reconstruction (GIR) based volume of fluid methods (VOF) [64, 188], such as piecewise-linear interface calculation (PLIC) [207] and the isoAdvector Method [149]. FT attempts to combine the characteristics of both Lagrangian and Eulerian schemes in order to maintain a sharp boundary. In this approach, Lagrangian markers are employed to distinguish the domains occupied by different fluids. However, this approach is computationally expensive, particularly in the context of complex geometries and strong topological deformations of the interface. Moreover, FT methods are not mass-conservative unless additional processing is employed. A traditional LS function is a signed-distance function that represents the shortest distance to the interface, wherein the interface is represented as the zero contour. It is an accurate method for computing surface normals and curvatures with a naturally smooth LS field, and is suitable for determining surface tension. However, the additional steps for reinitialisation and mass conservation involve additional computational cost because the LS function loses its signed distance property after the advection step, and the mass of each phase is not automatically conserved. Furthermore, if the topology changes, it is more expensive. GIR methods could also provide a clear/sharp two-phase interface, but are also computationally expensive.

In general, diffuse interfaces are introduced by phase field models (PF) [24, 69, 70, 84, 126] or (interface capturing type) algebraic interface sharpening (AIS) based models, where

no clear boundary between phases exists and the interface often encompasses more than a single cell. Phase-field methods typically employ the convective Cahn-Hilliard or Allen-Cahn equation to describe interfacial motion and naturally have anti-diffusive characteristics. However, these methods are limited in their applicability to realistic two-phase problems in industry. Examples of such problems include jet flow in dual-fuel combustion engines, transcritical flow with shocks, bubble collapse with shock wave formation. Some recent studies have analysed the conservative phase field model [70] and have made significant progress in shock-free compressible domains. Nevertheless, the utility of the phase field model for the aforementioned objectives has yet to be demonstrated. In general, the AIS model employs the Heaviside function or indicator function to differentiate between distinct phases. The AIS method typically exploits the inherent conservation of mass and the effective capture of changes in interface topology. The various fluid components are artificially induced to mix at the unresolved interface, thereby creating a thin mixing zone. This approach has the significant advantage of allowing a single set of equations to be used to describe the two-phase flow properties throughout the domain, obviating the need for explicit tracking of the sharp interface.

Approaches with diffuse interfaces are very effective and can be used in three-dimensional cases with different fluid components. These diffuse-interface effects approximate the behaviour of a sharp gradient as the size of the mesh approaches zero. Diffuse-interface approaches for the simulation of compressible two-phase flows can be categorised into a number of distinct types, including: the four-equation model, the five-equation model, the Baer-Nunziato model, etc. In the four-equation model [1, 2, 6, 32, 39, 45, 88, 115, 116, 134, 184], the mass fraction is typically employed as the Heaviside function, whereas in the five-equation model [6, 82], the volume fraction is commonly regarded as the Heaviside function. It is observed that the species-mass conservation is consistently upheld for the five-equation model, irrespective of the numerical treatment of the volume fraction of the advection equation. Conversely, the conservative form of the additional species-mass conservation equation must be meticulously achieved in the fully conservative four-equation model. The mass fraction-based four-equation model is capable of accounting for an additional component with an additional species-mass conservation equation, in contrast to the volume fraction-based five-equation model, which necessitates the inclusion of two equations for an additional species (an advection equation for the volume fraction and an equation for species mass conservation). Consequently, the five-equation model requires additional computational effort.

A key benefit of a mass fraction-based four-equation model [1, 2, 6, 32, 39, 45, 88, 113, 115, 116, 134, 155, 184] (in comparison to an LS formulation) is its capacity to accommodate flows where the species front is initially absent but forms during the calculation process (as in chemical reactions, cavitation, or condensation). While gamma-transport based four equation models [166](a combination of mass, momentum, energy and additional advection parameters) are optimal for stiffened gas-type EOS, mass-fraction-based four equation models can be effectively applied to real-fluid models. The principal disadvantage of quasi-conservative models is the poor conservation of species masses, whereby the mass of each species is not accurately conserved [1, 77, 78, 166]. Additionally, the occurrence of artificial temperature spikes has been observed in some instances [78].

Additionally, the Baer-Nunziato equations [11], originally proposed to describe reactive multiphase flow (the transition from deflagration to detonation), are a set of equations used to study compressible multiphase flows [7, 154, 178]. The BN model incorporates mass, momentum and energy conservation equations for each phase, and considers interfacial dynamics between phases. This includes the transfer of mass, momentum and energy between phases.

In general, each phase is considered a compressible fluid in local thermodynamic equilibrium, while allowing for non-equilibrium conditions across the interface within the mixture. This implies that the self-equilibration time scale within each phase is significantly shorter than the equilibration time scale between the phases [12, 113]. The BN model extends beyond traditional four- or five-equation models by incorporating interfacial forces, phase changes and phase compressibility [113, 155, 156], offering a more comprehensive approach to modeling compressible multiphase flows and facilitating a detailed understanding of complex multiphase flows involving gases, liquids or mixtures. BN approaches exhibit high numerical complexity, including detailed interface tracking, and necessitate the use of closure models for interface terms. This considerably complicates their applicability to industrial problems in the dual-fuel domain.

In essence, the approach is grounded in a four-equation model based on the mass fraction, which offers a straightforward means of incorporating additional species (dual-fuel conditions), is well-suited to real-fluid effects, and can be readily applied to complex flows including cavitation.

In the following section, a comprehensive discussion is presented on the advantages of AIS methods, with a particular focus on THINC-based approaches.

AIS methods strive to algebraically reconstruct the two-phase interface or modify the right-hand side (RHS) of the governing equations in order to avoid excessive interfacial diffusion, at relatively low additional computational cost. Examples of such methods include the Flux-Corrected Transport (FCT) scheme [15, 151, 209], post-processing anti-diffusion methods [169, 170], the Tangent of Hyperbola for INterface Capturing (THINC) method [34, 200, 201], Compressive Interface Capturing Schemes for Arbitrary Meshes (CICSAM) [188], additional (artificial) compression term approaches [130, 153, 165, 198], bounded variation or TVD methods [21, 132, 171], ENO or WENO approaches [79, 163, 190], Multi-dimensional Universal Limiters with Explicit Solution (MULES) [38, 98] and High Resolution Interface Capturing schemes (HRIC) [125]. Specifically, adjusting the limiters in the TVD-MUSCL scheme [98] or the weighting coefficients in the WENO scheme [72, 103] can help to reduce the numerical dissipation and avoid oscillations in the discontinuous interface region. Furthermore, the reconstruction of the parameter space near the cell surfaces (S_L and S_R)and the development of specific Riemann solvers ($S^* = f(S_L, S_R)$) can reduce the numerical dissipation at interfaces.

Among the various AIS methods, the THINC-based approaches are promising options because it generally requires less computational effort. In the THINC method presented by Xiao [200], the hyperbolic tangent function was employed to evaluate the numerical flux for the advection equation of the VOF function, with the objective of calculating the moving interface algebraically (without complex geometric reconstruction). To perform multidimensional calculations, the numerical flux for each direction was determined by operator splitting. Subsequently, the research was focused on improving the description of the interface shape and avoiding the surface curvature. Following this, a Boundary Variation Diminishing (BVD) scheme [172] was proposed and the following studies [34–37] focused on selecting different reconstruction candidates to minimize jumps at cell boundaries. BVD typically reconstructs variable candidates for each cell interface and subsequently determines the final candidates, which necessitates additional computational resources and communication time for parallel computations. Given this focus on a robust and compact four-stencil scheme, further details related to BVD are not part of this thesis.

The THINC method has thus far been developed and employed for the simulation of multiphase flows. However, it should be noted that THINC-based methods have been studied to a limited extent for complex compressible multi-component applications involving shock waves, turbulence, cavitation, real-fluid effects and moving interfaces. Daniel [20] employed

THINC in the MUSCL scheme for incompressible multiphase flows. In order to simulate a supersonic liquid jet [112], a five-equation model was combined with a volume fraction THINC when capillary forces were neglected. A five-equation model combined with a density THINC was further implemented to simulate atomization [52]. Nonomura et al. [127] developed the THINC method with two compressible fluids and sharpened the volume fraction only, while Shyue and Xiao [167] presented a single-fluid multi-component flow model and used the reconstructed volume fraction to extrapolate other conservative parameters across the cell interface, both neglecting the surface tension. It is further noted that a recent development (VOF-based) [25] or ongoing work [65, 66] of the THINC-based method is the combination with the AMR technique in multiphase simulation, but it is still not fully capable for the complex compressible simulation involving cavitation flow, turbulent flow and real-fluid effects with increasing computational cost. Furthermore, coupled methods such as THINC-LS [139] and THINC-LS-VOF [89] were developed to enhance the description of interfaces and numerical accuracy. However, they typically necessitate significantly greater computational resources to achieve optimal performance. The aforementioned THINC-based method is typically employed to reconstruct the volume fraction of a five-equation model. In such models, the direct consideration of a Riemann solver of the cell interface is not a common occurrence. Rather, the relationship between pressure and density, as well as internal energy, is decoupled in the reconstruction process. Furthermore, realistic flows, such as viscous terms, surface tension, gravity, real-fluid effects, and cavitation, are typically ignored or not fully considered.

1.2.2 Shock Interaction with Droplet/Cylinder at Transcritical Thermodynamic Conditions

In high-speed propulsion, improving the interaction between shock waves and the fuel-oxidiser interface is critical to improving mixing, reducing combustion distances and reducing engine volumes. Shock interactions with fuel-gas interfaces are particularly relevant in high-speed propulsion systems [30, 46], such as ramjets and scramjets, especially during processes such as start-up, mixing and combustion of high-speed liquid fuel injection. When a high-speed fuel jet enters a combustion chamber at a pressure close to the critical pressure of the fuel, it can induce shock waves that interact with the fuel. The study of such interactions provides valuable insights for improving fuel mixing in propulsion systems.

Near the critical point, it is important to consider "transcritical" properties, where the pressure in the chamber approaches the critical pressure of the fuel. Under these conditions, higher temperatures can cause a transition from a liquid-like state to gas-like behavior. At transcritical conditions, both supercritical (diffusion-controlled) behavior and subcritical (two-phase) properties can occur [31, 129]. For example, the critical properties of n-dodecane are defined by a critical pressure (p_c) of 1.82 MPa and a critical temperature (T_c) of 658.1 K. When n-dodecane fuel is injected into a combustion chamber at supercritical pressure ($p/p_c > 1$) and at a temperature below the critical temperature ($T/T_c < 1$), it mixes with hot ambient air/Nitrogen, causing the fuel to undergo a transformation from a liquid-like fluid to a gas-like supercritical fluid by crossing the Nishikawa-Widom line. This scenario [9, 107, 135], known as "pseudo-boiling," occurs at higher supercritical temperatures and pressures, where fuel fluids exhibit ideal gas behavior when their compressibility factor is equal to one.

While there have been numerous studies of transcritical fluids in low-speed convective environments, where fluid evaporation is significantly influenced by viscous effects and heat conduction [22, 28, 117, 119, 204–206], research on the interaction of transcritical fuel cylinders/droplets with shock waves or high-speed flows is limited. In these high-speed flows,

viscous diffusion, thermal diffusion, and surface tension forces are expected to have negligible effects. Obtaining detailed experimental data on such flows, particularly at high pressures and temperatures, remains a challenge. Therefore, numerical experiments have become essential for such flows at near-critical conditions in high-pressure, high-speed propulsion systems.

Classical simulations of shock-bubble interactions (SBIs) [57, 66, 90, 93–95, 128, 140, 145, 179, 180, 210] and shock-droplet interactions (SDIs) [32, 42, 50, 54, 120, 157, 189, 195] have been extensively studied, focusing primarily on scenarios involving pure droplets or pure bubbles. However, these studies have predominantly investigated subcritical and supercritical conditions, with limited investigation of near-critical or transcritical conditions. Fluids near their critical points exhibit distinct physical properties that differ significantly from classical liquid droplets or ideal gas bubbles [1, 8, 144], requiring a unique approach. In SDIs related studies, various processes such as primary shock impingement, droplet deformation and fragmentation have been extensively studied in the literature [33, 140, 145, 147, 177, 208]. Duke-Walker [44] investigated the effects of droplet evaporation and break-up in the context of mixing driven by shock-induced multiphase instabilities. Meng et al [120] investigated the interaction of shock waves with a water droplet, with detailed structures validated against experimental data. Kaiser et al [80] carried out numerical investigations of water droplet breakup induced by shock impingement and the resulting interface deformation. Sharma [161] established a criterion for the transition process between the shear-induced entrainment mode and the Rayleigh-Taylor piercing mode during droplet breakup. It is noteworthy that investigations [16, 17, 187] have not addressed the detailed simulation of real three-dimensional interface deformation at near-critical conditions.

Moreover, the interaction between shock waves and droplets containing gas or vapor-filled cavities, as well as the interaction between shock waves and bubbles containing droplets, represents a relatively unexplored area within the context of SDIs and SBIs. A significant knowledge gap remains regarding the interaction between shock waves and droplets containing embedded gas cavities, particularly under near-critical conditions and in three-dimensional scenarios. Previous investigations in this field have primarily focused on scenarios characterised by low temperatures and low pressures [48, 102, 123, 162, 191, 193, 199]. For example, the interaction of shock waves with droplets containing gas bubbles has been explored under ambient conditions [123], thereby elucidating the impact of bubble collapse on shock-droplet interactions. Wang's work [191] investigated the shock-accelerated gas ring, thereby providing insights into its evolution and proposing a straightforward method for predicting circulation. Feng [48] conducted an experimental investigation into the shock interaction with an SF_6 ring, examining the effects of the internal gas cylinder on the evolution of the SF_6 ring with various radius ratios. Liang [102] conducted an experimental examination of the shock interaction with a water droplet containing an internal vapor cavity. In the numerical realm, Xiang [199] conducted a numerical analysis of the shock interaction with a water column harboring an internally positioned air cavity.

It is important to note that shock-cylinder interactions (SCIs) are more accessible to experimental study than SDIs and SBIs. SCIs are valuable studies as the liquid/gas cylinder spans a wide range of angles between pressure and density gradient, thereby supporting various degrees of baroclinic production. SCIs have been extensively studied for many years [40, 41, 57, 67, 68, 99, 168, 194, 196], both numerically and experimentally. However, these studies have predominantly explored subcritical and supercritical conditions, with limited investigation into transcritical conditions. Previous investigations in this field have mainly focused on scenarios with low temperatures and pressures at ambient conditions [48, 102, 105, 162, 193, 195, 199, 202]. The interaction between shock waves and cylinders containing gas cavities is rarely explored for transcritical cases.

In the present thesis, the pre-shock pressure of nitrogen is 6MPa and the temperature is 650K, which markedly diverge from the previously referenced cases. Obtaining detailed experimental data on such flows remains a challenge. It is therefore evident that numerical experiments have become an indispensable tool for the study of such flows at near-critical conditions in high-pressure, high-speed propulsion systems. This highlights a significant gap in the understanding of the interaction between shock waves and cavity-embedded cylinders/droplets with a three-dimensional nature of droplets and varying parameters of the cavities at such conditions. One of the objectives of this thesis is to provide insights that can be applied in a variety of transcritical environments and high-speed propulsion systems.

1.3 Outline

The thesis is divided into five chapters and one appendix.

Chapter 1 introduces the motivation and application of the studies, as well as the numerical and physical problems encountered in the context of compressible multi-component flows. The interface sharpening method for compressible multi-component flows and shock-droplet and shock-cylinder interactions at transcritical thermodynamic conditions are the main contents of this chapter.

Chapter 2 presents the numerical and physical modeling used to deal with problems encountered in the compressible multi-component flows. This includes a comprehensive account of the governing equations, the finite volume method, flux calculation, turbulence and surface tension modeling, thermodynamic relationshiops, time integration method and the real-fluid hybrid scheme. Furthermore, reviews are integrated into the relevant sections.

Chapters 3 and 4 present the achievements and research results separately.

Chapter 5 synthesizes the pivotal findings and proffers prospective avenues for future investigations.

The appendix shows the journal articles and copyright permissions for reproduced material.

Chapter 2

Numerical and Physical Modeling

2.1 Governing Equations

A typical four-equation model, which incorporates viscous, surface tension and gravity effects, is depicted as flowing,

$$\partial_t \mathbf{U} + \nabla \cdot [\mathbf{C}(\mathbf{U}) + \mathbf{S}(\mathbf{U})] = \mathbf{Q}, \tag{2.1}$$

where, the state vector $\mathbf{U} = [\rho, \rho\mathbf{u}, \rho E, \rho\xi_i]^T$ contain the conserved variables for density, momentum, total energy and gas components. $\mathbf{C}(\mathbf{U})$, $\mathbf{S}(\mathbf{U})$ and $\mathbf{Q}$ refer to convective term, stress term and source term, respectively,

$$\mathbf{C}(\mathbf{U}) = \mathbf{u} \begin{bmatrix} \rho \\ \rho\mathbf{u} \\ \rho H \\ \rho\xi_i \end{bmatrix}, \mathbf{S}(\mathbf{U}) = \begin{bmatrix} 0 \\ p\mathbf{I} - \boldsymbol{\tau} \\ -\mathbf{u}\boldsymbol{\tau} - k_c \nabla T \\ 0 \end{bmatrix}, \text{and} \quad \mathbf{Q} = \begin{bmatrix} 0 \\ \rho\mathbf{f} \\ \mathbf{u}\rho\mathbf{f} \\ 0 \end{bmatrix}, \tag{2.2}$$

where $\mathbf{I}$ refers to the unit tensor; $\rho H = \rho E + p$ is the total enthalpy; $\boldsymbol{\tau}$ is the viscous stress tensor, $\boldsymbol{\tau} = \mu(\nabla\mathbf{u} + (\nabla\mathbf{u})^T - \frac{2}{3}(\nabla \cdot \mathbf{u})\mathbf{I})$ and μ refers to the dynamic viscosity; k_c refers to the thermal conductivity; $\mathbf{f}$ refers to the volume force.

2.2 Finite Volume Method

The main idea of finite volume method (FVM) is to discretize the spatial domain into a finite number of control volumes and apply the conservation laws to each control volume. The Gauss' theorem is applied. For the governing equations $\partial_t\mathbf{U} + \nabla \cdot \mathbf{F}(\mathbf{U}) = 0$, where $\mathbf{F}(\mathbf{U}) = \mathbf{C}(\mathbf{U}) + \mathbf{S}(\mathbf{U})$,

$$\partial_t \int_\Omega \mathbf{U}(\mathbf{x}, t) \, dV + \int_{\partial\Omega} \mathbf{F}(\mathbf{U}, \mathbf{x}, t) \, dA = 0, \tag{2.3}$$

where Ω denotes the control volume with the surface $\partial\Omega$. Equation (2.3) is solved numerically by spatially discretizing the computational domain into N grid cells i with a control volume Ω_i with volume $V_i = \int_{\Omega_i} dV$. The volume-averaged solution of a grid cell i can be presented as

$$\overline{\mathbf{U}}_i(t) = \frac{1}{V_i} \int_{\Omega_i} \mathbf{U}_i(\mathbf{x}, t) \, dV_i. \tag{2.4}$$

The surface integral for $\mathbf{F}(\mathbf{U}, \mathbf{x}, t)$ in Eq. (2.3) is numerically approximated as

$$\int_{\partial \Omega_i} \mathbf{F}(\mathbf{U}, \mathbf{x}, t)\, dA = \sum_j (\widetilde{\mathbf{F}}_j \cdot \mathbf{n}_j) A_j, \tag{2.5}$$

where the numerical flux $\widetilde{\mathbf{F}}$ approximates the physical flux $\mathbf{F}$, all cell faces j form $\partial \Omega_i$ with area A_j and unit normal $\mathbf{n}_j$. A semi-discretized form of Eq. (2.3) is then obtained

$$\partial_t \overline{\mathbf{U}}_i(t) \approx -\frac{1}{V_i} \sum_j (\widetilde{\mathbf{F}}_j \cdot \mathbf{n}_j) A_j. \tag{2.6}$$

The Equation (2.6) can be solved using a proper reconstruction approach for $\widetilde{\mathbf{F}}$ (see Flux Computation) and a time integration method (see Time integration).

2.3 Riemann Solver

An HLLC [181] Riemann solver is provided as an option. The basic idea of the HLLC solver is to approximate the solution of the Riemann problem by a piecewise constant solution with three states separated by two intermediate waves. The HLLC flux can be written as:

$$\mathbf{F}_{1/2}^H = \begin{cases} \mathbf{F}_L, & \text{if } 0 \leq S_L \\ \mathbf{F}_{*L}, & \text{if } S_L \leq 0 \leq S_* \\ \mathbf{F}_{*R}, & \text{if } S_* \leq 0 \leq S_R \\ \mathbf{F}_R, & \text{if } 0 \geq S_R \end{cases}, \tag{2.7}$$

where $\mathbf{F}_L$ and $\mathbf{F}_R$ are the fluxes on the left and right states, respectively. S_L and S_R are the wave speeds of the left and right-moving waves. S_* is the speed of the contact wave. $\mathbf{F}_{*L}$ and $\mathbf{F}_{*R}$ are the intermediate fluxes in the star region.

For the intermediate speed S_*, wave speed S_L and S_R.

$$S_* = \frac{p_R - p_L + \rho_L u_L (S_L - u_L) - \rho_R u_R (S_R - u_R)}{\rho_L (S_L - u_L) - \rho_R (S_R - u_R)}, \tag{2.8}$$

where wave speed $S_L = \min\{u_L - c_L, u_R - c_R\}$, $S_R = \max\{u_L + c_L, u_R + c_R\}$. The intermediate fluxes $\mathbf{F}_{*L}$ and $\mathbf{F}_{*R}$.

$$\mathbf{F}_{*K} = \mathbf{F}_K + S_K (\mathbf{U}_{*K} - \mathbf{U}_K), \tag{2.9}$$

where $K = L$ or R, and the intermediate states are shown below

$$\mathbf{U}_{*K} = \rho_K \left(\frac{S_K - u_K}{S_K - S_*} \right) \begin{bmatrix} 1 \\ S_* \\ v_K \\ w_K \\ \frac{E_K}{\rho_K} + (S_* - u_K)\left[S_* + \frac{p_K}{\rho_K (S_K - u_K)} \right] \end{bmatrix}. \tag{2.10}$$

2.4 Flux Computation

A compact four-cell stencil is employed in CATUM to reconstruct the cell face values to obtain the numerical flux $\widetilde{\mathbf{F}}$, as sketched in Figure 2.1. In the previous CATUM version, an upwind-biased scheme is used for discontinuity regions containing the shock waves, steep gradients or
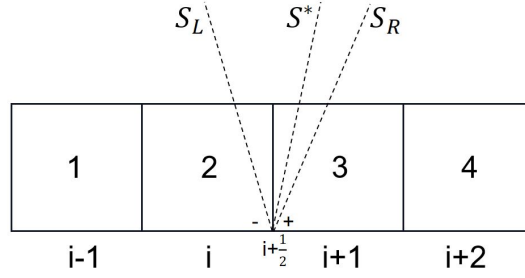
Figure 2.1: Sketch of the four-cell stencil.

pseudo phase-boundaries, and the higher-order central scheme can only be used in smooth regions. In the following, the THINC-TDU method is used to improve these schemes. An improved sensor functional is applied to detect the smoothness of the regions.

2.4.1 Upwind-biased Scheme Improved by THINC-TDU Method

2.4.1.1. Description of Riemann Solver

To overcome the low Mach number problem, the interface pressure reconstruction (asymptotically consistent pressure flux definition) and the modified numerical flux of Schmidt [158] is employed. It is important to note that most liquid-vapor two-phase flows exhibit low Mach numbers in regions where only the pure liquid phase is present. However, as the speed of sound in liquid-vapor mixtures significantly decreases, there arises a need for a robust flux formulation suitable for (very) high Mach numbers in such mixtures. The flux function selected has been shown to meet both of these requirements, as documented in the references. Nevertheless, in simulations involving supersonic or hypersonic gas flows, it is advisable to substitute this flux function with alternative methods, such as HLLC or the ROE flux.

$$p^*_{i+\frac{1}{2}} = \frac{p_L + p_R}{2}, \tag{2.11}$$

The numerical velocity $u^*_{i+\frac{1}{2}}$ is calculated as

$$u^*_{i+\frac{1}{2}} = \frac{\rho_L c_L u_L + \rho_R c_R u_R + p_L - p_R}{\rho_L c_L + \rho_R c_R}. \tag{2.12}$$

2.4.1.2. Reconstruction of Interface Variables

At distinct interfaces between a liquid and a gaseous component or mixture, THINC is used to reconstruct the mass fraction for the interface free-gas component(s) along with TDU to consistently reconstruct related thermodynamic quantities. Regions that do not contain (sharp) interfaces are treated as single fluid and MUSCL type reconstructions along with proper limiters are used.

Let ξ_{Gas} denote a scalar quantity, such as the mass fraction of a gas component. Let ξ^1_{Gas} through ξ^4_{Gas} be the cell averaged scalars in cells 1 to 4 as sketched in Figure 2.1.

· Discontinuous interface between cells 2 and 3

In order to compute the flux across the cell interface between cells 2 and 3,the left and right side values of the scalar ξ_{Gas} are reconstructed as

$$\xi_{\text{Gas}}^{L} = \min(\xi_{\text{Gas}}^{1}, \xi_{\text{Gas}}^{3}) + \frac{\max(\xi_{\text{Gas}}^{1}, \xi_{\text{Gas}}^{3}) - \min(\xi_{\text{Gas}}^{1}, \xi_{\text{Gas}}^{3})}{2} \left(1 + \theta \frac{\tanh(\beta) + E}{1 + E \cdot \tanh(\beta)}\right), \quad (2.13)$$

where

$$\theta = \begin{cases} 1 & \text{if } \xi_{\text{Gas}}^{3} \geq \xi_{\text{Gas}}^{1} \\ -1 & \text{otherwise} \end{cases}, \quad E = \frac{\exp(\theta\beta(2F-1))/\cosh(\beta) - 1}{\tanh(\beta)},$$

$$F = \frac{\xi_{\text{Gas}}^{2} - \min(\xi_{\text{Gas}}^{1}, \xi_{\text{Gas}}^{3}) + \gamma}{\max(\xi_{\text{Gas}}^{1}, \xi_{\text{Gas}}^{3}) + \gamma}.$$

Similarly,

$$\xi_{\text{Gas}}^{R} = \min(\xi_{\text{Gas}}^{2}, \xi_{\text{Gas}}^{4}) + \frac{\max(\xi_{\text{Gas}}^{2}, \xi_{\text{Gas}}^{4}) - \min(\xi_{\text{Gas}}^{2}, \xi_{\text{Gas}}^{4})}{2}(1 + \theta E), \quad (2.14)$$

where

$$\theta = \begin{cases} 1 & \text{if } \xi_{\text{Gas}}^{4} \geq \xi_{\text{Gas}}^{2} \\ -1 & \text{otherwise} \end{cases}, \quad E = \frac{\exp(\theta\beta(2F-1))/\cosh(\beta) - 1}{\tanh(\beta)},$$

$$F = \frac{\xi_{\text{Gas}}^{3} - \min(\xi_{\text{Gas}}^{2}, \xi_{\text{Gas}}^{4}) + \gamma}{\max(\xi_{\text{Gas}}^{2}, \xi_{\text{Gas}}^{4}) + \gamma}.$$

γ is a small number to avoid division by zero and the parameter $\beta = 1.6$ was found to give suitable results. The literature presented in the introduction section discusses values for β in the range between 1.6 and 3.

· Regions without discontinuous interfaces

In smooth regions, an MUSCL type reconstruction with proper limiters is used. Free-gas mass fractions are described here to illustrate the process. They are discretized by a second order upwind biased reconstruction with proper slope limiter.

In order to compute the flux across the interface between cells 2 and 3, left and right hand scalar values $\xi_{Gas}^{L} = \xi_{Gas}^{2} + \frac{1}{2}f\left(r_{i+\frac{1}{2}}^{-}\right)(\xi_{Gas}^{2} - \xi_{Gas}^{1})$ and $\xi_{Gas}^{R} = \xi_{Gas}^{3} - \frac{1}{2}f\left(r_{i+\frac{1}{2}}^{+}\right)(\xi_{Gas}^{4} - \xi_{Gas}^{3})$ represents the slope limiter function that the ratio of upwind to central differences could be adjusted according to various limiters, as shown in the Table 2.1.

The slope function is decided according to the upwind direction. If the upwind direction is in the positive direction, $r_{i+\frac{1}{2}}^{-} = (\xi_{\text{Gas}}^{2} - \xi_{\text{Gas}}^{1})/(\xi_{\text{Gas}}^{3} - \xi_{\text{Gas}}^{2})$, otherwise, $r_{i+\frac{1}{2}}^{+} = (\xi_{\text{Gas}}^{4} - \xi_{\text{Gas}}^{3})/(\xi_{\text{Gas}}^{3} - \xi_{\text{Gas}}^{2})$. Together with the following TDU idea, the All-Mach THINC-TDU method is obtained.

· TDU idea

Other interfacial parameters are updated based on the interfacial pressure and interfacial gas mass fraction according to the thermodynamic equilibrium function, so that the numerical discrete format of the indicator matches the discrete density format and thermodynamic consistency is maintained $\rho_{i+\frac{1}{2}} = f(p_{i+\frac{1}{2}}, \xi_{i+\frac{1}{2},\text{Gas1}}, \xi_{i+\frac{1}{2},\text{Gas2}})$.

Table 2.1: Limiters for scalar transportation.

Name	Expressions
VanAlbada's limiter [5]	$f(r) = \frac{r+r*r}{1.0+r*r}$
VanLeer's limiter [96]	$f(r) = \frac{r+abs(r)}{1.0+abs(r)}$
MinMod limiter [148]	$f(r) = \max(0.0, \min(1.0, r))$
Chatkravathy limiter [23]	$f(r) = \max(0.0, \min(1.0, 4r))$
Monotonized Central (MC) limiter [97]	$f(r) = \max(0.0, \min(2.0, 2r, 0.5 * (1.0 + r)))$
Koren's limiter [87]	$f(r) = \max(0.0, \min(2.0, 2r, (1.0 + 2.0 * r)/3.0))$

Another option is to reconstruct the density and then update the mass fraction according to the function $\xi_{i+\frac{1}{2},\text{Gas1}}$ & $\xi_{i+\frac{1}{2},\text{Gas2}} = f(p_{i+\frac{1}{2}}, \rho_{i+\frac{1}{2}})$. Then the volume fraction is obtained according to thermodynamic relations $\alpha_{i+\frac{1}{2},\text{Gas1}} \& \alpha_{i+\frac{1}{2},\text{Gas2}} = f(\rho_{i+\frac{1}{2}}, p_{i+\frac{1}{2}}, \xi_{i+\frac{1}{2},\text{Gas1}}, \xi_{i+\frac{1}{2},\text{Gas2}})$. Besides, reconstruction methods can take internal energy into account, see Appendix B of [73].

2.4.1.3. Sharpening the Liquid-vapor Interface

Moreover, in cases of cavitation/bubble collapse with liquid and liquid-vapor components, it is difficult to sharpen the liquid-vapor two-phase interface directly because the volume fraction of vapor is determined according to the barotropic relations, while in cases with liquid and non-condensable gas components, the gas-liquid two-phase interface is sharpened according to the above steps. Here, the procedure for sharpening the liquid-vapor two-phase interface is further elaborated.

Remark 1. For regions where liquid-vapor two-phase interface are detected by a sensor, or a discontinuous liquid-vapor interface region meets the requirements $\epsilon < \alpha < 1 - \epsilon$ and $(\alpha_i - \alpha_{i-1})(\alpha_i - \alpha_{i+1}) > 0$, where ϵ is a small positive parameter comparing with α_i, the density is constructed by the THINC-based idea,

$$\rho^L = \min(\rho^1, \rho^3) + \frac{\max(\rho^1, \rho^3) - \min(\rho^1, \rho^3)}{2} \left(1 + \theta \frac{\tanh(\beta) + E}{1 + E \cdot \tanh(\beta)}\right), \quad (2.15)$$

herein

$$\theta = \begin{cases} 1 & \text{if } \rho^3 \geq \rho^1 \\ -1 & \text{otherwise} \end{cases}, \quad E = \frac{\exp(\theta\beta(2F-1))/\cosh(\beta) - 1}{\tanh(\beta)}, \quad F = \frac{\rho^2 - \min(\rho^1, \rho^3) + \gamma}{\max(\rho^1, \rho^3) + \gamma}.$$

$$\rho^R = \min(\rho^2, \rho^4) + \frac{\max(\rho^2, \rho^4) - \min(\rho^2, \rho^4)}{2} (1 + \theta E), \quad (2.16)$$

where

$$\theta = \begin{cases} 1 & \text{if } \rho^4 \geq \rho^2 \\ -1 & \text{otherwise} \end{cases}, \quad E = \frac{\exp(\theta\beta(2F-1))/\cosh(\beta) - 1}{\tanh(\beta)}, \quad F = \frac{\rho^3 - \min(\rho^2, \rho^4) + \gamma}{\max(\rho^2, \rho^4) + \gamma}.$$

γ is a small number to avoid division by zero and the parameter $\beta = 1.6$ was found to give suitable results.

Subsequently, according to the barotropic relations, the vapor volume fraction is obtained. Other parameters like the speed of sound need also to be updated accordingly. Modified sensors can be used to detect liquid-vapor two-phase regions, which are introduced in Appendix D of [73].

Remark 2.   For complex cases with liquid, liquid vapor, non-condensable gas, firstly, THINC is applied for mass fraction of non-condensable gas of liquid-gas two phase interface $\xi_{i+\frac{1}{2},\text{Gas1}}$, $\xi_{i+\frac{1}{2},\text{Gas2}}$. Secondly, TDU is applied to obtain density of liquid-gas two phase interface, i.e. $\rho_{i+\frac{1}{2}} = f(p_{i+\frac{1}{2}}, \xi_{i+\frac{1}{2},\text{Gas1}}, \xi_{i+\frac{1}{2},\text{Gas2}})$; then THINC is applied for the density of liquid-vapor two phase interface ρ^* (*Remark 1*). Finally, TDU is applied to obtain vapor of liquid-liquid vapor two phase interface $\alpha_{v,i+\frac{1}{2}} = f(p_{i+\frac{1}{2}}, \rho_{i+\frac{1}{2}}, \xi_{i+\frac{1}{2},\text{Gas1}}, \xi_{i+\frac{1}{2},\text{Gas2}})$ as well as other parameters like speed of sound.

2.4.2   Higher-order Central Scheme Improved by THINC-TDU Method

In order to include the turbulence modeling, a high order improvement of All-Mach THINC-TDU is proposed with iLES approach, two extra gas components as well as modified sensor. For the iLES scheme of the Ref. [45], if discontinuous region is detected by sensor, upwind-biased reconstruction would be adopted. While in current scheme, the cell interface value reconstruction procedure is switched among an upwind-biased, a centered reconstruction and a THINC-based scheme. And TDU idea is adopted to continually keep the thermodynamic relationship coupled among variables.

· **Upwind-biased reconstruction scheme**

Procedures (Regions without discontinuous interfaces) shown in last section are adopted for the upwind-biased reconstructions of variables.

· **Central reconstruction scheme**

The above upwind-biased scheme has intrinsic numerical dissipation, thus the central reconstruction scheme is needed to reduce dissipation. And proper sensor function is used to switch between candidate schemes. A linear fourth order central scheme is applied,

$$\Phi_{i+1/2}^{*,C} = [u^*, v^*, w^*, p^*]_{i+1/2}^{C} = \frac{1}{12}\left[7\left(\overline{\Phi}_i + \overline{\Phi}_{i+1}\right) - \overline{\Phi}_{i-1} - \overline{\Phi}_{i+2}\right], \tag{2.17}$$

$$\Phi_{i+1/2}^{*,C} = [\rho^*]_{i+1/2}^{C} = \frac{1}{2}\left(\Phi_{I-1/2}^{*} + \Phi_{I+1/2}^{*}\right). \tag{2.18}$$

· **THINC-based reconstruction scheme**

In order to compute the flux across the cell interface between cells 2 and 3, left and right hand side values of the scalar ξ_{Gas} are reconstructed as the equations from (2.13) to (2.14) shown in last section. It is also noted that discontinuous two-phase interface region generally meet the requirements $\epsilon < \overline{\xi}_i < 1-\epsilon$ and $\left(\overline{\overline{\xi}}_i - \overline{\overline{\xi}}_{i-1}\right)\left(\overline{\overline{\xi}}_{i+1} - \overline{\overline{\xi}}_i\right) > 0$, where ϵ could be a small positive parameter comparing with $\overline{\xi}_i$.

· **Modified sensor**

This newly modified discontinuity sensor is used to identify the discontinuous region. The flow field smoothness is identified via a function of smooth sensor, which works as a switch

to change the type of the reconstruction method for the primitive variables $u, v, w, p, \rho, \xi_{\text{Gas1}}$, ξ_{Gas2} on the cell interface. The primitive variables on the cell interface denote:

$$
\begin{aligned}
\Phi^*_{i+1/2} &= [1-f(\theta)]\Phi^{\text{smooth}} + f(\theta)\Phi^{\text{discontinues}} \\
&= [1-f(\theta)]\Phi^{*,C}_{i+1/2} + f(\theta)\left((1-\sigma)\Phi^{*,U}_{i+1/2} + \sigma\Phi^{*,Th}_{i+1/2}\right),
\end{aligned}
\tag{2.19}
$$

where σ could be adjustable according to needed: generally for reconstruction step of pressure and velocity it becomes zero; for reconstruction step of two phase interface region, it becomes one while for other region it becomes zero.

Specifically, the vorticity-dilatation sensor developed by Ducros [43] is adopted to detect the compressible shock and expansion waves in present fully compressible flow: $\theta^D = (\nabla \cdot \boldsymbol{u})^2/(\nabla \cdot \boldsymbol{u})^2 + (\nabla \times \boldsymbol{u})^2 + \epsilon)$, where ϵ denotes a very small value ($\epsilon = 10^{-20}$), making denominator non-zero. Two-phase interface are detected with the variation of the total gas volume fraction in all three spatial directions: $\theta^{\text{Gas}} = \text{var}_i(\text{Gas}) + \text{var}_j(\text{Gas}) + \text{var}_k(\text{Gas})$, where $\text{var}_i(\text{Gas}) = \left\| \alpha_{\text{Gas1},i} + \alpha_{\text{Gas2},i} - \left(\alpha_{\text{Gas1},i-1} + \alpha_{\text{Gas2},i-1}\right)\right\| + \left\| \alpha_{\text{Gas1},i+1} + \alpha_{\text{Gas2},i+1} - \left(\alpha_{\text{Gas1},i} + \alpha_{\text{Gas2},i}\right)\right\|$. Same expressions are adopted for vapor volume fraction and its detector is denoted as θ^v.

Subsequently, the switch criteria is given:

$$
f(\theta^D, \theta^\alpha, \theta^{\text{Gas}}) = \begin{cases} 1, & \text{if } \theta^D > \theta^D_{th} \parallel \theta^\alpha > \theta^\alpha_{th} \parallel \theta^{\text{Gas}} > \theta^{\text{Gas}}_{th} \\ 0, & \text{others} \end{cases}.
\tag{2.20}
$$

It means that if one or more sensor exceeds its threshold value ($\theta^D > \theta^D_{th}$ or/and $\theta^\alpha > \theta^\alpha_{th}$ or/and $\theta^{\text{Gas}} > \theta^{\text{Gas}}_{th}$), the numerical scheme switches to the discontinuous reconstructions $\Phi^*_{i+1/2} = \Phi^{\text{discontinues}} = (1-\sigma)\Phi^{*,U}_{i+1/2} + \sigma\Phi^{*,Th}_{i+1/2}$. The threshold values $\theta^D_{th} = 0.95$ is suggested by Egerer et al. [45] and $\theta^{\text{Gas}}_{th} = 0.4$ is for the volume fraction of total gas phase suggested by Trummler et al. [184]. And these proposed modifications could help to avoid pressure oscillations while keeping contact waves crisp without artificial smearing.

Specifically, for smooth region, velocity and pressure adopt the linear fourth order reconstruction process, while a linear second order central approximation reconstruction is implemented for the density, internal energy (if have), as well as two additional mass fraction field. For discontinuous fields, an upwind biased reconstruction is generally implemented $\Phi^{\text{discontinues}} = \Phi^{*,U}_{i+1/2}$. Generally, velocity components are reconstructed using the third order slope limiter Koren [87] and the thermodynamic quantities density, pressure, internal energy (if have), two additional mass fraction are reconstructed using the second order Minmod slope limiter [148]. It should be noted that the new mass fraction ξ generally keep the same reconstruction scheme of density, $\xi^{\text{discontinues}} = \xi^{*,U}_{i+1/2}$. While in the discontinuous region of two phase interface, instead of using upwind biased reconstruction with slope limiter for two additional mass fraction (or density), THINC is combined for mass fraction (or density) $\xi^{\text{discontinues}} = (1-\sigma)\xi^{*,U}_{i+1/2} + \sigma\xi^{*,Th}_{i+1/2}$, and TDU idea is then adopted for density (or mass fraction) $\rho^{\text{discontinues}} = f(\xi^{\text{discontinues}}, \rho^{\text{discontinues}})$. In this way, variables are updated consistently, interface is sharpened and pressure oscillation is avoided.

Besides, the transport velocity and interface pressure are represented as

$$
u^* = (1-f(\theta))\left(u^{*,C}_{i+1/2} - \frac{\Delta^3 p^*_{i+1/2}}{I_L + I_R}\right) + f(\theta)\frac{I_L u_L + I_R u_R + p_L - p_R}{I_L + I_R},
\tag{2.21}
$$

$$
p^* = (1-f(\theta))p^{*,C}_{i+1/2} + f(\theta)\left(\frac{p_L + p_R}{2}\right),
\tag{2.22}
$$

where $I_L = \left((3\overline{\rho}_i + \overline{\rho}_{i+1}) \cdot \max(c_{l,i}, c_{l,i+1})\right)/4$, $I_R = \left((\overline{\rho}_i + 3\overline{\rho}_{i+1}) \cdot \max(c_{l,i}, c_{l,i+1})\right)/4$. $\Delta^3 p^*_{i+1/2}$ is an approximation of the third pressure derivative, the acoustic impedances are I_L and I_R, $\max(c_{l,i}, c_{l,i+1})$ is the maximum liquid speed of sound.

Other procedures (Remarks) are consistent with last section. Through complete implementation, liquid-liquid vapor and liquid-gas two phase interface are sharpened and dispersion of discontinuous region are reduced.

This higher-order scheme is less dissipative and thus suitable for LES of turbulent flows. The incorporation of a regularisation term renders it capable of sub-grid-scale modeling, as demonstrated in the subsequent turbulence modeling section.

2.5 Turbulence Modeling

For turbulence modeling, a high order improvement of THINC-TDU is proposed. To model the effects of sub-grid turbulence in the current four equation model, an implicit large eddy simulation (iLES) method is used. The iLES approach for compact stencils proposed by Egerer et al. [45] was based on the Adaptive Local Deconvolution Method (ALDM) by Adams et al. [3] and Hickel et al. [60, 62] to deal with resolved sub-grid turbulence. The truncation error of the discretization scheme is learned from the data to serve as a sub-grid scale (SGS) model for turbulence. Hickel et al. [62, 63] also developed a compressible version of ALDM, with shock capturing abilities while smooth pressure waves and turbulence are propagated without excessive numerical dissipation. More details related to ALDM are given in the work of Hickel [59–61] and Egerer et al. [45]. The ALDM method has been used by Örley [133, 134], Trummler [184, 185] in the two phase flow, which proves that it is a proper method in solving the fully compressible two phase turbulent flow. Based on previous work and in order to include the turbulence modeling, higher-order central scheme is improved by THINC-TDU method, in which the ALDM reconstruction is implemented to the momentum equation.

Here is a brief summary of the iLES method for a scalar nonlinear transport equation,

$$\frac{\partial u}{\partial t} + \frac{\partial}{\partial x} f(u) = 0. \tag{2.23}$$

And a linear low-pass filter operation could be represented as [62]

$$\overline{u}(x) = \int_{-\infty}^{+\infty} G(x - x') u(x') dx' = G * u. \tag{2.24}$$

By projecting the filtered continuous function onto the numerical grid $x_N = \{x_i\}$, the LES discretization of the transport equation is obtained as

$$\frac{\partial \overline{u}_N}{\partial t} + G * \partial_x f_N(u_N) = \epsilon_{\text{sgs}}. \tag{2.25}$$

And the sub-grid scale error/residual arises from the nonlinearity of $f(u)$ and is obtained as $\epsilon_{\text{sgs}} = G * \partial_x f_N(u_N) - G * \partial_x f_N(u)$, in which the inverse-filter operation $u_N = G^{-1} * \overline{u}_N$.

A finite-volume discretization could be presented as

$$\frac{\partial \overline{u}_N}{\partial t} + G * \partial_x \tilde{f}_N(\tilde{u}_N) = 0, \tag{2.26}$$

where $\overline{u}_N$ presents the approximately deconvolved parameter, and the top-hat filter kernel G is

$$G(x - x_i) = \begin{cases} 1/\Delta x, & |x - x_i| \le \Delta x/2 \\ 0, & \text{otherwise} \end{cases}. \tag{2.27}$$

A modified differential equation (MDE) can be formulated as [3]

$$\bar{u}(x) = \int_{-\infty}^{+\infty} G(x - x')u(x')dx' = G * u, \tag{2.28}$$

$$\frac{\partial \bar{u}_N}{\partial t} + G * \partial_x f_N(u_N) = \epsilon_N, \tag{2.29}$$

where $\epsilon_N = G * \partial_x f_N(u_N) - G * \partial_x \tilde{f}_N(\tilde{u}_N)$ presents the truncation error owing to the spatial discrete format.

When the truncation error reproduces the physical properties of the exact sub-grid scale error/residual, the numerical discretization is called physically consistent. In this case, the numerical truncation error functions as sub-grid scale model and the numerical scheme with ϵ_N is an iLES model. In other words, if ϵ_N approximates ϵ_{sgs} in some sense for finite Δx it gives an implicit SGS model contained within the discretization.

2.6 Surface Tension Modeling

Table 2.2: Classifications for surface tension modeling methods [73].

Classification Criteria	Examples	Comments
Heaviside function and its normal gradient, ∇H	Volume fraction function [18]; Level set function [174]; Dirac delta of ghost fluid method (GFM) [47, 81]	Obtain the unit normal across the interface
Methods for curvature calculation, k	Smoothed volume fraction method [18]; Height function method [4, 29, 173]; Smooth the original curvature through kernel [141] or weight coefficient method [53]	Obtain accurate curvature
Methods for Surface Tension Force discretization (explicit curvature maybe not required), f	Continuum surface force (CSF) [18], in some cases the curvature and norm-direction gradient of scalar are decoupled (like GFM method or level set method); Continuum surface stress (CSS) [55, 92]; Balanced Continuum surface force (bCSF) method or ghost fluid models [51]; Improved Riemann solver [53, 138]; Sharp Surface Force (SSF) model [141, 146]; Independent Source item effects methods [76]	Surface tension acts on pressure field but not the velocity field, thus the parasitic currents can be reduced

For surface tension modeling, the distribution characteristics of the indicator function or the Heaviside function (scalar in the two-phase flow) generally have a great impact on the surface tension calculation at the two-phase interface. By using various methods to sharpen the two-phase interface, the accuracy of the surface tension calculation can be improved. In addition, numerous numerical methods have been proposed to improve the balance between pressure

and surface tension effects to reduce the parasitic current or velocity. For example, balance between compressive and surface tension forces can be achieved by discretizing the surface tension and compressive forces at the same location. As shown in Table 2.2, the surface stress modeling features are divided into three types, according to their expressions and discrete forms.

In the current work, Continuum Surface Force (CSF) model [18] is used, along with proper methods to obtain norm-direction gradient of scalar and curvature. In the CSF model, the surface tension force $\mathbf{f}$ is expressed as a body force distributed over the interfacial region. It can be written as:

$$\mathbf{f} = \sigma \kappa \mathbf{n} \delta_s, \tag{2.30}$$

where σ is the surface tension coefficient, κ is the curvature of the interface, $\mathbf{n}$ is the unit normal vector to the interface, δ_s is the function that localizes the force at the interface. The curvature κ is given by the divergence of the unit normal vector: $\kappa = \nabla \cdot \mathbf{n}$. The unit normal vector $\mathbf{n}$ is computed as the gradient of α, $\mathbf{n} = \nabla \tilde{\alpha} / |\nabla \tilde{\alpha}|$. Details are explained in Section 3.2 of my publication [73].

2.7 Thermodynamics Relationship

2.7.1 Thermodynamic Relationship for Ideal Gases

The following thermodynamic relationships are presented for multi-component flows with several ideal gases. Chiapolino et al. [27] has demonstrated the equivalence between the ideal gas mixture model that follows Dalton's law, and a gas phase within each component is assumed to occupy its own volume, in the specific context of temperature and pressure equilibrium. The following is a brief summary of the results obtained under the corresponding mixture rules shown in Table 1. Here ξ_i denotes mass fraction of component i, i=1 for liquid component, i=2 for vapour component and i>2 for non-condensable gases.

Table 2.3: Multi-component flows with several ideal gases

Ideally mixed gases, Dalton's Law	Separate gas components, each gas component occupies its own volume
$V = V_i$, every component occupies the entire volume	$v = \sum_{i=2}^{N} \xi_i v_i$, the total specific volume is the sum of components' specific subvolumes
$T = T_i$, mixture in temperature equilibrium	$T = T_i$, mixture in temperature equilibrium
$p = \sum_{i=2}^{N} p_{\text{partial},i}$, the mixture pressure is the sum of partial pressures	$p = p_i$, pressure equilibrium among the components
$e = \sum_{i=2}^{N} \xi_i e_i$, mixture internal energy	$e = \sum_{i=2}^{N} \xi_i e_i$, mixture internal energy

First, the gas phase is ideally mixed according to Dalton's Law.

In the case of a given components, the ideal gas law can be defined as $p_{\text{partial},i} V = n_i \hat{R} T$. The gas mixture pressure is $pV = \hat{R}T \sum_{i=2}^{N} n_i$, where $\hat{R}$ is the universal gas constant in molar units and n_i denotes the number of moles. And the temperature could be obtained from the mixture caloric equation of state,

$$e = \hat{R}T \sum_{i=2}^{N} \frac{\xi_i / W_i}{\gamma_i - 1}, \tag{2.31}$$

where W_i is the molar mass and γ_i is the polytropic coefficient of components i. Use the internal energy relation to replace $\hat{R}T$ in the pressure relation,

$$p = \frac{e}{V} \frac{\sum_{i=2}^{N} n_i}{\sum_{i=2}^{N} \frac{\xi_i/W_i}{\gamma_i - 1}} = \frac{e \sum_{i=2}^{N} \frac{n_i W_i}{V} \frac{1}{W_i}}{\sum_{i=2}^{N} \frac{\xi_i/W_i}{\gamma_i - 1}} = \rho e \frac{\sum_{i=2}^{N} \frac{\xi_i}{W_i}}{\sum_{i=2}^{N} \frac{\xi_i/W_i}{\gamma_i - 1}}. \tag{2.32}$$

Then it is considered that each gas component occupies its own volume in the equilibrium of pressure and temperature. In the case of a given components, the ideal gas law can be defined as $p_i V_i = n_i \hat{R} T$. In mass units it becomes, $p_i = \frac{n_i W_i}{V_i} \frac{\hat{R}}{W_i} T = \rho_i \frac{\hat{R}}{W_i} T$. Accordingly, the specific volume of a given components as a function of pressure and temperature can be expressed as $v_i = \frac{\hat{R}T}{W_i p_i}$. For specific volume definition, $v = \sum_{i=2}^{N} \xi_i v_i$, the relation $\frac{p}{T} = \rho \sum_{i=2}^{N} \xi_i \frac{\hat{R}}{W_i}$ is obtained. The mixture energy definition is then in the same relation as in 2.31. The elimination of the temperature through the combination of these two relations yields the same result as 2.32. Both ideal mixtures and separate components assumptions are equivalent when the fluids are ideal gases evolving in both temperature and pressure equilibrium [27].

2.7.2 Thermodynamic Relationship for Liquid, Vapor and Non-condensable Gases

Every component (liquid, vapor, Non-condensable Gases) is assumed to follow the NASG EOS [122].

$$\begin{cases} p_i(v_i, e_i) = (\gamma_i - 1)\left(\dfrac{e_i - q_i}{v_i - b_i}\right) - \gamma_i p_{\infty,i} \\[2mm] T_i(p_i, v_i) = \dfrac{(v_i - b_i)(p_i + p_{\infty,i})}{C_{v,i}(\gamma_i - 1)} \\[2mm] g_i(p_i, T_i) = (\gamma_i C_{v,i} - q_i')T_i - C_{v,i} T_i \ln\left[\dfrac{T_i^{\gamma_i}}{(p_i + p_{\infty,i})^{\gamma_i - 1}}\right] + b_i p_i + q_i \\[2mm] c_i(p_i, v_i) = v_i \sqrt{\dfrac{\gamma_i v_i (p_i + p_{\infty,i})}{v_i - b_i}} \end{cases} \tag{2.33}$$

Here ξ_i denotes mass fraction of component i, i=1 for liquid component, i=2 for vapour component and i>2 for non-condensable gases. Parameters γ_i, $p_{\infty,i}$, $C_{v,i}$, q_i, q_i', and b_i are constant coefficients. b is the covolume of the fluid. g_i is the phase Gibbs free energy of fluid i, $g_i = h_i - T s_i$ with the specific enthalpy h_i and entropy s_i. c_i is the speed of sound of component i.

It is noted that Noble-Abel Stiffened-Gas equation of state degenerates to the Stiffened-Gas equation of state [121] by setting the covolume of the fluid $b_k = 0$. For gaseous components, it reduces to the ideal gas EOS (k>1) with $b_k = 0$ and $p_{\infty,k} = 0$. Mixture equation of state based on mechanical and thermal equilibrium, an inherent assumption of the mass fraction based four-equation model:

$$\begin{cases} T = T_i & \forall i \\ p = p_i & \forall i \\ v = \sum_{i=1}^{N} (\xi_i v_i) \\ e = \sum_{i=1}^{N} (\xi_i e_i) \end{cases}. \tag{2.34}$$

Considering this assumption for the mixture of gases is equivalent to Dalton's law. It means that the computed mixture pressure for the gas mixture agree with both Dalton's law in the gas mixture and with the liquid-gas interface condition of equal pressures ($\forall i$) [27].

From the expressions given in 2.33 for pure components, the specific volumes and internal energies read:

$$
\begin{cases}
v_i(p_i, T_i) = \frac{(\gamma_i - 1)C_{v,i} T_i}{p_i + p_{\infty,i}} + b_i \\
e_i(p_i, T_i) = \frac{p_i + \gamma_i p_{\infty,i}}{p_i + p_{\infty,i}} C_{v,i} T_i + q_i
\end{cases}
\quad ,
\tag{2.35}
$$

then two expressions for the temperature are obtained with conditions $T = T_i, \forall i$, they are $T = \frac{v - \sum_{i=1}^{N} \xi_i b_i}{\sum_{i=1}^{N} \xi_i (\gamma_i - 1) C_{v,i} \frac{p + p_{\infty,i}}{p + p_{\infty,i}}}$, and $T = \frac{e - \sum_{i=1}^{N} \xi_i q_i}{\sum_{i=1}^{N} \xi_i C_{v,i} \left(\frac{p + \gamma_i p_{\infty,i}}{p + p_{\infty,i}} \right)}$. Considering $p_{\infty,i} = 0$ and $b_i = 0, \forall i > 1$, the mixture pressure is then obtained as $p = \frac{b + \sqrt{b^2 + 4ac}}{2a}$ with $a = \bar{C}_v$, $b = \left(\frac{e - \bar{q}}{v - \bar{b}} \right) (\bar{C}_p - \bar{C}_v) - p_{\infty,1} \bar{C}_v - p_{\infty,1} \xi_1 (C_{p,1} - C_{v,1})$, $c = \left(\frac{e - \bar{q}}{v - \bar{b}} \right) p_{\infty,1} \left[\bar{C}_p - \bar{C}_v - \xi_1 (C_{p,1} - C_{v,1}) \right]$, where mixture quantities $\bar{C}_v = \sum_{i=1}^{N} \xi_i C_{v,i}$, $\bar{C}_p = \sum_{i=1}^{N} \xi_i C_{p,i}$, $\bar{q} = \sum_{i=1}^{N} \xi_i q_i$, $\bar{b} = \sum_{i=1}^{N} \xi_i b_i$. For the positivity of the mixture pressure in the presence and absence of liquid, see the reference [27].

2.7.3 Barotropic Thermodynamic Model for Liquid, Vapor and Non-condensable Gases

First, a single-fluid model is extended with an additional gas phase to a single-fluid multi-component model with multiple gas components, based on prior work by Örley et al. [134] and Trummler et al. [184]. This single-fluid approach means that within a finite volume cell all phases have the same velocity and pressure. The transport equation for the total energy is not needed [134].

A typical three-component two-phase fluid $\Phi = \{L, M, Gas1, Gas2\}$ is selected, which refers to a liquid component, a liquid-vapor mixture and two gas components denoted as Gas1 and Gas2, respectively.

For the liquid component

$$
\rho_L = \rho_{\text{sat, liq}} + \frac{1}{c_L^2} (p_L - p_{\text{sat}}), \quad p_L \geq p_{\text{sat}},
\tag{2.36}
$$

where $\rho_{\text{sat, liq}}$ is the liquid saturation density at its saturation pressure p_{sat}.

For the liquid-vapor mixture

$$
\rho_M = \rho_{\text{sat, liq}} + \frac{1}{c_M^2} (p_M - p_{\text{sat}}), \quad p_M < p_{\text{sat}}.
\tag{2.37}
$$

Since $c^2 = \left(\frac{\partial p}{\partial \rho} \right)_{\text{const}}$, the mixture speed of sound is approximated as $c_M = (p_{\text{sat}} / \rho_{\text{sat, liq}})^{1/2}$. For the non-condensable gas phase

$$
\rho_{\text{Gasi}} = \frac{P_{\text{Gasi}}}{R_{\text{Gasi}} T_{\text{refi}}},
\tag{2.38}
$$

i.e., both gas components are treated as ideal gas, R_{Gas1} and R_{Gas2} refer to the specific gas constant, T_{ref1} and T_{ref2} refer to the corresponding reference temperatures.

From the volume fraction $\alpha_\Phi = V_\Phi / V$ and the mass fraction $\xi_\Phi = m_\Phi / m$ of component Φ, it is obvious that $\rho_\Phi = m_\Phi / V_\Phi = \xi_\Phi \rho / \alpha_\Phi$, and $\rho = m / V = \sum_\Phi \xi_\Phi \rho = \sum_\Phi \alpha_\Phi \rho_\Phi$. Naturally $\sum_\Phi \alpha_\Phi = 1$ and $\sum_\Phi \xi_\Phi = 1$, $\rho = \alpha_L \rho_L / M + \alpha_{\text{Gas1}} \rho_{\text{Gas1}} + \alpha_{\text{Gas2}} \rho_{\text{Gas2}}$.

$$\rho_{\text{Gasi}} = \frac{\xi_{\text{Gasi}}}{\alpha_{\text{Gasi}}} \rho = \frac{P_{\text{Gasi}}}{R_{\text{Gasi}} T_{\text{refi}}}, \tag{2.39}$$

where $\alpha_{\text{Gasi}} = \xi_{\text{Gasi}} R_{\text{Gasi}} T_{\text{refi}} / P_{\text{Gasi}}$. Thus $\rho = \alpha_L \rho_L / M + \alpha_{\text{Gas1}} \rho_{\text{Gas1}} + \alpha_{\text{Gas2}} \rho_{\text{Gas2}} = (1 - \alpha_{\text{Gas1}} - \alpha_{\text{Gas2}}) \rho_L / M + \xi_{\text{Gas1}} \rho + \xi_{\text{Gas2}} \rho$. Finally, the coupled (one-fluid) multi-component equation of state is obtained $(1 - \sum_\Phi \xi_{\text{Gas}} R_{\text{Gas}} T_{\text{ref}} / P_{\text{Gas}})(\rho_{\text{sat, liq}} + \frac{1}{c_L^2}(P_M - P_{\text{sat}})) - (1 - \sum_\Phi \xi_{\text{Gas}}) \rho = 0$. It indicates $p = f(\rho, \xi_{\text{Gas}})$ with the equilibrium assumption. If the pressure is higher than the saturation pressure of the liquid, then is no vapor. Otherwise

$$\alpha_v = \frac{V_{\text{vap}}}{V} = \begin{cases} (1 - \alpha_{\text{Gas1}} - \alpha_{\text{Gas2}}) \frac{\rho_{\text{sat, liq}} - \rho_M}{\rho_{\text{sat, liq}} - \rho_{\text{sat, vap}}}, & \rho < \rho_{\text{sat, liq}} \\ 0, & \rho \geq \rho_{\text{sat, liq}} \end{cases}. \tag{2.40}$$

It is assumed that there is no pure vapor and limit the largest volume fraction of vapor component to 99.5%. The mixtures viscosity is

$$\mu_{\text{mix}} = (1 - \alpha_{\text{Gas1}} - \alpha_{\text{Gas2}}) \left[(1 - \alpha_v) \left(1 + \frac{5}{2} \alpha_v \right) \mu_{\text{liq}} + \alpha_v \mu_{\text{vap}} \right] + \alpha_{\text{Gas1}} \mu_{\text{Ga1}} + \alpha_{\text{Gas2}} \mu_{\text{Ga2}}. \tag{2.41}$$

2.7.4 Thermodynamic Relationship Including Real-fluid Effects

· Peng–Robinson equation of state (PR-EOS)

The Peng–Robinson equation of state (PR-EOS) [137] is employed for both liquid and gas components:

$$p = \frac{RT}{v - b} - \frac{a}{v^2 + 2bv - b^2}, \tag{2.42}$$

where T is the temperature, R is the universal gas constant, v is the molar volume, $v = M/\rho$, and M is the molar mass. Coefficients are $a = \sum_{\alpha=1}^N \sum_{\beta=1}^N X_\alpha X_\beta a_{\alpha\beta}$ and $b = \sum_{\alpha=1}^N X_\alpha b_\alpha$.

Specifically, X_α is the mole fraction of components α and in-total components number is N; coefficients $a_{\alpha\beta} = 0.457236(RT_{c,\alpha\beta})^2 / p_{c,\alpha\beta}(1 + c_{\alpha\beta}(1 - \sqrt{T/T_{c,\alpha\beta}}))^2$, $b_\alpha = 0.077796 RT_{c,\alpha} / p_{c,\alpha}$ are obtained according to the mixing rules [58]. $p_{c,\alpha\beta}$ is the critical mixture pressure and $p_{c,\alpha\beta} = Z_{c,\alpha\beta} RT_{c,\alpha\beta} / v_{c,\alpha\beta}$, $c_{\alpha\beta} = 0.37464 + 1.5422\omega_{\alpha\beta} - 0.26992\omega_{\alpha\beta}^2$, $T_{c,\alpha\beta}$ is the critical mixture temperature, and $T_{c,\alpha\beta} = \sqrt{T_{c,\alpha} T_{c,\beta}(1 - k_{\alpha\beta})}$. $T_{c,\alpha}$ and $T_{c,\beta}$ are critical temperatures for components α and β, and $k_{\alpha\beta}$ is the binary interaction parameter.

The critical mixture molar volume $v_{c,\alpha\beta}$, the critical mixture compressibility $Z_{c,\alpha\beta}$, and the acentric factor $\omega_{\alpha\beta}$ are denoted as $v_{c,\alpha\beta} = (1/8)(v_{c,\alpha}^{1/3} + v_{c,\beta}^{1/3})^3$, $Z_{c,\alpha\beta} = (1/2)(Z_{c,\alpha} + Z_{c,\beta})$, and $\omega_{\alpha\beta} = (1/2)(\omega_\alpha + \omega_\beta)$, where $v_{c,\alpha}^{1/3}$ and $v_{c,\beta}^{1/3}$ are critical molar volumes for components α and β, $Z_{c,\alpha}$ and $Z_{c,\beta}$ are critical compressibility factors for components α and β, and ω_α and ω_β are acentric factors for components α and β.

Besides, Ref. [118] provides the parameters for the NASA polynomials, which would be used to obtain the internal energy, enthalpy, and entropy.

· Modified Peng–Robinson equation of state (PR-EOS)

The modified PR-EOS is designed to represent the saturation line in a straightforward manner. Within the vapor dome region, an approximate saturation pressure for the mixture is utilized.

The algorithm for determining the pressure, which yields the temperature, density, and mass fraction, is as follows:

Step 1. Calculate the pressure from the PR-EOS giving the temperature and density, as well as the mass fraction. If nonpositive pressure ($p^* < 0$) is obtained from the relation $p^* = p_{\text{PR-EOS}}(T, \rho, \xi_i)$, a small arbitrarily positive value such as 1 would be adopted to replace this nonpositive value ($p^* = 1\,\text{Pa}$).

Step 2. Calculate the density from PR-EOS given the PR-EOS pressure p^*, temperature, and mass fraction, and check how many roots are obtained in the process $\rho^* = p_{\text{PR-EOS}}(p^*, T, \xi_i)$.

Step 3.1. If there is only one real value for ρ^*, then the PR-EOS pressure p^* is chosen as the corrected pressure.

Step 3.2. If there is more than one root for ρ^*, then the saturation pressure (p_{sat}) is given by calculating the root, $\partial p / \partial \rho = 0$, via PR-EOS. Generally, the one at the lower density value (ρ_{min}) would be selected from the two resulting roots. The saturation pressure (p_{sat}) is then defined as the pressure corresponding to this root (ρ_{min}).

Step 4. If the density that is given by the PR-EOS ($\rho^* = p_{\text{PR-EOS}}(p^*, T, \xi_i)$,lowest density root) is very similar to the density provided (ρ), like ($\rho^* - \rho)/\rho < 10^{-4}$, then return the PR-EOS pressure p^*; otherwise, return the saturation pressure (p_{sat}).

In the case of DF methods or hybrid numerical schemes with a modified PR-EOS, it is crucial to calculate the temperature (T) for a given set of pressure (p), density (ρ), and mass fraction (ξ_i) using the modified PR-EOS ($T = T_{\text{modified-PR-EOS}}(p, \rho, \xi_i)$). This can be expressed as follows:

Step 1. Initial guess (T_{guess}) temperature according to the initial condition and the temperature from the last time step.

Step 2. This T_{guess} is used to calculate the pressure, using modified PR-EOS, where the state inside the vapor dome has already been corrected ($p_{\text{guess}} = p_{\text{modified-PR-EOS}}(T_{\text{guess}}, \rho, \xi_i)$).

Step 3. If the pressure given by the modified PR-EOS ($p_{\text{guess}} = p_{\text{modified-PR-EOS}}(T_{\text{guess}}, \rho, \xi_i)$) is very similar to the pressure given by the modified PR-EOS (p^*), e.g., ($p_{\text{guess}} - p^*)/p^* < 10^{-6}$, then the temperature T_{guess} is selected as the correct temperature, $T = T_{\text{guess}}$.

Step 4. Otherwise, the guess temperature is updated according to the secant method or gradient descent or Newton method, and the criteria are $p^* = p_{\text{modified-PR-EOS}}(T_{\text{guess}}, \rho, \xi_i)$ and ($p^* - p)/p < 10^{-6}$.

Step 5. The modified PR-EOS [86] also limits the speed of sound to a minimum value—the minimum speed of sound value used in this paper is 1 m/s [86]. Three subcritical isotherms of varying composition are depicted in Fig. 30 of Ref. [16] to showcase the modified PR-EOS.

2.8 Time Integration

To march the volume-averaged solution forward in time, an explicit second-order, four-step low-storage Runge-Kutta method is used. Considering a simplified version of equation $\partial_t \overline{\mathbf{U}}_i(t) \approx -\frac{1}{V_i} \sum_j (\tilde{\mathbf{F}}_j \mathbf{n}_j) A_j$

$$\partial_t \overline{\mathbf{U}}_i(t) = \mathcal{L}_i(\overline{\mathbf{U}}_i), \tag{2.43}$$

with $\mathcal{L}$ representing the right-hand side terms, a multi-step time integration from $t = n$ to $t = n + 1$ reads

$$\overline{\mathbf{U}}_i^{n+1,k} = \overline{\mathbf{U}}_i^n + C_k \Delta t \mathcal{L}_i(\overline{\mathbf{U}}_i^{n+1,k-1}), \tag{2.44}$$

with $k = 1, \ldots, N_k$,

$$\overline{\mathbf{U}}_i^{n+1,0} = \overline{\mathbf{U}}_i^n \quad \text{and} \quad \overline{\mathbf{U}}_i^{n+1} = \overline{\mathbf{U}}_i^{n+1,N_k}. \tag{2.45}$$

For the employed four-step method ($N_k = 4$), the coefficients are $C_1 = 0.11$, $C_2 = 0.2766$, $C_3 = 0.5$, $C_4 = 1$. The global time step Δt in the simulations is determined by the minimum of the local time steps

$$\Delta t = \min(\Delta t_i), \tag{2.46}$$

which are evaluated by the Courant-Friedrichs-Lewy (CFL) criterion as $\Delta t_i = \text{CFL}\left(\frac{\Delta x_i}{|u_i| + c_i}\right)$.

The length scale Δx_i is calculated with a characteristic cell length l_i divided by the dimension N_d as $\Delta x_i = l_i/N_d$. u_i is a characteristic velocity, c_i the speed of sound. For viscous flow, further details can be found in the references [49, 183].

2.9 A Real-fluid Hybrid Scheme

For near-critical thermodynamic conditions, a hybrid numerical model is used that can seamlessly switch between a fully conservative (FC) scheme and a quasiconservative (QC) scheme under certain conditions [75]. The QC scheme usually uses a pressure evolution (PE) equation [85, 91, 159, 175, 176, 203] or the double-flux (DF) [2, 107] method. The DF method is used here. Figure 2.2(a) provides a flowchart of the model. The time integration is performed by an explicit, second-order-accurate low-storage four-step Runge-Kutta method with an enhanced stability region, which has been discussed previously. The Courant-Friedrichs-Lewy (CFL) value is generally set to 0.5 unless otherwise stated. The details of this model will be shown in the following sections.

2.9.1 Fully Conservative Scheme with PR-EOS

The fully conservative scheme has been discussed in the previous section. Here, the compressible Euler equations with the Peng-Robinson equation of state (PR-EOS) are adopted to model the behavior of the liquid and gas components at near-critical conditions. Several factors are neglected, including gravity, heat transfer (thermal conduction), viscous effects, surface tension, and chemical reactions. These omissions are justified by the extremely short interface interaction time in shock-droplet interaction. Gravity, heat transfer, and viscous effects may become relevant in longer-duration interactions or low-speed scenarios. Surface tension can be disregarded in transcritical flows [86, 116, 124, 129, 131, 152, 197] because the surface tension coefficient decreases significantly near the critical point.

The PR-EOS [137] is employed for both liquid and gas components.

In the fully conservative scheme, temperature is updated first, considering internal energy, density, and components mass fractions. This is accomplished using a gradient descent or Newton method. It should be noted that the convergence speed of the gradient descent or Newton method for temperature calculation could be improved by utilizing the temperature from the previous time step as an initial guess.

2.9.2 Quasiconservative Scheme with PR-EOS

Quasiconservative schemes, such as the DF method, have been developed in recent years and are well suited for addressing the challenges posed by near-critical flow scenarios. The DF method was initially proposed by Abgrall and Karni [2] for multi-component ideal-gas flows

(a)

(b)
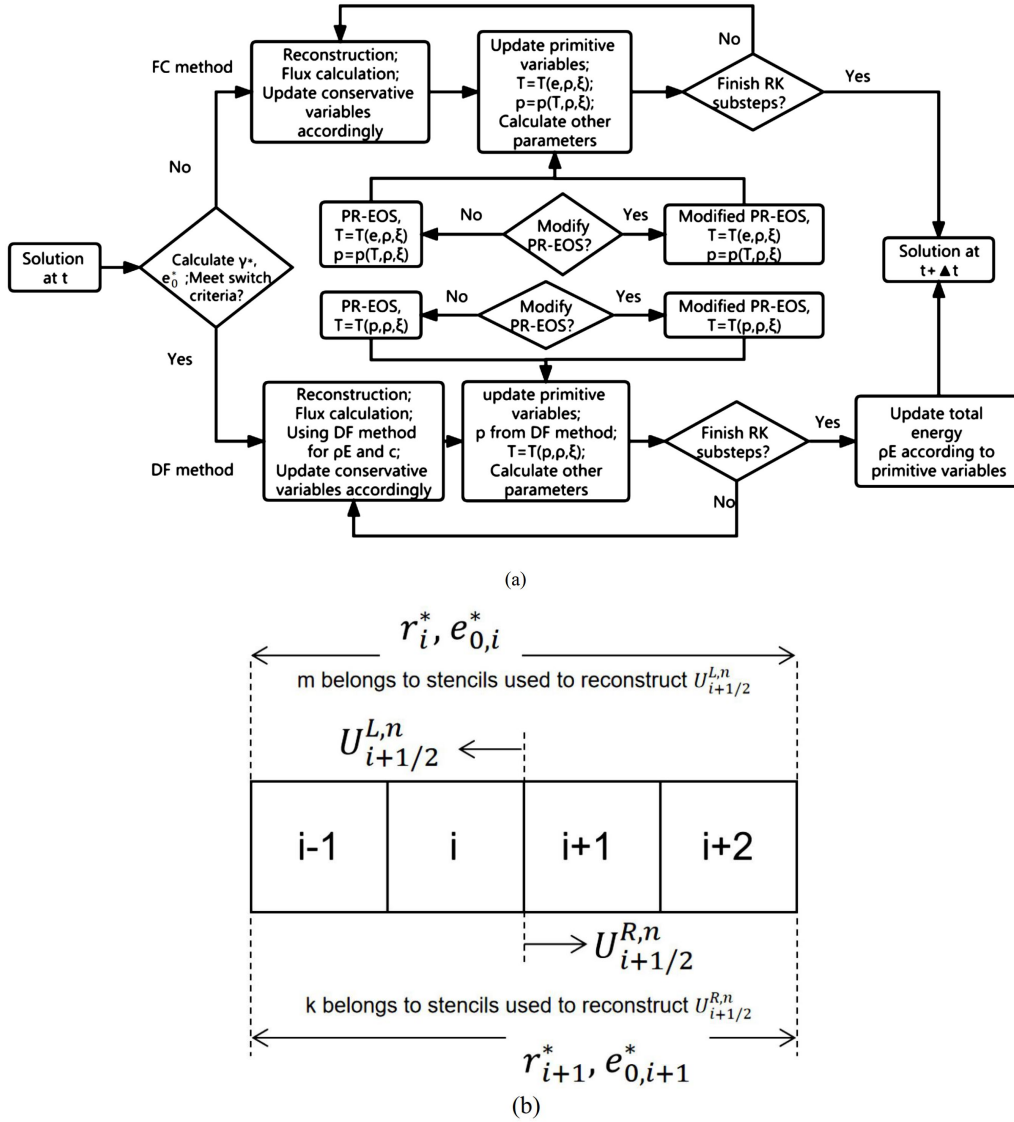
Figure 2.2: (a) Flowchart of the current numerical scheme: fully conservative scheme with PR-EOS/modified PR-EOS and quasiconservative scheme (double-flux method) with PR-EOS/modified PR-EOS. (b) Schematic diagram of the double flux model with the fluxes at the cell face $i + 1/2$. Reproduced with permission from [75].

and later extended by Billet and Abgrall [13] for ideal-gas reacting flow systems. Subsequently, high-order schemes based on the DF method have been developed [14, 106, 107]. Here the double-flux-based model [107, 108] is integrated to handle the current near-critical flows.

The double-flux model is used when specific parameters that exceed certain recommended values, as defined in the following two equations, are met:

$$\Delta \Gamma^*_{i,\max} = \max(|\Gamma^*_{i+1} - \Gamma^*_i|, |\Gamma^*_i - \Gamma^*_{i-1}|), \tag{2.47}$$

$$\Delta e^*_{0,i,\max} = \max(|e^*_{0,i+1} - e^*_{0,i}|, |e^*_{0,i} - e^*_{0,i-1}|). \tag{2.48}$$

In reference [16], it is recommended that $\Delta \Gamma^*_{i,\max} = 1$, $\Delta e^*_{0,i,\max} = 1000$ kJ/kg. Under these conditions, the fully conservative numerical scheme transitions to a quasiconservative scheme based on the criteria mentioned earlier.

The primary characteristic of the DF model [2, 13, 16, 107] is that it maintains the effective specific heat ratio (γ^*) and effective reference internal energy (e_0^*) as constant values in both space and time to mitigate spurious pressure oscillations and oscillations of other physical parameters that may result from pressure fluctuations. Essentially, the relationship between pressure and internal energy remains fixed in both space and time, effectively transforming the local system into a calorically perfect gas system.

The parameters γ^* and e_0^* are determined based on the values from the previous time step to establish relations between internal energy and pressure [108]. This approach [2, 107] is taken to prevent abrupt changes in γ^* (Γ^*) and e_0^* between cells, as such variations could disrupt pressure equilibrium and induce spurious pressure oscillations. In this process, the effective specific heat ratio (γ^*) is calculated as $\gamma^* = pc^2/\rho$, the effective reference internal energy (e_0^*) is obtained as $e_0^* = e - \Gamma^*p/\rho$, and Γ^* is calculated as $\Gamma^* = 1/(\gamma^*-1)$. These values are held constant throughout all Runge-Kutta (RK) substeps within each time step to ensure stability and accuracy. A schematic of the double-flux model is shown in Figure 2.2(b).

In each time step of the simulation, the following operations are implemented.

Step 1. Reconstruction and flux computation at the cell faces involves using the following two equations for left and right face reconstructions:

$$c = \sqrt{p\gamma^*/\rho}, \tag{2.49}$$

$$(\rho E)^* = \rho e_0^* + \frac{1}{2}\rho|\boldsymbol{u}|^2 + \Gamma^*p = \rho e_0^* + \frac{1}{2}\rho|\boldsymbol{u}|^2 + \frac{p}{\gamma^*-1}. \tag{2.50}$$

When reconstructing the total energy of the left-hand side (belonging to $U_{i+1/2}^{L,n}$) of the cell interface $i + 1/2$, the parameters γ_i^* and $e_{0,i}^*$ of the left first cell i and the values p_m, ρ_m, and u_m of cell m are used to update $(\rho E)_m^*$ of cell m (where m is part of the stencils used to reconstruct $U_{i+1/2}^{L,n}$), then the left-hand-side total energy is constructed according to the corresponding scheme:

$$(\rho E)_m^n = \rho_m^n e_{0,i}^{*,n} + \frac{1}{2}\rho_m^n|\boldsymbol{u}_m^n|^2 + \frac{p_m^n}{\gamma_i^{*,n}-1}. \tag{2.51}$$

Similarly, when reconstructing the total energy of the right-hand side (belonging to $U_{i+1/2}^{R,n}$) of the cell interface $i + 1/2$, the parameters γ_{i+1}^* and $e_{0,i+1}^*$ of the right first cell $i + 1$ and the values p_k, ρ_k, and $\boldsymbol{u}_k$ of cell k are used to update $(\rho E)_k^*$ of cell k (k belongs to stencils used to reconstruct $U_{i+1/2}^{R,n}$). The total energy of the right-hand side is then constructed accordingly:

$$(\rho E)_k^n = \rho_k^n e_{0,i+1}^{*,n} + \frac{1}{2}\rho_k^n|u_k^n|^2 + \frac{p_k^n}{\gamma_{i+1}^{*,n}-1}. \tag{2.52}$$

Step 2. Obtain the conservative variables and the corresponding primitive variables such as velocity, density, and energy.

Step 3. Update other primitive variables such as pressure for each cell using Eq. (8):

$$p = \frac{1}{\Gamma^*}\left(\rho E - \rho e_0^* - \frac{1}{2}\rho|\boldsymbol{u}|^2\right) = (\gamma^*-1)\left(\rho E - \rho e_0^* - \frac{1}{2}\rho|\boldsymbol{u}|^2\right). \tag{2.53}$$

When updating p_i^{n+1} of cell i, the frozen values $\gamma_i^{*,n}$, $e_{0,i}^{*,n}$, and $\Gamma_i^{*,n}$ from the last substep n and the updated $\boldsymbol{u}_i^{n+1}$, ρ_i^{n+1}, and $(\rho E)_i^{n+1}$ are used,

$$p_i^{n+1} = \frac{1}{\Gamma_i^{*,n}}\left((\rho E)_i^{n+1} - \rho_i^{n+1}e_{0,i}^{*,n} - \frac{1}{2}\rho_i^{n+1}|\boldsymbol{u}_i^{n+1}|^2\right), \tag{2.54}$$

$$p_i^{n+1} = (\gamma_i^{*,n} - 1)\left((\rho E)_i^{n+1} - \rho_i^{n+1} e_{0,i}^{*,n} - \frac{1}{2}\rho_i^{n+1}|u_i^{n+1}|^2\right). \tag{2.55}$$

Step 4. After obtaining the pressure, update the temperature using the equation of state (EOS) based on density, pressure, and components mass fraction.

Step 5. Update other parameters such as speed of sound, enthalpy, and entropy based on the temperature, pressure, density, velocity, total energy, and internal energy obtained.

At the end of all Runge-Kutta substeps within each time step, the total energy is updated. This update is done according to $\rho E = \rho e + \frac{1}{2}\rho|u|^2$ and thermodynamic relations $\rho E = \rho E(p, \rho, T, \xi)$ to ensure thermodynamic consistency since the temperature is updated after the pressure.

In the QC scheme, pressure is obtained directly from the DF model and is, therefore, more easily maintained as positive. The temperature is then updated according to the pressure, density, and components mass fraction [107]. However, because different values of γ^* and e_0^* are used for each cell, the two energy fluxes at a face are no longer the same, unlike in the FC scheme. This can result in an energy conservation error. Nevertheless, it has been reported [2, 107, 108] that the total energy conservation error decreases as the resolution increases and the difference in γ^* between neighboring cells decreases.

2.9.3 Hybrid Numerical Model with Modified PR-EOS

The hybrid numerical model, incorporating a modified PR-EOS, is introduced to address two primary challenges:

1. Conservative scheme-induced problem: When using a FC method with the classical PR-EOS, pressure is updated from temperature and density within each time step, involving a complex nonlinear real-fluid EOS. During this process, numerical diffusion and dispersion can result in negative pressure or induce pressure oscillations, which may lead to simulation failures. FC schemes struggle to maintain pressure equilibrium across transcritical contact interfaces. In contrast, QC schemes are more effective in reducing spurious pressure oscillations and achieving positive pressures.

2. Vapor dome problem: The classical PR-EOS is designed for use outside the vapor dome, and it needs to be modified to handle conditions within the vapor dome. In certain situations, negative pressures can occur for specific density values at relatively low temperatures, and the speed of sound may become complex valued in the vapor dome [109]. Inside the vapor dome, the thermodynamic state described by the classical PR-EOS is either metastable, or unstable or nonconvex.

To address the first issue, the QC scheme provides an effective solution. Moreover, by reducing the high-order numerical scheme to a low-order numerical scheme, pressure oscillations can be reduced.

To tackle the second issue, a modified PR-EOS [16] is introduced to approximate the fluid state within the vapor dome region. This modified PR-EOS ensures that the speed of sound remains above 1 m/s, enhancing the robustness of the numerical method when the state falls within the vapor dome. It is important to note that phase separation is not expected [10, 182], and the proposed numerical procedure in Ref. [116] is adequate for resolving pressure oscillations in transcritical flows.

2.10 Summary

In this chapter, the numerical and physical modeling for compressible multi-component flows including surface tension, cavitation, turbulence and real-fluid effects are discussed in detail.

From the numerical aspect, THINC-TDU is adopted to the upwind-based scheme and high-order central scheme, improving the surface tension, cavitation, turbulence and real-fluid results with sharpening interface on compact stencils.

From the physical aspect, thermodynamic relations are provided for liquid, vapor and non-condensable gases, enabling physical modeling of cavitation, turbulent jet flow, etc. Real-fluid effects are included via (modified) Peng-Robinson equation of state (PR-EOS), allowing physical modeling of near-critical flows.

These improve the CATUM solver's ability to handle simulations involving surface tension, cavitation, turbulence and real-fluid effects. They form the basis for the subsequent research presented in the following chapters.

Chapter 3

Accomplishments

This chapter provides a concise overview of the accomplishments associated with the thesis. The current state of the art is given for each topic. The achievements are published in three first-author publications [73–75], which are included in the Appendix.

3.1 A Numerical Scheme for Compressible Multi-Component Flows Including Surface Tension, Cavitation, Turbulence Modeling, and Interface Sharpening on Compact Stencils

3.1.1 State of the Art

Two numerical methodologies are typically employed for dealing with interfacial problems encountered in multi-component flows: those that assume sharp interfaces and those that rely on mixture assumptions. Given that the flow field and material properties are typically discontinuous across the interface between different phases or components, the treatment of material boundaries represents a pivotal challenge.

The achievement of sharp interfaces is typically accomplished through the utilisation of various techniques, including front-tracking (FT) [26, 186], level-set methods (LS) [136, 160, 174], and geometric interface reconstruction (GIR) based volume of fluid methods (VOF) [64, 188], such as piecewise-linear interface calculation (PLIC) [207] and the isoAdvector Method [149]. However, they are computationally expensive.

In general, diffuse interfaces are introduced by phase field models (PF) [24, 69, 70, 84, 126] or (interface capturing type) algebraic interface sharpening (AIS) based models, where no clear boundary between phases exists and the interface often encompasses more than a single cell. Phase-field methods are limited in their applicability to realistic two-phase problems in industry. The AIS approach has the significant advantage of allowing a single set of equations to be used to describe the two-phase flow properties throughout the domain, obviating the need for explicit tracking of the sharp interface.

Approaches with diffuse interfaces are very effective and can be used in three-dimensional cases with different fluid components. These diffuse-interface effects approximate the behaviour of a sharp gradient as the size of the mesh approaches zero. Diffuse-interface approaches for the simulation of compressible two-phase flows can be categorised into a number of distinct types, including: the four-equation model [1, 2, 6, 32, 39, 45, 88, 115, 116, 134, 184], the five-equation model [6, 82], the Baer-Nunziato model [7, 11, 113, 154–156, 178], etc.

The mass fraction-based four-equation model is capable of accounting for an additional component with an additional species-mass conservation equation, in contrast to the volume fraction-based five-equation model, which necessitates the inclusion of two equations for an

additional species. Consequently, the five-equation model requires additional computational effort. A key benefit of a mass fraction-based four-equation model [1, 2, 6, 32, 39, 45, 88, 113, 115, 116, 134, 155, 184] (in comparison to an LS formulation) is its capacity to accommodate flows where the species front is initially absent but forms during the calculation process (as in chemical reactions, cavitation, or condensation). While gamma-transport based four equation models [166] are optimal for stiffened gas-type EOS, mass-fraction-based four equation models can be effectively applied to real-fluid models. Besides, the BN model extends beyond traditional four- or five-equation models by incorporating interfacial forces, phase changes and phase compressibility [113, 155, 156]. BN approaches exhibit high numerical complexity, including detailed interface tracking, and necessitate the use of closure models for interface terms. This considerably complicates their applicability to industrial problems in the dual-fuel domain.

In essence, the approach is grounded in a four-equation model based on the mass fraction, which offers a straightforward means of incorporating additional species (dual-fuel conditions), is well-suited to real-fluid effects, and can be readily applied to complex flows including cavitation. In the following section, a discussion is presented on the advantages of AIS methods, with a particular focus on THINC-based approaches.

AIS methods strive to algebraically reconstruct the two-phase interface or modify the right-hand side (RHS) of the governing equations in order to avoid excessive interfacial diffusion, at relatively low additional computational cost. Examples of such methods include the Flux-Corrected Transport (FCT) scheme [15, 151, 209], post-processing anti-diffusion methods [169, 170], the Tangent of Hyperbola for INterface Capturing (THINC) method [34, 200, 201], Compressive Interface Capturing Schemes for Arbitrary Meshes (CICSAM) [188], additional (artificial) compression term approaches [130, 153, 165, 198], bounded variation or TVD methods [21, 132, 171], ENO or WENO approaches [79, 163, 190], Multidimensional Universal Limiters with Explicit Solution (MULES) [38, 98], High Resolution Interface Capturing schemes (HRIC) [125], adjusting the limiters in the TVD-MUSCL scheme [98] or the weighting coefficients in the WENO scheme [72, 103] and the development of Riemann solvers.

Among the various AIS methods, the THINC-based approaches are promising options because it generally requires less computational effort. In the THINC method presented by Xiao [200], the hyperbolic tangent function was employed to evaluate the numerical flux for the advection equation of the VOF function, with the objective of calculating the moving interface algebraically (without complex geometric reconstruction). To perform multidimensional calculations, the numerical flux for each direction was determined by operator splitting. Subsequently, the research was focused on improving the description of the interface shape and avoiding the surface curvature.

The THINC method has thus far been developed and employed for the simulation of multiphase flows. However, it should be noted that THINC-based methods have been studied to a limited extent for complex compressible multi-component applications involving shock waves, turbulence, cavitation, real-fluid effects and moving interfaces. Daniel [20] employed THINC in the MUSCL scheme for incompressible multiphase flows. In order to simulate a supersonic liquid jet [112], a five-equation model was combined with a volume fraction THINC when capillary forces were neglected. A five-equation model combined with a density THINC was further implemented to simulate atomization [52]. Nonomura et al. [127] developed the THINC method with two compressible fluids and sharpened the volume fraction only, while Shyue and Xiao [167] presented a single-fluid multi-component flow model and used the reconstructed volume fraction to extrapolate other conservative parameters across the cell interface, both neglecting the surface tension. It is further noted that a recent development (VOF-based) [25] or ongoing work [65, 66] of the THINC-based method is the combination

with the AMR technique in multiphase simulation, but it is still not fully capable for the complex compressible simulation involving cavitation flow, turbulent flow and real-fluid effects with increasing computational cost. Furthermore, coupled methods such as THINC-LS [139] and THINC-LS-VOF [89] were developed to enhance the description of interfaces and numerical accuracy. However, they typically necessitate significantly greater computational resources to achieve optimal performance. The aforementioned THINC-based method is typically employed to reconstruct the volume fraction of a five-equation model. In such models, the direct consideration of a Riemann solver of the cell interface is not a common occurrence. Rather, the relationship between pressure and density, as well as internal energy, is decoupled in the reconstruction process. Furthermore, realistic flows, such as viscous terms, surface tension, gravity, real-fluid effects, and cavitation, are typically ignored or not fully considered.

3.1.2 Summary of the Publication

Yu Jiao *, Steffen J. Schmidt, Nikolaus A. Adams. (2024). An All-Mach Consistent Numerical Scheme for Simulation of Compressible Multi-Component Fluids Including Surface Tension, Cavitation, Turbulence Modeling and Interface Sharpening on Compact Stencils. Computers & Fluids. [73]

This publication proposes a robust four equation model using one-fluid multi-component thermodynamics relations as well as an all-Mach number consistent THINC-TDU method, which prevents two-phase interfaces from smearing. Surface tension effects, viscous effects, gravity effects, as well as shock-wave phenomena have been assessed and the results are in good agreement with well-known reference results. The simulation of a liquid jet in a dual-fuel environment demonstrates the suitability of the methodology to complex real-world engineering applications.

An implementation of the methodology into existing MUSCLE or WENO-type compressible finite volume methods on block structured meshes is presented. A significant improvement of predicted details in compressible two-phase flows is reached while the additional computational costs are negligible. This is achieved by combining an algebraic sharpening method with a thermodynamically consistent correction procedure in the flux computation without the need of complex geometric reconstruction approaches.

The approach has been implemented into the in-house code CATUM [45, 158, 184, 185] validated against a series of references and has extended to be suitable for sub-grid turbulence modelling. A shock-droplet test-case in near critical conditions with a real-fluid model show that current results are superior to WENO3-JS and OWENO3 schemes (if using the same mesh resolution). In addition to gas bubble collapse, vapor bubble collapse was also performed to prove that the two-phase interface between liquid and vapor can also be sharpened using the current scheme. This demonstrates the ability of the current scheme to handle cavitation-related cases containing both condensable vapor and non-condensable gas, such as atomization using cavitation nozzles. The simulation of a three-dimensional turbulent jet flow with surface tension and viscous effects also demonstrates the high performance of the current scheme.

In short, these accomplishments based on compact stencils are applicable to various thermodynamic models for compressible flow with multi-component fluids, including the following features:

· Viscosity, gravity, surface tension, real-fluid and cavitation effects are considered, covering liquid, vapor, and non-condensable gas cases, such as low Mach flow and shock bubble/droplet interaction.

· A high-order improvement is proposed with iLES for turbulence modeling.

· THINC-based reconstruction functions are applied separately to sharpen the liquid-gas and liquid-vapour interfaces.

· Numerical and thermodynamic consistency between variables is ensured and the effects of the Riemann solver are included.

3.1.3   Individual Contributions of the Candidate

This article was published in the international peer-reviewed journal Computers & Fluids [73]. My contribution to this research paper was to propose the concept and idea of the paper, complete the programming codes and numerical methods, perform the validations, analyse the results, and write the manuscript.

3.2   Simulating Shock Interaction with a Cavity-Embedded Cylinder/Droplet Using a Real-Fluid Hybrid Scheme at Near-Critical Conditions

3.2.1   State of the Art

While there have been numerous studies of transcritical fluids in low-speed convective environments, where fluid evaporation is significantly influenced by viscous effects and heat conduction [22, 28, 117, 119, 204–206], research on the interaction of transcritical fuel cylinders/droplets with shock waves or high-speed flows is limited. Obtaining detailed experimental data on such flows, particularly at high pressures and temperatures, remains a challenge. Therefore, numerical experiments have become essential for such flows at near-critical conditions in high-pressure, high-speed propulsion systems.

Classical simulations of shock-bubble interactions (SBIs) [57, 66, 90, 93–95, 128, 140, 145, 179, 180, 210] and shock-droplet interactions (SDIs) [32, 42, 50, 54, 120, 157, 189, 195] have been extensively studied, focusing primarily on scenarios involving pure droplets or pure bubbles. However, these studies have predominantly investigated subcritical and supercritical conditions, with limited investigation of near-critical or transcritical conditions. Fluids near their critical points exhibit distinct physical properties that differ significantly from classical liquid droplets or ideal gas bubbles [1, 8, 144], requiring a unique approach. It is noteworthy that investigations [16, 17, 187] have not addressed the detailed simulation of real three-dimensional interface deformation at near-critical conditions.

Moreover, the interaction between shock waves and droplets containing gas or vapor-filled cavities, as well as the interaction between shock waves and bubbles containing droplets, represents a relatively unexplored area within the context of SDIs and SBIs. A significant knowledge gap remains regarding the interaction between shock waves and droplets containing embedded gas cavities, particularly under near-critical conditions and in three-dimensional scenarios. Previous investigations in this field have primarily focused on scenarios characterised by low temperatures and low pressures [48, 102, 123, 162, 191, 193, 199].

3.2.2   Summary of the Publication

Yu Jiao *, Steffen J. Schmidt, Nikolaus A. Adams. (2024). Simulating Shock Interaction with a Cavity-Embedded Cylinder/Droplet Using a Real-Fluid Hybrid Scheme at Near-Critical Conditions. Physical Review Fluids. [75]

3.2 Simulating Shock Interaction with a Cavity-Embedded Cylinder/Droplet Using a Real-Fluid Hybrid Scheme at Near-Critical Conditions

33

This publication investigates the behaviour of two-dimensional and three-dimensional numerical simulations of a droplet with an embedded gas cavity subjected to a normal shock wave at near-critical conditions. The approach involves modeling the cylinder/droplet and the surrounding gas flow using the compressible multi-component equations, incorporating real-fluid thermodynamic relationships, and implementing a finite-volume-based hybrid numerical framework capable of capturing shocks and interfaces. To establish the reliability of the approach, it is validated against reference data, demonstrating excellent agreement. Mesh independence studies are conducted using both qualitative and quantitative methodologies.

This paper presents a series of significant enhancements to the CATUM solver, including the integration of a hybrid numerical scheme with a double flux (DF) model and a (modified) real-fluid model. These developments enable shock-droplet simulations at near-critical conditions with the following features:

· Extension to 3D: The numerical model and scheme have been extended to three dimensions. Detailed validations and mesh independence studies are included, along with extensive investigations of numerical scheme, computational domain and boundary condition effects at near-critical conditions.

· High-Resolution 3D Simulations: Utilizing over 434 computational finite volumes per initial droplet/cylinder diameter, this translates to over 0.87 billion finite volumes in total, representing the largest droplet simulation undertaken at near-critical conditions so far.

· Novel Configuration: This study introduces a novel configuration, designated the "Cavity-Embedded n-Dodecane Cylinder/Droplet", which is examined under near-critical conditions.

In particular, the following observations have been made:

· Distinct wave patterns and morphology changes: The presence of an internal gas cavity significantly alters the observed wave patterns and interactions. A detailed analysis of various parameters, including cylinder and internal bubble morphological changes, provides valuable in-sights into shock-induced deformation and wave interactions. The internal structures observed resemble those reported in numerical and experimental studies of shocked light bubbles. Interestingly, while the wave patterns at near-critical conditions are similar to those obtained in the case with the cylinder consisting of SF_6 in air at subcritical conditions, the deformation behavior of the current cylinder under near-critical conditions is more akin to that of a water column in air under subcritical conditions.

· Vortex formation and baroclinic effects: The simulations demonstrate the emergence of vortices and the deposition of vorticity on the surfaces of the cylinder or droplet. Vortices develop on the external surfaces, and the presence of the gas cavity has a notable impact on the creation of liquid mushroom jets, vortex structures, and the rupture of the cavity bubble, all of which contribute to the deformation of the interface.

· Enstrophy and mixing: Enstrophy, reflecting the mixing process, evolves over time. The presence of the gas cavity results in increased enstrophy due to internal jet formation and distortion of the mushroom structure. The generation of baroclinic vorticity intensifies enstrophy, promoting liquid-gas mixing.

· Center-of-mass redistribution: The analysis includes the drift of the center-of-mass position and velocity. The presence of the gas cavity enhances the shift velocity in both cylinder and droplet cases.

· Three-dimensional interface deformation: Three-dimensional simulations are crucial for revealing complex, deformed structures near the two-phase interface, such as ligaments, lobes, petal shapes, and toroidal structures. These features, along with the three-dimensional vorticity distribution, cannot be captured by two-dimensional simulations. A comparative analysis is conducted to examine the similarities and differences between the cases involving droplets and the cylindrical column. Interestingly, the deformation of the droplet shell at

near-critical conditions resembles that of a water droplet containing a cavity in air under subcritical conditions, exhibiting similar ringlike structures and the transverse jet. While the simulations are comparable to the characteristics of shear-induced entrainment for a chosen mass fraction, a complete understanding of the underlying physics requires further experimental validation.

3.2.3   Individual Contributions of the Candidate

This article was published in the international peer-reviewed journal Physical Review Fluids [75]. My contribution to this research paper was to propose the concept and idea of the paper, complete the programming codes and numerical methods, perform the validations, analyse the results, and write the manuscript.

3.3   Effect of Gas Cavity Size and Eccentricity on Shock Interaction with a Cylinder at Near-critical Conditions

3.3.1   State of the Art

Shock-cylinder interactions (SCIs) are valuable studies as the liquid/gas cylinder spans a wide range of angles between pressure and density gradient, thereby supporting various degrees of baroclinic production. SCIs are more accessible to experimental study than shock-droplet interactions (SDIs) and shock-bubble interactions (SBIs). SCIs have been extensively studied for many years [40, 41, 57, 67, 68, 99, 168, 194, 196], both numerically and experimentally. However, these studies have predominantly explored subcritical and supercritical conditions, with limited investigation into transcritical conditions.

Furthermore, the interaction between shock waves and cylinders containing gas cavities is rarely explored for transcritical cases. Previous investigations in this field have mainly focused on scenarios with low temperatures and pressures at ambient conditions [48, 102, 105, 162, 193, 195, 199, 202]. Only a few studies have examined the impact of cavity size or position on shock-cylinder interaction [48, 195, 199, 202]. A few studies have explored shock interactions with the droplet [16] and the shock interaction of a droplet above the critical pressure at varying temperatures [17]. These studies have provided insights into the early deformation behavior and mixing efficiency of high-pressure fuel injection but have not addressed the effects of the cavity. Moreover, there is a significant gap in understanding the interaction between shock waves and cavity-embedded cylinders with varying parameters at near-critical conditions.

3.3.2   Summary of the Publication

Yu Jiao *, Steffen J. Schmidt, Nikolaus A. Adams. (2024). Effect of Gas Cavity Size and Eccentricity on Shock Interaction with a Cylinder at Near-critical Conditions. Physics of Fluids. [74]

This publication employs numerical experiments to investigate the interaction of a planar shock wave with a fuel cylinder, involving eccentric and concentric cavities with varying radius, at transcritical conditions. This research is the first to investigate the effects of varying cavities on a fuel cylinder at transcritical conditions using a hybrid scheme with a real-fluid

model. The findings provide valuable insights for practical applications in a variety of trans-critical environments and high-speed propulsion systems.

The effects of gas cavity size, eccentricity angle and distance on the shock–cylinder interaction with the intricate layered fluid/interfaces at near-critical conditions are elucidated through detailed simulations, each considering real-fluid effects. Specifically, various cases involving eccentric and concentric cavities with different cavity radii (0-0.875R), eccentricity angles (0-180°), and distances(0R-0.45R) are analyzed. The paper also includes mesh independence studies for the case with a cavity. These factors significantly impact various properties of fuel cylinders at near-critical conditions, leading to the following observations:

· Pronounced Wave Patterns and Morphological Changes: Gas cavity size and eccentricity significantly alter wave patterns and shock-induced deformation. Detailed examinations cover the early and late stages of wave interaction, including shock impingement and evolution, along with morphological changes like jet formation and cavity breakup. The streamwise distance between the upstream pole of the cavity and the cylinder crucially affects wave pattern evolution. Asymmetric properties emerge when the cavity is not centered on the equator, leading to unequal cavity sizes. However, the wave pattern outside the cylinder remains largely unaffected by varying cavity sizes in the early stages. Comparisons with subcritical cases are drawn.

· Vortex Generation and Baroclinic Effects: Simulations reveal the emergence of vortices and the deposition of baroclinic vorticity on cylinder and cavity surfaces. Vortices form on external surfaces, and the presence of a gas cavity significantly impacts liquid mushroom jet creation, vortex structures, and cavity rupture, contributing to interface deformation. Vortices on cavity surfaces exhibit opposite characteristics to those on the cylinder. Additionally, cavities not centered on the cylinder's equator exhibit asymmetric vortex distributions along the axis.

· Circulation Analysis: Variations in negative circulation, positive circulation, total real circulation, and total absolute circulation (TAC) over time are thoroughly documented. Interaction between the cavity and cylinder surfaces affects circulation development, with reduced TAC observed when the gap between them is small. Thinner gaps lead to earlier reductions compared to full cylinder cases. Concentric cavity scenarios (especially for cavity radius of 0.375R to 0.625R) show potential for enhancing circulation performance, aiding the mixing process.

· Theoretical Model for Deposited Circulation: An analytical model for deposited circulation is proposed by appropriately combining the YKZ and ZZ models, which agrees well with numerical findings for cases involving smaller cavities (r= 0.000R-0.625R).

· Prediction fit for center-of-mass displacement: Four predictive fits for the centre-of-mass position of the shocked cylinder under near-critical conditions are obtained. These fits, which are tailored for cases involving cavities of varying sizes, eccentricity angles, and distances, are as follows: the Time-Size Polynomial Prediction Fit (TS-PPF), the Time-Eccentricity Polynomial Prediction Fit (TE-PPF), the Time-Eccentricity Distance Polynomial Prediction Fit (TED-PPF), and the Connecting Rod Prediction Fit (CRPF). These fits demonstrate good predictive performance and offer valuable insights into the mixing behaviour of liquid fuel sprays in a diverse range of near-critical environments and high-speed propulsion systems.

3.3.3 Individual Contributions of the Candidate

This article was published in the international peer-reviewed journal Physics of Fluids [74]. My contribution to this research paper was to propose the concept and idea of the paper, complete the programming codes and numerical methods, perform the validations, analyse the results, and write the manuscript.

Chapter 4

List of Research Outcomes

4.1 Peer-Reviewed Journal Publications for Thesis

· [73] Yu Jiao *, Steffen J. Schmidt, Nikolaus A. Adams. (2024). An All-Mach Consistent Numerical Scheme for Simulation of Compressible Multi-Component Fluids Including Surface Tension, Cavitation, Turbulence Modeling and Interface Sharpening on Compact Stencils. Computers & Fluids.

· [75] Yu Jiao *, Steffen J. Schmidt, Nikolaus A. Adams. (2024). Simulating Shock Interaction with a Cavity-Embedded Cylinder/Droplet Using a Real-Fluid Hybrid Scheme at Near-Critical Conditions. Physical Review Fluids.

· [74] Yu Jiao *, Steffen J. Schmidt, Nikolaus A. Adams. (2024). Effect of Gas Cavity Size and Eccentricity on Shock Interaction with a Cylinder at Near-critical Conditions. Physics of Fluids.

4.2 International Conference Contributions

· Yu Jiao *, Deniz Bezgin, Steffen J. Schmidt, Aaron Buhendwa, Alexander Bußmann, Oliver Messe, Barbara Traenkenschuh, Nikolaus A. Adams. (2024). Modelling of Acoustic Bubble Dynamics and Simulation of Ultrasonic Cleaning in JAX-Fluids. The 12th Cavitation Symposium, Chania, Crete.

· Yu Jiao *, Steffen J. Schmidt, Nikolaus A. Adams. (2022). Large Eddy Simulation of Primary Breakup Processes in Dual Fuel Internal Combustion Engines Using a Fully Compressible Multicomponent Approach. The 8th European Congress on Computational Methods in Applied Sciences and Engineering. doi:https://doi.org/10.23967/eccomas.2022.161.

4.3 Other Contributions

· Yu Jiao *, Steffen J. Schmidt, Nikolaus A. Adams (2023). An Efficient and Robust All-Mach Consistent Numerical Scheme for Simulation of Compressible Multi-Component Fluids including Surface Tension, Cavitation, Turbulence Modeling and Interface Sharpening on Compact Stencils. Submitted on 31 Mar 2023, arXiv preprint, https://arxiv.org/abs/2304.00140.

Chapter 5

Discussion with Respect to the State of the Art, Conclusion and Outlooks

This work focuses on the numerical and physical modeling of compressible multi-component flows, which encompasses surface tension, cavitation, turbulence and real-fluid effects with interface sharpening on compact stencils. This makes CATUM solver more powerful in complex real-world engineering applications. Potential applications include jet flow in a dual-fuel environment, shock-fuel interaction and transcritical flows in propulsion systems.

Firstly, in the context of internal combustion engines, there are complex multi-component turbulent flows. The dissipation for the fuel-gas interfaces motivates the development of a robust numerical method that does not require a change to the four-stencil compact scheme of CATUM and is highly efficient.

The THINC method [200] has thus far been developed and employed for the simulation of multiphase flows. However, it should be noted that THINC-based methods have been studied to a limited extent for complex compressible multi-component applications involving shock waves, turbulence, cavitation, real-fluid effects and moving interfaces. Daniel [20] employed THINC in the MUSCL scheme for incompressible multiphase flows. In order to simulate a supersonic liquid jet [112], a five-equation model was combined with a volume fraction THINC when capillary forces were neglected. A five-equation model combined with a density THINC was further implemented to simulate atomization [52]. Nonomura et al. [127] developed the THINC method with two compressible fluids and sharpened the volume fraction only, while Shyue and Xiao [167] presented a single-fluid multi-component flow model and used the reconstructed volume fraction to extrapolate other conservative parameters across the cell interface, both neglecting the surface tension. It is further noted that a recent development (VOF-based) [25] or ongoing work [65, 66] of the THINC-based method is the combination with the AMR technique in multiphase simulation, but it is still not fully capable for the complex compressible simulation involving cavitation flow, turbulent flow and real-fluid effects with increasing computational cost. Furthermore, coupled methods such as THINC-LS [139] and THINC-LS-VOF [89] were developed to enhance the description of interfaces and numerical accuracy. However, they typically necessitate significantly greater computational resources to achieve optimal performance. The aforementioned THINC-based method is typically employed to reconstruct the volume fraction of a five-equation model. In such models, the direct consideration of a Riemann solver of the cell interface is not a common occurrence. Rather, the relationship between pressure and density, as well as internal energy, is decoupled in the reconstruction process. Furthermore, realistic flows, such as viscous terms, surface tension, gravity, real-fluid effects, and cavitation, are typically ignored or not fully considered.

In current work, the THINC-TDU method is initially applied as a means of sharpening the interfaces and significantly enhancing the accuracy of predictions in compressible two-phase flows. The additional computational costs are minimal. This is achieved by combining an algebraic sharpening method with a thermodynamically consistent correction procedure in the

flux computation, thus obviating the need for complex geometric reconstruction approaches. The impact of surface tension, viscous effects, gravity, and shock-wave phenomena have been evaluated, and the outcomes align with established benchmarks. It has also been extended to be suitable for sub-grid turbulence modeling. A shock-droplet test case in near-critical conditions with a real-fluid model demonstrates that the current results are superior to those obtained using the WENO3-JS and OWENO3 schemes (assuming the same mesh resolution). In addition to gas bubble collapse, vapor bubble collapse was also performed to demonstrate that the two-phase interface between liquid and vapor can be sharpened using the current scheme. This illustrates the capacity of the current scheme to address cavitation-related cases that contain both condensable vapor and non-condensable gas, such as atomization using cavitation nozzles. The simulation of a three-dimensional turbulent jet flow with surface tension and viscous effects also exemplifies the high performance of the current scheme.

Having studied turbulent jet flow, it is evident that observing the detailed evolution of fuel-gas interfaces is a worthwhile endeavour. It is therefore natural to study the evolution of a single fuel droplet. In high-speed propulsion, it is crucial to consider the effects of real-fluid and shock, which represent a natural transition from normal thermodynamic conditions under incompressible or weakly compressible flow to critical thermodynamic conditions under higher compressible flow.

While there have been numerous studies of transcritical fluids in low-speed convective environments, where fluid evaporation is significantly influenced by viscous effects and heat conduction [22, 28, 117, 119, 204–206], research on the interaction of transcritical fuel cylinders/droplets with shock waves or high-speed flows is limited. Obtaining detailed experimental data on such flows, particularly at high pressures and temperatures, remains a challenge. Therefore, numerical experiments have become essential for such flows at near-critical conditions in high-pressure, high-speed propulsion systems.

Classical simulations of shock-bubble interactions (SBIs) [57, 66, 90, 93–95, 128, 140, 145, 179, 180, 210], shock-droplet interactions (SDIs) [32, 42, 50, 54, 120, 157, 189, 195] and Shock-cylinder interactions (SCIs) [40, 41, 57, 67, 68, 99, 168, 194, 196] have been extensively studied, focusing primarily on scenarios involving pure droplets, pure bubbles or pure cylinders. However, these studies have predominantly investigated subcritical and supercritical conditions, with limited investigation of near-critical or transcritical conditions. Fluids near their critical points exhibit distinct physical properties that differ significantly from classical simulations, requiring a unique approach.

Moreover, the interaction between shock waves and droplets containing gas or vapor-filled cavities, as well as the interaction between shock waves and bubbles containing droplets, represents a relatively unexplored area within the context of SDIs and SBIs. A significant knowledge gap remains regarding the interaction between shock waves and droplets containing embedded gas cavities, particularly under near-critical conditions and in three-dimensional scenarios. Previous investigations in this field have primarily focused on scenarios characterised by low temperatures and low pressures [48, 102, 123, 162, 191, 193, 199].

A few studies have explored shock interactions with the droplet [16] and the shock interaction of a droplet above the critical pressure at varying temperatures [17]. These studies have provided insights into the early deformation behavior and mixing efficiency of high-pressure fuel injection but have not addressed the effects of the cavity. Furthermore, there is a significant gap in understanding the interaction between shock waves and cavity-embedded cylinders with varying parameters.

In high-speed propulsion systems, enhancing the interaction between shock waves and fuel-gas interfaces is crucial for enhancing mixing, reducing combustion distances and reducing engine volumes. This thesis examines the intricate interactions of shock waves with a cylinder or droplet containing a gas cavity, particularly under near-critical thermodynamic

conditions. The effects of gas cavity size, eccentricity angle and eccentricity distance on the shock-cylinder interaction with the intricate layered fluid/interfaces at near-critical conditions are elucidated through detailed simulations, each considering real-fluid effects. Specifically, various cases involving eccentric and concentric cavities with different cavity radius (0-0.875R), eccentricity angles (0-180°) and distances (0R-0.45R) are analyzed. The presence of a gas cavity has a significant impact on the properties of the cylinder or droplet, including flow wave patterns, morphological changes, vortex formation, enstrophy, and three-dimensional developmental characteristics. The following observations were obtained:

· Distinct Wave Patterns and Morphology Changes: The internal structures observed resemble those reported in numerical and experimental studies of shocked light bubbles. Interestingly, while the wave patterns at near-critical conditions are similar to those obtained in the case with the cylinder consisting of SF_6 in air at sub-critical conditions, the deformation behavior of the current cylinder under near-critical conditions is more akin to that of a water column in air under sub-critical conditions. Besides, gas cavity size and eccentricity significantly alter wave patterns and shock-induced deformation. The streamwise distance between the upstream pole of the cavity and the cylinder crucially affects wave pattern evolution. Asymmetric properties emerge when the cavity is not centered on the equator, leading to unequal cavity sizes. However, the wave pattern outside the cylinder remains largely unaffected by varying cavity sizes in the early stages. Comparisons with sub-critical cases are drawn.

· Vortex Formation and Baroclinic Effects: The simulations demonstrate the emergence of vortices and the deposition of vorticity on the surfaces of the cylinder or droplet. Vortices develop on the external surfaces, and the presence of the gas cavity has a notable impact on the creation of liquid mushroom jets, vortex structures, and the rupture of the cavity bubble, all of which contribute to the deformation of the interface. Vortices on cavity surfaces exhibit opposite characteristics to those on the cylinder. Additionally, cavities not centered on the cylinder's equator exhibit asymmetric vortex distributions along the axis.

· Enstrophy and Mixing: Enstrophy, reflecting the mixing process, evolves over time. The presence of the gas cavity results in increased enstrophy due to internal jet formation and distortion of the mushroom structure. The generation of baroclinic vorticity intensifies enstrophy, promoting liquid-gas mixing.

· Circulation Analysis and Theoretical Model for Deposited Circulation: Variations in negative circulation, positive circulation, total real circulation, and total absolute circulation (TAC) over time are thoroughly documented. Interaction between cavity and cylinder surfaces affects circulation development, with reduced TAC observed when the gap between them is small. Thinner gaps lead to earlier reductions compared to full cylinder cases. Besides, successful prediction of deposited circulation for concentric scenarios at near-critical conditions is achieved. Theoretical results from properly combining YKZ and ZZ models align well with numerical results for smaller cavity cases (r=0.000R-0.625R). However, for larger cavity cases, cavity-cylinder contact and induced coupling effects distort theoretical predictions. The normal distance between cavity and cylinder center has minimal effect on circulating production in early stages.

· Prediction Fit for Centre-of-Mass Displacement: The analysis includes the drift of the center-of-mass position and velocity. The presence of the gas cavity enhances the shift velocity in both cylinder and droplet cases. Four predictive fits for the center-of-mass position of shocked cylinders at near-critical conditions demonstrate excellent predictive performance. TS-PPF, TE-PPF, and TED-PPF are proposed for cases involving cavities of various sizes, eccentricity angles, and eccentricity distances. The hybrid fit (CRPF) incorporates evolution time, cavity size, and eccentricity, with minimal effect from the normal distance between cavity and cylinder center.

· Three-Dimensional Interface Deformation: Three-dimensional simulations are crucial for revealing complex, deformed structures near the two-phase interface, such as ligaments, lobes, petal shapes, and toroidal structures. These features, along with the three-dimensional vorticity distribution, cannot be captured by two-dimensional simulations. A comparative analysis is conducted to examine the similarities and differences between the cases involving droplets and the cylindrical column. Interestingly, the deformation of the droplet shell at near-critical conditions resembles that of a water droplet containing a cavity in air under sub-critical conditions, exhibiting similar ring-like structures and the transverse jet. While the simulations are comparable to the characteristics of shear-induced entrainment for a chosen mass fraction, a complete understanding of the underlying physics requires further experimental validation.

This study offers insights into mixing processes at near-critical conditions, with potential engineering applications in high-speed propulsion systems utilizing liquid fuel sprays. Future research may involve more extensive experimental investigations to deepen understanding of underlying mechanisms and disintegration processes.

For the advancement of SDIs and SCIs at near-critical conditions, the development of multiscale modeling approaches that integrate microscale, mesoscale and macroscale phenomena is of great importance. Molecular dynamics (MD) simulations provide detailed insights at the microscale, which are essential for understanding very fundamental interactions. The Lattice Boltzmann method (LBM) serves to bridge the gap at the mesoscale, thereby enabling the capture of fluid dynamics in instances where the application of continuum assumptions may prove to be inadequate. At the macroscale, FVM is employed to solve large-scale fluid dynamics equations. Integrating MD, LBM with FVM allows more physics to be included in macroscale models, thereby facilitating fundamental research and complex engineering problems. This multiscale approach serves to enhance the development of efficient, high-precision, and robust algorithms for compressible multi-component flows [111].

Subsequent investigation could focus on more specific issues related to compressible multi-component flows. For example, bubble clouds and cavitation nucleation [56, 110, 150, 192] is of paramount importance for the comprehension of the dynamics of compressible multi-component flows. The collective behaviour of numerous bubbles gives rise to bubble clouds, which significantly influence fluid properties and can lead to complex phenomena such as shock wave propagation and bubble-bubble interaction. The cavitation nucleation plays a pivotal role in various engineering applications, from hydraulic machinery to biomedical devices. To address these phenomena, comprehensive models that incorporate both physical principles and advanced numerical techniques are required, ensuring accurate prediction and control of bubble dynamics and cavitation processes. A two-way coupling method can be effectively employed to address bubble dynamics by utilising motion equations such as the Rayleigh-Plesset (RP) and Keller-Miksis (KM) equations. In this approach, particles can be used to represent underresolved bubbles. The latest codes [71, 100, 101] from CFD Community have been successfully implemented in the transition from the Eulerian (E) to Lagrangian (L) phases for cavitating flows. Nevertheless, additional validation of the criteria governing this transition is necessary to guarantee seamless phase transitions and to enhance the predictive capabilities of bubble dynamics models in multiphase flow simulations.

For surface tension effects, future advances could integrate machine learning techniques with physical principles to develop more robust and reliable models [19]. It is noted that Google, NVIDIA, and Baidu are developing frameworks for machine learning and partial differential equations, thereby enabling AI4CFD (Artificial Intelligence for Computational Fluid Dynamics). However, achieving higher model accuracy with fewer training resources remains a challenge. It is therefore essential that the evolution of physics-informed machine learning [83, 114, 142, 143], interpretable and lightweight neural network architectures

[104, 164], and strong generalization capabilities of the trained model be pursued.

Furthermore, as developers, our objective should be to provide efficient, high-precision, and robust algorithms for compressible multi-component flows encountered in complex engineering problems. Nevertheless, there is still considerable scope for further progress. A number of software packages have been developed to address the field of computational fluid dynamics, including ALPACA, JAX-Fluids, CATUM, OpenFOAM, Basilisk, MFC, UCNS3D, SU2, JAX-CFD, FluidX3D, SPHinXsys, PyFR, AMRVC, Lesgo, DUGKS-GPU, HORSES3D, BIM-BAMBUM, MFiX, ECOGEN and so on. However, despite the existence of these solvers, there is a lack of communication and collaboration between them, with development remaining isolated. This results in the replication of certain functionalities and the ineffective dissemination of the most sophisticated algorithms. While some solvers have incorporated compressible multi-component/multi-phase flow algorithms, their development has been relatively slow. The challenge lies in coupling physical mechanisms with engineering applications, ensuring a solid foundation in mathematical and physical theory, alongside experimental validation.

All in all, the study of compressible multi-component flows represents a compelling avenue of scientific inquiry. In order to fully comprehend related phenomena, it is essential to adopt a fundamental approach which emphasises the role of physics as the underlying foundation. By integrating numerical algorithms, experimental tools and machine learning techniques as auxiliary tools, the discovery of novel physical phenomena and laws can be facilitated.

Bibliography

[1] Abgrall, R. "How to prevent pressure oscillations in multicomponent flow calculations: a quasi conservative approach". In: *Journal of Computational Physics* 125.1 (1996), pp. 150–160.

[2] Abgrall, R. and Karni, S. "Computations of compressible multifluids". In: *Journal of Computational Physics* 169.2 (2001), pp. 594–623.

[3] Adams, N. A., Hickel, S., and Franz, S. "Implicit subgrid-scale modeling by adaptive deconvolution". In: *Journal of Computational Physics* 200.2 (2004), pp. 412–431.

[4] Afkhami, S. and Bussmann, M. "Height functions for applying contact angles to 3D VOF simulations". In: *International Journal of Numerical Methods in Fluids* 61.8 (2009), pp. 827–847.

[5] Albada, G. D. V., Leer, B. V., and Roberts, W. W. "A comparative study of computational methods in cosmic gas dynamics". In: *Astronomy and Astrophysics* 108.1 (1982), pp. 76–84.

[6] Allaire, G., Clerc, S., and Kokh, S. "A five-equation model for the simulation of interfaces between compressible fluids". In: *Journal of Computational Physics* 181.2 (2002), pp. 577–616.

[7] Andrianov, N. and Warnecke, G. "The Riemann problem for the Baer-Nunziato two-phase flow model". In: *Journal of Computational Physics* 201.2 (2004), pp. 226–252.

[8] Banuti, D., Raju, M., Ma, P. C., Ihme, M., and Hickey, J.-P. "Seven questions about supercritical fluids towards a new fluid state diagram". In: *Proceedings of the 55th AIAA Aerospace Sciences Meeting*. 2017, p. 1106.

[9] Banuti, D. T., Raju, M., and Ihme, M. "Supercritical pseudoboiling for general fluids and its application to injection". In: *Annual Research Briefs, Center for Turbulence Research, Stanford University*. 2016, pp. 3–16.

[10] Banuti, D. T., Ma, P. C., and Ihme, M. "Phase separation analysis in supercritical injection using large-eddy-simulation and vapor-liquid-equilibrium". In: *53rd AIAA/SAE/ /ASEE Joint Propulsion Conference*. 2017, p. 4764.

[11] Bauer, M. and Nunziato, J. "A two-phase mixture Theory for the deflagration-to-detonation Transition (DDT) in reactive granular materials". In: *International Journal of Multiphase Flow* 12.4 (1986), pp. 563–580.

[12] Bdzil, J. B., Menikoff, R., Son, S. F., Kapila, A. K., and Stewart, D. S. "Two-phase modeling of deflagration-to-detonation transition in granular materials: a critical examination of modeling issues". In: *Physics of Fluids* 11.2 (1999), pp. 378–402.

[13] Billet, G. and Abgrall, R. "An adaptive shock-capturing algorithm for solving unsteady reactive flows". In: *Computers and Fluids* 32.2 (2003), pp. 1473–1495.

[14] Billet, G. and Ryan, J. "A Runge-Kutta discontinuous Galerkin approach to solve reactive flows: The hyperbolic operator". In: *Journal of Computational Physics* 230.4 (2011), pp. 1064–1083.

[15] Boris, J. P. and Book, D. L. "Flux-corrected transport. I. SHASTA, A fluid transport algorithm that works". In: *Journal of Computational Physics* 11.1 (1973), pp. 38–69.

[16] Boyd, B. and Jarrahbashi, D. "A diffuse-interface method for reducing spurious pressure oscillations in multicomponent transcritical flow simulations". In: *Computers and Fluids* 216 (2021), p. 104924.

[17] Boyd, B. and Jarrahbashi, D. "Numerical study of the transcritical shock-droplet interaction". In: *Physical Review Fluids* 6.11 (2021), p. 113601.

[18] Brackbill, J., Kothe, D., and Zemach, C. "A continuum method for modeling surface tension". In: *Journal of Computational Physics* 100.2 (1992), pp. 335–354.

[19] Cahaly, A., Evrard, F., and Desjardins, O. "PLIC-Net: A machine learning approach for 3D interface reconstruction in volume of fluid methods". In: *International Journal of Multiphase Flow* (2024), p. 104888.

[20] Cassidy, D. A., Edwards, J. R., and Tian, M. "An investigation of interface-sharpening schemes for multi-phase mixture flows". In: *Journal of Computational Physics* 228.16 (2009), pp. 5628–5649.

[21] Castro, C. E. and Toro, E. F. "A Riemann solver and upwind methods for a two-phase flow model in non-conservative form". In: *International Journal of Numerical Methods in Fluids* 50.7 (2006), pp. 777–812.

[22] Chae, J. W., Yang, H. S., and Yoon, W. S. "Supercritical droplet dynamics and emission in low speed cross-flows". In: *Journal of Mechanical Science and Technology* 22.11 (2008), pp. 2099–2107.

[23] Chakravarthy, S. and Osher, S. "High resolution applications of the Osher upwind scheme for the Euler equations". In: *6th Computational Fluid Dynamics Conference*. AIAA. 1983, pp. 167–176.

[24] Chella, R. and Viñals, J. "Mixing of a two-phase fluid by cavity flow". In: *Physical Review E* 53.4 (1996), pp. 3832–3840.

[25] Chen, D., Tong, X., Xie, B., Xiao, F., and Li, Y. "An accurate and efficient multiphase solver based on THINC scheme and adaptive mesh refinement". In: *International Journal of Multiphase Flow* 149 (2023), p. 104073.

[26] Chern, I.-L., Glimm, J., Mcbryan, O., Plohr, B., and Yaniv, S. "Front tracking for gas dynamics". In: *Journal of Computational Physics* 62.1 (1986), pp. 83–110.

[27] Chiapolino, A., Boivin, P., and Saurel, R. "A simple and fast-phase transition relaxation solver for compressible Multicomponent Two-Phase Flows". In: *Computers and Fluids* 148 (2017), pp. 105–116.

[28] Crua, C., Manin, J., and Pickett, L. M. "On the transcritical mixing of fuels at diesel engine conditions". In: *Fuel* 210 (2017), pp. 826–839.

[29] Cummins, S. J., Francois, M. M., and Kothe, D. B. "Estimating curvature from volume fractions". In: *Computers and Structures* 83.6-7 (2005), pp. 425–434.

[30] Dahms, R. N., Manin, J., Pickett, L. M., and Oefelein, J. C. "Understanding high-pressure gas-liquid interface phenomena in diesel engines". In: *Proceedings of the Combustion Institute* 34.1 (2013), pp. 1667–1675.

[31] Dahms, R. N. "Understanding the breakdown of classic two-phase theory and spray atomization at engine-relevant conditions". In: *Physics of Fluids* 28.4 (2016).

[32] Das, P. and Udaykumar, H. S. "A sharp-interface method for the simulation of shock-induced vaporization of droplets". In: *Journal of Computational Physics* 404 (2020), p. 109120.

[33] Delale, C. F. *Bubble Dynamics and Shock Waves*. Springer Berlin Heidelberg, 2013.

[34] Deng, X., Inaba, S., Xie, B., Shyue, K.-M., and Xiao, F. "High fidelity discontinuity-resolving reconstruction for compressible multiphase flows with moving interfaces". In: *Journal of Computational Physics* 374 (2018), pp. 425–455.

[35] Deng, X., Jiang, Z.-h., Xiao, F., and Yan, C. "Implicit large eddy simulation of compressible turbulence flow with PnTm-BVD Scheme". In: *Applied Mathematical Modelling* 80 (2020), pp. 441–459.

[36] Deng, X., Shimizu, Y., and Xiao, F. "A fifth-order shock capturing scheme with two-stage boundary variation diminishing algorithm". In: *Journal of Computational Physics* 396 (2019), pp. 173–192.

[37] Deng, X., Shimizu, Y., Xie, B., and Xiao, F. "Constructing higher order discontinuity-capturing schemes with upwind-biased interpolations and boundary variation diminishing algorithm". In: *Computers and Fluids* 199 (2020), p. 104420.

[38] Deshpande, S. S., Anumolu, L., and Trujillo, M. F. "Evaluating the performance of the two-phase flow solver interFoam". In: *Computer Science and Discovery* 5.1 (2012), p. 014016.

[39] Diegelmann, F., Hickel, S., and Adams, N. A. "Shock Mach number influence on reaction wave types and mixing in reactive shock-bubble interaction". In: *Combustion and Flame* 172 (2016), pp. 1–20.

[40] Ding, J., Liang, Y., Chen, M., Zhai, Z., Si, T., and Luo, X. "Interaction of planar shock wave with three-dimensional heavy cylindrical bubble". In: *Physics of Fluids* 30.10 (2018), p. 106109.

[41] Ding, J., Si, T., Chen, M., Zhai, Z., Lu, X., and Luo, X. "On the interaction of a planar shock with a three-dimensional light gas cylinder". In: *Journal of Fluid Mechanics* 828 (2017), pp. 289–317.

[42] Dorschner, B., Biasiori-Poulanges, L., Schmidmayer, K., El-Rabii, H., and Colonius, T. "On the formation and recurrent shedding of ligaments in droplet aerobreakup". In: *Journal of Fluid Mechanics* 904 (2020), A20.

[43] Ducros, F., Ferrand, V., Nicoud, F., Weber, C., Darracq, D., Gacherieu, C., and Poinsot, T. "Large eddy simulation of the shock/turbulence interaction". In: *Journal of Computational Physics* 152.2 (1999), pp. 517–549.

[44] Duke-Walker, V., Maxon, W. C., Almuhna, S. R., and McFarland, J. A. "Evaporation and breakup effects in the shock-driven multiphase instability". In: *Journal of Fluid Mechanics* 908 (2021), A13.

[45] Egerer, C. P., Hickel, S., Schmidt, S. J., and Adams, N. A. "Large-eddy simulation of turbulent cavitating flow in a micro channel". In: *Physics of Fluids* 28.4 (2016), p. 045102.

[46] Falgout, Z., Rahm, M., Sedarsky, D., and Linne, M. "Gas/fuel jet interfaces under high pressures and temperatures". In: *Fuel* 168 (2016), pp. 14–21.

[47] Fedkiw, R. P., Aslam, T., Merriman, B., and Osher, S. "A non-oscillatory Eulerian approach to interfaces in multimaterial flows (the ghost fluid method)". In: *Journal of Computational Physics* 152.2 (1999), pp. 457–492.

[48] Feng, L., Xu, J., Zhai, Z., and Luo, X. "Evolution of shock-accelerated double-layer gas cylinder". In: *Physics of Fluids* 33.8 (2021), p. 086105.

[49] Ferziger, J. H. and Perić, M. *Computational methods for fluid dynamics*. Springer, 2002.

[50] Forehand, R. W., Nguyen, K. C., Anderson, C. J., Shannon, R., Grace, S. M., and Kinzel, M. P. "A numerical assessment of shock–droplet interaction modeling including cavitation". In: *Physics of Fluids* 35.2 (2023), p. 023315.

[51] Francois, M. M., Cummins, S. J., Dendy, E. D., Kothe, D. B., Sicilian, J. M., and Williams, M. W. "A balanced force algorithm for continuous and sharp interfacial surface tension models within a volume tracking framework". In: *Journal of Computational Physics* 213.1 (2006), pp. 141–173.

[52] Garrick, D. P., Hagen, W. A., and Regele, J. D. "An interface capturing scheme for modeling atomization in compressible flows". In: *Journal of Computational Physics* 339 (2017), pp. 46–67.

[53] Garrick, D. P., Owkes, M., and Regele, J. D. "A finite-volume HLLC-based scheme for compressible interfacial flows with surface tension". In: *Journal of Computational Physics* 339 (2017), pp. 46–67.

[54] Guan, B., Liu, Y., Wen, C. Y., and Shen, H. "Numerical study on liquid droplet internal flow under shock impact". In: *AIAA Journal* 56.9 (2018), pp. 3382–3387.

[55] Gueyffier, D., Li, J., Nadim, A., Scardovelli, R., and Zaleski, S. "Volume-of-fluid interface tracking with smoothed surface stress methods for three-dimensional flows". In: *Journal of Computational Physics* 152.2 (1999), pp. 423–456.

[56] Gutiérrez-Hernández, U. J., Reese, H., Ohl, C.-D., and Quinto-Su, P. A. "Controlled inertial nano-cavitation above 100 MHz". In: *Journal of Fluid Mechanics* 972 (2023), A16.

[57] Haas, J. F. and Sturtevant, B. "Interaction of weak shock waves with cylindrical and spherical gas inhomogeneities". In: *Journal of Fluid Mechanics* 181 (1987), pp. 41–76.

[58] Harstad, K. G., Miller, R. S., and Bellan, J. "Efficient high-pressure state equations". In: *AIChE Journal* 43.6 (1997), pp. 1605–1610.

[59] Hickel, S. and Adams, N. A. "On implicit subgrid-scale modeling in wall-bounded flows". In: *Physics of Fluids* 19.10 (2007), p. 105106.

[60] Hickel, S., Adams, N. A., and Domaradzki, J. A. "An adaptive local deconvolution method for implicit LES". In: *Journal of Computational Physics* 213.1 (2006), pp. 413–436.

[61] Hickel, S., Adams, N. A., and Mansour, N. N. "Implicit subgrid-scale modeling for large-eddy simulation of passive-scalar mixing". In: *Physics of Fluids* 19.9 (2007), p. 095102.

[62] Hickel, S., Egerer, C. P., and Larsson, J. "Subgrid-scale modeling for implicit large eddy simulation of compressible flows and shock-turbulence interaction". In: *Physics of Fluids* 26.10 (2014), p. 106101.

[63] Hickel, S. and Larsson, J. "On implicit turbulence modeling for LES of compressible flows". In: *Advances in Turbulence XII*. Ed. by Eckhardt, B. Springer, 2009, pp. 441–446.

[64] Hirt, C. and Nichols, B. "Volume of fluid (VOF) method for the dynamics of free boundaries". In: *Journal of Computational Physics* 39.1 (1981), pp. 201–225.

[65] Hoppe, N., Adami, S., and Adams, N. A. "A parallel modular computing environment for three-dimensional multiresolution simulations of compressible flows". In: *Computer Methods in Applied Mechanics and Engineering* 389 (2022), p. 114321.

[66]   Hoppe, N., Winter, J. M., Adami, S., and Adams, N. A. "ALPACA-a level-set based sharp-interface multiresolution solver for conservation laws". In: *Computer Physics Communications* 273 (2022), p. 108249.

[67]   Jacobs, J. "Shock-induced mixing of a light-gas cylinder". In: *Journal of Fluid Mechanics* 234 (1992), pp. 629–649.

[68]   Jacobs, J. W. "The dynamics of shock accelerated light and heavy gas cylinders". In: *Physics of Fluids A: Fluid Dynamics* 5.9 (1993), pp. 2239–2247.

[69]   Jacqmin, D. "Calculation of two-phase Navier-Stokes flows using phase-field modeling". In: *Journal of Computational Physics* 155.1 (1999), pp. 96–127.

[70]   Jain, S. S., Mani, A., and Moin, P. "A conservative diffuse-interface method for compressible two-phase flows". In: *Journal of Computational Physics* 418 (2020), p. 109606.

[71]   Ji, B., Wang, Z.-y., Cheng, H.-y., and Bensow, R. E. "Cavitation research with computational fluid dynamics: From Euler-Euler to Euler-Lagrange approach". In: *Journal of Hydrodynamics* 36.1 (2024), pp. 1–23.

[72]   Jiang, G.-S. and Shu, C.-W. "Efficient implementation of weighted ENO schemes". In: *Journal of Computational Physics* 126.1 (1996), pp. 202–228.

[73]   Jiao, Y., Schmidt, S. J., and Adams, N. A. "An all-Mach consistent numerical scheme for simulation of compressible multi-component fluids including surface tension, cavitation, turbulence modeling and interface sharpening on compact stencils". In: *Computers and Fluids* (2024), p. 106186.

[74]   Jiao, Y., Schmidt, S. J., and Adams, N. A. "Effect of gas cavity size and eccentricity on shock interaction with a cylinder at near-critical conditions". In: *Physics of Fluids* (2024).

[75]   Jiao, Y., Schmidt, S. J., and Adams, N. A. "Simulating shock interaction with a cavity-embedded cylinder/droplet using a real-fluid hybrid scheme at near-critical conditions". In: *Physical Review Fluids* (2024), p. 074002.

[76]   Jibben, Z., Velechovsky, J., Masser, T., and Francois, M. M. "Modeling surface tension in compressible flow on an adaptively refined mesh". In: *Computers and Mathematics with Applications* 77.4 (2019), pp. 1164–1177.

[77]   Johnsen, E. "Spurious oscillations and conservation errors in interface-capturing schemes". In: *Annual Research Briefs 2008, Center for Turbulence Research, NASA Ames and Stanford University* (2008), pp. 23–36.

[78]   Johnsen, E. and Ham, F. "Preventing numerical errors generated by interface capturing schemes in compressible multi-material flows". In: *Journal of Computational Physics* 231.2 (2012), pp. 5705–5717.

[79]   Johnsen, E. and Colonius, T. "Implementation of WENO schemes in compressible multicomponent flow problems". In: *Journal of Computational Physics* 219.2 (2006), pp. 715–732.

[80]   Kaiser, J. W. J., Winter, J. M., Adami, S., and Adams, N. A. "Investigation of interface deformation dynamics during high-Weber number cylindrical droplet breakup". In: *International Journal of Multiphase Flow* 125 (2020), p. 103409.

[81]   Kang, M., Fedkiw, R. P., and Liu, X. D. "A boundary condition capturing method for multiphase incompressible flow". In: *Journal of Scientific Computing* 15.3 (2000), pp. 323–360.

[82] Kapila, A., Menikoff, R., Bdzil, J., Son, S., and Stewart, D. "Two-phase modeling of the deflagration-to-detonation transition in granular materials: Reduced Equations". In: *Physics of Fluids* 13.10 (2001), pp. 3002–3024.

[83] Karniadakis, G. E., Kevrekidis, I. G., Lu, L., Perdikaris, P., Wang, S., and Yang, L. "Physics-informed machine learning". In: *Nature Reviews Physics* 3.6 (2021), pp. 422–440.

[84] Kim, J. "A continuous surface tension force formulation for diffuse-interface models". In: *Journal of Computational Physics* 204.2 (2004), pp. 784–804.

[85] Kitamura, K. and Shima, E. "Pressure-equation-based SLAU2 for oscillation-free, supercritical flow simulations". In: *Computers and Fluids* 163 (2018), pp. 86–96.

[86] Knudsen, E., Doran, E. M., Mittal, V., Meng, J., and Spurlock, W. "Compressible Eulerian needle-to-target large eddy simulations of a diesel fuel injector". In: *Proceedings of the Combustion Institute*. Vol. 36. 2. 2017, pp. 2459–2466.

[87] Koren, B. "A robust upwind discretization method for advection, diffusion, and source terms". In: *Numerical Methods for Advection-Diffusion Problems*. Vieweg, Braunschweig, Germany, 1993, pp. 117–138.

[88] Koukouvinis, P., Vidal-Roncero, A., Rodriguez, C., Gavaises, M., and Pickett, L. "High pressure/high temperature multiphase simulations of dodecane injection to nitrogen: Application on ECN Spray-A". In: *Fuel* 264 (2020), p. 116779.

[89] Kumar, R., Cheng, L., Xiong, Y., Xie, B., Abgrall, R., and Xiao, F. "THINC scaling method that bridges VOF and level set schemes". In: *Journal of Computational Physics* 426 (2021), p. 109915.

[90] Kumar, S., Orlicz, G., Tomkins, C., Goodenough, C., Prestridge, K., Vorobieff, P., and Benjamin, R. "Stretching of material lines in shock-accelerated gaseous flows". In: *Physics of Fluids* 17.8 (2005), p. 082103.

[91] Lacaze, G., Schmitt, T., Ruiz, A., and Oefelein, J. C. "Comparison of energy-, pressure- and enthalpy-based approaches for modeling supercritical flows". In: *Computers and Fluids* 181 (2019), pp. 35–56.

[92] Lafaurie, B., Nardone, C., Scardovelli, R., Zaleski, S., and Zanetti, G. "Modelling merging and fragmentation in multiphase flows with SURFER". In: *Journal of Computational Physics* 113.1 (1994), pp. 134–147.

[93] Layes, G., Jourdan, G., and Houas, L. "Distortion of a spherical gaseous interface accelerated by a plane shock wave". In: *Physical Review Letters* 91.17 (2003), p. 174502.

[94] Layes, G., Jourdan, G., and Houas, L. "Experimental investigation of the shock wave interaction with a spherical gas inhomogeneity". In: *Physics of Fluids* 17.2 (2005), p. 028103.

[95] Layes, G., Jourdan, G., and Houas, L. "Experimental study on a plane shock wave accelerating a gas bubble". In: *Physics of Fluids* 21.7 (2009), p. 074102.

[96] Leer, B. V. "Towards the ultimate conservative difference scheme II. monotonicity and conservation combined in a second order scheme". In: *Journal of Computational Physics* 14.4 (1974), pp. 361–370.

[97] Leer, B. V. "Towards the ultimate conservative difference scheme III. upstream-centered finite-difference schemes for ideal compressible Flow". In: *Journal of Computational Physics* 23.3 (1977), pp. 263–275.

[98]   Leer, B. V. "Towards the ultimate conservative difference scheme, V. a second order sequel to Godunov's method". In: *Journal of Computational Physics* 32.1 (1979), pp. 101–136.

[99]   Li, D., Wang, G., and Guan, B. "On the circulation prediction of shock-accelerated elliptical heavy gas cylinders". In: *Physics of Fluids* 31.5 (2019), p. 056104.

[100]   Li, L., Niu, Y., Wei, G., Manickam, S., Sun, X., and Zhu, Z. "Investigation of cavitation noise using Eulerian-Lagrangian multiscale modeling". In: *Ultrasonics Sonochemistry* 97 (2023), p. 106446.

[101]   Li, L., Pei, C., Wang, Z., Lin, Z., Li, X., and Zhu, Z. "Assessment of cavitation erosion risk by Eulerian–Lagrangian multiscale modeling". In: *International Journal of Mechanical Sciences* 262 (2024), p. 108735.

[102]   Liang, Y., Jiang, Y., Wen, C., and Liu, Y. "Interaction of a planar shock wave and a water droplet embedded with a vapour cavity". In: *Journal of Fluid Mechanics* 885 (2020), R6.

[103]   Liu, X.-D., Osher, S., and Chan, T. "Weighted essentially non-oscillatory schemes". In: *Journal of Computational Physics* 115.1 (1994), pp. 200–212.

[104]   Liu, Z., Wang, Y., Vaidya, S., Ruehle, F., Halverson, J., Soljačić, M., Hou, T. Y., and Tegmark, M. "Kan: Kolmogorov-arnold networks". In: *arXiv preprint arXiv:2404.19756* (2024).

[105]   Lü, M., Ning, Z., and Sun, C. "Numerical simulation of cavitation bubble collapse within a droplet". In: *Computers and Fluids* 152 (2017), pp. 157–163.

[106]   Lv, Y. and Ihme, M. "Discontinuous Galerkin method for multi-component chemically reacting flows and combustion". In: *Journal of Computational Physics* 270 (2014), pp. 105–137.

[107]   Ma, P. C., Lv, Y., and Ihme, M. "An entropy-stable hybrid scheme for simulations of transcritical real-fluid flows". In: *Journal of Computational Physics* 340 (2017), pp. 330–357.

[108]   Ma, P. C., Wu, H., Banuti, D. T., and Ihme, M. "On the numerical behavior of diffuse-interface methods for transcritical real-fluids simulations". In: *International Journal of Multiphase Flow* 113 (2019), pp. 231–249.

[109]   Ma, P. C., Wu, H., Jaravel, T., Bravo, L., and Ihme, M. "Large-eddy simulations of transcritical injection and auto-ignition using diffuse-interface method and finite-rate chemistry". In: *Proceedings of the Combustion Institute* 37.3 (2019), pp. 3303–3310.

[110]   Maeda, K. and Fuster, D. "Regressing bubble cluster dynamics as a disordered many-body system". In: *Journal of Fluid Mechanics* 985 (2024), A23.

[111]   Magiera, J. and Rohde, C. "A Multiscale Method for Two-Component, Two-Phase Flow with a Neural Network Surrogate". In: *Communications on Applied Mathematics and Computation* (2024), pp. 1–30.

[112]   Majidi, S. and Afshari, A. "Supersonic liquid jets into quiescent gaseous media: an adaptive numerical study". In: *Journal of Fluids Engineering* 138.11 (2016), p. 111202.

[113]   Maltesev, V., Skote, M., and Tsoutsanis, P. "High-order methods for diffuse-interface models in compressible multi-medium flows: a review". In: *Physics of Fluids* 34.3 (2022), p. 030901.

[114]   Mao, Z., Jagtap, A. D., and Karniadakis, G. E. "Physics-informed neural networks for high-speed flows". In: *Computer Methods in Applied Mechanics and Engineering* 360 (2020), p. 112789.

[115] Marquina, A. and Mulet, P. "A flux-split algorithm applied to conservative models for multicomponent compressible flows". In: *Journal of Computational Physics* 185.1 (2003), pp. 120–138.

[116] Matheis, J. and Hickel, S. "Multi-component vapor-liquid equilibrium model for LES of high-pressure fuel injection and application to ECN Spray A". In: *International Journal of Multiphase Flow* 99 (2018), pp. 294–311.

[117] Mayer, W. O. H., Schik, A. H. A., Vielle, B., Chauveau, C., Gokalp, I., Talley, D. G., and Woodward, R. D. "Atomization and breakup of cryogenic propellants under high-pressure subcritical and supercritical conditions". In: *Journal of Propulsion and Power* 14.5 (1998), pp. 835–842.

[118] McBride, B. J. *Coefficients for calculating thermodynamic and transport properties of individual species*. Tech. rep. NASA Langley Research Center, 1993.

[119] Meng, H., Hsiao, G. C., Yang, V., and Shuen, J. S. "Transport and dynamics of liquid oxygen droplets in supercritical hydrogen streams". In: *Journal of Fluid Mechanics* 527 (2005), pp. 115–139.

[120] Meng, J. C. and Colonius, T. "Numerical simulation of the aerobreakup of a water droplet". In: *Journal of Fluid Mechanics* 835 (2018), pp. 1108–1135.

[121] Métayer, O. L., Massoni, J., and Saurel, R. "Elaborating equations of state of a liquid and its vapor for two-phase flow models". In: *International Journal of Thermal Sciences* 43.3 (2004), pp. 265–276.

[122] Métayer, O. L. and Saurel, R. "The Noble-Abel Stiffened-Gas equation of state". In: *Physics of Fluids* 28.4 (2016), p. 046102.

[123] Ming, L., Zhi, N., and Chunhua, S. "Numerical simulation of cavitation bubble collapse within a droplet". In: *Computers and Fluids* 152 (2017), pp. 157–163.

[124] Müller, H., Niedermeier, C. A., Matheis, J., Pfitzner, M., and Hickel, S. "Large-eddy simulation of nitrogen injection at trans-and supercritical conditions". In: *Physics of Fluids* 28.1 (2016), p. 015102.

[125] Muzaferija, S., Peric, M., Sames, P., and Schellin, T. "A two-fluid Navier-Stokes solver to simulate water entry". In: *Proceedings of the 22nd symposium on naval hydrodynamics*. National Academies Press, Washington, DC. 1998, pp. 715–737.

[126] Nadiga, B. and Zaleski, S. "Investigations of a two-phase fluid model". In: *European Journal of Mechanics B-Fluids* 15.4 (1996), pp. 885–896.

[127] Nonomura, T., Kitamura, K., and Fujii, K. "A simple interface sharpening technique with a hyperbolic tangent function applied to compressible two-fluid modeling". In: *Journal of Computational Physics* 265 (2014), pp. 110–127.

[128] Nowakowski, A. F., Ballil, A., and Nicolleau, F. C. G. A. "Passage of a shock wave through inhomogeneous media and its impact on gas-bubble deformation". In: *Physical Review E* 92.2 (2015), p. 023028.

[129] Oefelein, J., Lacaze, G., Dahms, R., Ruiz, A., and Misdariis, A. "Effects of real-fluid thermodynamics on high-pressure fuel injection processes". In: *SAE International Journal of Engines* 7.3 (2014), pp. 1125–1136.

[130] Okagaki, Y., Yonomoto, T., Ishigaki, M., and Hirose, Y. "Numerical study on an interface compression method for the volume of fluid approach". In: *Fluids* 6.3 (2021), p. 108.

[131] Okong'o, N. and Bellan, J. "Perturbation and initial Reynolds number effects on transition attainment of supercritical, binary, temporal mixing layers". In: *Computers and Fluids* 33.10 (2004), pp. 1359–1385.

[132] Olsson, E. and Kreiss, G. "A conservative level set method for two phase flow". In: *Journal of Computational Physics* 210.1 (2005), pp. 225–246.

[133] Örley, F., Hickel, S., Schmidt, S. J., and Adams, N. A. "Large-eddy simulation of turbulent, cavitating fuel flow inside a 9-hole diesel injector including needle movement". In: *International Journal of Engine Research* 18.3 (2017), pp. 195–217.

[134] Örley, F., Trummler, T., Hickel, S., Mihatsch, M. S., Schmidt, S. J., and Adams, N. A. "Large-eddy simulation of cavitating nozzle flow and primary jet break-up". In: *Physics of Fluids* 27.8 (2015), p. 085102.

[135] Oschwald, M., Smith, J., Branam, R., Hussong, J., Schik, A., Chehroudi, B., and Talley, D. "Injection of fluids into supercritical environments". In: *Combustion Science and Technology* 178.1-3 (2006), pp. 49–100.

[136] Osher, S. and Sethian, J. "Fronts propagating with curvature-dependent speed: algorithms based on Hamilton-Jacobi formulations". In: *Journal of Computational Physics* 79.1 (1988), pp. 12–49.

[137] Peng, D.-Y. and Robinson, D. B. "A new two-constant equation of state". In: *Industrial Engineering Chemistry Fundamentals* 15.1 (1976), pp. 59–64.

[138] Perigaud, G. and Saurel, R. "A compressible flow model with capillary effects". In: *Journal of Computational Physics* 209.1 (2005), pp. 139–178.

[139] Qian, L., Wei, Y., and Xiao, F. "Coupled THINC and Level Set method: a conservative interface capturing scheme with arbitrary-order surface representations". In: *Journal of Computational Physics* 374 (2018), pp. 1193–1212.

[140] Quirk, J. and Karni, S. "On the dynamics of a shock-bubble interaction". In: *Journal of Fluid Mechanics* 318 (1996), pp. 129–163.

[141] Raeini, A. Q., Blunt, M. J., and Bijeljic, B. "Modelling two-phase flow in porous media at the pore scale using the volume-of-fluid method". In: *Journal of Computational Physics* 231.17 (2012), pp. 5653–5668.

[142] Raissi, M. and Karniadakis, G. E. "Hidden physics models: Machine learning of nonlinear partial differential equations". In: *Journal of Computational Physics* 357 (2018), pp. 125–141.

[143] Raissi, M., Perdikaris, P., and Karniadakis, G. E. "Physics-informed neural networks: A deep learning framework for solving forward and inverse problems involving nonlinear partial differential equations". In: *Journal of Computational physics* 378 (2019), pp. 686–707.

[144] Raju, M., Banuti, D. T., Ma, P. C., and Ihme, M. "Widom lines in binary mixtures of supercritical fluids". In: *Scientific Reports* 7.1 (2017), p. 3027.

[145] Ranjan, D., Oakley, J., and Bonazza, R. "Shock-bubble interactions". In: *Annual Review of Fluid Mechanics* 43 (2011), pp. 117–140.

[146] Renardy, Y. and Renardy, M. "PROST: a parabolic reconstruction of surface tension for the volume-of-fluid method". In: *Journal of Computational Physics* 183.2 (2002), pp. 400–421.

[147] Richtmyer, R. D. "Taylor instability in shock acceleration of compressible fluids". In: *Communications on Pure and Applied Mathematics* 13 (1960), pp. 297–319.

[148] Roe, P. L. "Characteristic-based schemes for the Euler equations". In: *Annual Review of Fluid Mechanics* 18 (1986), pp. 337–365.

[149] Roenby, J., Bredmose, H., and Jasak, H. "A computational method for sharp interface advection". In: *Royal Society Open Science* 3.11 (2016), p. 160405.

[150] Rosselló, J. M., Reese, H., Raman, K. A., and Ohl, C.-D. "Bubble nucleation and jetting inside a millimetric droplet". In: *Journal of Fluid Mechanics* 968 (2023), A19.

[151] Rudman, M. "Volume-tracking methods for interfacial flow calculations". In: *International Journal of Numerical Methods in Fluids* 24.7 (1997), pp. 671–691.

[152] Ruiz, A. M., Lacaze, G., Oefelein, J. C., Mari, R., Cuenot, B., Selle, L., and Poinsot, T. "Numerical benchmark for high-Reynolds-number supercritical flows with large density gradients". In: *AIAA Journal* 54.5 (2016), pp. 1125–1136.

[153] Rusche, H. "Computational fluid dynamics of dispersed two-phase flows at high phase fractions". PhD thesis. Imperial College London, 2002.

[154] Saurel, R. and Abgrall, R. "A multiphase Godunov method for compressible multifluid and multiphase flows". In: *Journal of Computational Physics* 150.2 (1999), pp. 425–467.

[155] Saurel, R. and Pantano, C. "Diffuse-interface capturing methods for compressible two-phase flows". In: *Annual Review of Fluid Mechanics* 50 (2018), pp. 105–130.

[156] Saurel, R., Petitpas, F., and Berry, R. A. "Simple and efficient relaxation methods for interfaces separating compressible fluids, Cavitating Flows, and Shocks in Multiphase Mixtures". In: *Journal of Computational Physics* 228.5 (2009), pp. 1678–1712.

[157] Schmidmayer, K. and Biasiori-Poulanges, L. "Geometry effects on the droplet shock-induced cavitation". In: *Physics of Fluids* 35.6 (2023), p. 067116.

[158] Schmidt, S. J. "A Low Mach number Consistent Compressible Approach for Simulation of Cavitating Flow". PhD thesis. Technical University of Munich, 2015.

[159] Schmitt, T., Selle, L., Ruiz, A., and Cuenot, B. "Large-eddy simulation of supercritical-pressure round jets". In: *AIAA Journal* 48.9 (2010), pp. 2133–2144.

[160] Sethian, J. and Smereka, P. "Level set methods for fluid interfaces". In: *Annual Review of Fluid Mechanics* 35 (2003), pp. 341–372.

[161] Sharma, S., Singh, A. P., Rao, S. S., Kumar, A., and Basu, S. "Shock induced aero-breakup of a droplet". In: *Journal of Fluid Mechanics* 929 (2021), A27.

[162] Shpak, O., Verweij, M., Jong, N. de, and Versluis, M. "Droplets, bubbles and ultrasound interactions". In: *Therapeutic Ultrasound*. 2016, pp. 157–174.

[163] Shu, C. W., Zang, T. A., Erlebacher, G., Whitaker, D., and Osher, S. "High-order ENO schemes applied to two-and three-dimensional compressible flow". In: *Applied Numerical Mathematics* 9.1 (1992), pp. 45–71.

[164] Shukla, K., Toscano, J. D., Wang, Z., Zou, Z., and Karniadakis, G. E. "A comprehensive and FAIR comparison between MLP and KAN representations for differential equations and operator networks". In: *arXiv preprint arXiv:2406.02917* (2024).

[165] Shukla, R. K., Pantano, C., and Freund, J. B. "An interface capturing method for the simulation of multi-phase compressible flows". In: *Journal of Computational Physics* 229.19 (2010), pp. 7411–7439.

[166] Shyue, K. M. "An efficient shock-capturing algorithm for compressible multicomponent problems". In: *Journal of Computational Physics* 142.1 (1998), pp. 208–242.

[167] Shyue, K. M. and Xiao, F. "An Eulerian interface sharpening algorithm for compressible two-phase flow: the algebraic THINC approach". In: *Journal of Computational Physics* 268 (2014), pp. 326–354.

[168] Singh, S., Battiato, M., and Myong, R. "Impact of bulk viscosity on flow morphology of shock-accelerated cylindrical light bubble in diatomic and polyatomic gases". In: *Physics of Fluids* 33.6 (2021), p. 066103.

[169] So, K. K., Hu, X. Y., and Adams, N. A. "Anti-diffusion method for interface steepening in two-phase incompressible flow". In: *Journal of Computational Physics* 230.13 (2011), pp. 5155–5177.

[170] So, K. K., Hu, X. Y., and Adams, N. A. "Anti-diffusion interface sharpening technique for two-phase compressible flow simulations". In: *Journal of Computational Physics* 231.11 (2012), pp. 4388–4405.

[171] Sokolichin, A., Eigenberger, G., Lapin, A., and Lübert, A. "Dynamic numerical simulation of gas-liquid two-phase flows Euler/Euler versus Euler/Lagrange". In: *Chemical Engineering Science* 52.4 (1997), pp. 611–628.

[172] Sun, Z., Inaba, S., and Xiao, F. "Boundary variation diminishing (BVD) reconstruction: a new approach to improve Godunov schemes". In: *Journal of Computational Physics* 323 (2016), pp. 330–348.

[173] Sussman, M. "A second order coupled level set and volume of-fluid method for computing growth and collapse of vapor bubbles". In: *Journal of Computational Physics* 187.1 (2003), pp. 110–136.

[174] Sussman, M., Smereka, P., and Osher, S. "A level set approach for computing solutions to incompressible two-phase flow". In: *Journal of Computational Physics* 114.1 (1994), pp. 146–159.

[175] Terashima, H. and Koshi, M. "Approach for simulating gas-liquid-like flows under supercritical pressures using a high-order central differencing scheme". In: *Journal of Computational Physics* 231.20 (2012), pp. 6907–6923.

[176] Terashima, H. and Koshi, M. "Strategy for simulating supercritical cryogenic jets using high-order schemes". In: *Computers and Fluids* 85 (2013), pp. 39–46.

[177] Theofanous, T. "Aerobreakup of Newtonian and viscoelastic liquids". In: *Annual Review of Fluid Mechanics* 43.1 (2011), pp. 661–690.

[178] Tokareva, S. and Toro, E. F. "HLLC-type Riemann solver for the Baer-Nunziato equations of compressible two-phase flow". In: *Journal of Computational Physics* 229.10 (2010), pp. 3573–3604.

[179] Tomkins, C., Kumar, S., Orlicz, G., and Prestridge, K. "An experimental investigation of mixing mechanisms in shock accelerated flow". In: *Journal of Fluid Mechanics* 611 (2008), pp. 131–150.

[180] Tomkins, C., Prestridge, K., Rightley, P., Marr-Lyon, M., Vorobieff, P., and Benjamin, R. "A quantitative study of the interaction of two Richtmyer-Meshkov-unstable gas cylinders". In: *Physics of Fluids* 15.4 (2003), pp. 986–1004.

[181] Toro, E. F. *Riemann solvers and numerical methods for fluid dynamics: A practical introduction*. 3rd. Dordrecht, New York: Springer, 2009.

[182] Traxinger, C., Pfitzner, M., Baab, S., Lamanna, G., and Weigand, B. "Experimental and numerical investigation of phase separation due to multicomponent mixing at high-pressure conditions". In: *Physical Review Fluids* 4.7 (2019), p. 074303.

[183]   Trummler, T. "Numerical investigations of cavitation phenomena". PhD thesis. Technische Universität München, 2021.

[184]   Trummler, T., Rahn, D., Schmidt, S. J., and Adams, N. A. "Large eddy simulations of cavitating flow in a step nozzle with injection into gas". In: *Atomization and Sprays* 28.5 (2018), pp. 445–466.

[185]   Trummler, T., Schmidt, S. J., and Adams, N. A. "Investigation of condensation shocks and re-entrant jet dynamics in a cavitating nozzle flow by large-eddy simulation". In: *International Journal of Multiphase Flow* 128 (2020), p. 103245.

[186]   Tryggvason, G., Scardovelli, R., and Zaleski, S. *Direct numerical simulations of gas-liquid multiphase flows*. Cambridge University Press, 2011.

[187]   Tudisco, P. and Menon, S. "Numerical investigations of phase-separation during multi-component mixing at super-critical conditions". In: *Flow, Turbulence and Combustion* 104 (2020), pp. 693–724.

[188]   Ubbink, O. and Issa, R. "A method for capturing sharp fluid interfaces on arbitrary meshes". In: *Journal of Computational Physics* 153.1 (1999), pp. 26–50.

[189]   Wan, H. J. Q., Deiterding, R., and Eliasson, V. "Numerical and experimental investigation of oblique shock wave reflection off a water wedge". In: *Journal of Fluid Mechanics* 826 (2017), pp. 732–758.

[190]   Wang, B., Xiang, G., and Hu, X. "An incremental-stencil WENO reconstruction for simulation of compressible two-phase flows". In: *International Journal of Multiphase Flow* 99 (2018), pp. 383–393.

[191]   Wang, G., Wang, Y., Li, D., and Guan, B. "Numerical study on shock-accelerated gas rings". In: *Physics of Fluids* 32.2 (2020), p. 026102.

[192]   Wang, L., Liu, J., Li, W., Wang, P., Huang, B., and Wu, D. "Stabilize cloud cavitation with an obstacle near hydrofoil's trailing edge and conduct local entropy production analysis". In: *Physics of Fluids* 36.1 (2024).

[193]   Wang, S., Jiao, Z., Huang, X., Yang, C., and Nguyen, N. "Acoustically induced bubbles in a microfluidic channel for mixing enhancement". In: *Microfluidics and Nanofluidics* 6.6 (2009), pp. 847–852.

[194]   Wang, X., Yang, D., Wu, J., and Luo, X. "Interaction of a weak shock wave with a discontinuous heavy-gas cylinder". In: *Physics of Fluids* 27.6 (2015), p. 064104.

[195]   Wang, Z., Hopfes, T., Giglmaier, M., and Adams, N. A. "Effect of Mach number on droplet aerobreakup in shear stripping regime". In: *Experiments in Fluids* 61 (2020), p. 147.

[196]   Wang, Z., Yu, B., Chen, H., Zhang, B., and Liu, H. "Scaling vortex breakdown mechanism based on viscous effect in shock cylindrical bubble interaction". In: *Physics of Fluids* 30.12 (2018), p. 126103.

[197]   Wei, W., Liu, H., Xie, M., Jia, M., and Yue, M. "Large eddy simulation and proper orthogonal decomposition analysis of fuel injection under trans/supercritical conditions". In: *Computers and Fluids* 179 (2019), pp. 777–792.

[198]   Weller, H. *A New Approach to VOF-based Interface capturing methods for incompressible and compressible flow*. Tech. rep. OpenCFD, 2008.

[199]   Xiang, G. and Wang, B. "Numerical study of a planar shock interacting with a cylindrical water column embedded with an air cavity". In: *Journal of Fluid Mechanics* 825 (2017), R2.

[200]   Xiao, F., Honma, Y., and Kono, T. "A simple algebraic interface capturing scheme using hyperbolic tangent function". In: *International Journal of Numerical Methods in Fluids* 48.9 (2005), pp. 1023–1040.

[201]   Xie, B., Jin, P., and Xiao, F. "An unstructured-grid numerical model for interfacial multiphase fluids based on multi-moment finite volume formulation and THINC method". In: *International Journal of Multiphase Flow* 89 (2017), pp. 235–246.

[202]   Xu, J., Wang, H., Feng, L., Zhai, Z., and Luo, X. "Interaction of a shock with two concercric/eccentric cylinders". In: *Experiments in Fluids* 62.2 (2021), pp. 1–12.

[203]   Yang, K. and Aoki, T. "Weakly compressible Navier-Stokes solver based on evolving pressure projection method for two-phase flow simulations". In: *Journal of Computational Physics* 431 (2021), p. 110113.

[204]   Yang, V. "Modeling of supercritical vaporization, mixing, and combustion processes in liquid-fueled propulsion systems". In: *Proceedings of the Combustion Institute* 28.2 (2000), pp. 925–942.

[205]   Yang, V., Hsiao, G. C., Shuen, J. S., and Hsieh, K. C. "Droplet behavior at supercritical conditions". In: *Recent advances in spray combustion: Spray atomization and drop burning phenomena*. Vol. 1. 1996, pp. 413–437.

[206]   Yang, V., Natan, N., and Shuen, J.-S. "Vaporization of liquid oxygen (LOX) droplets in supercritical hydrogen environments". In: *Combustion Science and Technology* 99.1-6 (1994), pp. 357–382.

[207]   Youngs, D. "Time-dependent multi-material flow with large fluid distortion". In: *Numerical Methods for Fluid Dynamics*. Americal Press, New York, 1982, pp. 273–285.

[208]   Zabusky, N. J. "Vortex paradigm for accelerated inhomogeneous flows: Visiometrics for the Rayleigh-Taylor and Richtmyer-Meshkov environments". In: *Annual Review of Fluid Mechanics* 31 (1999), pp. 495–536.

[209]   Zalesak, S. T. "Fully multidimensional flux-corrected transport algorithms for fluids". In: *Journal of Computational Physics* 31.3 (1979), pp. 335–362.

[210]   Zhu, Y., Yu, L., Pan, J., Pan, Z., and Zhang, P. "Jet formation of SF_6 bubble induced by incident and reflected shock waves". In: *Physics of Fluids* 29.12 (2017), p. 126105.

Peer-reviewed Journal Publications for Thesis

The peer-reviewed journal publications of this thesis are attached here.

A.1 Paper I

An all-Mach consistent numerical scheme for simulation of compressible multi-component fluids including surface tension, cavitation, turbulence modeling and interface sharpening on compact stencils

Yu Jiao, Steffen J. Schmidt, Nikolaus A. Adams

Contribution: My contribution to this research paper was to propose the concept and idea of the paper, complete the programming codes and numerical methods, perform the validations, analyse the results, and write the manuscript.

An all-Mach consistent numerical scheme for simulation of compressible multi-component fluids including surface tension, cavitation, turbulence modeling and interface sharpening on compact stencils

Author: Yu Jiao,Steffen J. Schmidt,Nikolaus A. Adams

Publication: Computers & Fluids

Publisher: Elsevier

Date: 30 April 2024

An all-Mach consistent numerical scheme for simulation of compressible multi-component fluids including surface tension, cavitation, turbulence modeling and interface sharpening on compact stencils

Yu Jiao [a],[*], Steffen J. Schmidt [a], Nikolaus A. Adams [a],[b]

[a] *Department Engineering Physics and Computation, Chair of Aerodynamics and Fluid Mechanics, School of Engineering and Design, Technische Universität München, Boltzmannstr. 15, Garching bei München 85748, Germany*
[b] *Munich Institute of Integrated Materials, Energy and Process Engineering, Technical University of Munich, Lichtenbergstr. 4a, Garching 85748, Germany*

ABSTRACT

We present a numerical scheme valid in the range of highly to weakly compressible flows using a single-fluid four equation approach together with multi-component thermodynamic models. The approach can easily be included into existing finite volume methods on compact stencils and enables handling of compressibility of all involved phases including surface tension, cavitation and viscous effects. The mass fraction (indicator function) is sharpened in the two-phase interface region using the algebraic interface sharpening technique Tangent of Hyperbola for INterface Capturing (THINC). The cell face reconstruction procedure for mass fractions switches between an upwind-biased and a THINC-based scheme, along with proper slope limiters and a suitable compression coefficient, respectively. For additional sub-grid turbulence modeling, a fourth order central scheme is included into the switching process, along with a modified discontinuity sensor. The proposed "All-Mach" Riemann solver consistently merges the thermodynamic relationship of the components into the reconstructed thermodynamic variables (like density, internal energy), wherefore we call them All-Mach THINC-based Thermodynamic-Dependent Update (All-Mach THINC-TDU) method. Both, liquid-gas and liquid-vapor interfaces can be sharpened. Surface tension effects are taken into account by using a Continuum Surface Force (CSF) model. In order to reduce spurious oscillations at interfaces we decouple the computation of the interface curvature from the computation of the gradient of the Heaviside function. An explicit, four stage low storage Runge-Kutta method is used for time integration. The proposed methodology is validated against a series of reference cases, such as bubble oscillation/advection/deformation, shock-bubble interaction, a vapor/gas bubble collapse and a multi-component shear flow. The results of a near-critical shock/droplet interaction case are superior to those obtained by WENO3 and OWENO3 schemes and support that the proposed methodology works well with various thermodynamic relations, like the Peng-Robinson equation of state. Finally, the approach is applied to simulate the three-dimensional primary break-up of a turbulent diesel jet in a nitrogen/methane mixture including surface tension effects under typical dual-fuel conditions. The obtained results demonstrate that the methodology enables robust and accurate simulations of compressible multi-phase/multi-component flows on compact computational stencils without excessive spurious oscillations or significant numerical diffusion/dissipation.

1. Introduction

Simulation of flow processes in internal combustion engines (ICE) usually involves multicomponent flows with phenomena such as deformation of material interfaces, interaction with shock waves, and evaporation and condensation. Here, we focus on compressible two-phase flows with multicomponent fluids, with two-phase jet flows or droplet breakup in internal combustion engines being practical applications. Basically, there are two different numerical approaches for such flows: Methods that assume sharp interfaces and those that rely on mixture assumptions. Since the flow field and material properties are generally discontinuous across the interface between different phases or

components, treating material boundaries becomes a key problem.

1.1. Sharp interface and diffuse interface methods

Sharp interfaces are generally achieved by (Interface tracking type) Front-Tracking [1,2], (Interface capturing type) Level-Set methods (LS) [3–5], Geometric interface reconstruction (GIR) based volume of fluid methods (VOF) [6,7] like Piecewise-Linear Interface Calculation (PLIC) [8] and the isoAdvector Method [9]. Front tracking attempts to combine the characteristics of both Lagrangian and Eulerian schemes to maintain a sharp boundary, where Lagrangian markers are adopted to distinguish the domains taken by different fluids. However, this is computationally expensive for complex geometries especially for strong topological deformations of the interface. Furthermore, Front-Tracking methods are not mass-conservative without extra treatment. A traditional Level-Set (LS) function is a signed-distance function, that represents the shortest distance to the interface, where the interface is represented as the zero contour. It is accurate in computing surface normals and curvatures with naturally smooth LS field and is suitable for determining surface tension. However, the additional steps for reinitialization and mass conservation involve additional computational cost because the LS function loses its signed distance property after the advection step and the mass of each phase is not automatically conserved. Moreover, it is expensive if the topology changes. GIR methods could also provide a clear/sharp two-phase interface, but are also computationally expensive.

Generally, diffuse interfaces are introduced by phase field models (PF) [10–14] or (interface capturing type) algebraic interface sharpening (AIS) based models, where no clear boundary between phases exists and the interface often covers more than a single cell. Phase-field methods generally adopt the convective Cahn-Hilliard or the Allen-Cahn equation to describe interfacial motions and naturally have anti-diffusive characteristics. However, these methods require considerable computational effort to resolve interfacial structures and have limited applicability to realistic two-phase problems in industry, e.g., jet flow in dual-fuel combustion engines, transcritical flow with combustion, bubble collapse with shock wave formation and shock bubble interaction. Some recent works analyze the conservative phase field model [14] and achieved great progress in shock-free compressible domains. However, the applicability of the phase field model for the questions defined here as objectives have not yet been demonstrated. Typically, the AIS model uses the Heaviside function or indicator function to distinguish different phases. The AIS method usually takes advantage of the natural conservation of mass and the effective capture of changes in interface topology, such as the breaking or reconnecting of interfaces. The various fluid components are artificially induced to mix at the unresolved interface. In this way, a thin mixing zone is created, even with non-miscible fluids. This has the great advantage that a single set of equations can be used to describe the two-phase flow properties throughout the domain, without having to explicitly track the sharp interface.

Approaches with diffuse interfaces are efficient and also suitable for three-dimensional cases with different fluid components. The corresponding diffuse interface effects are purely due to numerical processes and approximate a sharp gradient with the mesh size approaching zero. Diffuse-interface approaches for the simulation of compressible two-phase flows can be classified into certain categories: the four-equation model, the five-equation model, the Baer-Nunziato model, etc. In the four-equation model [15–26], the mass fraction is usually used as the Heaviside function, whereas in the five-equation model [27,28], the volume fraction is usually considered as the Heaviside function. It is noted that the species-mass conservation is always maintained for the five-equation model, regardless of the numerical treatment of the volume fraction of the advection equation, while the conservative form of the additional species-mass conservation equation should be carefully achieved in the fully conservative four-equation model. The mass fraction-based four-equation model can account for an additional

component with an additional species-mass conservation equation, in contrast to the volume fraction-based five-equation model, which requires two equations for an additional species (advection equation for the volume fraction and equation for species mass conservation) and thus requires additional computational effort.

An advantage of a mass fraction-based four-equation model [15–26, 29,30] (over an LS formulation) is that it can handle flows where the species front is not initially present but forms during the calculation (as in chemical reactions, cavitation, or condensation). While Gama-transport based four equation models [31] (mixture of mass, momentum, energy and additional advection parameters) are ideal for stiffened gas type EOS, mass-fraction-based four equation models can be efficiently applied to real fluid models. The disadvantage of quasi-conservative models is poor conservation of species masses (the mass of each species is not accurately conserved) [15,31–33] and that artificial temperature spikes can occur [32].

In addition, the Baer-Nunziato equations [34], originally proposed to describe reactive multiphase flow (the transition from deflagration to detonation), are a set of equations used to study compressible multiphase flows [35–37]. The BN model includes conservation equations for mass, momentum and energy for each phase, which also take into account the interfacial dynamics between phases, e.g. the transfer of mass, momentum and energy between phases. In general, each phase is considered a compressible fluid in local thermodynamic equilibrium, while allowing for non-equilibrium conditions across the interface within the mixture. This implies that the self-equilibration time scale within each phase is significantly shorter than the equilibration time scale between the phases [29,38]. The BN model goes beyond traditional four- or five-equation models by considering interfacial forces, phase changes and phase compressibility [29,30,39], providing a more comprehensive approach to modelling compressible multiphase flows and enabling a detailed understanding of complex multiphase flows involving gases, liquids or mixtures. BN approaches exhibit very high numerical complexity including detailed interface tracking and require closure models for interface terms. This considerably complicates their applicability to industrial problems in the dual-fuel domain.

In summary, we focus on a four-equation model based on the mass fraction, which is easily extensible to additional species (dual-fuel conditions), suitable for real fluids, and usable for complex flows including cavitation. Since the working fluids in DFICE always contain a fraction of free gas, the proposed model is extended to include such a gas fraction in the fluid.

1.2. Algebraic interface sharpening methods and THINC-based methods

Algebraic interface sharpening methods (AIS) strive to algebraically reconstruct the two-phase interface or modify the RHS of the governing equations to avoid excessive interfacial diffusion, at relatively low additional computational cost. Examples include the Flux-Corrected Transport (FCT) scheme [40–42], post-processing anti-diffusion methods [43,44], the Tangent of Hyperbola for INterface Capturing (THINC) method [45–47], Compressive Interface Capturing Schemes for Arbitrary Meshes (CICSAM) [7], additional (artificial) compression term approaches [48–51], bounded variation or TVD methods [52–54], ENO or WENO approaches [55–57], Multidimensional Universal Limiters with Explicit Solution (MULES) [58,59] and High Resolution Interface Capturing schemes (HRIC) [60].

Various methods have been developed to bring the numerical two-phase interface with the least dissipation into agreement with the macroscopic hypothesis of a continuous medium. For example, adjusting the limiters in the TVD-MUSCL scheme [59] or the weighting co-efficients in the WENO scheme [61,62] can help reduce the numerical dissipation and avoid oscillations in the discontinuous interface region. Furthermore, the reconstruction of the parameter space near the cell surfaces(S_L and S_R) and the development of specific Riemann solvers ($S^*=f(S_L,S_R)$) can reduce the numerical dissipation at interfaces.

Among all types of AIS methods, the THINC-based method is an interesting option because it generally requires less computational effort. In the THINC method presented by Xiao [45], the hyperbolic tangent function was used to evaluate the numerical flux for the advection equation of the VOF function, which aimed to calculate the moving interface algebraically (without complex geometric reconstruction). For multidimensional calculations, the numerical flux for each direction was determined by operator splitting. Then, the research focused on improving the description of the interface shape and avoiding the surface curvature. Subsequently, a Boundary Variation Diminishing (BVD) scheme [63] was proposed and the following studies [47, 64–66] focus on selecting different reconstruction candidates to minimize jumps at cell boundaries. BVD usually reconstructs variable candidates for each cell interface and then decides on the final candidates, which results in additional computational resources and communication time for parallel computations. We focus on a robust and compact four-cell scheme, so further details related to BVD are not part of this work.

So far, the THINC method has been developed and used for multiphase flows. However, it should be noted that THINC-based methods have been studied to a limited extent for complex compressible multicomponent applications involving shock waves, turbulence, cavitation, and moving interfaces, e.g., for high-speed atomization in a compressible multicomponent environment. Daniel [67] use THINC in MUSCL scheme for incompressible multiphase flows. To simulate a supersonic liquid jet [68], a five-equation model was combined with a volume fraction THINC when capillary forces were neglected. A five-equation model combined with a density THINC was further implemented to simulate atomization [69]. Nonomura et al. [70] developed the THINC method with two compressible fluids and sharpened the volume fraction only, while Shyue and Xiao [71] presented a single-fluid multicomponent flow model and used the reconstructed volume fraction to extrapolate other conservative parameters across the cell interface, both neglecting the surface tension. It is further noted that a recent development (VOF-based) [72] or ongoing work [73,74] of the THINC-based method is the combination with the AMR technique in multiphase simulation, but it is still not fully capable for the complex compressible simulation involving cavitation flow, turbulent flow and real fluid effects with increasing computational cost.

Coupled methods such as THINC-LS [75] and THINC-LS-VOF [76] were developed to improve the interface description and numerical accuracy, but they generally require significantly more computational resources to achieve good performance. The above THINC-based method is generally used to reconstruct the volume fraction of a five-equation model. Generally such models do not directly consider a Riemann solver of the cell interface. Rather, they decouple the relationship between pressure and density as well as internal energy in the reconstruction process. In addition, a realistic-flow such as the viscous term, surface tension, gravity, real-fluid and cavitation effects are generally ignored or not fully considered.

1.3. Motivations and aims

Our findings have inspired the creation of a numerical method that possesses the following key properties:

- Ease of Implementation: The method should be straightforward to implement.
- Robust Performance: It must perform reliably in industrial flow problems, even in challenging scenarios like transcritical flows or jet flows under internal combustion engine conditions, where the combination of high-order schemes and complex real fluid models often results in simulation instability.
- Accuracy and Flexibility: The method should be accurate and flexible, serving as an independent model applicable to various variables and capable of extension into higher-order schemes.

- Suitability for Low Mach Number Flows in pure liquids as well as for high Mach numbers in liquid/gas or liquid/vapor mixtures.
- Direct Combination of Turbulence Models: The method should allow for the direct integration of turbulence models.
- Physical Consistency: It must maintain physical consistency.

Developing such a method comes with its own set of challenges:

- Spurious Oscillations: Complex two-phase simulations, particularly when dealing with large discontinuities, can lead to spurious oscillations.
- Interface Smearing: Reducing interface smearing while ensuring high computational efficiency for practical three-dimensional problems is not straightforward.
- Robustness Across Flow Types: Maintaining robustness across various flow types is essential.
- Surface Tension Modeling: Describing surface tension effects with low computational cost while minimizing spurious velocities is a challenge.
- Thermodynamic Consistency: Achieving thermodynamic consistency between variables is a requirement.

To address these challenges, we propose a robust Finite Volume Method (FVM) density-based framework with the following features:

(1) Four-Equation Model: Our approach employs a four-equation model without the need for additional advection equations for volume fraction. It is fully conservative when no additional source terms are introduced.
(2) THINC-Based Reconstruction: THINC-based reconstruction functions are separately applied for the liquid-gas and liquid-vapor interfaces.
(3) Compact Four-Cell Stencil (4-Cell) Scheme: We use a relatively straightforward implementation involving a compact four-cell stencil.
(4) Inclusion of Surface Tension Effects: Our method incorporates surface tension effects.
(5) Thermodynamic Consistency: We ensure thermodynamic consistency between variables through the Thermodynamic-Dependent Update (TDU), which incorporates the effects of the Riemann solver into the computational interaction process.

We propose a new four-equation (mass fraction) all-Mach method (consistent for Mach number approaching 0), which uses a single-fluid thermodynamic model to represent a multicomponent fluid. This model accounts for viscosity, surface tension, gravity, real-fluid effects, and cavitation effects. It effectively captures two-phase interfaces (liquid-gas and liquid-vapor) while maintaining interfacial equilibrium. Additionally, the discretization scheme offers implicit subgrid-scale modeling capabilities.

2. Numerical model

In present work, the proposed numerical model adopts the form of the compressible Navier-Stokes equations for two or more compressible fluids and adds additional conservation equations for the mass of (at least) one of the components. This approach is usually referred as 4 equation model [16,77], which, in our case, includes viscous effects, surface tension and gravity effects. Besides, the approach discussed in the following sections can easily be integrated into existing compressible finite volume methods with only minor effort due to the compact (4-cell) stencil.

2.1. Governing equations

The governing equations are the well known Navier-Stokes equations

in conservation from for compressible fluids and fluid mixtures. q denotes mixture properties as obtained from the total mass, total momentum and total energy of the mixture and ξ_{Gasi} denote the mass fraction of species "i" for a mixture of i+1 fluids. In the following, the governing equations for a compressible mixture of three fluids are presented:

$$\partial_t q + \nabla \cdot [C(q) + S(q)] = Q \tag{2-1}$$

Where, the state vector $\mathbf{q} = [\rho, \rho\mathbf{u}, \rho E, \rho\xi_{Gas1}, \rho\xi_{Gas2}]^T$ contain the conserved variables for density, momentum, total energy and gas species. $C(\mathbf{q})$, $S(\mathbf{q})$ and $\mathbf{Q}$ refer to convective term, stress term and source term, respectively,

$$C(\pmb q) = \pmb u \pmb q = \pmb u \begin{bmatrix} \rho \\ \rho\pmb u \\ \rho H \\ \rho\xi_{Gas1} \\ \rho\xi_{Gas2} \end{bmatrix}, S(\pmb q) = \begin{bmatrix} 0 \\ p\pmb I - \pmb\tau \\ -\pmb u\pmb\tau - k_c\nabla T \\ 0 \\ 0 \end{bmatrix}, \text{ and } = \begin{bmatrix} 0 \\ \rho f \\ \pmb u\rho f \\ 0 \\ 0 \end{bmatrix}, \tag{2-2}$$

where I refers to the unit tensor; $\rho H = \rho E + p$ is the total enthalpy; τ is the viscous stress tensor, $\tau = \mu(\nabla u + (\nabla u)^T - 2/3(\nabla \cdot u)I)$ and μ refers to

$$\mu_{mix} = (1 - \alpha_{Gas1} - \alpha_{Gas2})\big[(1 - \alpha_v)(1 + 5/2\alpha_v)\mu_{liq} + \alpha_v\mu_{vap}\big] + \alpha_{Gas1}\mu_{Ga1} + \alpha_{Gas2}\mu_{Ga2} \tag{2-8}$$

the dynamic viscosity; k_c refers to the thermal conductivity; f refers to the volume force, for surface tension and gravity, $f = [f_1, f_2, f_3]^T = [\delta\sigma kn_1, \delta\sigma kn_2 + g, \delta\sigma kn_3]^T$; k is the curvature, δ refers to the Dirac function that is nonzero only on the interface, σ denotes surface tension coefficient, n refers to the normal gradient of an indicator function; g refers to the gravity term.

2.2. Barotropic thermodynamics equilibrium model for coupled (one-fluid) multi-component flow

First, we extend a single-fluid model with an additional gas phase to a single-fluid multicomponent model with multiple gas components, based on prior work by Örley et al. [22] and Trummler et al. [23].

A typical three-component two-phase fluid $\Phi = \{L, M, Gas1, Gas2\}$ is selected, which refers to a liquid component, a liquid-vapor mixture and two gas components denoted as Gas1 and Gas2, respectively.

For the liquid component

$$\rho_L = \rho_{sat, liq} + \frac{1}{c_L^2}(p_L - p_{sat}) \quad , p_L \geq p_{sat} \ , \tag{2-3}$$

where $\rho_{sat, liq}$ is the liquid saturation density at its saturation pressure p_{sat}.

For the liquid-vapor mixture

$$\rho_M = \rho_{sat, liq} + \frac{1}{c_M^2}(p_M - p_{sat}) \quad , p_M < p_{sat} \ . \tag{2-4}$$

Since $c^2 = (\partial p/\partial \rho)|_{s=\text{const}}$, the mixture speed of sound is approximated as $c_M = (p_{sat}/\rho_{sat, liq})^{1/2}$.

For the non-condensable gas phase

$$\rho_{Gasi} = \frac{p_{Gasi}}{R_{Gasi}T_{refi}}, \tag{2-5}$$

i.e., both gas components are treated as ideal gas, R_{Gas1} and R_{Gas2} refer to the specific gas constant, T_{ref1} and T_{ref2} refer to the corresponding

temperatures.

From the volume fraction $\alpha_\Phi = V_\Phi/V$ and the mass fraction $\xi_\Phi = m_\Phi/m$ of component Φ, it is obvious that $\rho_\Phi = m_\Phi/V_\Phi = \xi_\Phi m/(\alpha_\Phi V) = \xi_\Phi\rho/\alpha_\Phi$, and $\rho = m/V = \sum_\Phi \xi_\Phi\rho = \sum_\Phi \alpha_\Phi\rho_\Phi$. Naturally $\sum_\Phi \alpha_\Phi = 1$ and $\sum_\Phi \xi_\Phi = 1$, $\rho = \alpha_{L/M}\rho_{L/M} + \alpha_{Gas1}\rho_{Gas1} + \alpha_{Gas2}\rho_{Gas2}$.

$$\rho_{Gasi} = \frac{\xi_{Gasi}}{\alpha_{Gasi}}\rho = \frac{p_{Gasi}}{R_{Gasi}T_{refi}}. \tag{2-6}$$

Where $\alpha_{Gasi} = \xi_{Gasi}\rho R_{Gasi}T_{refi}/p_{Gasi}$. Thus $\rho = \alpha_{L/M}\rho_{L/M} + \alpha_{Gas1}\rho_{Gas1} + \alpha_{Gas2}\rho_{Gas2} = (1 - \alpha_{Gas1} - \alpha_{Gas2})\rho_{L/M} + \xi_{Gas1}\rho + \xi_{Gas2}\rho$. Finally, we obtain the coupled (one-fluid) multi-component equation of state $(1 - \sum \rho\xi_{Gasi}R_{Gasi}T_{refi}/p_{Gasi})(\rho_{sat, liq} + \frac{1}{c^2}(p_M - p_{sat})) - (1 - \sum \xi_{Gasi})\rho = 0$. It indicates $p = f(\rho, \xi_{Gasi})$ with the equilibrium assumption. If the pressure is higher than the saturation pressure of the liquid, then is no vapor. Otherwise we have

$$\alpha_v = \frac{V_{vap}}{V} = \begin{cases} (1 - \alpha_{Gas1} - \alpha_{Gas2})\dfrac{\rho_{sat,liq} - \rho_M}{\rho_{sat,liq} - \rho_{sat,vap}} & , \ \rho < \rho_{sat,liq} \\ 0 & , \ \rho \geq \rho_{sat,liq} \end{cases}. \tag{2-7}$$

We assume that there is no pure vapor and limit the largest volume fraction of vapor component to 99.5%. The mixtures viscosity is

The thermodynamic equilibrium model for coupled (one-fluid) multi-component flow is detailed in Appendix A. It should also be noted that some of the phase transition models [78] can also be applied to the diffuse interface method.

2.3. Surface tension modeling

For surface tension modeling, the distribution characteristics of the indicator function or the Heaviside function (scalar in the two-phase flow) generally have a great impact on the surface tension calculation at the two-phase interface. By using various methods to sharpen the two-phase interface, the accuracy of the surface tension calculation can be improved. In addition, numerous numerical methods have been proposed to improve the balance between pressure and surface tension effects to reduce the parasitic current or velocity. For example, balance between compressive and surface tension forces can be achieved by discretizing the surface tension and compressive forces at the same location. As shown in Table 2.1, we divide the surface stress modeling features into three types, according to their expressions and discrete forms. In the current work, Continuum Surface Force (CSF) model [79] is used(f), along with proper methods to obtain norm-direction gradient of scalar(∇H) and curvature(k). Details are explained in Section 3.2.

2.4. Turbulence modeling

For turbulence modeling, a high order improvement of THINC-TDU is proposed. To model the effects of sub-grid turbulence in the current four equation model, an implicit large eddy simulation (iLES) method is used. The iLES approach for compact stencils proposed by Egerer et al. [24] was based on the Adaptive Local Deconvolution Method (ALDM) by Adams et al. [93] and Hickel et al. [94,95] to deal with resolved sub-grid turbulence. The truncation error of the discretization scheme is learned from the data to serve as a sub-grid scale (SGS) model for turbulence. Hickel et al. [95,96] also developed a compressible version of ALDM,

Table 2.1
Classifications for surface tension modelling methods.

Types	Classification Criteria	Terms/ Functions	Examples	Comments
1	Heaviside function and its normal gradient	$\delta_s n = \nabla H$	• Volume fraction function [79] • Level set function [4] • Dirac delta of ghost fluid method (GFM) [80,81]	Obtain the unit normal across the interface
2	Methods for curvature calculation	k	• Smoothed volume fraction method [79] • Height function method [82–84] • Smooth the original curvature through kernel [85] or weight coefficient method [86]	Obtain accurate curvature
3	Methods for Surface Tension Force discretization (explicit curvature maybe not required)	f	• Continuum surface force (CSF) [79], in some cases the curvature and norm-direction gradient of scalar are decoupled (like GFM method or level set method) • Continuum surface stress(CSS) [87,88] • Balanced Continuum surface force (bCSF) method or ghost fluid models [89] • Improved Riemann solver [90,86] • ·Sharp Surface Force (SSF) model [91,85] • Independent Source item effects methods [92]	Surface tension acts on pressure field but not the velocity field, thus the parasitic currents can be reduced

with shock capturing abilities while smooth pressure waves and turbulence are propagated without excessive numerical dissipation. More details related to ALDM are given in the work of Hickel [94,97,98] and Egerer et al. [24]. The ALDM method has been used by Örley [22,99], Trummler [23,100] in the two phase flow, which proves that it is a proper method in solving the fully compressible two phase turbulent flow. Based on previous work and in order to include the turbulence modeling, a high order improvement of THINC-TDU is proposed, in which the ALDM reconstruction is implemented to the momentum equation.

Here we briefly summary the iLES method for a scalar nonlinear transport equation,

$$\frac{\partial u}{\partial t} + \frac{\partial}{\partial x} f(u) = 0 \tag{2–9}$$

And a linear low-pass filter operation could be represented as [95]

$$\bar{u}(x) = \int_{-\infty}^{+\infty} G(x - x^{\cdot})u(x^{\cdot})dx^{\cdot} = G * u \tag{2–10}$$

By projecting the filtered continuous function onto the numerical grid $x_N = \{x_i\}$, the LES discretization of the transport equation is obtained as

$$\frac{\partial \bar{u}_N}{\partial t} + G * \partial_x f_N(u_N) = \varepsilon_{sgs} \tag{2–11}$$

And the sub-grid scale error/residual arises from the nonlinearity of f(u) and is obtained as $\varepsilon_{sgs} = G * \partial_x f_N(u_N) - G * \partial_x f_N(u)$, in which the inverse-filter operation $u_N = G^{-1} * \bar{u}_N$.

A finite-volume discretization could be presented as

$$\frac{\partial \bar{u}_N}{\partial t} + G * \partial_x \widetilde{f}_N(\widetilde{u_N}) = 0 \tag{2–12}$$

where $\bar{u}_N$ presents the approximately deconvolved parameter, and the top-hat filter kernel G is

$$G(x - x_i) = \begin{cases} 1/\Delta x, & |x - x_i| \le \Delta x/2, \\ 0, & otherwise. \end{cases} \tag{2–13}$$

A modified differential equation (MDE) can be formulated as [93]

$$\bar{u}(x) = \int_{-\infty}^{+\infty} G(x - x^{\cdot})u(x^{\cdot})dx^{\cdot} = G * u \tag{2–14}$$

$$\frac{\partial \bar{u}_N}{\partial t} + G * \partial_x f_N(u_N) = \varepsilon_N \tag{2–15}$$

Where $\varepsilon_N = G * \partial_x f_N(u_N) - G * \partial_x \widetilde{f}_N(\widetilde{u_N})$ presents the truncation error owning to the spatial discrete format.

When the truncation error reproduces the physical properties of the exact sub-grid scale error/residual, we call the numerical discretization physically consistent. In this case, the numerical truncation error functions as sub-grid scale model and we call the numerical scheme with ε_N an iLES model. In other words, if ε_N approximates ε_{sgs} in some sense for finite Δx we obtain an implicit SGS model contained within the discretization.

3. Numerical methods

3.1. Overall description

Based on the finite volume method CATUM [22–24,99,100] (CAvitation Technical University of Munich), we propose the following numerical scheme where surface tension effects, a modified discontinuity sensor and real fluid effects are newly considered. In addition, numerical dissipation reduction and thermodynamic consistency at interfaces are achieved.

As shown in Fig. 3.1, the following algorithm is based on a compact four-cell stencil, but it can be extended to a higher order with a larger stencil. It should be noted that a number of compact schemes have been proposed and can be found in the Refs. [101–103]. Here, we give this easy-to-implement four-cell stencil algorithm to solve the proposed model including viscous effects, surface tension effects, and gravity effects. The thermodynamic model used in the following part is related to the barotropic thermodynamic equilibrium model for coupled (single-fluid) multicomponent flows proposed in Section 2.2. It can be extended to consider internal energy and real fluid effects, see Appendix B.

In the following, we present the Riemann solver and introduce the reconstruction procedure for sharpening the liquid-gas interface. We also specifically propose procedures for sharpening the liquid-vapor interface, and describing surface tension discretization as well as high order improvement with turbulence modeling, finally give the flowchart
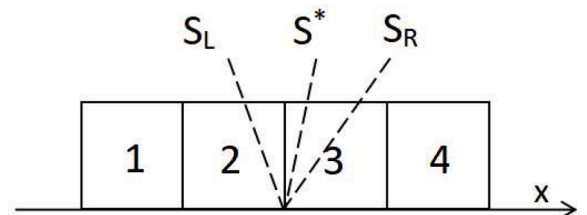

Fig. 3.1. Schematic diagram of four-cell stencil.

of the newly developed algorithm.

3.2. Description of Riemann solver

To overcome the low Mach number problem, we use the "all-Mach" interface pressure reconstruction (asymptotically consistent pressure flux definition) and the modified numerical flux of Schmidt et al. [104]. It is important to note that most liquid-vapor two-phase flows exhibit low Mach numbers in regions where only the pure liquid phase is present. However, as the speed of sound in liquid-vapor mixtures significantly decreases, there arises a need for a robust flux formulation suitable for (very) high Mach numbers in such mixtures. The flux function we've selected has been shown to meet both of these requirements (therefore it is called "all-Mach"), as documented in the references. Nevertheless, we must emphasize that in simulations involving supersonic or hypersonic gas flows, it is advisable to substitute this flux function with alternative methods, such as HLLC or the ROE flux.

$$p^* = \frac{p_L + p_R}{2} \tag{3-1}$$

The following Riemann solver is applied for the interface velocity $S^* = u^*$, which determines the upstream direction.

$$u^* = \frac{\rho_L c_L u_L + \rho_R c_R u_R + p_L - p_R}{\rho_L c_L + \rho_R c_R} \tag{3-2}$$

3.3. Reconstruction of interface variables

At distinct interfaces between a liquid and a gaseous component or mixture we use THINC to reconstruct the mass fraction for the interface free-gas component(s) along with TDU to consistently reconstruct related thermodynamic quantities. Regions that do not contain (sharp) interfaces are treated as single fluid and MUSCL type reconstructions along with proper limiters are used.

Let ξ_{Gas} denote a scalar quantity, such as the mass fraction of a gas component. Let ξ^1_{Gas} through ξ^4_{Gas} be the cell averaged scalars in cells 1 to 4 as sketched in Fig. 3.1.

- Discontinuous interface between cells 2 and 3

In order to compute the flux across the cell interface between cells 2 and 3 we reconstruct left and right side values of the scalar ξ_{Gas} as

$$\xi^L_{Gas} = min\left(\xi^1_{Gas},\ \xi^3_{Gas}\right) + \frac{max\left(\xi^1_{Gas},\ \xi^3_{Gas}\right) - min\left(\xi^1_{Gas},\ \xi^3_{Gas}\right)}{2}$$
$$\left(1 + \theta\frac{tanh(\beta) + E}{1 + E \cdot tanh(\beta)}\right), \tag{3-3}$$

where $\theta = \begin{cases} 1 \ if \ \xi^3_{Gas} \geq \xi^1_{Gas} \\ -1 \ otherwise \end{cases}$, $E = \frac{exp(\theta\beta(2F-1))/cosh(\beta)-1}{tanh(\beta)}$, $F = \frac{\xi^2_{Gas} - min(\xi^1_{Gas},\ \xi^3_{Gas})+\gamma}{max(\xi^1_{Gas},\ \xi^3_{Gas})} + \gamma$

$$\xi^R_{Gas} = min\left(\xi^2_{Gas},\ \xi^4_{Gas}\right) + \frac{max\left(\xi^2_{Gas},\ \xi^4_{Gas}\right) - min\left(\xi^2_{Gas},\ \xi^4_{Gas}\right)}{2}(1 + \theta E), \tag{3-4}$$

where $\theta = \begin{cases} 1 \ if \ \xi^4_{Gas} \geq \xi^2_{Gas} \\ -1 \ otherwise \end{cases}$, $E = \frac{exp(\theta\beta(2F-1))/cosh(\beta)-1}{tanh(\beta)}$ $\left(\frac{\xi^3_{Gas} - min(\xi^2_{Gas},\ \xi^4_{Gas})+\gamma}{max(\xi^2_{Gas},\ \xi^4_{Gas})} + \gamma\right)$ $F=$

γ is a small number to avoid division by zero and the parameter $\beta = 1.6$ was found to give suitable results. The literature [45,63–67,75,76, 105–110] discusses values for β in the range between 1.6 and 3.

- **Regions without discontinuous interfaces**

In smooth regions, an All-Mach MUSCL type reconstruction with proper limiters is used. Free-gas mass fractions are described here to illustrate the process. They are discretized by a second order upwind biased reconstruction with proper slope limiter.

In order to compute the flux across the cell interface between cells 2 and 3 we reconstruct left and right hand values of the scalar ξ_{Gas} as $\xi^L_{Gas} = \xi^2_{Gas} + 1/2f(r^-_{i+1/2})(\xi^2_{Gas} - \xi^1_{Gas})$ and $\xi^R_{Gas} = \xi^3_{Gas} - 1/2f(r^+_{i+1/2})(\xi^4_{Gas} - \xi^3_{Gas})$. $f(r)$ represents the slope limiter function that the ratio of upwind to central differences could be adjusted according to various limiters, for example,

·Minmod limiter: $f(r) = max(0,\ min(1, 2r), min(r, 2))$.

·Koren limiter 3rd-order accurate for smooth data: When $r > 0$, $f(r) = min(2.0,\ 2.0 * r,\ (1.0 + 2.0 * r)/3.0)$; otherwise $f(r) = 0$.

The slope function is decided according to the upwind direction. If upwind direction is in the positive direction, $r^-_{i+1/2} = (\xi^2_{Gas} - \xi^1_{Gas})/(\xi^3_{Gas} - \xi^2_{Gas})$, otherwise, $r^+_{i+1/2} = (\xi^4_{Gas} - \xi^3_{Gas})/(\xi^3_{Gas} - \xi^2_{Gas})$.

Together with following TDU idea, the All-Mach THINC-TDU method is obtained.

- TDU idea

Other interfacial parameters are updated based on the interfacial pressure and interfacial gas mass fraction according to the thermodynamic equilibrium function, so that the numerical discrete format of the indicator matches the discrete density format and thermodynamic consistency is maintained

$$\rho^* = f\left(p^*,\ \xi^*_{Gas1},\ \xi^*_{Gas2}\right) \tag{3-5}$$

Another option is to reconstruct the density and then update the mass fraction according to function ξ^*_{Gas1} & $\xi^*_{Gas2} = f(p^*, \rho^*)$. Then we obtain the volume fraction according to thermodynamic relations

$$\alpha^*_{Gas1} \& \alpha^*_{Gas2} = f\left(\rho^*,\ p^*,\ \xi^*_{Gas1},\ \xi^*_{Gas2}\right) \tag{3-6}$$

Besides, reconstruction methods can take internal energy into account, see Appendix B.

3.4. Sharpening the liquid-vapor interface

Moreover, in cases of cavitation/bubble collapse with liquid and liquid-vapor components, it is difficult to sharpen the liquid-vapor two-phase interface directly because the volume fraction of vapor is determined according to the barotropic relations in Section 2.2, while in cases with liquid and non-condensable gas components, the gas-liquid two-phase interface is sharpened according to the above steps. Here, the procedure for sharpening the liquid-vapor two-phase interface is further elaborated.

Remark 1. For regions where liquid-vapor two phase interface are detected by a sensor, or a discontinuous liquid-vapor interface region meets the requirements $\varepsilon < \alpha < 1 - \varepsilon$ and $(\overline{\alpha_i} - \overline{\alpha_{i-1}})(\overline{\alpha_{i+1}} - \overline{\alpha_i}) > 0$, where ε is a small positive parameter comparing with $\overline{\alpha_i}$, the density is constructed by the THINC-based idea,

$$\rho^L = min\left(\rho^1,\ \rho^3\right) + \frac{max(\rho^1,\ \rho^3) - min(\rho^1,\ \rho^3)}{2}\left(1 + \theta\frac{tanh(\beta) + E}{1 + E \cdot tanh(\beta)}\right), \tag{3-7}$$

herein $\theta = \begin{cases} 1 \ if \ \rho^3 \geq \rho^1 \\ -1 \ otherwise \end{cases}$, $E = \frac{exp(\theta\beta(2F-1))/cosh(\beta)-1}{tanh(\beta)}$, $F = \frac{\rho^2 - min(\rho^1,\ \rho^3)+\gamma}{max(\rho^1,\ \rho^3)} + \gamma$,

$$\rho^R = min\left(\rho^2, \ \rho^4\right) + \frac{max\left(\rho^2, \ \rho^4\right) - min\left(\rho^2, \ \rho^4\right)}{2}(1 + \theta E) \tag{3–8}$$

where $\theta = \begin{cases} 1 \ if \ \rho^4 \geq \rho^2 \\ -1 \ otherwise \end{cases}$, $E = \dfrac{=exp(\theta\beta(2F-1))/cosh(\beta)-1}{tanh(\beta)}\right)$, $F = \dfrac{\rho^3 - min(\rho^2, \ \rho^4) + \gamma}{max(\rho^2, \ \rho^4)} + \gamma$). γ is a small number to avoid division by zero and the parameter $\beta = 1.6$ was found to give suitable results.

Subsequently, according to the thermodynamic relations (2–4) and (2–7), the vapor volume fraction is obtained. Other parameters like the speed of sound need also to be updated accordingly. Modified sensors can be used to detect liquid-vapor two phase regions, which are introduced in Appendix D.

Remark 2. For complex cases with liquid, liquid vapor, non-condensable gas, firstly, THINC is applied for mass fraction of non-condensable gas of liquid-gas two phase interface ξ^*_{Gas1}, ξ^*_{Gas2}. Secondly, TDU is applied to obtain density of liquid-gas two phase interface, i.e. $\rho^* = f(p^*, \ \xi^*_{Gas1}, \ \xi^*_{Gas2})$; then THINC is applied for the density of liquid-vapor two phase interface ρ^* (Remark 1). Finally, TDU is applied to obtain vapor of liquid-liquid vapor two phase interface $\alpha^*_v = f(p^*, \rho^*, \xi^*_{Gas1}, \ \xi^*_{Gas2})$ as well as other parameters like speed of sound.

3.5. Discretization of surface tension

The calculation of the normal gradient and curvature depends on which surface tension model is used. Here we decouple the calculation of the gradient of the Heaviside approximation from the curvature calculation. We use a Gaussian convolution kernel (filter) to smooth this indicator function, and then use the smoothed parameters for the curvature calculation(along with appropriate discrete method with weight factors). This simple method attempts to strike a balance between robustness and time overhead in all-Mach THINC-based interface compression.

2D Gaussian convolution kernel (filter) $\dfrac{1}{16}\begin{bmatrix} 1 & 2 & 1 \\ 2 & 4 & 2 \\ 1 & 2 & 1 \end{bmatrix}$ $\tag{3–9}$

As shown in Fig. 3.2, this 2D kernel is adapted for three dimensional cases, where the normalization coefficient is 1/64,

After the smoothing step, the curvature is obtained from

$$k = \nabla \cdot \left(\frac{\nabla\widetilde{\alpha}}{|\nabla\widetilde{\alpha}|}\right) \tag{3–10}$$

For the calculation of the curvature, the discrete shape of the gradient part can follow the Gaussian divergence theorem or the following method can be used.
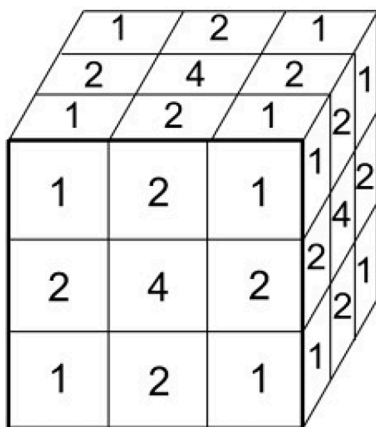
Fig. 3.2. 3D Gaussian convolution kernel blurring filters (with the normalization coefficient 1/64).
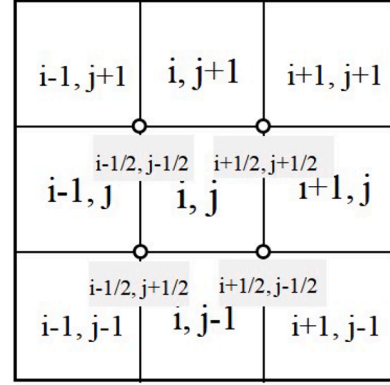
Fig. 3.3. The diagram to calculate curvature.

As shown in Fig. 3.3, the curvature is calculated through adjacent 9 cells in 2D (27 cells are used for the 3D case). The gradient in each cell interface is first calculated repeatedly in x and y directions. Then the gradient of the four vertices [i+1/2,j+1/2], [i+1/2,j-1/2], [i-1/2,j+1/2], [i-1/2,j-1/2] is calculated. The last step consists in finding the gradient of the middle grid [i, j] by averaging the gradient of the smoothed volume fraction in the four vertices [i+1/2,j+1/2], [i+1/2,j-1/2], [i-1/2,j+1/2], [i-1/2,j-1/2]. The weights of the smoothed volume fraction of the neighboring cells are implicitly considered and act like the effects of a Gaussian convolution kernel (filter).

As explained in Section 2.3, there are some other options/methods to describe surface tension effects in a surface tension dominant flow, and most of them could give even better results when combined with the adaptive mesh refinement (AMR) method.

For example, the height function (HF) method with $3 \times 3 \times 3$, $3 \times 3 \times 5$, or $3 \times 3 \times 7$ cells for the 3D case and 3×3, 3×5, or 3×7 cells for the 2D case; can provide better accuracy but is more time-consuming. With a large number of templates requires special treatment (template reduction), which reduces its robustness. Here we give only expressions that can be directly combined with the current scheme: $k = -\nabla \cdot \mathbf{n} = -H''(x_0)/[1 + H'(x_0)^2]^{3/2}$, where, $\mathbf{n} = -\frac{1}{[1+H'(x_0)^2]^{1/2}}\left(H'(x_0) \ 1\right)$, $H_i = \sum_{j-3}^{j+3}\alpha_{i,j} \cdot \Delta y_{i,j}$, $H'_{(x_0)} = (H_{i+1} - H_{i-1})/2\Delta x$, $H''_{(x_0)} = (H_{i+1} + H_{i-1} - 2H_i)/(\Delta x)^2$. Δx and Δy are the mesh size in x and y direction respectively.
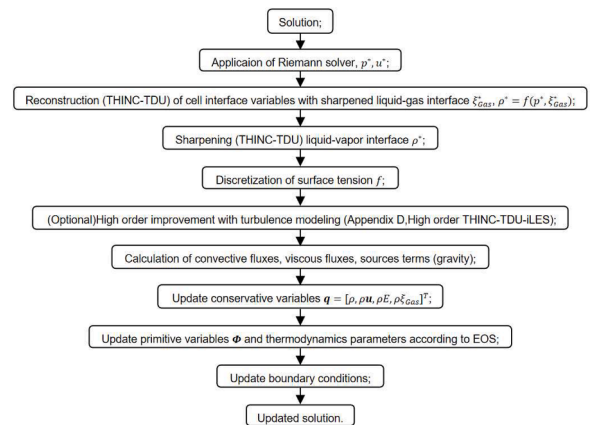

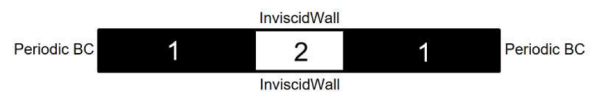**Fig. 3.4.** Flowchart of the current numerical scheme.

Fig. 4.1. Interface only problem: the 1D advection of a square column.

Table 4.1

Thermodynamics parameters of current case.

Component	γ	R (kJ/(kg· K))	C_v (kJ/(kg· K))	P_∞ (Pa)	T (K)	ρ (kJ/m^3)	P_0 (Pa)	U (m/s)
1	5	7500.75	1875.18	0	300	4.444	10^7	5
2	1.6	283.33	472.22	0	300	117.647	10^7	5

Table 4.2

Limiters for scalar transportation.

Name	Expressions $r_i = \dfrac{\overline{\Phi_i} - \overline{\Phi_{i-1}}}{\overline{\Phi_{i+1}} - \overline{\Phi_i}}$
VanAlbada's limiter [114]	f(r) = (r + r∗r)/ (1 + r∗r)
VanLeer's limiter [115]	f(r) = (r + abs(r))/(1.0 + abs(r))
MinMod limiter [116]	f(r) = max(0.0, min(1,r)).
Chatkravathy limiter [117]	f(r) = max(0.0, min(1.0,4r))
Monotonized Central (MC) limiter [118]	f(r) = max(0.0, min(2,2r,0.5(1 + r)))
Koren's limiter [119]	f(r) = max(0.0,min(2.0, 2.0∗r, (1.0 + 2.0∗r)/3.0)

An associated Riemann solver with the model for flows with interfaces including capillary effects was proposed [90], by replacing the pressure jump condition across contact discontinuities $[P] = 0$, by $[P] = -\sigma k[a], \Delta P^* = -\sigma k \Delta \alpha, s^* = [p_R - p_L + \rho_L u_L(s_L - u_L) - \rho_R u_R(s_R - u_R) - \sigma k(\alpha_R - \alpha_L)]/[\rho_L(s_L - u_L) + \rho_R(s_R - u_R)]$. Therefore, the original

Riemann solver (such as HLLC) could be improved to balance the surface force well and reduce the parasitic currents. Another possibility would be the CSS model, which uses the surface tension at the cell surface and can be cast in conservative form, but also tends to generate spurious currents. The performance of the current surface tension modeling will be discussed in details.

3.6. Flowchart of the current algorithm

We implement a four-equation model for the compressible single-fluid multicomponent flow, which includes the thermodynamic relation between single-fluid and multicomponent flow. The THINC-based reconstruction method is combined with the correction of the thermodynamic relations in the reconstruction step with the Riemann solver (TDU). Mass fraction and density as well as the process of internal energy reconstruction are associated with the same thermodynamic relations (EOS). An explicit, four stage low storage Runge-Kutta method is used for time integration.

Fig. 3.4 shows the flowchart of the newly developed algorithm,

(a)

(b)
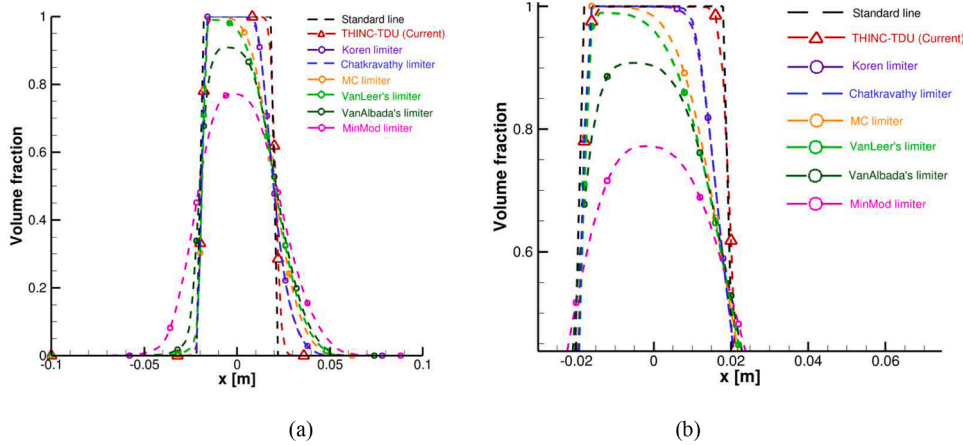
Fig. 4.2. Effects of different flux limiters on the 1D interface advection in the convective dominant two phase flow (a) volume fraction distribution using All-Mach MUSCL-TVD-TDU method with different limiters or All-Mach THINC-TDU method after 4 times periodic flow, at T=0.16s, (b) zoomed view of (a).
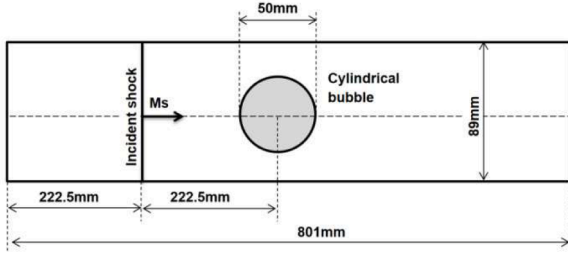

(a) Volume fraction evolution for two-phase interface at T=0.1s, 0.2s, 0.3s, 0.4s, 0.6s, 1.0s, 1.3s, 1.4s, 1.5s, 1.6s.

(b)Velocity distribution at T=0.16s.

(c)Pressure distribution at T=0.16s.
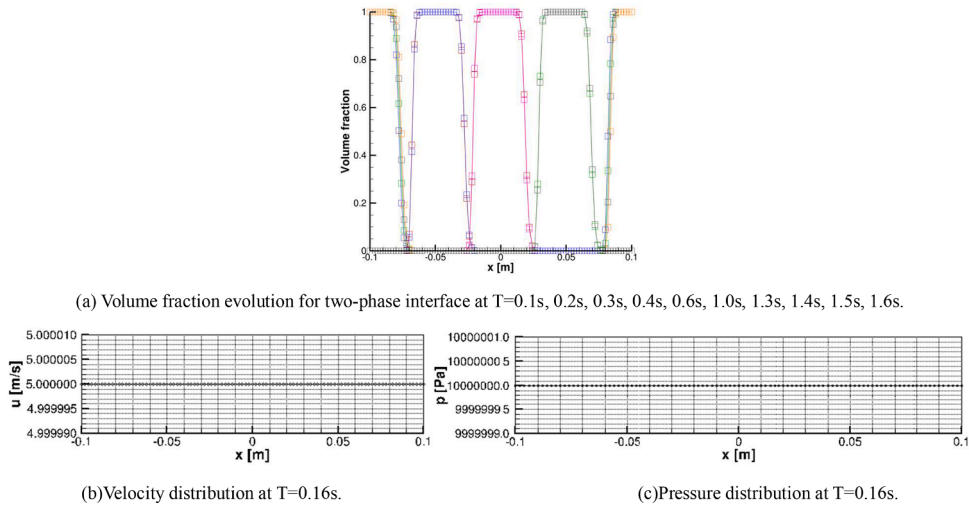
Fig. 4.4. The schematic of shock-bubble interaction computational domain (sketch map).

Table 4.3
Initial conditions for shock bubble interaction case.

Stage	p [Pa]	u [m/s]	v [m/s]	ρ [kg/m³]	Non-dimension (p,u,v,ρ)
pre-shocked air	101,325	0	0	1.225	(1,0,0,1)
post-shocked air	159,059	113.5	0	1.686	(1.5698,-0.394,0,1.3764)
Helium	101,325	0	0	0.169	(1,0,0,0.138)

which summarizes the procedures shown in Sections 3.2–3.5. After applying THINC for the mass fraction reconstruction step (ξ^*_{Gas}) for liquid-gas cases, the Riemann solver is used in combination with the EOS to update the mass fraction primitive parameters (such as density, $\rho^* = f(p^*, \xi^*_{Gas1}, \xi^*_{Gas2})$). In this way, some parameters (like density ρ^*) are automatically sharpened, maintaining thermodynamic consistency and

reducing numerical error by using the same numerical scheme. For the case with liquid-vapor interface, THINC is applied to the density (ρ^*) instead of the scalar. This THINC thermodynamic-dependent update (THINC-TDU) method preserves physical compatibility and is conservative. It sharpens the two-phase interface (including the liquid-vapor region and the liquid-gas region). An advection equation for the volume fraction is not required since it can be obtained from thermodynamic relations. Appendix D describes details of sub-grid turbulence model, as an extension. Although the sketch of the algorithm shows multiple branches for specific cases or models, the production algorithm uses pre-compiler flags to avoid if/else switching during computation. The performance and scalability of the system is shown in Chapter 5.

To provide more specifics, the current THINC-TDU scheme streamlines the reconstruction process by reducing the number of independent reconstruction methods required for individual parameters. The fundamental concept is that certain unknown parameters can be computed based on the information available, particularly through thermodynamic relationships. This approach eliminates the need for independent reconstruction of each parameter during the reconstruction step. As a result:

- Some parameters, not directly subject to THINC-based reconstruction, exhibit sharper effects due to the incorporation of thermodynamics.
- This approach is particularly advantageous for sharpening the liquid-vapor interface, where no mass fraction equation is available. THINC-TDU assists in initially sharpening density and subsequently refining the volume fraction based on thermodynamic relationships.

Table 4.4
Gas properties adopted in the shock-bubble interaction simulations [120].

Gas Component	γ	R [kJ/(kg·K)]	Cv [kJ/(kg·K)]	Ms	Mesh number
Air	1.400	0.287	0.720	1.22	14,400 × 1600 (0.055625mm)
He	1.670	2.080	3.110		

(a)

(b)

(c)

(d)

(e)
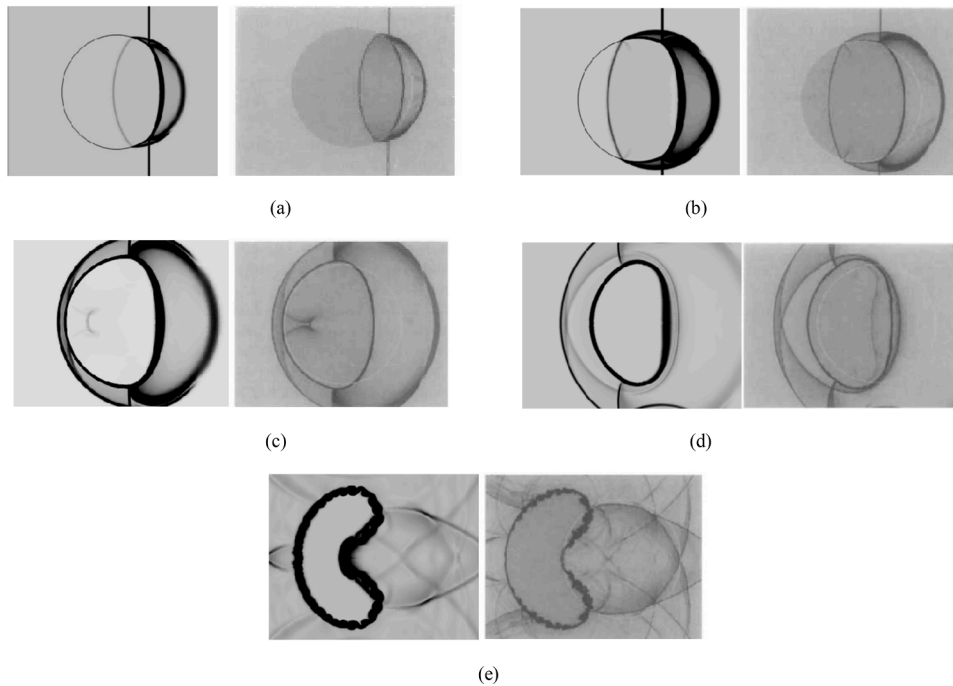
Fig. 4.5. Numerical schlieren images for the evolution of shocked air-helium interaction. (a)32μs, (b)52μs, (c)72μs, (d)102μs, (e)245μs; the first column presents current numerical results, while others show results from reference.
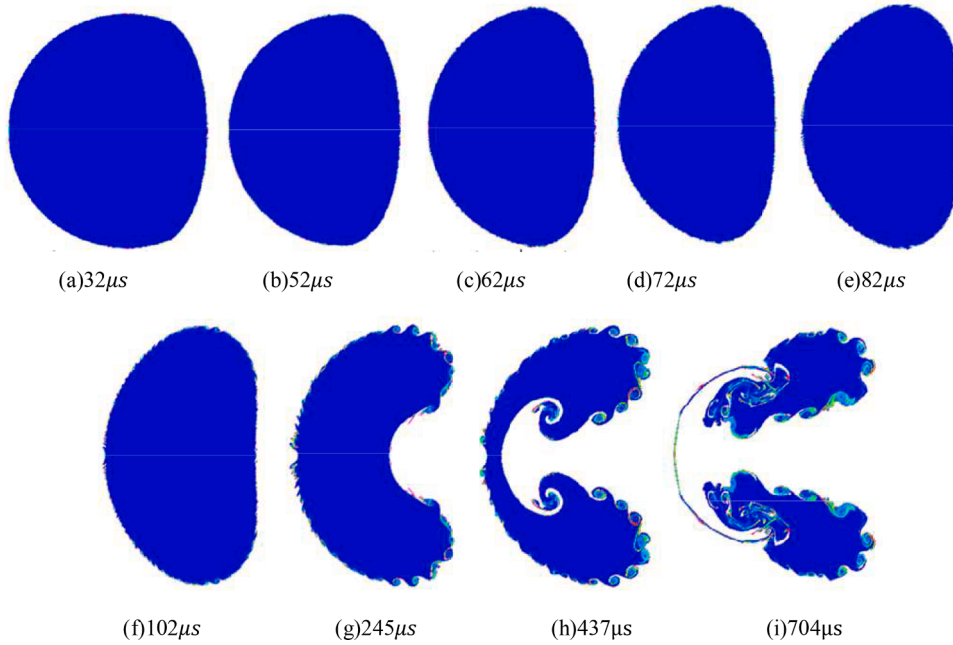
Fig. 4.6. Evolution of volume fraction from the interaction of shocked air-helium interaction. (a)32μs, (b)52μs, (c)62μs, (d)72μs, (e)82μs, (f)102μs, (g)245μs, (h) 437μs, (i)704μs.

- It ensures numerical and thermodynamic consistency when dealing with cases involving liquid, vapor, and non-condensable gas. Parameters are interdependent during the reconstruction step, with thermodynamic relationships serving as constraints.

4. Validations and results

4.1. Interface only problem

The "interface only problem" is used to verify the applicability of the method for simulating two-phase flows without spurious pressure/velocity oscillations or strong interface smearing. In the following, the one-dimensional advection of a two component fluid, representative for convection-dominant two-phase flows, is investigated. Initial and boundary conditions are shown in Fig. 4.1. A computational domain of length 0.2m is discretized with 100 cells in x-direction. Here, we use the thermodynamic closure relations presented in Eqs. (2.5) and (2.6) with parameters including initial pressure and velocity listed in Table 4.1. The detailed proof of this closure is available in Refs. [111–113]. The temperature for two components is assumed to be constant throughout the process, together with the mechanical and thermal equilibrium

conditions, to avoid effects from multiple factors and to highlight the effects of different methods on interface reconstruction. The CFL number is 1.4.

For the All-Mach MUSCL-TVD-TDU scheme, limiters are used to control the reconstruction of the primitive variables at cell interfaces. As shown in Table 4.2, we compare various limiters and discuss their suitability in the following section. Koren's limiter is used for velocity and various limiters are applied to reconstruct the mass fraction. Density and pressure at cell interfaces are obtained as described in Section 3.2~3.4.

Fig. 4.2 compares the volume fractions after four flow through times (at t=0.16s) as obtained by the investigated limiters and by the proposed sharpening methodology "THINC-TDU". Obviously, the phase interface shows significant smearing for most of the limiters, although Korens' limiter gives superior results. However, the proposed methodology outperforms all others noticeably as shown in Fig. 4.2.

As shown in Fig. 4.3 (a), using the All-Mach THINC-TDU method, the distribution of the phase interface remains sharp over time. Fig. 4.3 (b),

Fig. 4.7. Space-time diagram for three characteristic two phase interface points in the shock-bubble problem, comparing with results from Quirk and Karni.
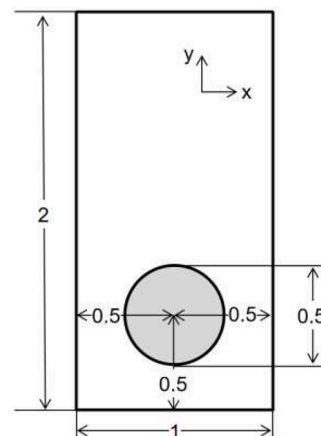
Fig. 4.8. Computation domain of rising bubble test case.

Table 4.5
parameters for two rising bubble cases.

	ρ_1 (kg/m³)	ρ_2(kg/m³)	μ_1(Pa·s)	μ_2(Pa·s)	g(m/s²)	σ(N/m)
Case1	1000	100	10	1.0	0.98	24.5
Case2	1000	1.0	10	0.1	0.98	1.96

4.3 (c) show that pressure as well as velocity maintain in their initial condition even after four periodic flow through times, which proves that the method can keep interface sharp and avoid pressure or velocity oscillations.

4.2. Shock wave interaction with a helium cylinder

In this part we assess the ability of the proposed methodology to capture the shock-wave bubble interaction processes on example of a the well-known test-case specified in [120]. The computational domain and the initial conditions are shown in Fig. 4.4 and summarized below. A uniform mesh with 14,400 × 1600 cells in stream-wise and normal direction (0.055625mm resolution) are adopted. The upper and lower boundary of the computational domain are inviscid solid walls while on the left and right boundary zero gradients for the flow variables [120, 121] are prescribed. Table 4.4 shows the fluid properties and their thermodynamic modeling. The thermodynamic closure relations used in this case are given in Eqs. (A.1.1)–(A.1.5) of Appendix A.

During the evolution process, the two phase interface is kept sharp by the proposed methodology.

The specific conditions are presented in Table 4.3, which correspond to the non-dimensionalized initial conditions in [121]

As shown in Fig. 4.5, we can see that the results of the helium-air test-case are in good agreement with the results from Quirk and Karni [120]. Highly detailed structures are obtained and shown in Fig. 4.6. The

methodology clearly resolves the physical phenomena while ensuring robust performance.

For the idealized Schlieren images, the following form to set pseudo-schlieren values is adopted,

$$\varnothing = exp\left(- C\frac{|\nabla\rho| + A}{B + A} \right) \tag{4–1}$$

Here, $\varnothing$ refers to the pseudo-schlieren value, $|\nabla\rho| = [(\partial\rho/\partial x)^2 + (\partial\rho/\partial y)^2]^{1/2}$, and the three values A,B,C can be adjusted according to display effects. Generally, A=0 and B = $|\nabla\rho|_{max}$ and it decays to $\varnothing = \exp(- C|\nabla\rho|/|\nabla\rho|_{max})$. The displayed gray scales are adjusted according to the method recommended in the Ref. [120].

The evolution time steps selected are most close to the reference time, so small deviation are acceptable since results of the reference time could not be perfectly found.

As shown in Fig. 4.7, the evolution history of three characteristic two phase interface points are also in very good agreement with Quirk and Karni [120].

4.3. Rising bubble

In order to validate the proposed methodology with respect to effects caused by surface tension, viscous forces as well as gravity, we simulate the classical rising bubble case [122] with a mesh resolution of 100 × 200 cells for Case1 and 160 × 320 cells for Case2 in x- and y-direction. The computational domain is shown in Fig. 4.8. As illustrated in Table 4.5, two different cases are investigated. The thermodynamic closure relations presented in Eqs. (2-3)–(2-8) are used. The CFL number is 1.4.

In order to demonstrate the significant improvement of the proposed methodology compared to previous work we first show results obtained
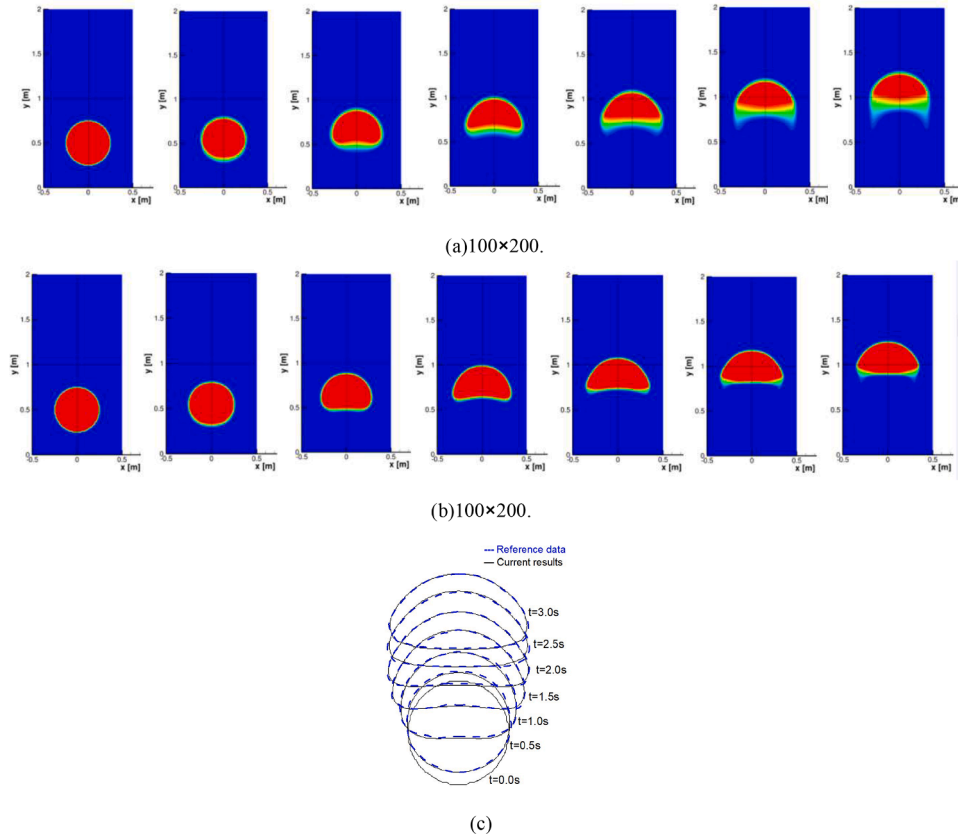

(a)100×200.

(b)100×200.

(c)

Fig. 4.9. Rising bubble evolution of case1 at t=0s, 0.5s, 1s, 1.5s, 2s, 2.5s, 3s (from left to right) (a)Results of All-Mach MUSCL-TVD-TDU method, (b)Results of All-Mach THINC-TDU, (c)Comparison of results between Ref. [124] and All-Mach THINC-TDU.
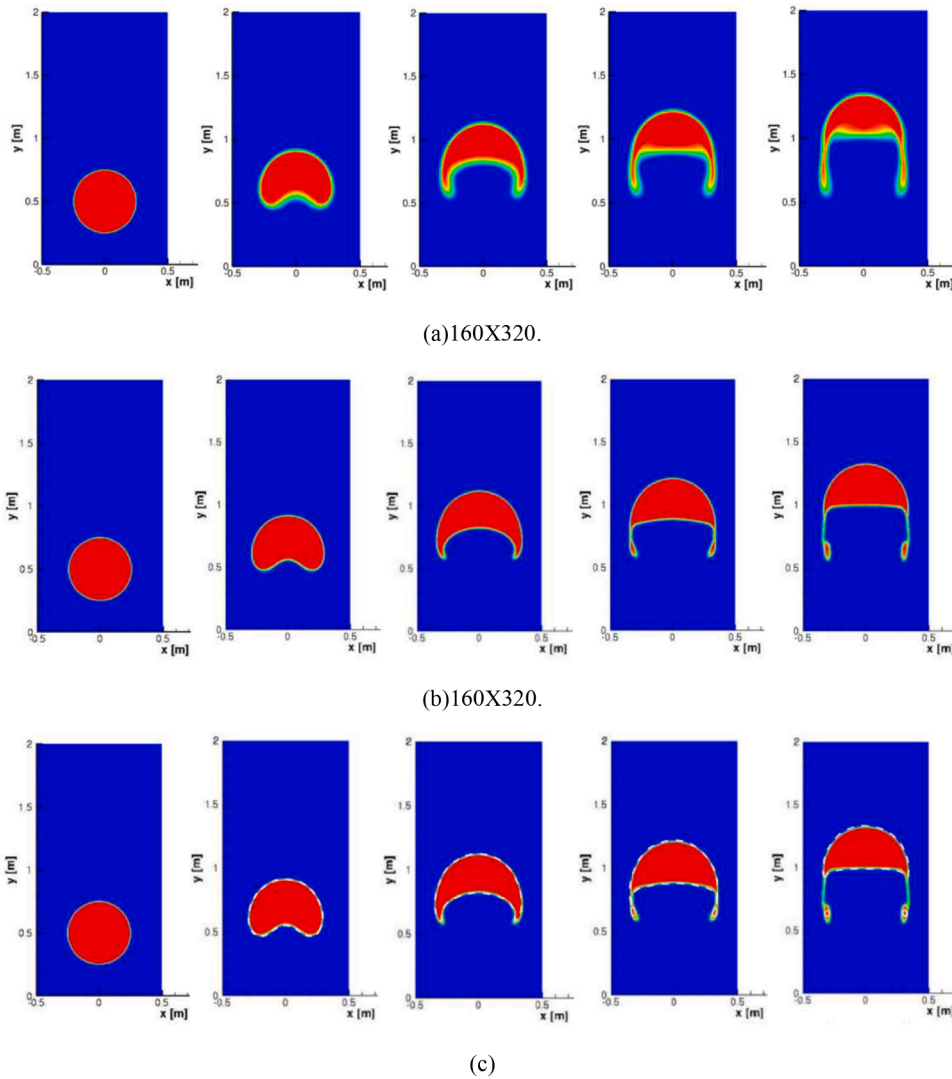
(a)160X320.

(b)160X320.

(c)

Fig. 4.10. Rising bubble evolution of case2, at t=0s, 1s, 2s, 2.4s, 3s (from left to right), (a)All-Mach MUSCL-TVD-TDU method, (b)All-Mach THINC-TDU results, (c) Comparison of results between Reference marked with dotted line [123] and All-Mach THINC-TDU.

Table 4.6
Thermodynamics parameters of current case.

Component	γ	R (kJ/(kg· K))	C_v (kJ/(kg· K))	P_∞ (Pa)	T (K)	ρ (kJ/m^3)	P_0 (Pa)	U_0 (m/s)
1	5	7500.75	1875.18	0	300	4.444	10^7	(0,0)
2	1.6	283.33	472.22	0	300	117.647	10^7	(0,0)

with the All-Mach MUSCL-TVD-TDU in Figs. 4.9(a) and 4.10(a). As one can see, the two phase interface heavily smears out, although positions and shapes show reasonable agreement with the references given in Figs. 4.9(c) and 4.10(c) [123,124], respectively. In contrast, the proposed All-Mach THINC-TDU method produces excellent results as shown in Figs. 4.9(b) and 4.10(b) [123,124]. Thus, the applicability of our numerical scheme for the cases including low Mach numbers, surface

tension, viscous effects, large density rations as well as gravity is demonstrated.

4.4. Oscillating ellipsoidal drop

An oscillating ellipsoidal drop is used to verify the ability of the method to predict the dynamics of surface tension. We use the

(a) (b) (c)

(d) (e)
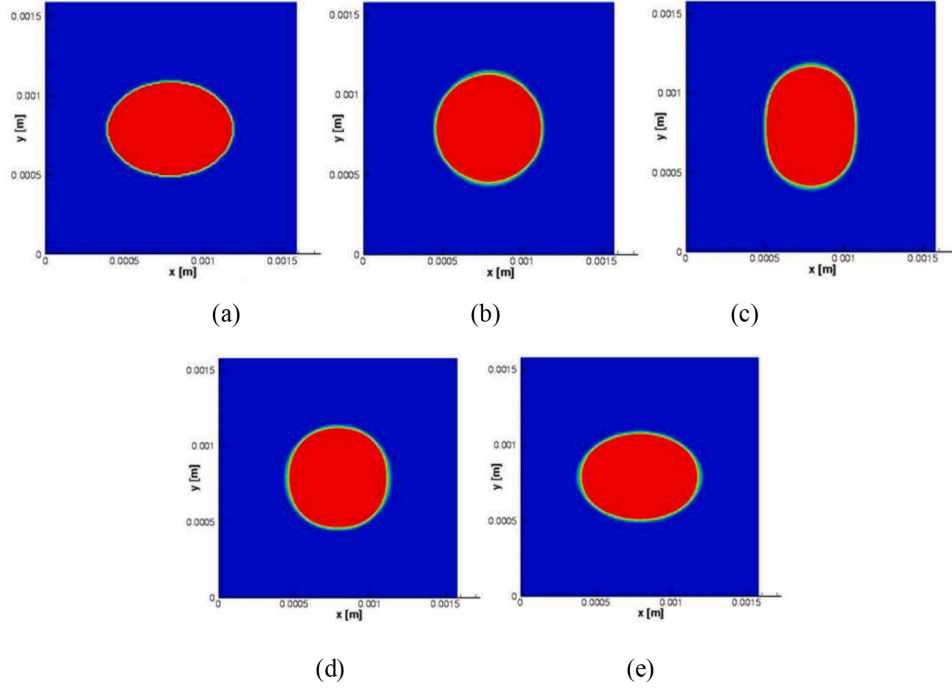
Fig. 4.11. Oscillating bubble shape at (a)T1=0s, (b)T2=5×10^{-6}s, (c)T3=10^{-5}s, (d)T4=1.5×10^{-5}s (e)T5=2×10^{-5}s.
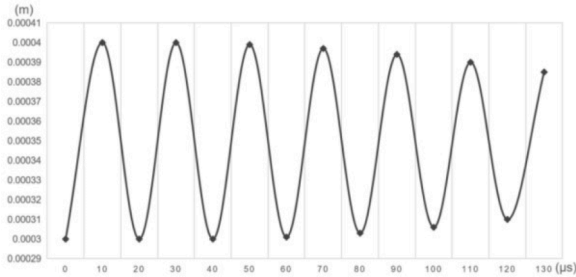
Fig. 4.12. The time dependent semi-length of minor axis.

thermodynamic closure relations presented in Eqs. (A.1.1)–(A.1.5) with parameters shown in Table 4.6,

The quadratic computational domain is $(1.58 \times 10^{-3}) \times (1.58 \times 10^{-3})$ m^2 which is discretized with 158×158 square cells. Initial pressure is $P_0 = 10^7$Pa. Non-reflective boundary conditions are used. The original bubble shape is

$$\frac{(10000x - 7.9)^2}{4^2} + \frac{(10000y - 7.9)^2}{3^2} = 1 \tag{4–2}$$

We compare our results with an analytic expression for the oscillation period of the liquid droplet given by Fyfe et al. [125,126]:

$$T = 2\pi \sqrt{\frac{(\rho_1 + \rho_2)(ab)^{3/2}}{48\sigma}} \tag{4–3}$$

In our case, the densities are 117.647 kg/m^3 and 4.444kg/m^3, respectively. The initial ellipsoid has short axis a=6×10^{-4} m and major axis b=8×10^{-4} m, surface tension coefficient is $\sigma = 80$N /m, thus a

periodic time is T ≈ 2×10^{-5}s is obtained [86,125–128] .

In Fig. 4.11, the oscillating bubble shape evolution are shown. The bubble shape changes into a circular shape at times T2=5×10^{-6}s and T4=1.5×10^{-5}s, while at T5=2×10^{-5}s the ellipsoidal shape is recovered. Fig. 4.12 it shows the temporal evolution of the semi-length of the minor axis, from which an oscillation period of T=2×10^{-5}s is found in accordance to the analytic expression.

After an initial transient we compute averaged pressure fields inside and outside of the bubble and obtain a value of 241017Pa. Since the equivalent radius of the ellipsoidal bubble is R=0.346 mm and the surface tension coefficient is 80N/m,

$$[P] = \frac{\sigma}{R} \tag{4–4}$$

the theoretical value of the pressure jump for a spherical bubble is about 231214Pa, corresponding to a relative pressure error of about 4.24%, which is acceptable for the given mesh resolution.

4.5. Recovery of circular or spherical shape

In this section we investigate a two-dimensional and a three-dimensional transition from a quadratic or cubic "bubble" towards its circular or spherical shape. The two-dimensional case is identical to the one presented in the Ref. [129], where the computational domain is 0.75m × 0.75m with mesh resolution of 150 × 150 cells in x-direction and y-direction, respectively. A square bubble is centred in the computational domain with an initial side length L=0.2m. The surface tension coefficient is 800N/m and the density ratio between the liquid bubble and the gaseous ambient is 1000, with $\rho_{gas} = 1$kg/m^3 and $\rho_{liquid} = 1000$kg/m^3. Non-reflective boundary conditions are used. Viscous effects as well as gravity are neglected. For this test-case, all substances are modeled by barotropic thermodynamic relations according to Eqs. (2-3)
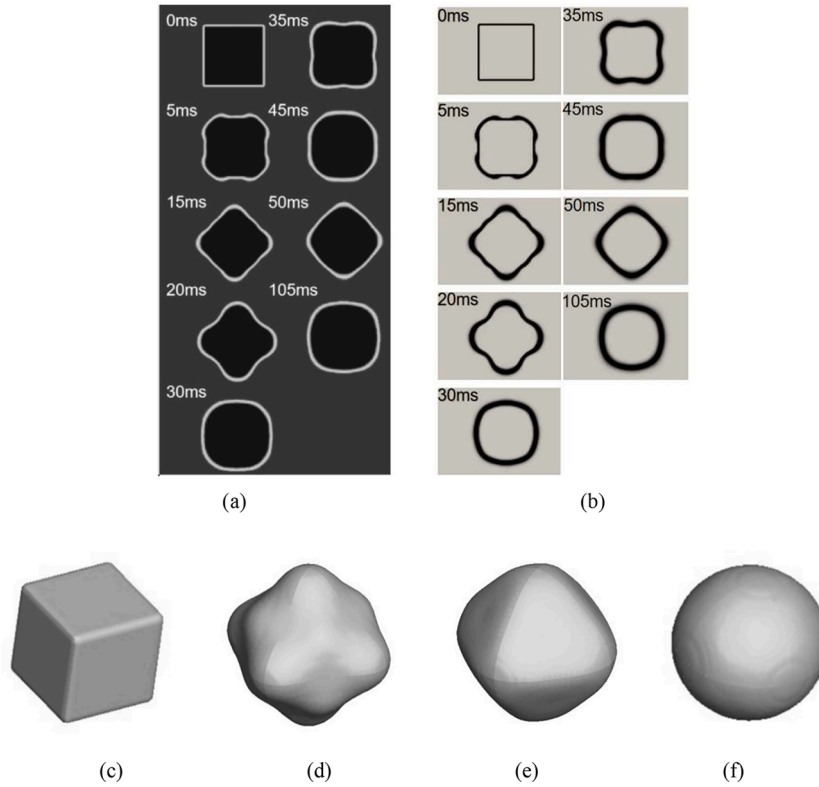
Fig. 4.13. Bubble shape evolution using volume fraction contour (a) current two dimensional recovery bubble case with uniform mesh resolution 0.005m and surface tension coefficient is 800N/m, (b) Reference of two dimensional recovery bubble case with uniform mesh resolution 0.005m and surface tension coefficient is 800N/m [129], (c)~(f) evolution of three dimension recovery bubble case.
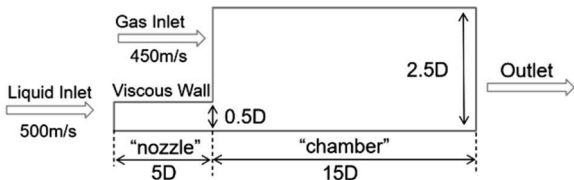

Fig. 4.14. Sketch Map of "SprayA- 210,675 model" Benchmark Case.

till (2-8), where,

$$\rho_{sat, \, liq} = 1000 kg/m^3, \ p_{sat} = 2340, \ T = 336.9K, \ c = 1500m/s, \ p_0$$
$$= 1bar, \ R_{Gas} = 296.8, \ k_{Gas} = 1.4$$

Our results presented in Fig. 4.13(a) are in very good agreement with the reference shown in Fig. 4.13(b) [129]. Note that, contrary to the reference, we show the volume fraction while "magnified schlieren images of the mixture density" are shown in the reference but a description of the numerical method to generate schlieren images is missing.

We extend this two-dimensional recovery case to three dimensions. As shown in Fig. 4.13(c)–(f), a spherical bubble evolves from an initially cubic "bubble" under the effects of surface tension, which proves the ability of current methodology to predict three-dimensional flow physics including surface tension effects.

4.6. Two dimensional simulation of primary breakup

We apply the proposed algorithm to one of our target applications, which cover dual fuel internal combustion engine (DFICE) flow physics. In order to demonstrate the benefits of the interface sharpening approach, we simulate a two-dimensional planar shear layer under typical DFICE conditions. Fig. 4.14 shows the numerical domain and the boundary conditions. The characteristic length is D=89.4 μm and the grid resolution is 0.75 μm. Identical to the upcoming chapter 4.7, the fluid properties correspond to the "SprayA-210,675″ test-case [130], where liquid n-Dodecane and a gas mixture of 20% Methane and 80% Nitrogen enter the domain from left, separated by a viscous wall. Symmetry boundary conditions at the top and at the bottom surfaces are prescribed. The initial chamber and ambient pressure is 60MPa. The inlet velocity of the liquid is 500 m/s and the velocity of the gas mixture is 450 m/s. For this test-case, all substances are modeled by barotropic thermodynamic relations according to Eqs.(2-3) till (2-8).

In Fig. 4.15 we compare the predicted evolution of the two-phase interface and its sharpness using our standard model (a and c, left) and the recently developed sharpening approach (b and d, right). The later one leads to a significant improvement in the prediction quality, preventing the interface from getting smeared and allowing for higher details, such as the liquid tip. Since the numerical complexity of both approaches compares well, the improved interface quality either allows
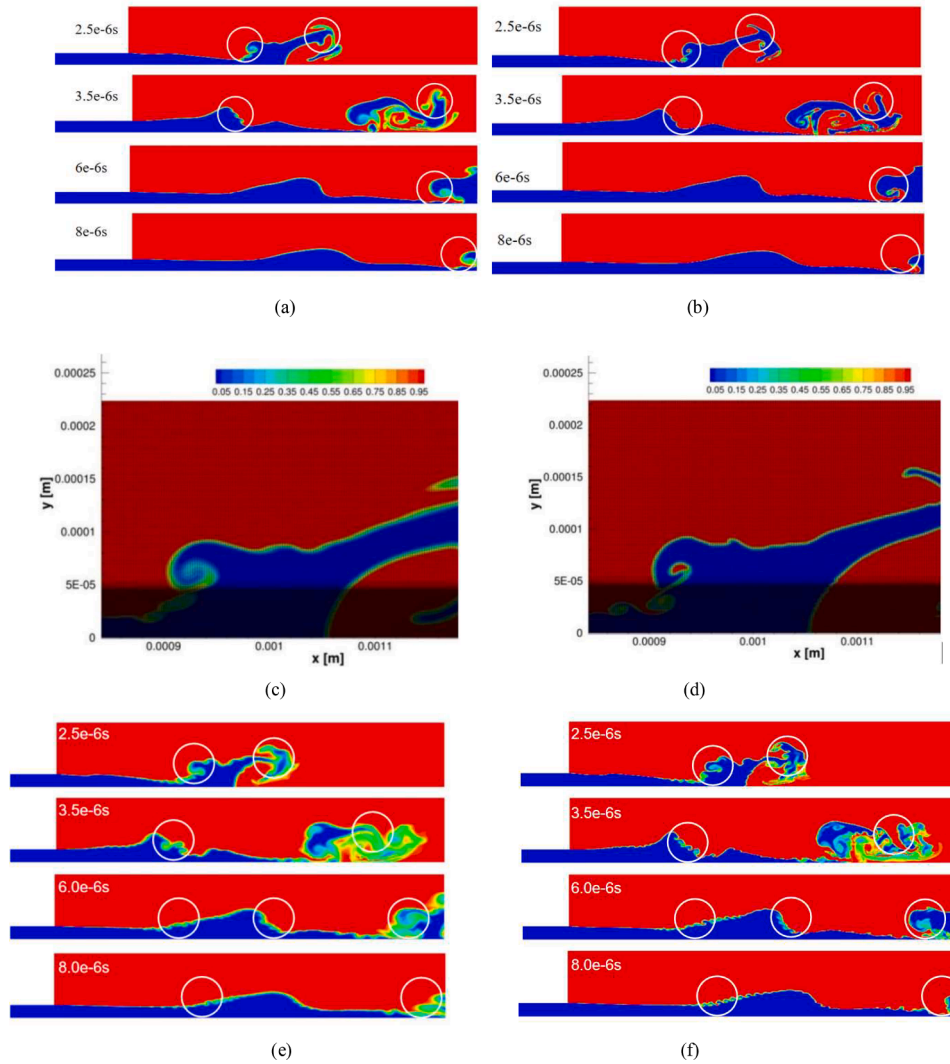
Fig. 4.15. Two phase interface evolution of 2D "SprayA-210,675 model" Benchmark Case (60Mpa, ΔV=50m/s), All-Mach MUSCL-TVD-TDU: (a) and (c), All-Mach THINC-TDU: (b) and(d), Original iLES (e), and high order THINC-TDU-iLES:(f).

for a reduction in mesh resolution or in a gain in quality.

Moreover, according to Section 2.4 and Appendix D, we compare the results of our original iLES scheme and the newly developed THINC-TDU high-order iLES algorithm. It is evident that the improved iLES scheme yields sharper two-phase interfaces. Moreover, the viscous sublattice effects (structures) in Fig. 4.15 (e)(f) obtained with the iLES scheme are more obvious than those in Fig. 4.15 (a)(b) obtained with the scheme without SGS model (Section 4.6). In Sections 4.7 and 4.8, we will show three-dimensional cases simulated with the THINC-TDU and THINC-TDU-iLES high-order algorithms.

4.7. Three dimensional simulation of primary breakup in dual-fuel conditions by THINC-TDU scheme

This test-case demonstrates the ability and robustness of the two-phase interface treatment methodology to be applied in engineering applications such as a high speed liquid jet discharging into a dual-fuel ambient. The test-case is commonly referred as "SprayA-210,675″ [130]. A block-structured o-grid with a total number of 55 million cells at a resolution of minimum 0.04μm at a time-step of 0.1 nanoseconds is used. As shown in Fig. 4.16, the computational domain is 10D × 10D × 20D (D=89.4μm) in x/y/z-direction, respectively. The initial chamber and ambient pressure is 60MPa and the discharge velocity of the jet is 500 m/s. The liquid jet consists of n-Dodecane and the gas mixtures includes

20% Methane and 80% Nitrogen. For this test-case, all substances are modeled by barotropic thermodynamic relations according to Eqs. (2-3) through (2-8). Due to the high inertia of the jet and as our focus is on the robustness of the methodology, we neglect surface tension and gravity.

In Fig. 4.17, the mushroom head shape, bridges, lobes, droplets, and other typical structures can be seen in this high-resolution simulation, showing the robust performance of our method. This three-dimensional simulation represents an under-resolved DNS of high-speed primary breakup, with inherent numerical dissipation keeping the computation stable. In this case, the compression method is applied only to the region of the two-phase interface, so some nearly pure fluid regions still exhibit a tendency to smear, but it is minor.
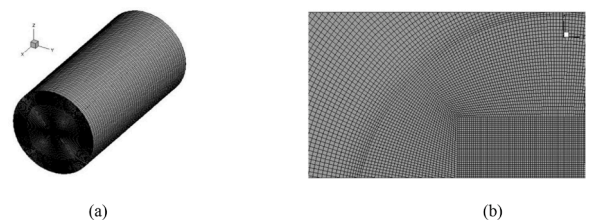

Fig. 4.16. Computational domain for "Spray A-210,675 model" (a) and detail of the o-grid (b).
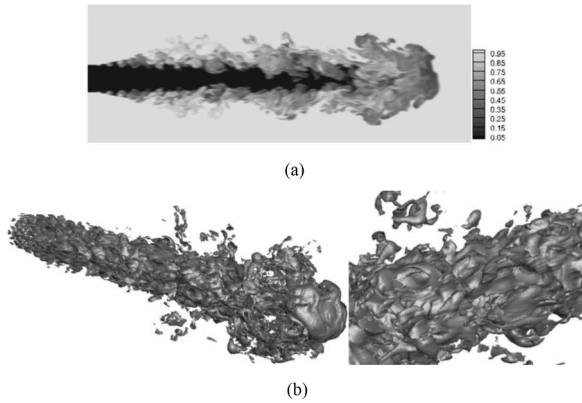
Fig. 4.17. Volume fraction of Mixture gas in stream-wise middle plane with interface sharpening at T= 4.79026×10^{-6}s, (a) contour of volume fraction (b) ISO-surface of 50%.
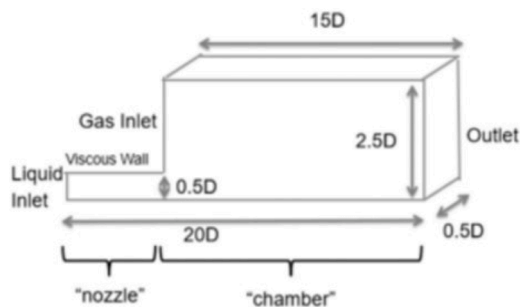

Fig. 4.18. Sketch Map of "SprayA- 210,675 model" three dimensional Benchmark Case.

4.8. Three dimensional simulation of turbulent jet flow in dual-fuel conditions

In this section we extend the two dimensional case of Fig. 4.14 to a three dimensional counterpart shown in Fig. 4.18 by applying periodic boundary conditions in span-wise direction. The smallest mesh size near the wall is $0.1\mu m$, which meets the requirement $y^+ < 1$ based on liquid diesel properties and the relative velocity between liquid and gas. We compare the three dimensional results from the original iLES and the current high order THINC-TDU-iLES algorithm(Appendix D) along with surface tension. The surface tension coefficient of diesel adopted is 0.028N/m. The initial pressure and the ambient pressure is 6 MPa, lower than case of Section 4.7, while other parameters are identical. Actually, the effects of surface tension can be ignored in this convectional-dominant flow with large Weber number (in the region near the nozzle exit). However, we includes viscous effects as well as surface tension in order to show the performance and robustness of the current scheme.

The development of the shear layer is shown in Fig. 4.19 (a). It is obvious in Fig. 4.19 that the improved iLES method (Fig. 4.19 (a), (c)) provides sharper interfaces than the original one (Fig. 4.19 (b), (d)) and the primary breakup is well captured (Fig. 4.19 (b), (d)).

4.9. Gas/vapor bubble collapse with interface sharpening

In the following, vapor and gas bubble collapses are simulated using the method of interface sharpening and TDU. In this simulation, we use the thermodynamic relations from Section 2.2 and Appendix A. All configuration settings such as initial pressure distribution and initial bubble position are similar to [131]. As shown in Fig. 4.20, the distance between the gas or vapor bubble and the wall is H=440μm and the radius of the bubble is R=400 μm. As shown in Fig. 4.21, the meshes

near the bubble are refined and the mesh size is 4μm. Around the far-field region, the meshes are enlarged. For the gas bubble we use the initial gas pressure of 3000 Pa and for the vapor bubble we assume a vapor pressure of 1342 Pa. From Figs. 4.21–4.23, it can be seen that the present scheme is suitable for bubble collapses with a sharp two-phase interface between liquid and gas or (condensable) vapor, which allows for more complicated applications such as turbulent cavitating liquid jets into a gas environment.

5. Performance and scalability

The parallel computational framework of our in-house code CATUM has been optimized for better parallel scalability and has been used for many large computational problems on supercomputers [21–24,99,100, 104]. The now newly proposed scheme retains the original framework of CATUM, while only minor modifications are required to verify and validate the proposed model and numerical method. The compact four-cells FVM framework remains unchanged and no additional equations are added. On the other hand, diffuse interface methods are recognized [14] to be inherently less expensive and easier to parallelize than sharp interface methods, since no expensive and localized geometric reconstruction of the interface is required, which could potentially lead to load balancing problems. The diffuse interface method, in conjunction with compact four-cell methods, provides a cost-effective, robust, and scalable method. In particular, for the turbulent jet flow problem shown in Section 4.8 and the gas bubble collapse problem shown in Section 4.9, the new combined scheme significantly reduces diffusion while requiring only about 6.65% and 2.06% additional cost (on the Linux cluster at Leibniz Computing Center), respectively, compared to the original scheme shown in the respective chapters.

To evaluate the parallelization efficiency of this new scheme of the in-house CATUM solver, strong-scaling and weak-scaling tests were performed on the Leibniz Computing Center (LRZ) for the case in Section 4.2. The results of the strong-scaling test are shown in Fig. 5.1(a), where the actual speedup is compared to the ideal speedup. The results of the weak scaling test are shown in Fig. 5.1(b), where the ideal time and the actual time are plotted against the number of cores. The results show that the weak scaling is nearly constant up to 1372 cores. After that, the efficiency drops to about 76% for 1792 cores. The strong scaling test results show good performance for large grid sizes per core (51.2K cells/core, 12.8K cells/core). Increasing the number of processors leads to a decrease in the problem size (number of cells) per core. The difference between the ideal and actual speedup is due to a higher communication overhead compared to the computation time for smaller grid sizes. This could be caused by a very low total computation time per time step [14], which is the result of an optimized single-core performance of the solver and a low-cost numerical method, leading to a higher ratio of communication to computation time and a non-ideal parallel scalability. Overall, a deviation from ideal performance is expected due to the increasing amount of MPI communication.

6. Conclusions

In this work we propose a robust four equation model using one-fluid multi-component thermodynamics relations as well as an All-Mach number consistent THINC-TDU method, which prevents two-phase interfaces from smearing. Surface tension effects, viscous effects, gravity effects, as well as shock-wave phenomena have been assessed and the results are in very good agreement with well-known reference results. Our simulation of a liquid jet in a dual-fuel environment demonstrates the suitability of the methodology to complex real-world engineering applications. An implementation of the methodology into existing MUSCLE or WENO-type compressible finite volume methods on block-structured meshes is presented. A significant improvement of predicted details in compressible two-phase flows is reached while the additional computational costs are negligible. This is achieved by
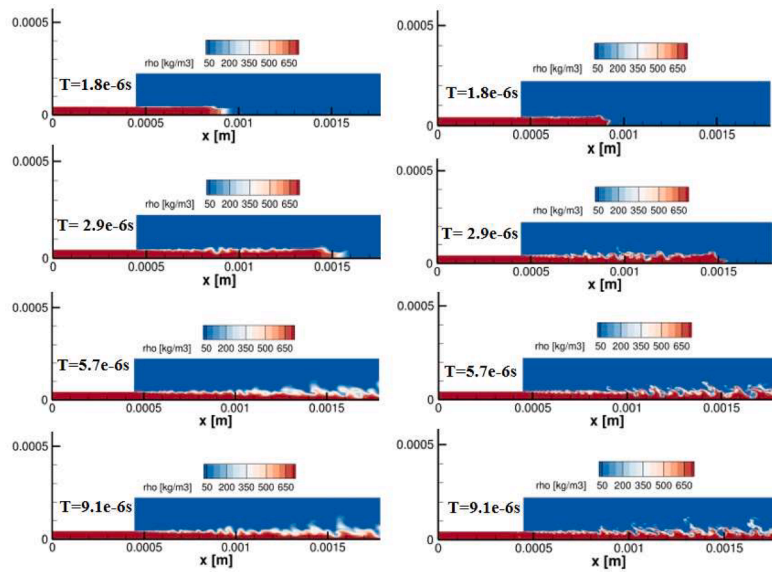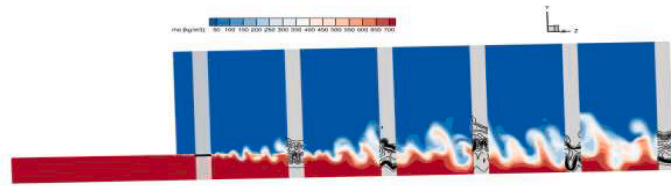
(a)Original iLES: left column, and high order THINC-TDU-iLES algorithm: Right column T=1.8×10⁻⁶s, 2.9×10⁻⁶s, 5.7×10⁻⁶s, 9.1×10⁻⁶s.
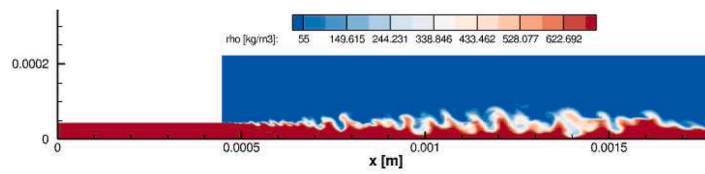
(b)Original iLES, T=0.354331×10⁻⁵s
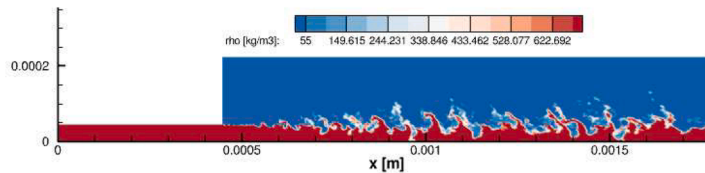
(c)High order THINC-TDU-iLES algorithm, T=0.354331×10⁻⁵s.

(d)Original iLES, T=0.354331×10⁻⁵s
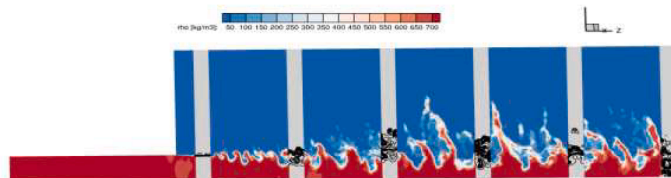
(e)High order THINC-TDU-iLES algorithm, T=0.354331×10⁻⁵s.

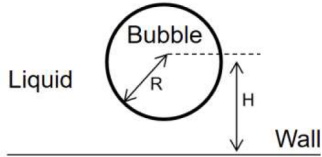**Fig. 4.19.** 2D density contour (a)–(c), and 3D density contour (d), (e) .

Fig. 4.20. Sketch map of bubble collapse.

combining an algebraic sharpening method with a thermodynamically consistent correction procedure in the flux computation without the need of complex geometric reconstruction approaches. The approach has been implemented into our in-house code CATUM validated against a series of references and has extended to be suitable for sub-grid turbulence modelling. A shock-droplet test-case in near critical conditions with a real fluid model show that current results are superior to WENO3-JS and OWENO3 schemes (if using the same mesh resolution). In addition to gas bubble collapse, vapor bubble collapse was also performed to

(a)

(b)
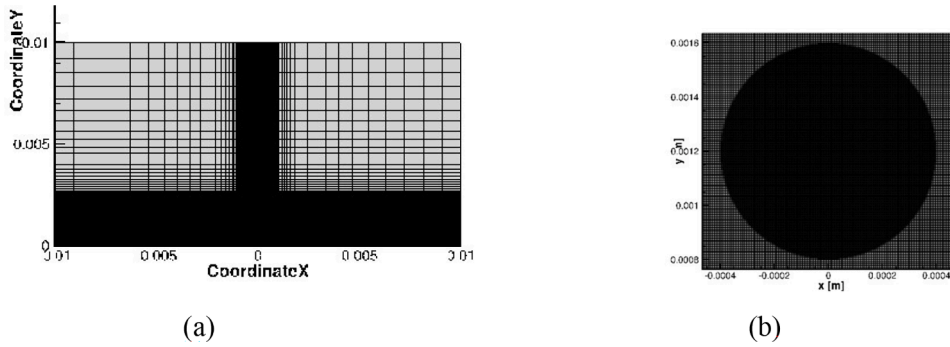
Fig. 4.21. Sketch map of bubble collapse mesh (a), enlarged mesh around bubble (b) with smallest mesh resolution 4μm.

(a)

(b)
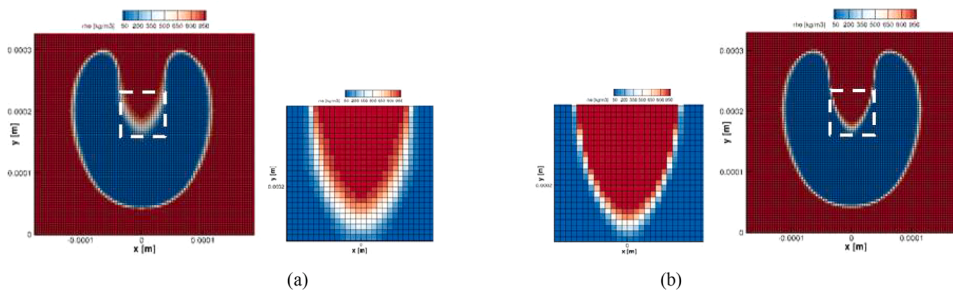
Fig. 4.22. Gas bubble collapse with smallest mesh resolution 4μm: density contour of All-Mach MUSCL-TVD-TDU method:(a); density contour of All-Mach THINC-TDU:(b).
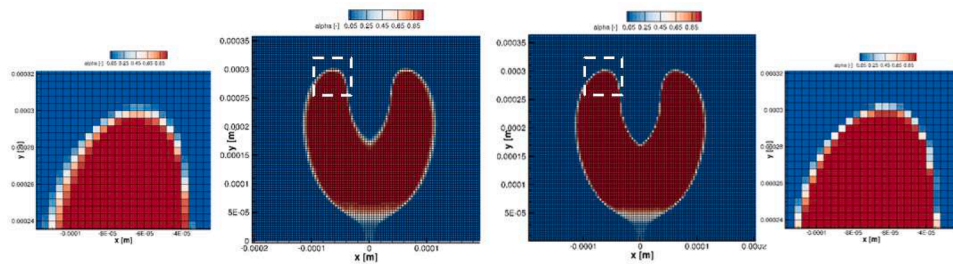
(a)Vapor contour of All-Mach MUSCL-TVD-TDU method:Left, vapor contour of All-Mach THINC-TDU:Right.
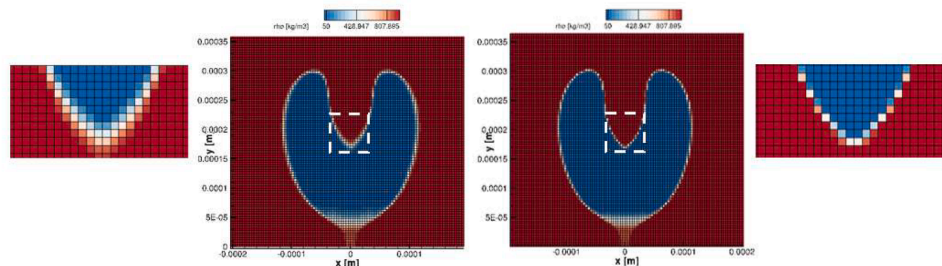
(b)Density contour of All-Mach MUSCL-TVD-TDU method:Left, Density contour of All-Mach THINC-TDU:Right.

Fig. 4.23. Vapor Bubble collapse with smallest mesh resolution 4μm.
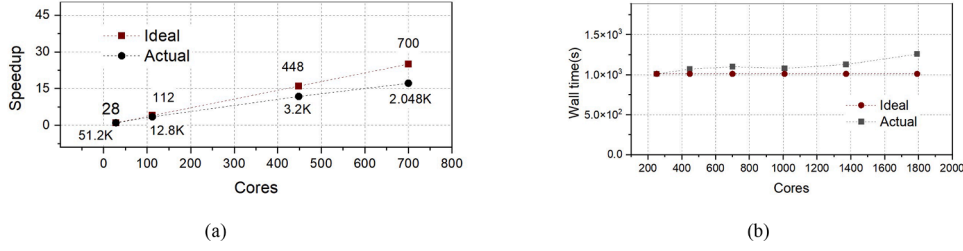
Fig. 5.1. Scaling of the CATUM on the Linux-Cluster at Leibniz Supercomputing Centre, (a) Strong scaling, the number above the lines is the number of cores used, the number below the lines is the number of grids per core; (b) Weak scaling.

prove that the two-phase interface between liquid and vapor can also be sharpened using the current scheme. This demonstrates the ability of the current scheme to handle cavitation-related cases containing both condensable vapor and non-condensable gas, such as atomization using cavitation nozzles. The simulation of a three-dimensional turbulent jet flow with surface tension and viscous effects also demonstrates the high performance of the current scheme.

CRediT authorship contribution statement

Yu Jiao: Conceptualization, Methodology, Software, Investigation, Visualization, Writing – original draft, Writing – review & editing. **Steffen J. Schmidt:** Writing – review & editing, Funding acquisition, Project administration, Resources, Supervision. **Nikolaus A. Adams:** Writing – review & editing, Funding acquisition, Project administration, Resources, Supervision.

Declaration of competing interest

The authors declare that they have no known competing financial interests or personal relationships that could have appeared to influence the work reported in this paper.

Data availability

Data will be made available on request.

Acknowledgement

Appendix A. Thermodynamics equilibrium model for coupled (one-fluid) multi-component flow

A.1. Stiffened gas equation of state

In this part we take internal energy into account. The variables of the mixtures in the one-fluid multi-component model are shown in Table A.1. The detailed prove of thermodynamic equilibrium closure could be observed in Refs. [111–113]. It is noted that Noble-Abel Stiffened-Gas equation of state degenerates to the Stiffened-Gas equation of state by setting the covolume of the fluid b=0.

Table A.1
Variables of the mixtures in the one-fluid multi-component model.

Variables	Descriptions
Volume fractions	$\alpha_{Gas1} + \alpha_{Gas2} + \alpha_L = 1$
Mass fractions	$\xi_{Gas1} + \xi_{Gas2} + \xi_L = 1, \ \xi_{Gas1} = \alpha_{Gas1}\rho_{Gas1}/\rho, \ \xi_{Gas2} = \alpha_{Gas2}\rho_{Gas2}/\rho, \ \xi_L = \alpha_L\rho_L/\rho$
Pressure	$P = (\alpha_{Gas2} + \alpha_{Gas2} + \alpha_L)P = (\xi_{Gas1} + \xi_{Gas2} + \xi_L)P$
Density	$\rho = \alpha_{Gas1}\rho_{Gas1} + \alpha_{Gas2}\rho_{Gas2} + \alpha_L\rho_L = (\xi_{Gas1} + \xi_{Gas2} + \xi_L)\rho$
Specific total energy	$E = e + |u^2|/2$
Internal energy	$\rho e = \alpha_{Gas1}\rho_{Gas1}e_{Gas1} + \alpha_{Gas2}\rho_{Gas2}e_{Gas2} + \alpha_L\rho_L e_L = \rho\xi_{Gas1}e_{Gas1} + \rho\xi_{Gas2}e_{Gas2} + \rho\xi_L e_L$
	$e = \xi_{Gas1}e_{Gas1} + \xi_{Gas2}e_{Gas2} + \xi_L e_L$
Specific total enthalpy	$H = E + P/\rho = e + |u^2|/2 + P/\rho$
Specific enthalpy	$\rho h = \alpha_{Gas1}\rho_{Gas1}h_{Gas1} + \alpha_{Gas2}\rho_{Gas2}h_{Gas2} + \alpha_L\rho_L h_L = \xi_{Gas1}\rho h_{Gas1} + \xi_{Gas2}\rho h_{Gas2} + \xi_L\rho h_L$
Mixed viscosity	$\mu_{mix} = (1 - \alpha_{Gas1} - \alpha_{Gas2})[(1 - \alpha_v)(1 + 5/2\alpha_v)\mu_{liq} + \alpha_v\mu_{vap}] + \alpha_{Gas1}\mu_{Ga1} + \alpha_{Gas2}\mu_{Ga2}$

Here we use "stiffened Gas" EOS for liquid and two gas components,

$$P = (\gamma - 1)\rho(e - q) - \gamma P_\infty \tag{A.1.1}$$

where, γ is the heat capacity ratio C_P/C_V. In this way, $\rho_L = (P_L + \gamma_L P_{\infty,L})/((\gamma_L - 1)(e_L - q_L))$. Gas fluid could decay to ideal gas with $P_{\infty,Gas}=0$. Generally, for ideal gas q=0, $P_{Gas} = (\gamma_{Gas} - 1)\rho_{Gas}e_{Gas}$ and $\rho_{Gas} = P_{Gas}/((\gamma_{Gas} - 1)e_{Gas})$; the specific heat capacity $R_{Gas} = C_{P,Gas} - C_{V,Gas} = \gamma_{Gas}C_{V,Gas} - C_{V,Gas} = (\gamma_{Gas} - 1)C_{V,Gas}$, $e_{Gas} = C_{V,Gas}T_{Gas}$, thus $P_{Gas} = (\gamma_{Gas} - 1)\rho_{Gas}e_{Gas} = (\gamma_{Gas} - 1)\rho_{Gas}C_{V,Gas}T_{Gas} = \rho_{Gas}R_{Gas}T_{Gas}$, $\rho_{Gas} = P_{Gas}/(\gamma_{Gas} - 1)C_{V,Gas}T_{Gas} = P_{Gas}/(R_{Gas}T_{Gas})$.

Then the mixture density is

$$\rho = \alpha_{Gas1}\rho_{Gas1} + \alpha_{Gas2}\rho_{Gas2} + \alpha_L\rho_L = \alpha_{Gas1}\frac{P_{Gas1}}{(\gamma_{Gas1} - 1)C_{V,Gas1}T_{Gas1}} + \alpha_{Gas2}\frac{P_{Gas2}}{(\gamma_{Gas2} - 1)C_{V,Gas2}T_{Gas2}} + \alpha_L\frac{P_L + \gamma_L P_{\infty,L}}{(\gamma_L - 1)(e_L - q_L)} \tag{A.1.2}$$

The internal energy for liquid is $e_L(P_L, \rho_L) = (P_L + \gamma_L P_{\infty,L})/((\gamma_L - 1)\rho_L) + q_L$, internal energy for gas is $e_{Gas}(P_{Gas}, \rho_{Gas}) = P_{Gas}/(\gamma_{Gas} - 1)\rho_{Gas}$, thus internal energy for fluid mixtures are

$$e = \xi_{Gas1}e_{Gas1} + \xi_{Gas2}e_{Gas2} + \xi_L e_L = \xi_{Gas1}C_{V,Gas1}T_{Gas1} + \xi_{Gas2}C_{V,Gas2}T_{Gas2} + \xi_L\left(\frac{P_L + \gamma_L P_{\infty,L}}{(\gamma_L - 1)\rho_L} + q_L\right) \tag{A.1.3}$$

The speed of sound for liquid and gas could be obtained through $c_L = \sqrt{\gamma_L(P_L + P_{\infty,L})/\rho_L} = \sqrt{\gamma_L(P_L + P_{\infty,L})/(\rho\xi_L/\alpha_L)}$ and $c_{Gas} = \sqrt{\gamma_{Gas}P_{Gas}/\rho_{Gas}} = \sqrt{\gamma_{Gas}R_{Gas}T_{Gas}}$.
The volume fraction for components are

$$\alpha_{Gasi} = \xi_{Gasi}\frac{\rho}{\rho_{Gasi}} = \xi_{Gasi}\frac{\rho}{\frac{P_{Gasi}}{(\gamma_{Gasi}-1)e_{Gasi}}} = \xi_{Gasi}\frac{\rho}{\frac{P_{Gasi}}{(\gamma_{Gasi}-1)C_{V,Gasi}T_{Gasi}}} = \frac{\xi_{Gasi}\rho(\gamma_{Gasi}-1)C_{V,Gasi}T_{Gasi}}{P_{Gasi}} \tag{A.1.4}$$

$$\alpha_L = 1 - \sum \alpha_{Gasi} \tag{A.1.5}$$

A.2.1. Peng-Robinson Equation of State

Besides, the "Peng-Robinson" EOS [132] is also combined into current four equation scheme and the related test case, near-critical shock droplet interaction, is presented in A.2.2.
For the liquid and gas components,

$$p = \frac{RT}{v - b} - \frac{a}{v^2 + 2bv - b^2} \tag{A.2.1}$$

where T is the temperature; R is the universal gas constant; V is the molar volume, $V = M/\rho$, M is the molar mass. Coefficients $a = \sum_{\alpha=1}^{N}\sum_{\beta=1}^{N}X_\alpha X_\beta a_{\alpha\beta}$ and $b = \sum_{\alpha=1}^{N}X_\alpha b_\alpha$. X_α is the mole fraction of species α and in-total species number is N; coefficients $a_{\alpha\beta} = 0.457236(RT_{c,\alpha\beta})^2/p_{c,\alpha\beta}(1 + c_{\alpha\beta}(1 - \sqrt{T/T_{c,\alpha\beta}}))^2$ and $b_\alpha = 0.077796RT_{c,\alpha}/p_{c,\alpha}$ are obtained according to the mixing rules [133]. $p_{c,\alpha\beta}$ is the critical mixture pressure and $p_{c,\alpha\beta} = \frac{Z_{c,\alpha\beta}RT_{c,\alpha\beta}}{\nu_{c,\alpha\beta}}$, $c_{\alpha\beta} = 0.37464 + 1.5422\omega_{\alpha\beta} - 0.26992\omega_{\alpha\beta}^2$, $T_{c,\alpha\beta}$ is the critical mixture temperature and $T_{c,\alpha\beta} = \sqrt{T_{c,\alpha}T_{c,\beta}}(1 - k_{\alpha\beta})T_{c,\alpha}$. and $T_{c,\beta}$ are critical temperature for species α and β, $k_{\alpha\beta}$ is the binary interaction parameter. The critical mixture molar volume $\nu_{c,\alpha\beta}$, the critical mixture compressibility $Z_{c,\alpha\beta}$, the acentric factor $\omega_{\alpha\beta}$ denote as $\nu_{c,\alpha\beta} = 1/8(\nu_{c,\alpha}^{1/3} + \nu_{c,\beta}^{1/3})^3$, $Z_{c,\alpha\beta} = 1/2(Z_{c,\alpha} + Z_{c,\beta})$, $\omega_{\alpha\beta} = 1/2(\omega_\alpha + \omega_\beta)$, where $\nu_{c,\alpha}^{1/3}$ and $\nu_{c,\beta}^{1/3}$ are critical molar volume for species α and β, $Z_{c,\alpha}$ and $Z_{c,\beta}$ are critical compressibility factor for species α and β, ω_α and ω_β are acentric factor for species α and β.
Besides, Ref. [134] provides the parameters for the NASA polynomials, which would be used to obtain the internal energy, enthalpy, and entropy.

A.2.2. PR-EOS for (near-critical) Shock Droplet Interaction

We validate the shock interaction in a nitrogen environment with a sphere of n-Dodecane droplet [135] in order to show the performance of current numerical scheme in complex realistic conditions. Same parameters are adopted as the reference except for the mesh resolution. The uniform mesh size(0.115mm) is adopted near the droplet, which is finer than that of reference(0.23mm). In this way, it should be noted that higher mesh resolution is adopted for current scheme in order to be comparable to results from high order WENO5 scheme of reference. Ref. [134] provides the parameters for the NASA polynomials. Numerical scheme could be found in the Appendix B.
In Fig. A.2.1, results show good agreement with those from Ref. [135]. It shows that current scheme could be combined with real fluid model directly, further proving its robust performance. Moreover, based on same meth resolution(0.115mm) and same initial conditions, current results are superior to these of WENO3(HLLC) and OWENO3(HLLC) scheme, especially near the two phase interface, which simply shows its comparable performance over higher order method.
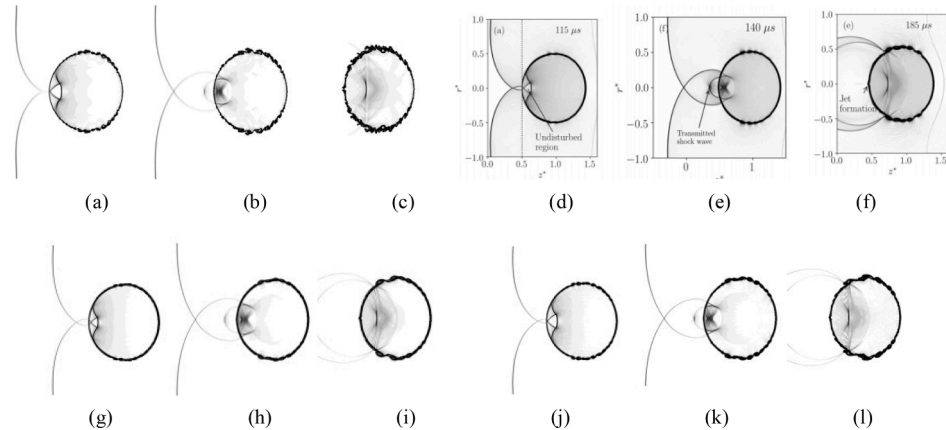

Fig. A.2.1. Shock n-Dodecane in the Nitrogen environment:115μs,(a), (d), (g), (j);140μs,(b), (e), (h), (k);185μs,(c), (f), (i), (l). Current results (a–c); Reference (d–f) [135];WENO3 (g–i);OWENO3 (j–l).

Appendix B. Internal energy and real fluid effects

Internal energy, as an additional parameter, needs to be taken into account. Most procedures, such as step adopting All-Mach Riemann solver and reconstruction steps for mass fraction, are the same as those in Chapter3. While following aspects are excepted.

The thermodynamic model adopted here is related to Appendix A. Variables including velocities, pressure, mass fraction and temperature are given, others like density and internal energy could be obtained according to the thermodynamic relations, $\rho = \mathrm{f}(\mathrm{p}, \mathrm{T}, \xi_{\mathrm{Gasi}})$, $\mathrm{e} = \mathrm{f}(\rho, \mathrm{T}, \xi_{\mathrm{Gasi}})$.

In a general way, variables u^*, v^*, w^*, ρ^*, p^*, ξ^*_{Gasi} adopt the same reconstruction method as explained in Chapter3 and internal energy e^* just need follow the reconstruction method of density ρ^*. While in the current scheme, after obtaining the interface internal energy e^*, the TDU idea would be applied to update variables like density ρ^*. Specifically, during the reconstruction process, interface parameters like density are updated from the interface pressure, as mass fraction and internal energy, $\rho^* = \mathrm{f}(p^*, \xi^*_{Gasi}, e^*)$, thus the numerical format of density keeps numerical consistent with other variables. Moreover, volume fraction could be obtained according to $\alpha^*_i = f(\rho^*, p^*, \xi^*_{Gasi}, e^*)$.

If the current FC scheme is combined with thermodynamics relations from Appendix.A.2.1, temperature is updated firstly according to internal energy, density, species mass fraction $\mathrm{T} = \mathrm{f}(e, \rho, \xi_{Gasi})$ (by Gradient descent/Newton method), then pressure is updated from temperature, density and species mass fraction $\mathrm{p} = \mathrm{f}(\rho, \mathrm{T}, \xi_{Gasi})$. A small note is that the convergence speed of the Gradient descent/Newton method in obtaining the temperature could be improved by storing the temperature from the previous time step and using it as the initial guess to calculate the updated temperature. In the FC scheme, the numerical flux evaluated from the two neighboring cells of the face is exactly the same, which guaranty strict conservation of all variables.

Appendix C. A spherical drop in static equilibrium

A spherical drop in static equilibrium is adopted to show the balanced effects between pressure and surface tension force since imbalance between them induce the parasitic velocities. Parameters are adopted according to the classical Ref. [136]. Density ratio of two in-viscid fluids is 10. The side length of computational cube domain is 8 and 40 uniform meshes are applied in every direction. Initial pressure drop between inside fluid and outside fluid is equal to the theoretical equilibrium value, $\sigma = 73, \mathrm{R} = 2$, thus $p_{\mathrm{inside}} - p_{\mathrm{outside}} = 2\sigma/\mathrm{R} = 73$.

For our current method, the max-mum parasitic speed at t≈0.001s and t≈0.05s are about 0.004m/s and 0.11m/s respectively (Fig. C.1), which is comparable to best results 0.0855m/s and 0.386m/s shown in the Ref. [136]. Thus, current surface tension model performs well.
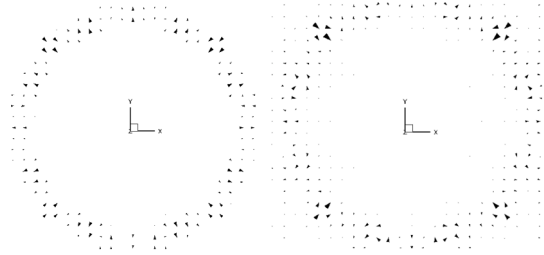
$$(a)|V|_{\max} = 0.004\mathrm{m/s}. \qquad (b)|V|_{\max} = 0.11\mathrm{m/s}.$$

Fig. C.1. The velocity vector (vector length is grid units divide magnitude) field of an x-y plane. Plots (a) is at t≈0.001s with vector length 40, (b) is at t≈0.05s with vector length 1.5.

Appendix D. High order improvement with turbulence modeling (iLES)

In order to include the turbulence modeling, a high order improvement of All-Mach THINC-TDU is proposed with iLES approach, two extra gas components as well as modified sensor. For the iLES scheme of the Ref. [24], if discontinues region is detected by sensor, upwind-basied reconstruction (density) would be adopted. While in current scheme, the cell interface value reconstruction procedure is switched among an upwind-biased, a centered reconstruction and a THINC-based scheme. And TDU idea is adopted to continually keep the thermodynamic relationship coupled among variables(pressure, density, gas mass fraction).

- **Upwind-biased reconstruction scheme**

Procedures(Regions without discontinuous interfaces) shown in 3.3 are adopted for the upwind-biased reconstructions of variables.

- **Central reconstruction scheme**

The above upwind-biased scheme has intrinsic numerical dissipation, thus the central reconstruction scheme is needed to reduce dissipation. And proper sensor function is used to switch between candidate schemes. A linear fourth order central scheme is applied,

$$\Phi^{*,C}_{i+1/2} = \left[\mathrm{u}^*, \ \mathrm{v}^*, \ \mathrm{w}^*, \ \mathrm{p}^*, \ \xi^*_{Gas1}, \ \xi^*_{Gas2}\right]^{C}_{i+1/2} = 1\Big/12[7(\overline{\Phi_i} + \overline{\Phi_{i+1}}) - \overline{\Phi_{i-1}} - \overline{\Phi_{i+2}}] \tag{D.1}$$

$$\Phi^{*,C}_{i+1/2} = [\rho^*]^{C}_{i+1/2} = 1\Big/2\Big(\Phi^*_{I-1/2} + \Phi^*_{I+1/2}\Big) \tag{D.2}$$

- **THINC-based reconstruction scheme**

In order to compute the flux across the cell interface between cells 2 and 3, we reconstruct left and right hand side values of the scalar ξ_{Gas} as the equations from (3-3) to (3-4) shown in 3.3. It's also noted that discontinuous two-phase interface region generally meet the requirements $\varepsilon < \overline{\xi}_i < 1 - \varepsilon$ and $(\overline{\xi}_i - \overline{\xi}_{i-1})(\overline{\xi}_{i+1} - \overline{\xi}_i) > 0$, where ε could be a small positive parameter comparing with $\overline{\xi}_i$.

- **Modified sensor**

This newly modified discontinuity sensor is used to identify the discontinues region. The flow field smoothness is identified via a function of smooth sensor, which works as a switch to change the type of the reconstruction method for the primitive variables u, v, w, ρ, p, ξ_{Gas1}, ξ_{Gas2} on the cell interface. The primitive variables on the cell interface denote:

$$\Phi^*_{i+1/2} = [1 - f(\theta)]\Phi^{smooth} + f(\theta)\Phi^{discontinues} = [1 - f(\theta)]\Phi^{*,C}_{i+1/2} + f(\theta)\left(\left(1 - \sigma\right)\Phi^{*,U}_{i+1/2} + \sigma\Phi^{*,Th}_{i+1/2}\right) \tag{D.3}$$

σ is a Dirichlet function, which could be adjustable according to needed: generally for reconstruction step of pressure and velocity it becomes zero; for reconstruction step of two phase interface region, it becomes one while for other region it becomes zero.

Specifically, we use vorticity-dilation sensor developed by Ducros et al. [137] to detect the compressible shock and expansion waves in present fully compressible flow: $\theta^D = (\nabla \cdot u)^2 / ((\nabla \cdot u)^2 + (\nabla \times u)^2 + \epsilon)$, where, ϵ denotes a very small value ($\epsilon = 10^{-20}$), making denominator non-zero.

Two-phase interface are detected with the variation of the total gas volume fraction in all three spatial directions: $\theta^{Gas} = var_i(Gas) + var_j(Gas) + var_k(Gas)$, where, $var_i(Gas) = \| \alpha_{Gas1,\,i} + \alpha_{Gas2,\,i} - (\alpha_{Gas1,\,i-1} + \alpha_{Gas2,\,i-1})\| + \| \alpha_{Gas1,\,i+1} + \alpha_{Gas2,\,i+1} - (\alpha_{Gas1,\,i} + \alpha_{Gas2,\,i})\|$. Same expressions are adopted for vapor volume fraction and its detector is denoted as θ^α.

Subsequently, we give the switch criteria:

$$f\left(\theta^D, \theta^\alpha, \theta^{Gas}\right) = \begin{cases} 1, \ if \ \theta^D > \theta^D_{th} \ || \ \theta^\alpha \rangle \theta^\alpha_{th} \ || \ \theta^{Gas} \rangle \theta^{Gas}_{th} \\ 0, \ others \end{cases} \tag{D.4}$$

It means that if one or more sensor exceeds its threshold value ($\theta^D > \theta^D_{th}$ or/and $\theta^\alpha > \theta^\alpha_{th}$ or/and $\theta^{Gas} > \theta^{Gas}_{th}$), the numerical scheme switches to the discontinues reconstructions $\Phi^*_{i+1/2} = \Phi^{discontinues} = (1 - \sigma)\Phi^{*,U}_{i+1/2} + \sigma\Phi^{*,Th}_{i+1/2}$. The threshold values $\theta^D_{th} = 0.95$ is suggested by Egerer et al. [24] and $\theta^{Gas}_{th} = 0.4$ is for the volume fraction of total gas phase suggested by Trummler et al. [23]. And these proposed modifications could help to avoid pressure oscillations while keeping contact waves crisp without artificial smearing.

Specifically, for smooth region, velocity and pressure adopt the linear 4th order reconstruction process, while a linear 2nd order central approximation reconstruction is implemented for the density, internal energy(if have), as well as two additional mass fraction field. For discontinues fields, a upwind biased reconstruction is generally implemented $\Phi^{discontinues} = \Phi^{*,U}_{i+1/2}$. Generally, velocity components are reconstructed using the third order slope limiter Koren [119] and the thermodynamic quantities density, pressure, internal energy(if have), two additional mass fraction are reconstructed using the second order Minmod slope limiter [116]. It should be noted that the new mass fraction ξ generally keep the same reconstruction scheme of density, $\xi^{discontinues} = \xi^{*,U}_{i+1/2}$. While in the discontinuous region of two phase interface, instead of using upwind biased reconstruction with slop limiter for two additional mass fraction(or density), THINC is combined for mass fraction(or density) $\xi^{discontinues} = (1 - \sigma)\xi^{*,U}_{i+1/2} + \sigma\xi^{*,Th}_{i+1/2}$, and TDU idea is then adopted for density(or mass fraction) $\rho^{discontinues} = f(\xi^{discontinues}, p^{discontinues})$. In this way, variables are updated consistently, interface is sharpened and pressure oscillation is avoided.

Besides, the transport velocity and interface pressure are represented as

$$u^* = (1 - f(\theta))\left(u^{*,C}_{i+1/2} - \frac{\Delta^3 p^*_{i+1/2}}{I_L + I_R}\right) + f(\theta)\frac{I_L u_L + I_R u_R + p_L - p_R}{I_L + I_R} \tag{D.5}$$

$$p^* = (1 - f(\theta))p^{*,C}_{i+1/2} + f(\theta)\left(\frac{p_L + p_R}{2}\right) \tag{D.6}$$

$I_L = ((3\overline{\rho_i} + \overline{\rho_{i+1}}) * max(c_{l,i}, c_{l,i+1}))/4$, $I_R = ((\overline{\rho_i} + 3\overline{\rho_{i+1}}) * max(c_{l,i}, c_{l,i+1}))/4$, $\Delta^3 p^*_{i+1/2}$ is an approximation of the third pressure derivative, the acoustic impedances are I_L and I_R, $max(c_{l,i}, c_{l,i+1})$ is the maximum liquid speed of sound.

Other procedures (Remarks) are consistent with Ch:arpter3. Through complete implementation, liquid-liquid vapor and liquid-gas two phase interface are sharpened and disspasion of discontinues region are reduced.

References

[1] Chern I-L, Glimm J, Mcbryan O, Plohr B, Yaniv S. Front tracking for gas dynamics. J Comput Phys 1986;62(1):83–110.

[2] Tryggvason G, Scardovelli R, Zaleski S. Direct numerical simulations of gas-liquid multiphase flows. Cambridge University Press; 2011.

[3] Osher S, Sethian JA. Fronts propagating with curvature-dependent speed: algorithms based on hamilton-jacobi formulations. J Comput Phys 1988;79(1): 12–49.

[4] Sussman M, Smereka P, Osher S. A level set approach for computing solutions to incompressible two-phase flow. J Comput Phys 1994;114(1):146–59.

[5] Sethian JA, Smereka P. Level set methods for fluid interfaces. Annu Rev Fluid Mech 2003;35(1):341–72.

[6] Hirt CW, Nichols BD. Volume of fluid (VOF) method for the dynamics of free boundaries. J Comput Phys 1981;39(1):201–25.

[7] Ubbink O, Issa RI. A method for capturing sharp fluid interfaces on arbitrary meshes. J Comput Phys 1999;153(1):26–50.

[8] Youngs DL. Time-dependent multi-material flow with large fluid distortion. Numerical methods for fluid dynamics. New York: Americal Press; 1982.

[9] Roenby J, Bredmose H, Jasak H. A computational method for sharp interface advection. R Soc Open Sci 2016;3(11):160405.

[10] Nadiga BT, Zaleski S. Investigations of a two-phase fluid model. Eur J Mech B Fluids 1996;15:885–96.

[11] Chella R, Viñals J. Mixing of a two-phase fluid by cavity flow. Phys Rev E 1996;53 (4):3832.

[12] Jacqmin D. Calculation of two-phase Navier-Stokes flows using phase-field modeling. J Comput Phys 1999;155(1):96–127.

[13] Kim JS. A continuous surface tension force formulation for diffuse-interface models. J Comput Phys 2004;204(2):784–804.

[14] Jain SS, Mani A. Parviz Moin. A conservative diffuse-interface method for compressible two-phase flows. J Comput Phys 2020;418:109606.

[15] Abgrall R. How to prevent pressure oscillations in multicomponent flow calculations: a quasi conservative approach. J Comput Phys 1996;125(1):150–60.

[16] Abgrall R, Karni S. Computations of compressible multifluids. J Comput Phys 2001;169(2):594–623.

[17] Allaire G, Clerc S, Kokh S. A five-equation model for the simulation of interfaces between compressible fluids. J Comput Phys 2002;181(2):577–616.

[18] Marquina A, Mulet P. A flux-split algorithm applied to conservative models for multicomponent compressible flows. J Comput Phys 2003;185(1):120–38.

[19] Diegelmann F, Hickel S, Adams NA. Shock Mach number influence on reaction wave types and mixing in reactive shock-bubble interaction. Combust Flame 2016;174:85–99.

[20] Matheis J, Hickel S. Multi-component vapor-liquid equilibrium model for LES of high-pressure fuel injection and application to ECN Spray A. Int J Multiph Flow 2018;99:294–311.

[21] Egerer CP, Hickel S, Schmidt SJ, Adams NA. Large-eddy simulation of turbulent cavitating flow in a micro channel. Phys Fluids 2016;26(8).

[22] Örley F, Trummler T, Hickel S, Mihatsch MS, Schmidt SJ, Adams NA. Large-eddy simulation of cavitating nozzle flow and primary jet break-up. Phys. Fluids 2015; 27(8).

[23] Trummler T, Rahn D, Schmidt SJ, Adams NA. Large eddy simulations of cavitating flow in a step nozzle with injection into gas. At Sprays 2018;28(10).

[24] Egerer CP, Schmidt SJ, Hickel S, Adams NA. Efficient implicit LES method for the simulation of turbulent cavitating flows. J Comput Phys 2016;316:453–69.

[25] Das P, Udaykumar HS. A sharp-interface method for the simulation of shock-induced vaporization of droplets. J Comput Phys 2020;405:109005.

[26] Koukouvinis P, Vidal-Roncero A, Rodriguez C, Gavaises M, Pickett L. High pressure/high temperature multiphase simulations of dodecane injection to nitrogen: Application on ECN Spray-A. Fuel 2020;275:117871.

[27] Allaire G, Clerc S, Kokh S. A five-equation model for the simulation of interfaces between compressible fluids. J Comput Phys 2002;181(2):577–616.

[28] Kapila AK, Menikoff R, Bdzil JB, Son SF, Stewart DS. Two-phase modeling of the deflagration-to-detonation transition in granular materials: Reduced Equations. Phys Fluids 2001;13(10):3002–24.

[29] Maltsev V, Skote M, Tsoutsanis P. High-order methods for diffuse-interface models in compressible multi-medium flows: a review. Phys Fluids 2022;34(2).

[30] Saurel R, Pantano C. Diffuse-interface capturing methods for compressible two-phase flows. Annu Rev Fluid Mech 2018;50:105–30.

[31] Shyue KM. An efficient shock-capturing algorithm for compressible multicomponent problems. J Comput Phys 1998;142(1):208–42.

[32] Johnsen E, Ham F. Preventing numerical errors generated by interface capturing schemes in compressible multi-material flows. J Comput Phys 2012;231(17): 5705–17.

[33] Johnsen E. Spurious oscillations and conservation errors in interface-capturing schemes. Annual Research Briefs 2008. Center for Turbulence Research, NASA Ames and Stanford University; 2008. p. 115–26.

[34] Bauer M, Nunziato J. A two-phase mixture Theory for the deflagration-to-detonation Transition (DDT) in reactive granular materials. Int J Multiph Flow 1986;12(6):861–89.

[35] Saurel R, Abgrall R. A multiphase Godunov method for compressible multifluid and multiphase flows. J Comput Phys 1999;150(2):425–67.

[36] Andrianov N, Warnecke G. The Riemann problem for the Baer-Nunziato two-phase flow model. J Comput Phys 2004;195(2):434–64.

[37] Tokareva S, Toro EF. HLLC-type Riemann solver for the Baer-Nunziato equations of compressible two-phase flow. J Comput Phys 2010;229(10):3573–604.

[38] Bdzil JB, Menikoff R, Son SF, Kapila AK, Stewart DS. Two-phase nodeling of deflagration-to-detonation transition in Granular materials: a critical examination of modeling issues. Phys. Fluids 1999;11(2):378–402.

[39] Saurel R, Petitpas F, Berry RA. Simple and efficient relaxation methods for interfaces separating compressible fluids, Cavitating Flows, and Shocks in Multiphase Mixtures. J Comput Phys 2009;228(5):1678–712.

[40] Boris JP, Book DL. Flux-corrected transport. I. SHASTA, A fluid transport algorithm that works. J Comput Phys 1973;11(1):38–69.

[41] Zalesak ST. Fully multidimensional flux-corrected transport algorithms for fluids. J Comput Phys 1979;31(3):335–62.

[42] Rudman M. Volume-tracking methods for interfacial flow calculations. Int J Numer Methods Fluids 1997;24(7):671–91.

[43] So KK, Hu XY, Adams NA. Anti-diffusion method for interface steepening in two-phase incompressible flow. J Comput Phys 2011;230(13):5155–77.

[44] So KK, Hu XY, Adams NA. Anti-diffusion interface sharpening technique for two-phase compressible flow simulations. J Comput Phys 2012;231(11):4304–23.

[45] Xiao F, Honma Y, Kono T. A simple algebraic interface capturing scheme using hyperbolic tangent function. Int J Numer Methods Fluids 2005;48(9):1023–40.

[46] Xie B, Jin P, Xiao F. An unstructured-grid numerical model for interfacial multiphase fluids based on multi-moment finite volume formulation and THINC method. Int J Multiph Flow 2017;89:375–98.

[47] Deng X, Inaba S, Xie B, Shyue K-M, Xiao F. High fidelity discontinuity-resolving reconstruction for compressible multiphase flows with moving interfaces. J Comput Phys 2018;371:945–66.

[48] Weller HG. A New Approach to VOF-based Interface capturing methods for incompressible and compressible flow. Technical Report OpenCFD 2008.

[49] Shukla RK, Pantano C, Freund JB. An interface capturing method for the simulation of multi-phase compressible flows. J Comput Phys 2010;229(19): 7411–39.

[50] Okagaki Y, Yonomoto T, Ishigaki M, Hirose Y. Numerical study on an interface compression method for the volume of fluid approach. Fluids 2021;6(2):80.

[51] Rusche H. Computational fluid dynamics of dispersed two-phase flows at high phase fractions. Imperial College London; 2002. Ph.D. thesis.

[52] Sokolichin A, Eigenberger G, Lapin A, Lübert A. Dynamic numerical simulation of gas-liquid two-phase flows Euler/Euler versus Euler/Lagrange. Chem Eng Sci 1997;52(4):611–26.

[53] Olsson E, Kreiss G. A conservative level set method for two phase flow. J Comput Phys 2005;210(1):225–46.

[54] Castro CE, Toro EF. A Riemann solver and upwind methods for a two-phase flow model in non-conservative form. Int J Numer Methods Fluids 2006;50(3): 275–307.

[55] Shu CW, Zang TA, Erlebacher G, Whitaker D, Osher S. High-order ENO schemes applied to two-and three-dimensional compressible flow. Appl Numer Math 1992; 9(1):45–71.

[56] Johnsen E, Colonius T. Implementation of WENO schemes in compressible multicomponent flow problems. J Comput Phys 2006;219(2):715–32.

[57] Wang B, Xiang G, Hu XY. An incremental-stencil WENO reconstruction for simulation of compressible two-phase flows. Int J Multiph Flow 2018;104:20–31.

[58] Deshpande SS, Anumolu L, Trujillo MF. Evaluating the performance of the two-phase flow solver interFoam. Comput Sci Discov 2012;5(1):014016.

[59] Van Leer B. Towards the ultimate conservative difference scheme, V. a second order sequel to Godunov's method. J Comput Phys 1979;32(1):101–36.

[60] Muzaferija S, Peric M, Sames P, Schellin T. A two-fluid Navier-Stokes solver to simulate water entry. In: Proceedings of the 22nd symposium on naval hydrodynamics. Washington, DC: National Academies Press; 1998.

[61] Liu X-D, Osher S, Chan T. Weighted essentially non-oscillatory schemes. J Comput Phys 1994;115(1):200–12.

[62] Jiang G-S, Shu C-W. Efficient implementation of weighted ENO schemes. J Comput Phys 1996;126(1):202–28.

[63] Sun Z, Inaba S, Xiao F. Boundary variation diminishing (BVD) reconstruction: a new approach to improve Godunov schemes. J Comput Phys 2016;322:309–25.

[64] Deng X, Shimizu Y, Xiao F. A fifth-order shock capturing scheme with two-stage boundary variation diminishing algorithm. J Comput Phys 2019;386:323–49.

[65] Deng X, Shimizu Y, Xie B, Xiao F. Constructing higher order discontinuity-capturing schemes with upwind-biased interpolations and boundary variation diminishing algorithm. Comput Fluids 2020;200:104433.

[66] Deng X, Jiang Z-H, Xiao F, Yan C. Implicit large eddy simulation of compressible turbulence flow with PnTm-BVD scheme. Appl Math Model 2020;77:17–31.

[67] Cassidy DA, Edwards JR, Tian M. An investigation of interface-sharpening schemes for multi-phase mixture flows. J Comput Phys 2009;228(16):5628–49.

[68] Majidi S, Afshari A. Supersonic liquid jets into quiescent gaseous media: an adaptive numerical study. J Fluids Eng 2016;138(1):011103.

[69] Garrick DP, Hagen WA, Regele JD. An interface capturing scheme for modeling atomization in compressible Flows. J Comput Phys 2017;344:260–80.

[70] Nonomura T, Kitamura K, Fujii K. A simple interface sharpening technique with a hyperbolic tangent function applied to compressible two-fluid modeling. J Comput Phys 2014;258:95–117.

[71] Shyue KM, Xiao F. An Eulerian interface sharpening algorithm for compressible two-phase flow: the algebraic THINC approach. J Comput Phys 2014;268: 326–54.

[72] Chen D, Tong X, Xie B, Xiao F. Ye Li. An accurate and efficient multiphase solver based on THINC scheme and adaptive mesh refinement. Int J Multiph Flow 2023; 162:104409.

[73] Hoppe N, Winter JM, Adami S, Adams NA. ALPACA-a level-set based sharp-interface multiresolution solver for conservation laws. Comput Phys Commun 2022;272:108246.

[74] Hoppe N, Adami S, Adams NA. A parallel modular computing environment for three-dimensional multiresolution simulations of compressible flows. Comput Methods Appl Mech Eng 2022;391:114486.

[75] Qian L, Wei Y, Xiao F. Coupled THINC and Level Set method: a conservative interface capturing scheme with arbitrary-order surface representations. J Comput Phys 2018;373:284–303.

[76] Kumar R, Cheng L, Xiong Y, Xie B, Abgrall R, Xiao F. THINC scaling method that bridges VOF and level set schemes. J Comput Phys 2021;436:110323.

[77] Larouturou B. How to preserve the mass fraction positive when computing compressible multi-component flows. J Comput Phys 1991;95(1):59–84.

[78] Deng X, Boivin P. Diffuse interface modelling of reactive multi-phase flows applied to a sub-critical cryogenic jet. J Comput Phys 2020;84:405–24.

[79] Brackbill JU, Kothe DB, Zemach C. A continuum method for modeling surface tension. J Comput Phys 1992;100(2):335–54.

[80] Fedkiw RP, Aslam T, Merriman B, Osher S. A non-oscillatory Eulerian approach to interfaces in multimaterial flows (the ghost fluid method). J Comput Phys 1999; 152(2):457–92.

[81] Kang M, Fedkiw RP, Liu XD. A boundary condition capturing method for multiphase incompressible flow. J Sci Comput 2000;15:323–60.

[82] Sussman M. A second order coupled level set and volume of-fluid method for computing growth and collapse of vapor bubbles. J Comput Phys 2003;187(1): 110–36.

[83] Cummins SJ, Francois MM, Kothe DB. Estimating curvature from volume fractions. Comput Struct 2005;83(6-7):425–34.

[84] Afkhami S, Bussmann M. Height functions for applying contact angles to 3D VOF simulations. Int J Numer Methods Fluids 2009;57(4):453–72.

[85] Raeini AQ, Blunt MJ, Bijeljic B. Modelling two-phase flow in porous media at the pore scale using the volume-of-fluid method. J Comput Phys 2012;231(17): 5653–68.

[86] Garrick DP, Owkes M, Regele JD. A finite-volume HLLC-based scheme for compressible interfacial flows with surface tension. J Comput Phys 2017;339: 46–67.

[87] Lafaurie B, Nardone C, Scardovelli R, Zaleski S, Zanetti G. Modelling merging and fragmentation in multiphase flows with SURFER. J Comput Phys 1994;113(1):134–47.

[88] Gueyffier D, Li J, Nadim A, Scardovelli R, Zaleski S. Volume-of-fluid interface tracking with smoothed surface stress methods for three-dimensional flows. J Comput Phys 1999;152(2):423–56.

[89] Francois MM, Cummins SJ, Dendy ED, Kothe DB, Sicilian JM, Williams MW. A balanced force algorithm for continuous and sharp interfacial surface tension models within a volume tracking framework. J Comput Phys 2006;213(1):141–73.

[90] Perigaud G, Saurel R. A compressible flow model with capillary effects. J Comput Phys 2005;209(1):139–78.

[91] Renardy Y, Renardy M. PROST: a parabolic reconstruction of surface tension for the volume-of-fluid method. J Comput Phys 2002;183(2):400–21.

[92] Jibben Z, Velechovsky J, Masser T, Francois MM. Modeling surface tension in compressible flow on an adaptively refined mesh. Comput Math Appl 2019;78(2):504–16.

[93] Adams NA, Hickel S, Franz S. Implicit subgrid-scale modeling by adaptive deconvolution. J Comput Phys 2004;200(2):412–31.

[94] Hickel S, Adams NA, Domaradzki JA. An adaptive local deconvolution method for implicit LES. J Comput Phys 2006;213(1):413–36.

[95] Hickel S, Egerer CP, Larsson J. Subgrid-scale modeling for implicit large eddy simulation of compressible flows and shock-turbulence interaction. Phys. Fluids 2014;26(10).

[96] edited by Hickel S, Larsson J. On implicit turbulence modeling for LES of compressible Flows. In: Eckhardt B, editor. Advances in Turbulence XII. Berlin: Springer; 2009. edited by.

[97] Hickel S, Adams NA, Mansour NN. Implicit subgrid-scale modeling for large-eddy simulation of passive-scalar mixing. Phys. Fluids 2007;19(9).

[98] Hickel S, Adams NA. On implicit subgrid-scale modeling in wall-bounded flows. Phys. Fluids 2007;19(10).

[99] Örley F, Hickel S, Schmidt SJ, Adams NA. Large-eddy simulation of turbulent, cavitating fuel flow Inside a 9-hole diesel injector including needle movement. Int. J. Engine Res. 2017;18(3):195–211.

[100] Trummler T, Schmidt SJ, Adams NA. Investigation of condensation shocks and re-entrant jet dynamics in a cavitating nozzle flow by large-eddy simulation. Int J Multiph Flow 2020;125:103215.

[101] Zhao F, Pan L, Li Z, Wang S. A new class of high-order weighted essentially non-oscillatory schemes for hyperbolic conservation laws. Comput Fluids 2017;159:81–94.

[102] Zhao F, Ji X, Shyy W, Xu K. Compact higher-order gas-kinetic schemes with spectral-like resolution for compressible flow simulations. Adv Aerodyn 2019;1(1):13.

[103] Deng X. A unified framework for non-linear reconstruction schemes in a compact stencil. part 1: beyond second order. J Comput Phys 2023:112052.

[104] Schmidt S, Sezal I, Schnerr G, Talhamer M. Riemann techniques for the simulation of compressible liquid flows with phase-transition at all Mach numbers - shock and wave dynamics in cavitating 3-D micro and macro Systems. In: 46th AIAA Aerospace Sciences Meeting and Exhibit; 2008.

[105] Yokoi K. Efficient implementation of THINC scheme: a simple and practical smoothed VOF algorithm. J Comput Phys 2007;226(2):1985–2002.

[106] Xiao F, Ii S, Chen C. Revisit to the THINC scheme: a simple algebraic VOF algorithm. J Comput Phys 2011;230(19):7086–92.

[107] Ii S, Sugiyama K, Takeuchi S, Takagi S, Matsumoto Y, Xiao F. An interface capturing method with a continuous function: the THINC method with multi-dimensional reconstruction. J Comput Phys 2012;231(5):2328–58.

[108] Xie B, Ii S, Xiao F. An efficient and accurate algebraic interface capturing method for unstructured grids in 2 and 3 dimensions: the THINC method with quadratic surface representation. Int. J. Numer. Meth. Fluids 2014;76(12):1025–42.

[109] Xie B, Jin P, Xiao F. An unstructured-grid numerical Model for interfacial multiphase fluids based on multi-moment finite volume formulation and THINC method. Int J Multiph Flow 2017;89:375–98.

[110] Xie B, Xiao F. Toward efficient and accurate interface capturing on arbitrary hybrid unstructured grids: the THINC method with quadratic surface representation and gaussian quadrature. J Comput Phys 2017;349:415–40.

[111] Métayer OL, Massoni J, Saurel R. Elaborating equations of state of a liquid and its vapor for two-phase flow models. Int J Therm Sci 2004:43.

[112] Métayer OL, Saurel R. The Noble-Abel Stiffened-Gas equation of state. Phys Fluids 2016;28(4).

[113] Chiapolino A, Boivin P, Saurel R. A simple and fast-phase transition relaxation solver for compressible Multicomponent Two-Phase Flows. Comput Fluids 2017;150:31–45.

[114] Van Albada GD, Van Leer B, Roberts WW. A comparative study of computational methods in cosmic gas dynamics. Astron Astrophys 1982;108:76–84.

[115] Van Leer B. Towards the ultimate conservative difference scheme II. monotonicity and conservation combined in a second order scheme. J Comput Phys 1974;14(4):361–70.

[116] Roe PL. Characteristic-based schemes for the Euler equations. Annu Rev Fluid Mech 1986;18(1):337–65.

[117] Chakravarthy S, Osher S. High resolution applications of the Osher upwind scheme for the Euler equations. In: 6th Computational Fluid Dynamics Conference Danvers; 1983.

[118] Van Leer B. Towards the ultimate conservative difference scheme III. upstream-centered finite-difference schemes for ideal compressible Flow. J Comput Phys 1977;23(3):263–75.

[119] B. Koren. A robust upwind discretization method for advection, diffusion, and source terms. Numerical Methods for Advection-Diffusion Problems, Vieweg, Braunschweig, Germany, 1993; 45: 117-138.

[120] Quirk S, Karni S. On the dynamics of a shock-bubble interaction. J Fluid Mech 1996;318:129–63.

[121] Fedkiw RP, Aslam T, Merriman B, Osher S. A non-oscillatory Eulerian approach to interfaces in multimaterial flows (the ghost fluid method). J Comput Phys 1999;152(2):457–92.

[122] Hysing S, Turek S, Kuzmin D, Parolini N, Burman E, Ganesan S, Tobiska L. Quantitative benchmark computations of two-dimensional bubble dynamics. Int J Numer Methods Fluids 2009;60(11):1259–88.

[123] Ling K, Zhang S, Wu P-Z, Yang S-Y, Tao W-Q. A coupled volume-of-fluid and level-set method (VOSET) for capturing interface of two-phase flows in arbitrary polygon grid. Int J Heat Mass Transf 2019;143:118565.

[124] Hysing JSR, Turek S. Evaluation of commercial and academic CFD codes for a two-phase flow benchmark test case. Int J Comput Sci Eng 2015;10(4):387–94.

[125] Fyfe DE, Oran ES, Fritts MJ. Surface tension and viscosity with lagrangian hydrodynamics on a triangular mesh. J Comput Phys 1988;76(2):349–84.

[126] Jibben Z, et al. Modeling surface tension in compressible flow on an adaptively refined mesh. Comput Math Appl 2018;78(2):504–16.

[127] Shukla RK. Nonlinear preconditioning for efficient and accurate interface capturing in simulation of multicomponent Compressible Flows. J Comput Phys 2014;276:508–40.

[128] Perigaud G, Saurel R. A compressible flow model with capillary effects. J Comput Phys 2005;209(1):139–78.

[129] Schmidmayer K, Petitpas F, Daniel E, Favrie N, Gavrilyuk S. A model and numerical method for compressible flows with capillary effects. J Comput Phys 2017;334:468–96.

[130] ECN. ECN- Engine Combustion Network (Spray A&B). 2019 [Online]. Available: https://ecn.sandia.gov/diesel-spray-combustion/target-condition/spray-ab/.

[131] Trummler T, Bryngelson SH, Schmidmayer K, Schmidt SJ, Colonius T, Adams NA. Near-surface dynamics of a gas bubble collapsing above a crevice. J. Fluid Mech. 2020;899:A16.

[132] Peng D-Y, Robinson DB. A new two-constant equation of state. Indust. Eng. Chem. Fundam. 1976;15(1):59–64.

[133] Harstad KG, Miller RS. Efficient high-pressure state equations. AIChE J 1997;43(6):1605–10.

[134] McBride BJ. Coefficients for calculating thermodynamic and transport properties of individual species. NASA Langley Research Center 1993:4513.

[135] Boyd B, Jarrahbashi D. Numerical study of the transcritical shock-droplet interaction. Phys Rev Fluids 2021;6(11):113601.

[136] Williams MW, Kothe DB, Puckett EG. Accuracy and convergence of continuum surface tension models. Fluid Dyn Interfaces 1998:294–305.

[137] Ducros F, Ferrand V, Nicoud F, Weber C, Darracq D, Gacherieu C, Poinsot T. Large eddy simulation of the shock/turbulence interaction. J Comput Phys 1999;152(2):517–49.

A.2   Paper II

Simulating shock interaction with a cavity-embedded cylinder/droplet using a real-fluid hybrid scheme at near-critical conditions

Yu Jiao, Steffen J. Schmidt, Nikolaus A. Adams

Contribution: My contribution to this research paper was to propose the concept and idea of the paper, complete the programming codes and numerical methods, perform the validations, analyse the results, and write the manuscript.

American Physical Society
Reuse and Permissions License

04-Sep-2024

This license agreement between the American Physical Society ("APS") and Yu Jiao ("You") consists of your license details and the terms and conditions provided by the American Physical Society and SciPris.

Licensed Content Information

License Number: RNP/24/SEP/083006

License date: 04-Sep-2024

DOI: 10.1103/PhysRevFluids.9.074002

Title: Simulating shock interaction with a cavity-embedded cylinder/droplet using a real-fluid hybrid scheme at near-critical conditions

Author: Yu Jiao, Steffen J. Schmidt, and Nikolaus A. Adams

Publication: Physical Review Fluids

Publisher: American Physical Society

Cost: USD $ 0.00

Request Details

Does your reuse require significant modifications: No

Specify intended distribution locations: Worldwide

Reuse Category: Reuse in a thesis/dissertation

Requestor Type: Author of requested content

Items for Reuse: Whole Article

Format for Reuse: Electronic and Print

Total number of print copies: Up to 1000

Information about New Publication:

University/Publisher: Technical University of Munich

Title of dissertation/thesis: Numerical and Physical Modeling of Compressible Multi-component Flows Including Surface Tension, Cavitation, Turbulence, and Real-Fluid Effects

Author(s): Yu Jiao

Expected completion date: Jan. 2025

License Requestor Information

Name: Yu Jiao

Affiliation: Individual

Email Id: yu.jiao@tum.de

Country: Germany

American Physical Society
Reuse and Permissions License

TERMS AND CONDITIONS

The American Physical Society (APS) is pleased to grant the Requestor of this license a non-exclusive, non-transferable permission, limited to Electronic and Print format, provided all criteria outlined below are followed.

1. You must also obtain permission from at least one of the lead authors for each separate work, if you haven't done so already. The author's name and affiliation can be found on the first page of the published Article.

2. For electronic format permissions, Requestor agrees to provide a hyperlink from the reprinted APS material using the source material's DOI on the web page where the work appears. The hyperlink should use the standard DOI resolution URL, http://dx.doi.org/{DOI}. The hyperlink may be embedded in the copyright credit line.

3. For print format permissions, Requestor agrees to print the required copyright credit line on the first page where the material appears: "Reprinted (abstract/excerpt/figure) with permission from [(FULL REFERENCE CITATION) as follows: Author's Names, APS Journal Title, Volume Number, Page Number and Year of Publication.] Copyright (YEAR) by the American Physical Society."

4. Permission granted in this license is for a one-time use and does not include permission for any future editions, updates, databases, formats or other matters. Permission must be sought for any additional use.

5. Use of the material does not and must not imply any endorsement by APS.

6. APS does not imply, purport or intend to grant permission to reuse materials to which it does not hold copyright. It is the requestor's sole responsibility to ensure the licensed material is original to APS and does not contain the copyright of another entity, and that the copyright notice of the figure, photograph, cover or table does not indicate it was reprinted by APS with permission from another source.

7. The permission granted herein is personal to the Requestor for the use specified and is not transferable or assignable without express written permission of APS. This license may not be amended except in writing by APS.

8. You may not alter, edit or modify the material in any manner.

9. You may translate the materials only when translation rights have been granted.

10. APS is not responsible for any errors or omissions due to translation.

11. You may not use the material for promotional, sales, advertising or marketing purposes.

12. The foregoing license shall not take effect unless and until APS or its agent, Aptara, receives payment in full in accordance with Aptara Billing and Payment Terms and Conditions, which are incorporated herein by reference.

13. Should the terms of this license be violated at any time, APS or Aptara may revoke the license with no refund to you and seek relief to the fullest extent of the laws of the USA. Official written notice will be made using the contact information provided with the permission request. Failure to receive such notice will not nullify revocation of the permission.

14. APS reserves all rights not specifically granted herein.

15. This document, including the Aptara Billing and Payment Terms and Conditions, shall be the entire agreement between the parties relating to the subject matter hereof.

Simulating shock interaction with a cavity-embedded cylinder/droplet using a real-fluid hybrid scheme at near-critical conditions

Yu Jiao [1,*] Steffen J. Schmidt [1] and Nikolaus A. Adams [1,2]

[1] *Chair of Aerodynamics and Fluid Mechanics, TUM School of Engineering and Design,*
Technical University of Munich, 85748 Garching bei München, Germany
[2] *Munich Institute of Integrated Materials, Energy and Process Engineering (MEP),*
Technical University of Munich, 85748 Garching bei München, Germany

Examining the influence of shock waves on cylinders and droplets at near-critical conditions, especially when accounting for real fluid effects, represents a relatively unexplored frontier. This research gap becomes even more relevant when extending the investigation to three-dimensional scenarios. The underlying evolution mechanisms at these conditions remain elusive, with limited existing literature. In this study, we present a thorough exploration employing two-dimensional and three-dimensional numerical simulations of a droplet with an embedded gas cavity subjected to a normal shock wave at near-critical conditions. Our approach involves modeling the cylinder/droplet and the surrounding gas flow using the compressible multicomponent equations, incorporating real fluid thermodynamic relationships, and implementing a finite-volume-based hybrid numerical framework capable of capturing shocks and interfaces. To establish the reliability of our approach, we validate it against reference data, demonstrating excellent agreement. We also conduct mesh independence studies, both qualitatively and quantitatively. Our analysis is comprehensive, considering the intricacies of shock impingement, the morphological deformation of the cylinder/droplet and cavity, and the development of vortices. We discuss and analyze various phenomena, including the evolution of wave patterns, jet formation, sheet formation, hole appearance, the emergence of petal-shaped structures or lobes, ligament formation, shear-induced entrainment, and internal cavity (bubble) breakup. We compare the results obtained from the cylinder/droplet with a cavity to those from a planar shock wave impacting a pure cylinder/droplet. We provide a holistic view of the two-dimensional cylinder and three-dimensional droplet's evolution before and after the impact of a shock wave, accompanied by quantitative data regarding the positions of characteristic points along the column over time. Our analysis further scrutinizes the geometrical characteristics of the cylinder and the trends in the distribution of baroclinic vorticity at various stages. Our findings reveal that the presence of a gas cavity plays a pivotal role in shaping the shock wave, which, in turn, influences the generation and distribution of baroclinic vorticity. This leads to a transformation in the unstable evolution process of both the cylinder and the droplet. Importantly, shock waves impacting the evolving interfaces of the cylinder/droplet and the internal gas cavity generate baroclinic vorticity, which subsequently affects the transport and distribution of vorticity, thereby influencing the evolution of the cylinder/droplet interface. In the case of three-dimensional droplets, baroclinic vorticity induces complex, intricate three-dimensional structure transformations.

---

*Contact author: yu.jiao@tum.de

I. INTRODUCTION

The Richtmyer-Meshkov instability (RMI) manifests when an interface separating two fluids of different densities is suddenly subjected to impacting shock waves. This instability undergoes a linear growth phase followed by nonlinear development, culminating in the formation of numerous small-scale vortices near the interface and ultimately leading to a turbulent mixture [1–4]. This intriguing phenomenon has been studied both theoretically by Richtmyer [5] and experimentally by Meshkov [6], with their contributions laying the foundation for our understanding of shock-induced instabilities.

The implications of RMI extend to various fields, including inertial confinement fusion, space rocket engines, and astrophysics. For space rocket engines, the interaction between shock waves and the fuel-oxidizer interface within the combustion chamber plays a pivotal role in enhancing fuel and oxidizer mixing, thereby reducing combustion distances and engine volumes. This, in turn, significantly improves combustion efficiency and propulsion performance. Shock-droplet interactions are particularly relevant in high-speed propulsion systems [7,8], such as liquid-fueled ramjets and scramjets, especially during processes like startup, mixing, and combustion of high-speed liquid diesel injection. When a high-speed diesel jet enters a combustion chamber where the pressure is near the critical pressure of the fuel droplet, it can induce shock waves that interact with the fuel spray. Hence, exploring RMI and shock-droplet interactions offers valuable insights for optimizing fuel mixing in propulsion systems.

In cases near the critical point, it is essential to consider "transcritical" characteristics, where the combustion chamber pressure approaches the critical pressure of the fuel fluids. Under such conditions, higher temperatures can induce a transition from a liquidlike state to a gaslike behavior, leading to a two-phase mixture [9,10]. For instance, the critical properties of n-dodecane are defined by a critical pressure (p_c) of 1.82 MPa and a critical temperature (T_c) of 658.1 K. If n-dodecane fuel is injected into a combustion chamber at supercritical pressure ($p/p_c > 1$) and at a temperature below the critical temperature ($T/T_c < 1$), it mixes with hot ambient air or nitrogen, and the temperature of the fuel increases. This can cause the fuel to cross the Nishikawa-Widom line, transforming from a liquidlike fluid to a gaslike supercritical fluid. This unique scenario [11–13], known as "pseudo-boiling," occurs at higher supercritical temperatures and pressures, where fuel fluids exhibit ideal gas behavior when their compressibility factor equals 1.

While many studies have explored near-critical droplets in low-speed convective environments, where droplet evaporation is significantly influenced by viscous effects and heat conduction [14–20], investigations of near-critical droplet interaction with shock waves or high-speed flows are limited. In such high-speed flows, the impact of viscous diffusion, thermal diffusion, and surface tension forces is expected to be negligible. Obtaining detailed experimental data on multiphase shock-driven instabilities, particularly at high pressures and temperatures, remains a challenge. Therefore, numerical experiments have become essential for studying the interaction between shock waves and fuel droplets at near-critical conditions.

In summary, the study of RMI and shock-droplet interactions at near-critical conditions is of great importance and presents various challenges due to the scarcity of experimental data. By conducting numerical experiments, we aim to fill this knowledge gap and contribute to our understanding of fuel mixing processes in high-pressure, high-speed propulsion systems.

Classical simulations of shock-bubble interactions (SBIs) [21–32] and shock-droplet interactions (SDIs) [33–40] have been extensively documented, primarily focusing on scenarios involving pure droplets or pure bubbles. However, these studies have predominantly explored subcritical and supercritical conditions, with limited investigation into near-critical or transcritical conditions. Fluids near their critical points exhibit distinct physical characteristics that differ significantly from classical liquid droplets or ideal-gas bubbles [41–43], necessitating a unique approach.

In SBI-related research, Haas and Sturtevant [21] originally described the intricate phenomena during shock interactions with helium and R22 refrigerant bubbles. Quirk and Karni [22] conducted numerical simulations to characterize SBIs. Bubble compositions of SF_6 and krypton were

subsequently studied [23–31]. However, these investigations were conducted under atmospheric pressure and room-temperature conditions, with the fluids in their gaseous state, classifying them as SBIs.

In SDI-related studies, various processes such as primary shock impingement, droplet deformation, and droplet breakup have been extensively discussed in the literature [5,22,28,44–46]. Duke-Walker *et al.* [47] explored the effects of droplet evaporation and breakup in the context of mixing driven by shock-induced multiphase instabilities. Meng and Colonius [33] investigated the interaction of shock waves with a water droplet, with detailed structures validated against experimental data, including the chaotic flow features in the wake region caused by instability growth. Kaiser *et al.* [48] conducted numerical investigations into water droplet breakup induced by shock impingement and the resulting interface deformation. Sharma *et al.* [49] established a criterion for the transition process between a shear-induced entrainment mode and a Rayleigh-Taylor piercing mode during droplet breakup. Notably, these findings were obtained through both numerical simulations and experimental studies, yet research on near-critical or transcritical conditions [42,43] remains scarce.

Despite existing research, investigations into shock interactions with fuel droplets under near-critical or transcritical conditions remain limited [50–52]. A few studies have explored shock interactions with the *n*-dodecane droplet at near-critical conditions [51] and the shock interaction of a droplet above the critical pressure at varying temperatures around the Widom line [52]. While these studies have provided valuable insights into early droplet breakup behavior and mixing efficiency in high-pressure fuel injection, they have not delved into the detailed simulation of real three-dimensional interface deformation.

Furthermore, the interaction between shock waves and droplets containing gas- or vapor-filled cavities, as well as the interaction between shock waves and bubbles containing droplets, remains a relatively unexplored area within the context of SDIs and SBIs. Previous investigations in this field have primarily focused on scenarios characterized by low temperatures and low pressures [53–59]. In certain industrial contexts, liquid droplets may contain gas cavities, as seen in scenarios involving fuel droplet deformation in scramjet engines or fluid mixing processes [53]. Additionally, there are complexities associated with fluid structures that encapsulate volatile substances, such as perfluoropentane used in ultrasound therapy [54].

A substantial knowledge gap persists regarding the interaction between shock waves and droplets containing embedded gas cavities, particularly under near-critical conditions and in three-dimensional scenarios. Conducting experiments under these demanding conditions is challenging, necessitating robust numerical methods capable of handling intricate flow characteristics. Only a limited number of studies [55–59] have addressed this issue, and those have been conducted at low temperatures and low pressures (at ambient conditions). For example, the interaction of shock waves with droplets containing gas bubbles has been explored under ambient conditions [55], shedding light on the impact of bubble collapse on shock-droplet interactions. Wang *et al.*'s work [56] investigated the shock-accelerated gas ring, providing insights into its evolution and proposing a straightforward method for predicting circulation. Feng *et al.* [57] experimentally delved into the shock interaction with an SF_6 ring, studying the effects of the internal gas cylinder on the evolution of the SF_6 ring with various radius ratios. Liang *et al.* [58] experimentally examined the shock interaction with a water droplet containing an internal vapor cavity. In the numerical realm, Xiang and Wang [59] scrutinized the shock interaction with a water column harboring an internally positioned air cavity.

To the best of our knowledge, the interaction of a shockwave with a droplet embedded with a gas cavity under near-critical conditions has not been investigated in three-dimensional cases. The present study employs numerical simulations to investigate the interaction of a planar shock wave with a diesel cylinder/droplet, both with and without a gas cavity, under near-critical conditions. This research marks the investigation into the effects of an embedded cavity on a droplet under near-critical conditions using a hybrid scheme with a real fluid model. It takes into consideration the three-dimensional nature of the droplet, providing valuable insights for practical applications.
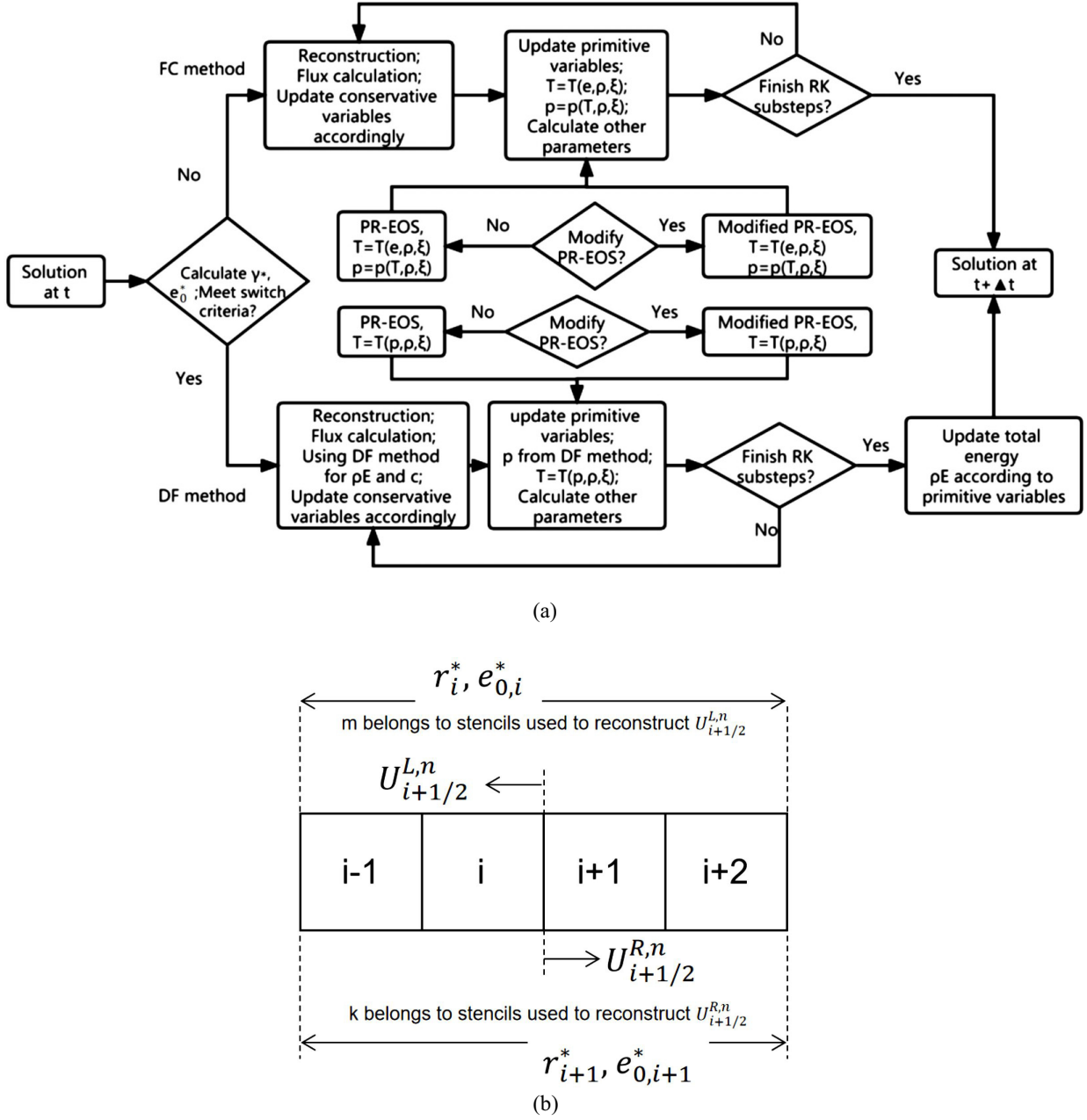
(a)

(b)

FIG. 1. (a) Flowchart of the current numerical scheme: fully conservative scheme with PR-EOS/modified PR-EOS and quasiconservative scheme (double-flux method) with PR-EOS/modified PR-EOS. (b) Schematic diagram of the double flux model with the fluxes at the cell face $i + 1/2$.

II. METHODOLOGY

A. Hybrid numerical model

In our study, we employ a hybrid numerical model that can seamlessly transition between a fully conservative (FC) scheme and a quasiconservative (QC) scheme under specific conditions. This hybrid approach significantly reduces pressure oscillations [41] and minimizes energy conservation losses [51] when a shock wave interacts with the interface, e.g., between nitrogen and n-dodecane.

The QC scheme employs either a pressure evolution (PE) equation [60–65] or the double-flux (DF) [11,66] method. In this particular study, we utilize the DF method. Figure 1(a) provides a flowchart of the model. We will elaborate on the specific details of this model in the subsequent sections. PR-EOS denotes Peng-Robinson equation of state.

The time integration is performed by an explicit, second-order-accurate low-storage four-step Runge-Kutta method with an enhanced stability region. A detailed description can be found in Refs. [67,68]. The Courant-Friedrichs-Lewy (CFL) value is generally set to 0.5 unless otherwise stated.

1. Fully conservative scheme with PR-EOS

In this section, we describe our fully conservative scheme with the Peng-Robinson equation of state (PR-EOS) for modeling the behavior of the liquid and gas components in our system.

We have extended and enhanced an existing fully compressible one-fluid model, which is an integral part of our proprietary solver, CATUM [67–70]. This model is based on the compressible Euler equations, where the vector of conserved quantities $\mathbf{q} = (\rho, \rho\mathbf{U}, \rho E, \rho\xi_i)$ is computed from $\partial \mathbf{q}/\partial t + \nabla \cdot \mathbf{F}_i(\mathbf{q}) = 0$. Here, ρ is the density, $\mathbf{F}_i(\mathbf{q})$ is the flux vector, $\mathbf{U}$ is the velocity vector, $\rho E = \rho(e + |\mathbf{U}|^2/2)$ is the total energy and e is the internal energy, and ξ_i refers to the mass fraction of component i and for in-total mass fraction of l species $\sum_{i=1}^{l} \xi_i = 1$. For two species, $\xi_1 + \xi_2 = 1$.

In our mathematical model, we neglect several factors, including gravity, heat transfer (thermal conduction), viscous effects, surface tension, and chemical reactions. These omissions are justified due to the extremely short interface interaction time in shock-droplet interaction. Gravity, heat transfer, and viscous effects may become relevant in longer-duration interactions or low-speed scenarios. Surface tension can be disregarded in transcritical flows [10,71–76] because the surface tension coefficient decreases significantly near the critical point. To simplify representation, we refer to the contiguous fuel region as "droplet."

We employ the PR-EOS [77] for both liquid and gas components, as expressed in Eq. (1):

$$p = \frac{RT}{v - b} - \frac{a}{v^2 + 2bv - b^2},\tag{1}$$

where T is the temperature, R is the universal gas constant, V is the molar volume, $V = M/\rho$, M is the molar mass, and a and b are coefficients. Detailed information on the parameters for the NASA polynomials [78] used to calculate internal energy, enthalpy, and entropy can be found in Appendix A.

In the fully conservative scheme, temperature is updated first, considering internal energy, density, and species mass fractions. This is accomplished using a gradient descent or Newton method. Notably, we can improve the convergence speed of the gradient descent or Newton method for temperature calculation by utilizing the temperature from the previous time step as an initial guess.

2. Quasiconservative scheme with PR-EOS

In this section, we discuss the quasiconservative scheme utilizing the PR-EOS and the DF method [11,66,79] to model near-critical flows. Quasiconservative schemes, such as the DF method, have been developed in recent years and are well suited for addressing the challenges posed by near-critical flow scenarios.

The DF method [11,66,79] was initially proposed by Abgrall and Karni [66] for multicomponent ideal-gas flows and later extended by Billet and Abgrall [79] for ideal-gas reacting flow systems. Subsequently, high-order schemes based on the DF method have been developed [11,80,81]. In our work, we integrate the double-flux-based model of Ma *et al.* [11,82] to handle the current near-critical flows. It is worth noting that the numerical analysis, processing, and discussion are applicable to both the PE [62,83] and DF methods. These two methods exhibit similar performance and conservation behavior in transcritical flows and are comparable to each other in handling contact interface problems [82].

The double-flux model is employed when specific parameters that exceed certain recommended values, as defined in Eqs. (2) and (3), are met:

$$\Delta\Gamma_{i,\max}^* = \max(|\Gamma_{i+1}^* - \Gamma_i^*|, |\Gamma_i^* - \Gamma_{i-1}^*|),\tag{2}$$

$$\Delta e_{0,i,\max}^* = \max(|e_{0,i+1}^* - e_{0,i}^*|, |e_{0,i}^* - e_{0,i-1}^*|),\tag{3}$$

In Ref. [51], it is recommended that $\Delta\Gamma^*_{i,\max} = 1$, $\Delta e^*_{0,i,\max} = 1000$ kJ/kg. Under these conditions, the fully conservative numerical scheme transitions to a quasiconservative scheme based on the criteria mentioned earlier. Another parameter, $|\nabla\rho|/\rho = 0.3$, could also be employed for this purpose [50]. It should be noted that this parameter $|\nabla\rho|/\rho$ is not adopted, but is provided as an option.

The primary characteristic of the DF model [11,51,66,79] is that it maintains the effective specific heat ratio (γ^*) and effective reference internal energy (e^*_0) as constant values in both space and time to mitigate spurious pressure oscillations and oscillations of other physical parameters that may result from pressure fluctuations. Essentially, the relationship between pressure and internal energy remains fixed in both space and time, effectively transforming the local system into a calorically perfect gas system.

The parameters $\gamma^*(\Gamma^*)$ and e^*_0 are determined based on the values from the previous time step to establish relations between internal energy and pressure [82]. This approach [11,66] is taken to prevent abrupt changes in $\gamma^*(\Gamma^*)$ and e^*_0 between cells, as such variations could disrupt pressure equilibrium and induce spurious pressure oscillations. In this process, the effective specific heat ratio (γ^*) is calculated as $\gamma^* = \rho c^2/p$, the effective reference internal energy (e^*_0) is obtained as $e^*_0 = e - \Gamma^* p/\rho$, and Γ^* is calculated as $\Gamma^* = 1/(\gamma^* - 1)$. These values are held constant throughout all Runge-Kutta (RK) substeps within each time step to ensure stability and accuracy. A schematic of the double-flux model is shown in Fig. 1(b).

In each time step of our simulation, the following operations are implemented.

Step 1. Reconstruction and flux computation at the cell faces involves using Eqs. (4) and (5) for left and right face reconstructions:

$$c = \sqrt{p\gamma^*/\rho}, \tag{4}$$

$$(\rho E)^* = \rho e^*_0 + \frac{1}{2}\rho|\mathbf{u}|^2 + \Gamma^* p = \rho e^*_0 + \frac{1}{2}\rho|\mathbf{u}|^2 + \frac{p}{\gamma^* - 1}. \tag{5}$$

When reconstructing the total energy of the left-hand side (belonging to $U^{\mathrm{L},n}_{i+1/2}$) of the cell interface $i + 1/2$, the parameters γ^*_i and $e^*_{0,i}$ of the left first cell i and the values p_m, ρ_m, and u_m of cell m are used to update $(\rho E)^*_m$ of cell m (where m is part of the stencils used to reconstruct $U^{\mathrm{L},n}_{i+1/2}$), then the left-hand-side total energy is constructed according to the corresponding scheme:

$$(\rho E)^n_m = \rho^n_m e^{*,n}_{0,i} + \frac{1}{2}\rho^n_m|u^n_m|^2 + \frac{p^n_m}{\gamma^{*,n}_i - 1}. \tag{6}$$

Similarly, when reconstructing the total energy of the right-hand side (belonging to $U^{\mathrm{R},n}_{i+1/2}$) of the cell interface $i + 1/2$, the parameters γ^*_{i+1} and $e^*_{0,i+1}$ of the right first cell $i + 1$ and the values p_k, ρ_k, and u_k of cell k are used to update $(\rho E)^*_k$ of cell k (k belongs to stencils used to reconstruct $U^{\mathrm{R},n}_{i+1/2}$). The total energy of the right-hand side is then constructed accordingly:

$$(\rho E)^n_k = \rho^n_k e^{*,n}_{0,i+1} + \frac{1}{2}\rho^n_k|u^n_k|^2 + \frac{p^n_k}{\gamma^{*,n}_{i+1} - 1}. \tag{7}$$

Step 2. Obtain the conservative variables and the corresponding primitive variables such as velocity, density, and energy.

Step 3. Update other primitive variables such as pressure for each cell using Eq. (8):

$$p = \frac{1}{\Gamma^*}\left(\rho E - \rho e^*_0 - \frac{1}{2}\rho|\mathbf{u}|^2\right) = (\gamma^* - 1)\left(\rho E - \rho e^*_0 - \frac{1}{2}\rho|\mathbf{u}|^2\right). \tag{8}$$

When updating p_i^{n+1} of cell i, the frozen values $\gamma_i^{*,n}$, $e_{0,i}^{*,n}$, and $\Gamma_i^{*,n}$ from the last substep n and the updated $\mathbf{u}_i^{n+1}$, ρ_i^{n+1}, and $(\rho E)_i^{n+1}$ are used,

$$
\begin{aligned}
p_i^{n+1} &= \frac{1}{\Gamma_i^{*,n}} \left((\rho E)_i^{n+1} - \rho_i^{n+1} e_{0,i}^{*,n} - \frac{1}{2} \rho_i^{n+1} \left| u_i^{n+1} \right|^2 \right) \\
&= \left(\gamma_i^{*,n} - 1 \right) \left((\rho E)_i^{n+1} - \rho_i^{n+1} e_{0,i}^{*,n} - \frac{1}{2} \rho_i^{n+1} \left| u_i^{n+1} \right|^2 \right).
\end{aligned}
\tag{9}
$$

Step 4. After obtaining the pressure, update the temperature using the equation of state (EOS) based on density, pressure, and species mass fraction.

Step 5. Update other parameters such as speed of sound, enthalpy, and entropy based on the temperature, pressure, density, velocity, total energy, and internal energy obtained.

At the end of all Runge-Kutta substeps within each time step, the total energy is updated. This update is done according to $\rho E = \rho e + 1/2\rho |u|^2$ and thermodynamic relations $\rho E = \rho E(p, \rho, T, Y)$ to ensure thermodynamic consistency since the temperature is updated after the pressure in Eq. (6).

In the QC scheme, pressure is obtained directly from the DF model [Eq. ((8) and is, therefore, more easily maintained as positive. The temperature is then updated according to the pressure, density, and species mass fraction [11]. However, because different values of γ^* and e_0^* are used for each cell, the two energy fluxes at a face are no longer the same, unlike in the FC scheme. This can result in an energy conservation error. Nevertheless, it has been reported [11,66,82] that the total energy conservation error decreases as the resolution increases and the difference in γ^* between neighboring cells decreases.

3. Hybrid numerical model with modified PR-EOS

The hybrid numerical model, incorporating a modified PR-EOS, is introduced to address two primary challenges:

(1) Conservative scheme-induced problem: When using a FC method with the classical PR-EOS, pressure is updated from temperature and density within each time step, involving a complex nonlinear real-fluid EOS. During this process, numerical diffusion and dispersion can result in negative pressure or induce pressure oscillations, which may lead to simulation failures. FC schemes struggle to maintain pressure equilibrium across transcritical contact interfaces. In contrast, QC schemes are more effective in reducing spurious pressure oscillations and achieving positive pressure. Additionally, reducing the high-order numerical scheme to a low-order numerical scheme can help to mitigate pressure oscillations.

(2) Vapor dome problem: The classical PR-EOS is designed for use outside the vapor dome, and it needs to be modified to handle conditions within the vapor dome. In certain situations, negative pressures can occur for specific density values at relatively low temperatures, and the speed of sound may become complex valued in the vapor dome [84]. Inside the vapor dome, the thermodynamic state described by the classical PR-EOS is either metastable, or unstable or nonconvex.

To address the first issue, the QC scheme provides an effective solution. Moreover, by reducing the high-order numerical scheme to a low-order numerical scheme, pressure oscillations can be reduced.

To tackle the second issue, a modified PR-EOS [51] is introduced to approximate the fluid state within the vapor dome region. This modified PR-EOS ensures that the speed of sound remains above 1 m/s, enhancing the robustness of the numerical method when the state falls within the vapor dome. It is important to note that phase separation is not expected [85,86], and the proposed numerical procedure in Ref. [71] is adequate for resolving pressure oscillations in transcritical flows.

This modification to the PR-EOS enhances the accuracy and stability of simulations, particularly in cases where conditions within the vapor dome need to be represented. For more details, please refer to Appendix C.

B. Numerical methods

It is worth noting that, within the references related to transcritical flow [51,52], it has been observed that the WENO3-type scheme outperforms WENO5 in terms of pressure oscillations, particularly in near-critical or transcritical scenarios. Reference [52] specifically recommends the use of the WENO3-type scheme to simulate higher-strength shock-droplet interactions, thus improving numerical stability. In the case of a Mach 2 shock, they even employ a minmod flux limiter based on the gradient of the mass fraction [52]. Reference [51] demonstrates that reducing the order of reconstruction from WENO5 to WENO3 results in a significant reduction in pressure fluctuations, from 8 to 3.2 MPa. This reduction is attributed to the increased numerical diffusion provided by WENO3. It is evident that WENO3 enhances the numerical stability of the solver and the robustness of the numerical scheme. However, it is important to acknowledge that while the compact reconstruction stencils can reduce computational effort, they also yield results of reduced accuracy when compared to the same mesh resolution with WENO5. To overcome this accuracy limitation of WENO3, an increase in mesh resolution and computational resources is required. At this higher resolution, the results can be made comparable to those obtained with WENO5 [51].

In light of these findings, the current study replaces WENO5 [51] with a WENO3-type scheme to enhance the numerical stability in complex cases. This ensures that the current numerical scheme maintains the key characteristics of the reference scheme. It will be meticulously validated to handle the near-critical shock interactions with *n*-dodecane. The results of these validation cases will be presented in detail and compared with the previous results obtained using the WENO5-type scheme, which can be found in Sec. II C and Appendixes D and E.

The following section describes the classic JS-WENO3 and OWENO3 [87] schemes that will be employed in the validation cases. Specifically, a WENO3-type scheme is employed for reconstruction of pressure, density, velocity, internal energy, and mass fraction to achieve numerical consistency. Interface diffusion is controlled by local adjustment of smoothness indicators and ENO stencil weights. Consider the JS-WENO3 reconstruction for mass fraction ξ as an example:

$$\xi_{\text{gas}}\left(x_{\frac{1}{2}}\right) = w_0 \xi_{\text{gas}}^{\text{L}} + w_1 \xi_{\text{gas}}^{\text{R}}. \tag{10}$$

The left- and right-hand-side interpolation polynomials at the cell interface are $\xi_{\text{gas}}^{\text{L}} = -(1/2)f_{-1} + (3/2)f_0$, $\xi_{\text{gas}}^{\text{R}} = (1/2)f_0 + (1/2)f_1$. Smoothness indicators are defined as $I_0 = (f_0 - f_{-1})^2$, $I_1 = (f_1 - f_0)^2$. f_i is the variable embedded in cell i. The nonlinear ENO stencil weights are denoted as $w_0 = \alpha_0/(\alpha_0 + \alpha_1)$ and $w_1 = \alpha_1/(\alpha_0 + \alpha_1)$, where $\alpha_0 = c_0/(I_0 + \varepsilon)$ and $\alpha_1 = c_1/(I_1 + \varepsilon)$, with c_0 and c_1 being 1/3 and 2/3, respectively.

Additionally, an improved WENO3 scheme, OWENO3 [87], is adopted for comparsion, which maintains the advantages of JS-WENO3 with reduced dissipation. For OWENO3, an additional fourth node is included in the calculation of weights (measuring smoothness), based on a WENO approach with unconditional third-order optimal accuracy on smooth data, and without relying on any tuning parameters. The reconstruction domain is kept to a maximum of four points, consistent with classical WENO3 schemes. The corrected OWENO3 stencil weights are defined as follows:

$$w_0 = \tfrac{1}{3}w + (1 - w)\widetilde{w_0}, \quad w_1 = \tfrac{2}{3}w + (1 - w)\widetilde{w_1}, \tag{11}$$

where $\widetilde{w_0} = (I_1 + \varepsilon)/(I_0 + I_1 + 2\varepsilon)$ and $\widetilde{w_1} = (I_0 + \varepsilon)/(I_0 + I_1 + 2\varepsilon) = 1 - \widetilde{w_0}$, with ε being a small value ($\varepsilon = 1 \times 10^{-6}$), and a corrector weight defined as $w = \text{J}/(\text{J} + \tau + \varepsilon)$, where $J = I_0(I_1 + I_2) + (I_0 + I_1)I_2$ and $0 \leqslant w \leqslant 1$. τ represents the product of the square of the undivided difference associated with the extended stencil (four stencils) and the sum of the smoothness indicators, $\tau = dI$, where $d = (-f_{-1} + 3f_0 - 3f_1 + f_2)^2$ and $I = I_0 + I_1 + I_2$. An additional smoothness indicator I_2 using the additional node is employed for smooth indicators, leading to $I_0 = (f_0 - f_{-1})^2$, $I_1 = (f_1 - f_0)^2$, and $I_2 = (f_2 - f_1)^2$.

OWENO3 is a valuable choice for the following reasons:

(1) It achieves unconditionally optimal accuracy when the data are smooth, and provides second-order accuracy when a discontinuity crosses the stencil. The accuracy properties of OWENO3 are

TABLE I. Initial conditions for shock-cylinder interaction at near-critical conditions.

Stage	p (MPa)	u (m/s)	v (m/s)	ρ (kg/m^3)	T (K)
Preshocked nitrogen	6.0	0	0	30.46	650.0
Postshocked nitrogen	9.096	−160.3	0	40.38	736.2
n-Dodecane	6.0	0	0	419.9	650.0

theoretically proven and confirmed through numerical experiments involving algebraic problems and hyperbolic conservation laws.

(2) Several numerical experiments indicate that this scheme is more efficient in terms of error reduction versus CPU time compared to traditional third-order schemes and, in most cases, even outperforms classical higher-order WENO schemes (WENO5-JS).

(3) It allows for higher values of the CFL number in complex problems.

Moreover, an Harten-Lax-van Leer contact (HLLC) Riemann solver is applied, and additional details can be found in Ref. [88].

In summary, the adoption of the WENO3-type scheme, along with finer meshes, allows for robust, compact, easily implemented, and accurate studies of complex shock-droplet interactions across a wide range of conditions. The effects of mesh resolution and validations are thoroughly compared with results obtained using WENO5, as detailed in Sec. II C and Appendixes D and E.

C. Verification of shock interaction with a two-dimensional cylindrical fuel column

This section focuses on the validation of shock interaction with a cylindrical fuel column, taking into account various factors such as mesh resolution, computational domain, boundary conditions, and the chosen numerical scheme.

To generate numerical schlieren images, we employ the following formula to define the pseudoschlieren value:

$$\emptyset = \exp\left(-C\frac{|\nabla\rho| + A}{B + A}\right). \tag{12}$$

The pseudoschlieren value, denoted as $\emptyset$, is determined using the formula $|\nabla\rho| = [(\partial\rho/\partial x)^2 + (\partial\rho/\partial y)^2]^{1/2}$, where three adjustable parameters, A, B, and C, influence its calculation. Typically, A is set to zero, and B equals $|\nabla\rho|_{max}$, gradually leading to $\emptyset = \exp(-C|\nabla\rho|/|\nabla\rho|_{max})$. The gray values displayed in the schlieren images are fine-tuned based on the approach recommended in Ref. [22]. It is important to note that the constant "C" plays a role here, taking the value of 600 for light fluids (such as helium) and 120 for heavy fluids (like R22). In the case of shock interaction with a cylindrical fuel column, C is set to 600 for the nitrogen environment and 120 for the n-dodecane cylinder.

1. Detailed evolution of shock interaction with a cylinder at near-critical conditions

We conduct a validation study to investigate the evolution of shock interaction with an n-dodecane cylinder at near-critical conditions in a nitrogen environment. The parameters for this study closely match those in Ref. [52], with the exception of a finer mesh resolution of 0.115 mm in the region where $z = -160$ mm and 160 mm, compared to their 0.23 mm. The initial conditions, which include thermodynamic parameters, cylinder position, diameter, boundary conditions, and the computational domain with the shaded fine-mesh region, are presented in Fig. 2 and Table I.

In this scenario, we aim to illustrate the shock interaction with a near-critical droplet. This interaction occurs at a supercritical pressure and subcritical temperature, placing the n-dodecane in a liquidlike supercritical state. The critical properties of n-dodecane are defined by a critical pressure (p_c) of 1.82 MPa and a critical temperature (T_c) of 658.1 K. As a result, the n-dodecane droplet begins in a supercritical state where it is pressurized at subcritical temperature.
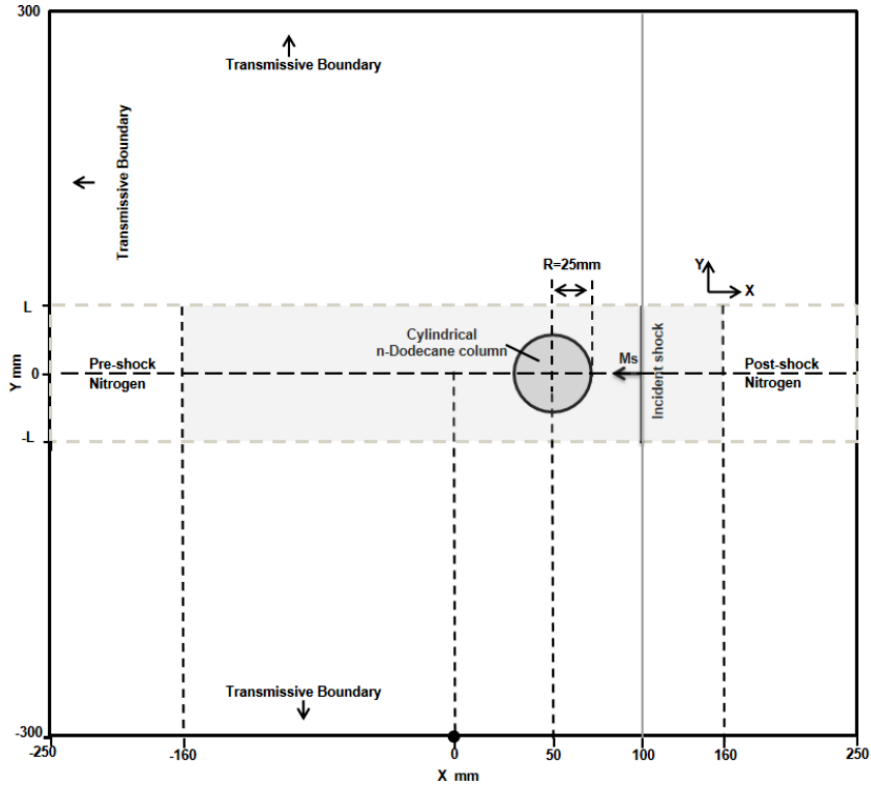
FIG. 2. Scheme of the computational domain for the shock-cylinder interaction at near-critical conditions.

For the nitrogen environment, it is crucial to note that its temperature exceeds the critical temperature, and its pressure is above the critical pressure. Nitrogen's critical properties are characterized by a critical pressure (p_c) of 3.369 MPa and a critical temperature (T_c) of 126.2 K. The shock wave in this environment maintains a Mach number of 1.2. Reference [78] provides the NASA polynomial parameters, and for this part of the study, we employ OWENO3 as the numerical scheme.

In this section, our primary focus is to analyze the morphological aspects of shock interaction with a pure cylinder. While Boyd and Jarrahbashi provide a useful overview of the main features [52], we seek a more comprehensive description of the morphology at near-critical conditions.

As illustrated in Fig. 3, the incident shock wave (IS) initially passes the upstream pole and travels towards the downstream pole. The time instance when the shock contacts the upstream surface of the cylinder (USC) is defined as 0μs. Once the IS reaches the USC, it leads to the formation of a curved refracted shock (TS) within the cylinder and a shock reflection (RS) from the USC. The RS in n-dodecane is slower than the IS due to the lower speed of sound (SoS).

Around 105 μs, surface-vertical diffracted shocks (DSs) emerge on the downstream surface of the cylinder (DSC). The sweep of these DSs subsequently induces the generation of an incident diffracted transmitted shock (DTS). To balance the pressure difference between the converging (refracted) transmitted shock (TS1) and the incident DTS, a new small shock (NSS1) is formed. This leads to the gradual reduction of both the angle between the DTS and the TS1 and the undisturbed zone (UZ).

By 115 μs, the crossover point of the incident shock is noticeable, and the convergence of NSS1, DTS, and TS1 results in the formation of high-pressure zones. At 120 μs, the converged refracted shock becomes evident, and by 125 μs, the original TS1 impinges on the Mach stem (generated by the internal convergence of the DTS), creating an even higher pressure oval region (OZ).

At 130 μs, it is observed that the newly formed internal Mach stem (IMS, representing one edge of the oval region) impinges on the downstream interface and generates a transmitted Mach stem (TMS). Gradually, a surface jet formation (JF) is observed at 185 μs. This evolution, from the

(a) Typical views at the time: 105 µs, 115 µs, 120 µs, 125 µs, 130 µs, 140 µs, 185 µs.

(b) Enlarged view at the relevant time: 125 µs, 130 µs.
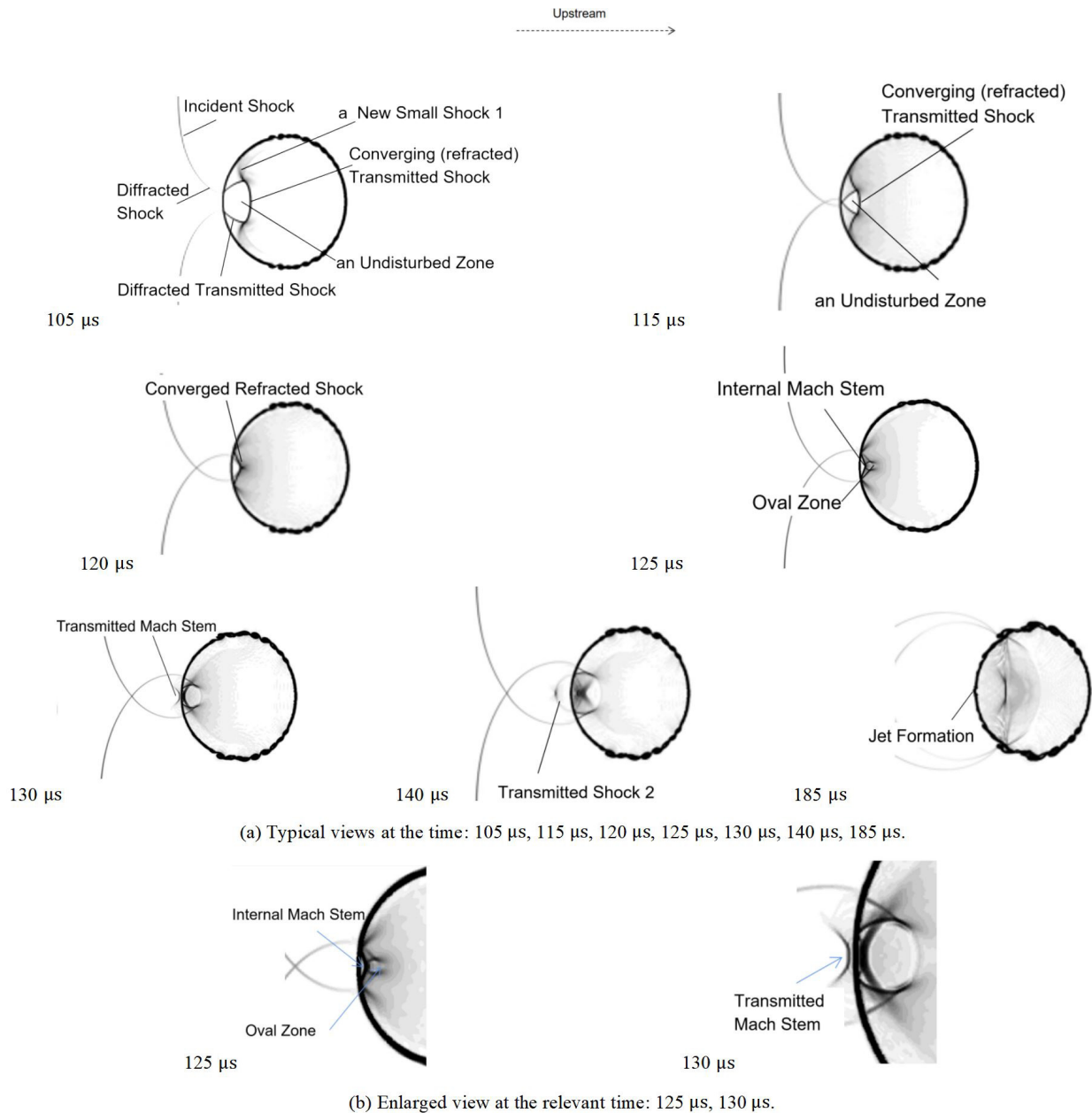
FIG. 3. Representative view of the flow morphology in a shock-accelerated cylinder. Typical views at the time (a) 105 µs–185 µs, (b) 125 µs, 130 µs.

converged refracted shock (CRS) focal wedge, to the OZ, to the TMS, represents the mechanism behind the development of the surface jet.

It is important to note that this morphological evolution is akin to the cases of shock interaction with a heavy bubble (e.g., R22, SF_6, Kr) studied by various researchers, such as Haas and Sturtevant [21], Jacobs [89], Zhai *et al.* [90], Zou *et al.* [91], Fan *et al.* [92], and Guan *et al.* [93]. The process depicted in Fig. 3 aligns well with the findings in Ref. [52], providing qualitative validation for our methods and affirming that the mesh resolution is sufficient to capture these intricate features. Further discussion and details are provided in Sec. III A.

Additionally, we conducted a quantitative comparison by examining pressure distributions and comparing them with the results presented in the reference study. In Fig. 4, the black lines represent the pressure distribution achieved using a mesh resolution of 0.115 mm and the OWENO3 numerical scheme. The pressure distribution closely matches the reference data, although there is a minor

(a)

(b)
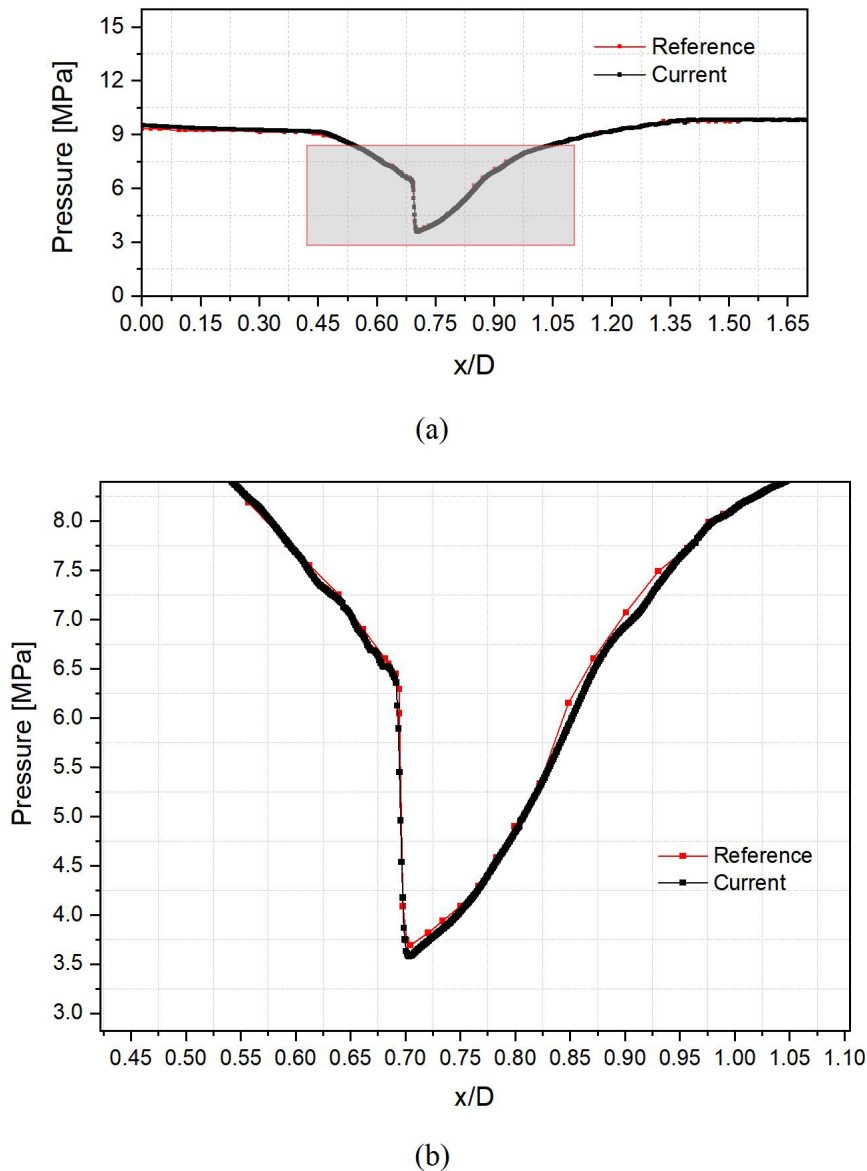
FIG. 4. The pressure distributions of the current case and the reference case at time 185 μs.

pressure difference (less than 1%) near the discontinuity region. This discrepancy can be attributed to the weak pressure oscillations that occur in the vicinity of the discontinuity region. For further validation, a case involving shock interaction with a helium bubble is provided in Appendix E.

In summary, we have successfully demonstrated that our numerical scheme produces accurate results and that the current mesh resolution is sufficient to capture the essential features of near-critical shock-cylinder interactions.

2. Effects of mesh resolution and numerical scheme on near-critical shock-cylinder interactions

Mesh resolution studies are of particular importance, as essential flow characteristics may still be observed with coarser mesh resolutions. We consider meshes up to four times finer than 0.23 mm.

In Figs. 5 and 6, we present simulations conducted within a larger computational domain with coarser meshes near the boundaries. In this setup, wave reflections from the top and bottom walls are suppressed to isolate the planar shock effects. We compare various mesh resolutions and OWENO3 and WENO3, assessing the level of dissipation. The results demonstrate that OWENO3 yields improved results with reduced dissipation compared to WENO3. OWENO3, with a mesh

Upstream

------------------------------>

(a) Large domain with WENO3 (mesh resolution: 0.23 mm).

(b) Large domain with WENO3 (mesh resolution: 0.115 mm).

(c) Large domain with WENO3 (mesh resolution: 0.0767 mm).

(d) Large domain with WENO3 (mesh resolution: 0.0575 mm).
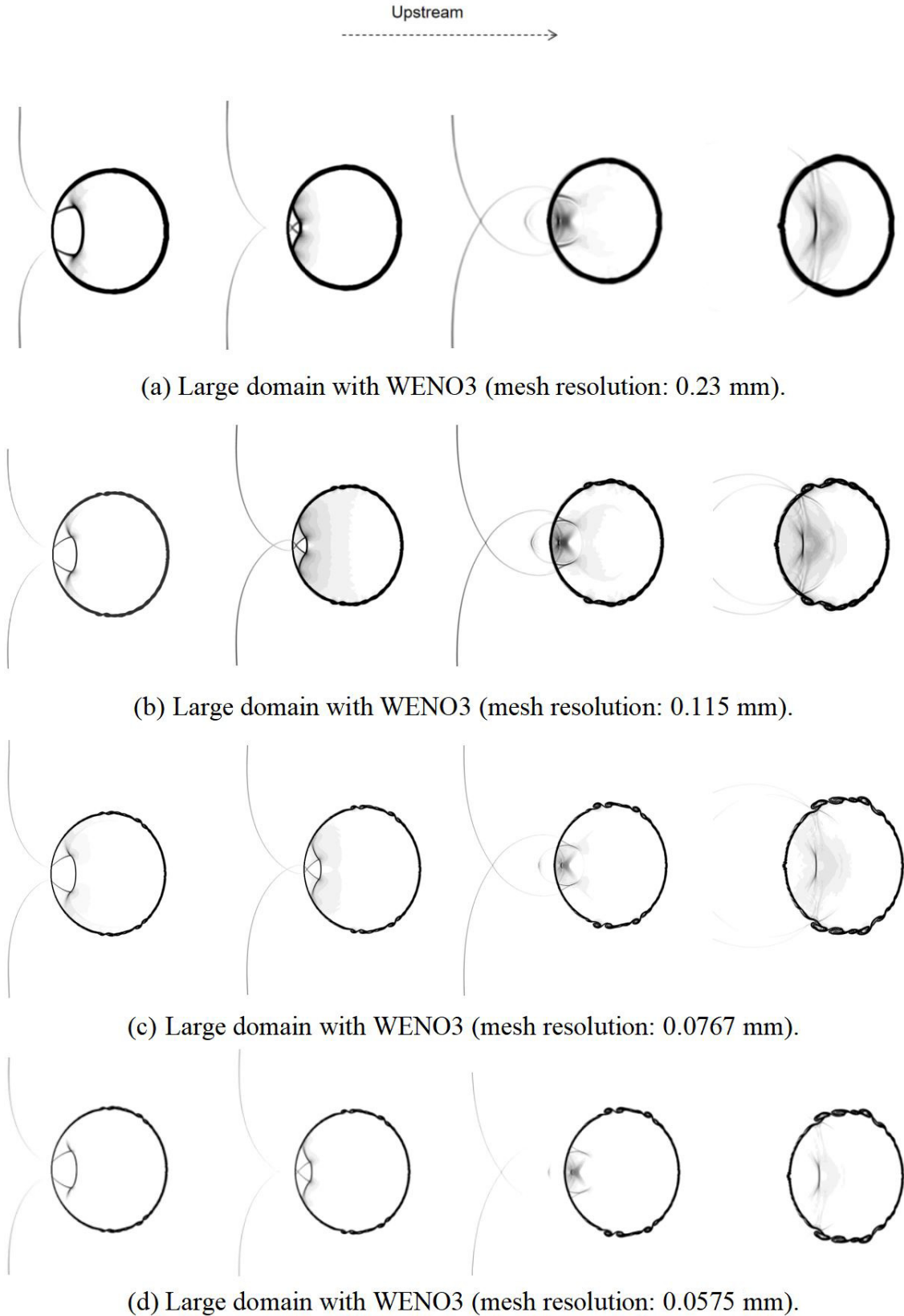
FIG. 5. The shock *n*-dodecane cylinder interaction within the large domain at times 105, 115, 140, and 185 μs (from left to right). WENO3 with a mesh resolution of (a) 0.23 mm, (b) 0.115 mm, (c) 0.076 mm, (d) 0.0575 mm.

(a) Large domain with OWENO3 (mesh resolution: 0.23 mm).

(b) Large domain with OWENO3 (mesh resolution: 0.115 mm).

(c) Large domain with OWENO3 (mesh resolution: 0.0767 mm).

(d) Large domain with OWENO3 (mesh resolution: 0.0575 mm).

(e) Reference results [52], large domain with WENO5 (mesh resolution: 0.23 mm).
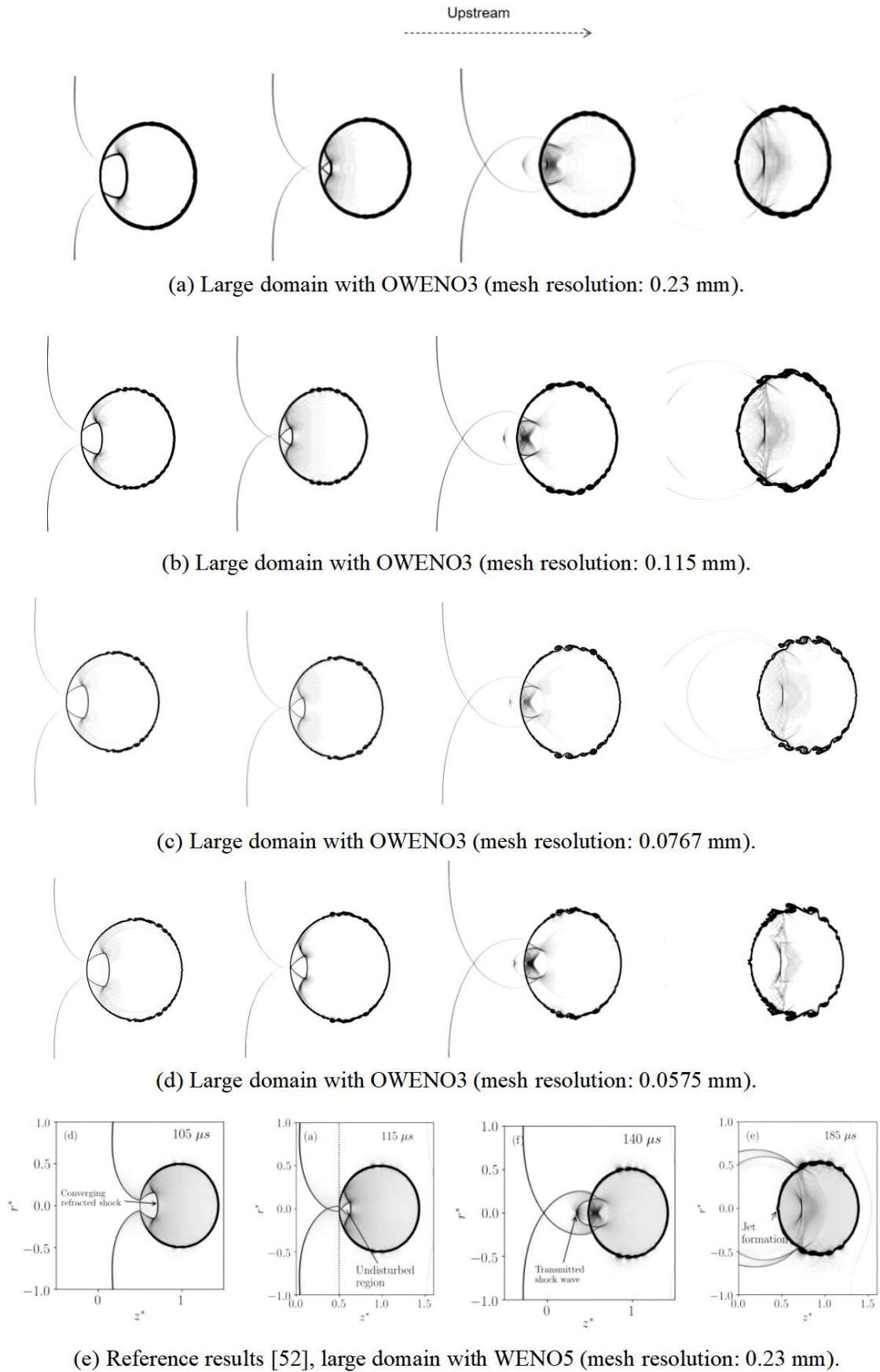
FIG. 6. The shock n-dodecane cylinder interaction within the large domain at times 105, 115, 140, and 185 μs (from left to right). OWENO3 with a mesh resolution of (a) 0.23 mm, (b) 0.115 mm, (c) 0.0767 mm, (d) 0.0575 mm. WENO5 with a mesh resolution of (e) 0.23 mm from Ref. [52]. Reproduced from Ref. [52].
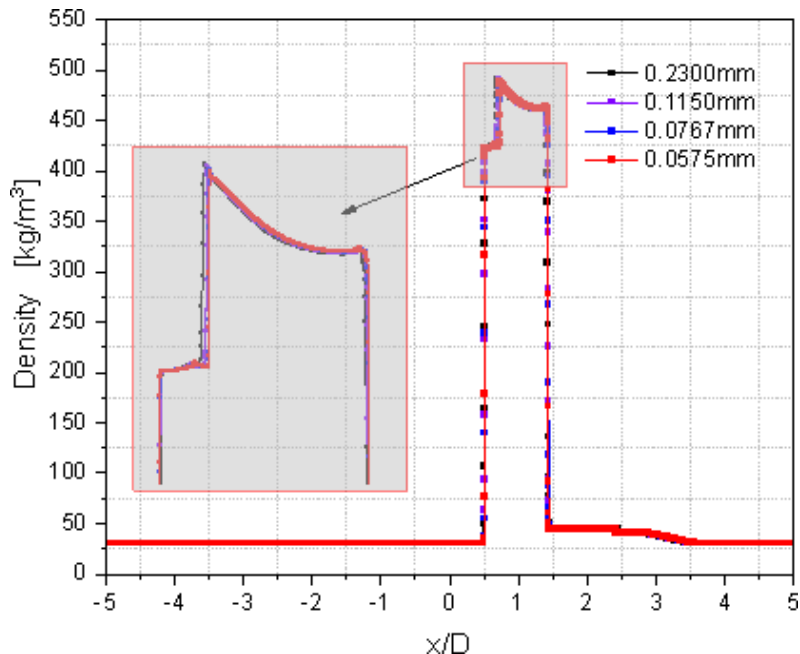
FIG. 7. Grid convergence test on the shock n-dodecane cylinder interaction by OWENO3 within large domain at time 143 μs.

resolution of 0.115 mm, can provide results that are comparable to those obtained with WENO5 from Ref. [52].

For assessing mesh independence, we also analyze the density distribution, as depicted in Fig. 7. The density distributions directly display the contact positions of both fluids and converge to the red line with the finest mesh resolution of 0.0575 mm. Notably, there are minimal differences between the results obtained with mesh resolutions of 0.115 and 0.0575 mm. Therefore, for a well-balanced consideration of accuracy and computational efficiency, a mesh resolution of 0.115 mm is a suitable choice.

In this way, a high mesh resolution, exceeding 434 computational cells per droplet diameter (diameter = 50 mm), is employed. This translates to more than 0.87 billion equivalent finite volumes for the entire three-dimensional n-dodecane droplet simulation, potentially making it the largest simulation of n-dodecane at near-critical conditions reported to date.

Even finer meshes would likely capture more small-scale structures, as demonstrated in our mesh independence study. However, these tiny vortex structures are ephemeral in reality, quickly dissipating due to physical processes (physical diffusion). In simulations, numerical viscosity (inherent to the simulation scheme) also acts to dissipate these structures rapidly, preventing them from influencing the larger structures of interest. In essence, these small structures become so short-lived that they are negligible. As in Refs. [52,82], viscous terms are insignificant in short-duration processes with rapid shock interactions.

Our results accurately capture the interface structures and shock wave patterns (Fig. 6) when compared with reference data [52]. In cases where different mesh resolutions are used, the main roll-up structures are captured in a comparable manner. As discussed above, while finer meshes might reveal even smaller two-phase structures, these would likely have minimal influence on the dominant processes governing the deformation of the two-phase interface and the evolution of shock waves. Therefore, the focus on capturing the key characteristics and conducting mesh independence studies is justified.

Furthermore, the relative total energy error values are calculated at $t = 105$ μs, where $\epsilon = |(\int_{\Omega}(\rho E)^t - \int_{\Omega}(\rho E)^0)/\int_{\Omega}(\rho E)^0|$. The values are 0.0405, 0.0219, 00110, and 0.0009 for cases with mesh resolution of 0.2300, 0.1150, 0.0767, and 0.0575 mm, respectively. It is consistent with Refs. [11,51,66] that the total energy conservation error decreases with increasing resolution.
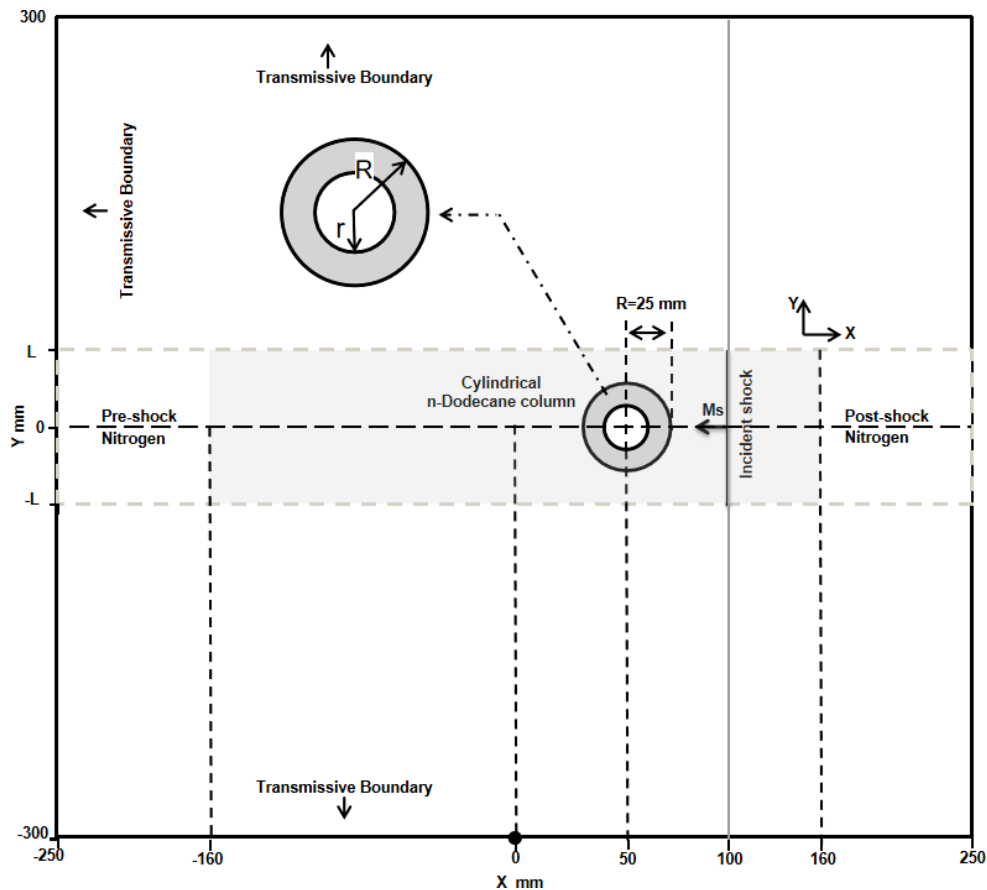
FIG. 8. The schematic for the computational domain of the shock-cylinder ring interaction.

Additionally, we also consider various cases involving different computational domains and boundary conditions to demonstrate the robustness and accuracy of our current numerical scheme (see Appendixes D and E for these additional cases).

III. RESULTS AND DISCUSSION

A. Analysis of a cylinder with an internal gas cavity

As depicted in Fig. 8, a gaseous cavity is situated at the center of the cylindrical column with a diameter $r/R = 0.5$. The thermodynamic properties, such as pressure, velocity, density, and temperature, of the internal gas bubble are maintained consistent with the preshock nitrogen environment.

One way to define the characteristics of the shock interactions in such cases is by considering the speed-of-sound (SoS) ratio, as suggested by Ref. [21]. In the present scenarios, the speed of sound (c_S) in the surrounding preshock nitrogen environment is greater than that in the n-dodecane cylinder (c_D). This results in a SoS ratio ($n = c_S/c_D$) greater than 1, indicating a convergent situation, where the refracted shock within the n-dodecane cylinder is slower than the incident shock wave. This is analogous to the convergent situation seen in shock–R22 bubble cases, in contrast to the divergent situation in shock–helium bubble cases. Additionally, $\delta Z > 0$ is a typical description of a convergent case [28].

The acoustic impedance mismatch across the material interface between the n-dodecane cylinder and the surrounding nitrogen fluid, denoted as $\delta Z = (\rho c)_D - (\rho c)_S > 10^5$, significantly influences the transition of a shock wave across the interface. In the current cases, when the incident shock reaches the upstream surface of the cylinder (USC), it forms a refracted wave as well as a reflected shock wave due to the fact that $\delta Z \gg 0$ (similar to shock–R22 bubble cases). Conversely, if there

is no gas cavity within the cylinder (a pure cylinder), and the refracted shock travels through the cylinder to the downstream surface of the cylinder (DSC), an opposite impedance mismatch occurs with $\delta Z \ll 0$, causing the reflected wave to become a rarefaction wave for the current case, much like in shock–R22 bubble cases.

Another important parameter to consider is the Atwood number (A), which is defined as $A = (\rho_D - \rho_S)/(\rho_D + \rho_S)$ and characterizes the effect of density variation between the n-dodecane cylinder and the surrounding nitrogen fluid. The dimensionless time t^* corresponds to the simulated physical time t, divided by an arbitrarily chosen reference time $t_{\text{ref}} = 8.68 \times 10^{-6}$ s.

1. Early wave pattern evolution of the shock-cylinder ring interaction at near-critical conditions

This section offers an in-depth analysis of the early wave pattern evolution during the interaction between a shock and a cylindrical ring at near-critical conditions. Figure 9(a) illustrates the initial phase of the interaction. The incident shock (IS) passes over the USC, leading to the generation of the reflected shock (RS) and the converging (refracted) transmitted shock (TS1). Simultaneously, the cylinder undergoes deformation and initiates downstream movement. These processes are designated as "1."

Subsequently, after TS1 encounters the upstream surface of the embedded gas bubble (USB), the angle between USB and TS1 begins to increase from zero. During this early stage, two significant events occur:

(1) The second reflected rarefaction wave (RR) is generated.

(2) The diverging (refracted) transmitted shock 2 (TS2) begins to take shape.

Both begin at relatively small angles. Simultaneously, the embedded gas bubble also starts moving and deforming downstream. These processes are marked as "2." These early wave pattern changes, constituting the inner shock-bubble interaction process, resemble typical refraction processes, akin to shock interactions with lighter gas bubbles, as seen in shock–helium bubble cases.

Given the higher impedance of the n-dodecane cylinder compared to nitrogen, TS2 inside the nitrogen bubble moves faster than TS1 inside the cylinder. This results in the generation of a side shock (SS) and a new shock 1 (NS1), as depicted in Fig. 9(b). SS is often referred to as the free-precursor shock wave (FPS) in the literature [57]. At this stage, TS1, SS, NS1, and reflected shock 2 (RS2) converge at a point marked as "P4," which resembles the free precursor refraction (FPR) phenomenon [57,94].

As RS2 and SS propagate in different directions, they form an angle between them. Consequently, as shown in Fig. 9(c), P4 is replaced by two distinct intersection points (P2) and the formation of a Mach stem. This wave pattern is reminiscent of the twin von Neumann refraction (TNR) [94].

In Fig. 9(d), as TS2 reaches the downstream surface of the bubble (DSB), it gives rise to a transmitted shock (TS3) and a reflected shock (RS3), both traveling in opposite directions. The points of intersection for these three shock waves (P3) arise from the movement of TS1. Moving on to Fig. 9(e), both the transmitted wave TS5 and the reflected wave RS5 emerge near the USB. RS2 refracts from the DSC, forming a transmitted shock from RS2 (TRS2). Additionally, diffracted shock waves form a crossover point outside the DSC. Furthermore, as depicted in Fig. 9(f), TS3 passes through the DSC, creating a fourth transmitted shock (TS4) and a rarefaction wave heading towards the DSB. The diffracted shock, TRS2, and TS4 comprise the primary structures of the wave pattern outside the cylinder ring. Inside the cylinder ring, further development of NS1, TS1, the rarefaction wave of TS3, and other waves form a more intricate pattern of waves.

A comparison between Fig. 3 and Figs. 9(a)–9(g) reveals that the evolution of the outer cylinder surface in the ring case mirrors that of the pure cylinder case, akin to shock interactions with heavy fluids [21,89–93]. The two-phase interface between the cylinder ring and the outer nitrogen environment resembles the previous results of a pure cylinder. However, the jet formation at the DSC is diminished, attributed to the newly formed complex wave pattern interaction, such as the interaction between P3 and DSC.
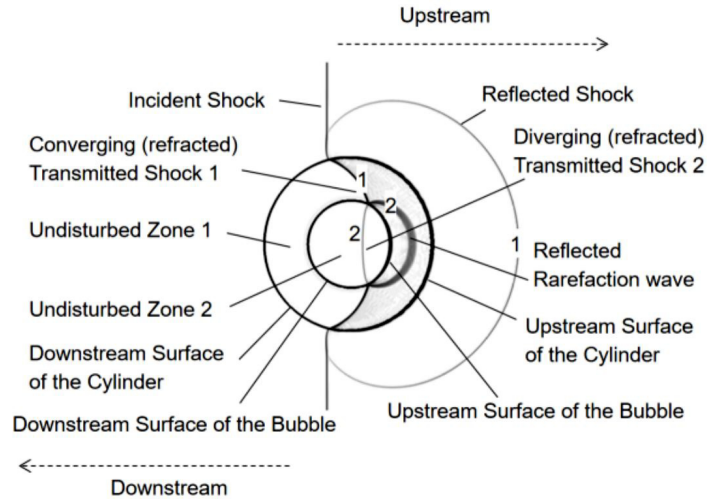
(a) $t^*=9$.
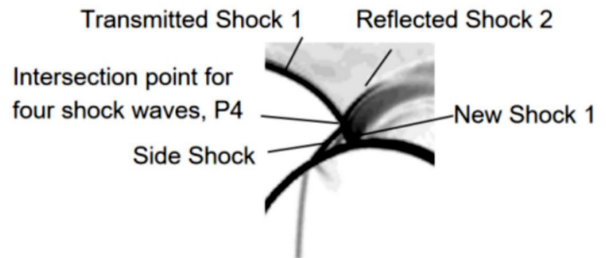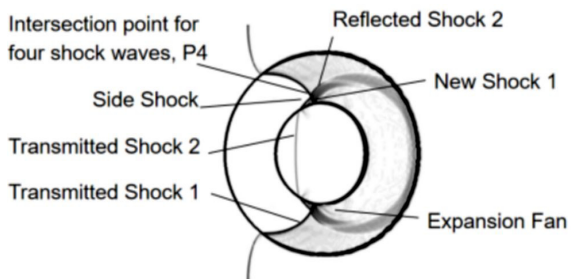
(b) $t^*=11$.
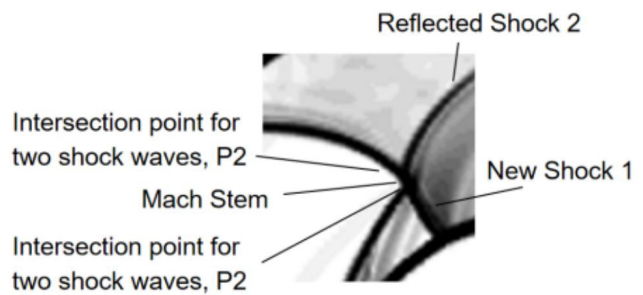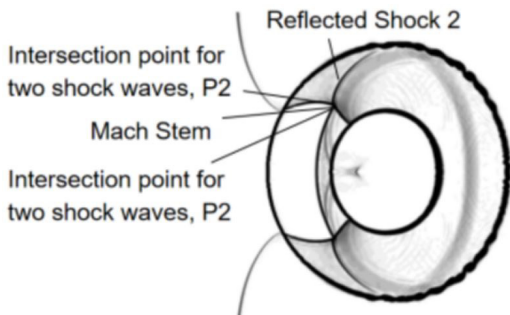
(c) $t^*=13$.

FIG. 9. Representative view of the flow morphology and wave pattern evolution in a shock-accelerated cylinder ring at near-critical conditions.

Figures 9(a)–9(g) show the progression of the shock wave pattern in a case involving a gas cavity. Over time, the USB presses into the center of the nitrogen, taking on a kidney shape, reminiscent of shock-accelerated light bubbles (shock helium bubble). It is noteworthy that the internal shock wave pattern bears resemblances to shock–helium bubble (light gas) interaction cases. In the current cylinder ring scenario, the IS of shock–helium bubble cases is replaced by TS1, a reasonable substitution given the shared attributes of "heavy-light layer" cases.

(d) $t^*=15$.

(e) $t^*=16$.

(f) $t^*=17$.

(g) $t^*=18$, 19, 20, 21, 22, 23, 24 (from top left to bottom right).
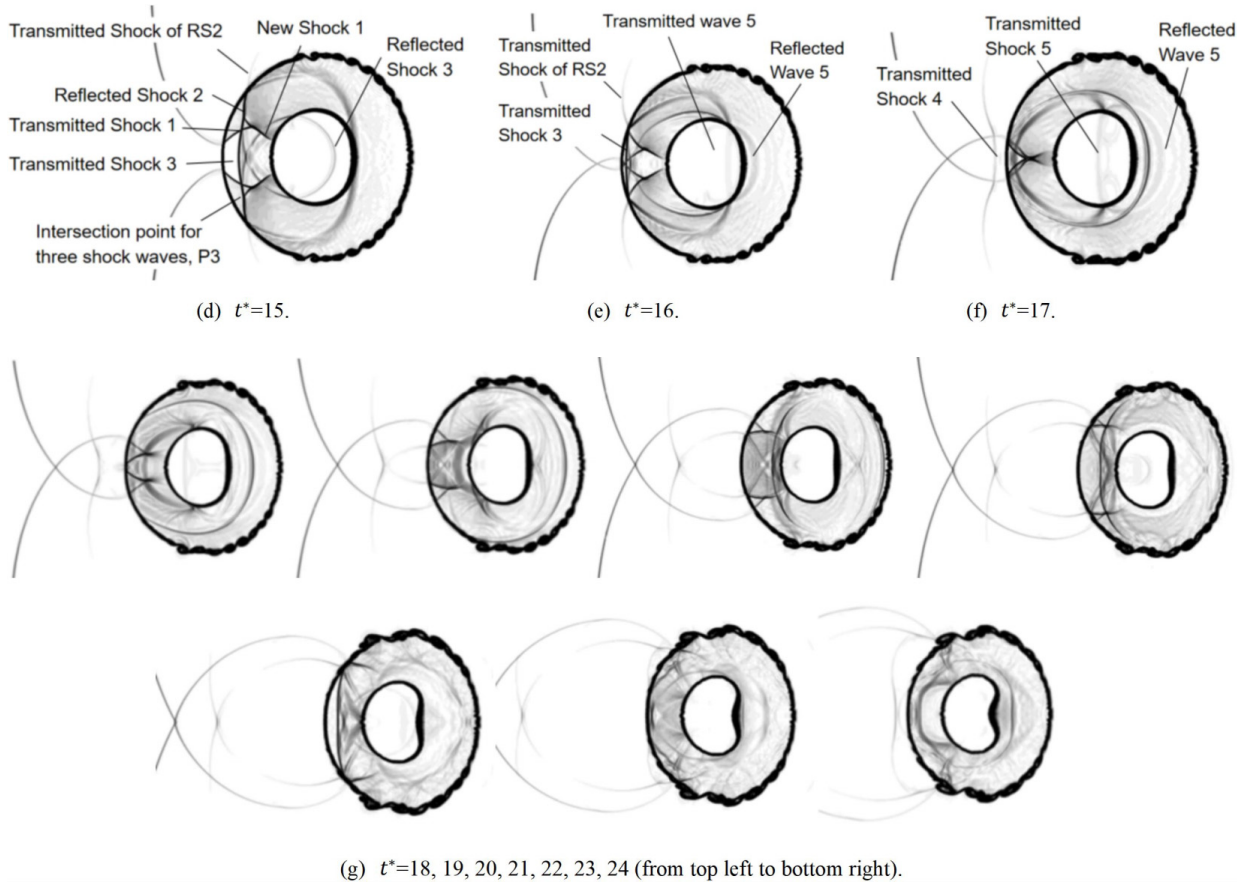
FIG. 9. (*Continued*).

2. Late development of pure cylinder and cylinder ring

In the later stages of the evolution process, the internal kidney-shaped gas bubble continues to move downstream, as seen in Figs. 10(a)–10(g). For the internal bubble region in the case with a cavity, it is observed that a cylindrical jet forms and grows over time, displaying similarities to the shock–helium bubble case. Initially, a mushroomlike structure containing a pair of vortices [Fig. 10(h)] develops in the downstream direction and then reaches the DSB [Fig. 10(i)]. The distance between the USB and DSB decreases, and the internal bubble gradually splits into two smaller bubbles [Fig. 10(j)]. Subsequently, two pairs of vortices move in opposite directions and spray separately into two nitrogen bubbles, forming several smaller jets [Fig. 10(k)]. These newly formed small curved jets spin around and move towards the cylinder-bubble interface again, rolling the small bubble interface upstream. Finally, the curved interfaces form another mushroom containing a pair of vortices and tend to impact the USB [Fig. 10(l)]. These processes introduce complex impacts and interactions into the internal region of an originally pure cylinder, enhancing the mixing of gas and cylinder.

Additionally, in a shocked pure cylinder, the high pressures (OZ) generated by the shock focusing inside the cylinder lead to the formation of an outward jet, as shown in Fig. 3. Gradually, the induced jet approaches the DSC of a pure cylinder. However, in the case with a cavity, the internal bubble alters the motion of the shock waves, disrupting the OZ and reducing the tendency for jet formation, as also observed in Fig. 9.

In the literature [5,33,47–49,55–59], investigations of configurations similar to ours, but under subcritical conditions, are presented. We compare our results with existing subcritical studies [57,59] to understand the influence of near-critical conditions. Both Feng *et al.* [57] (gas cylinder)
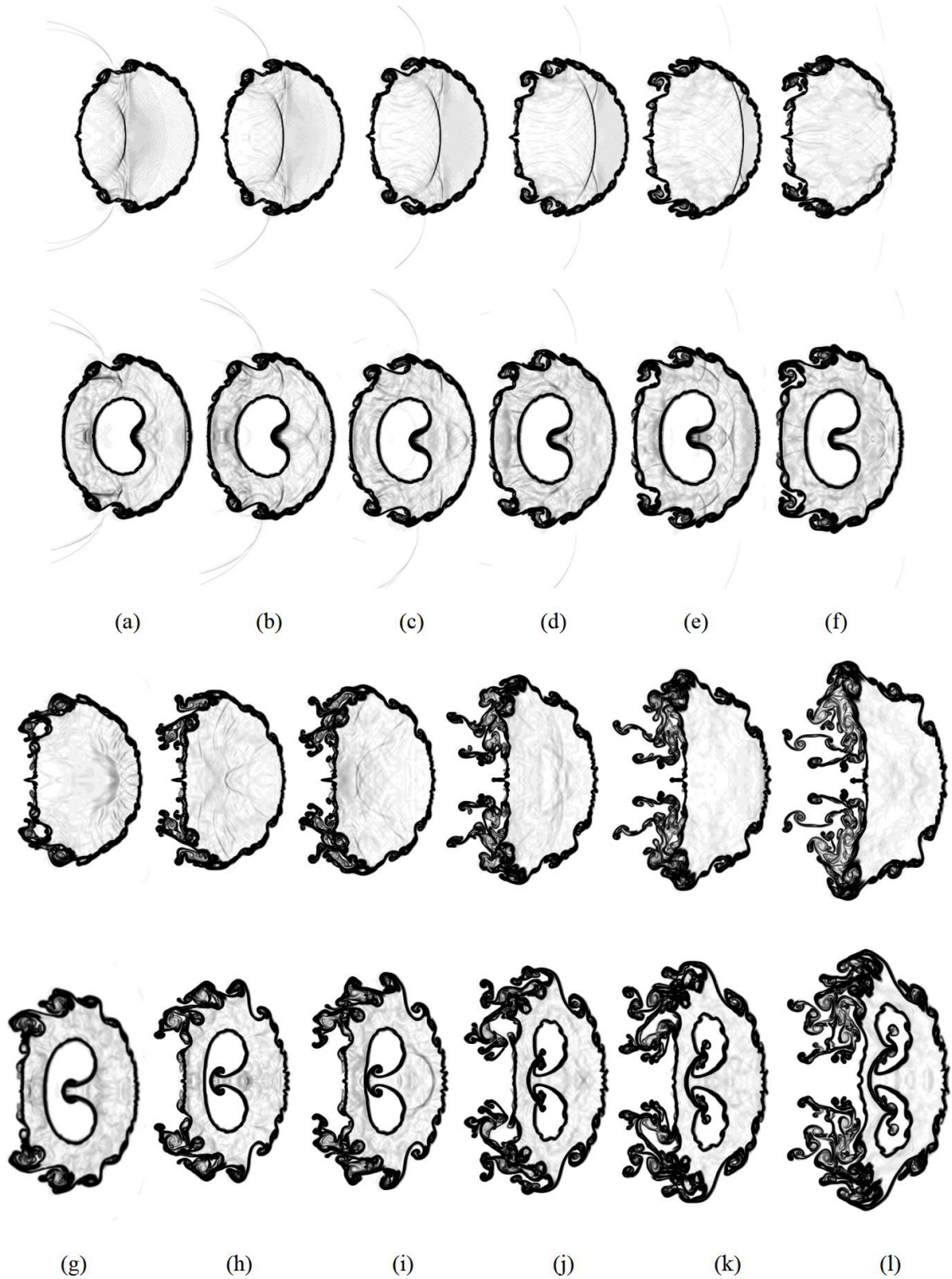
FIG. 10. Late evolution of the jet formation of pure cylinder and cylinder ring at near-critical conditions at $t^* =$ (a) 27, (b) 29, (c) 31, (d) 33, (e) 35, (f) 37, (g) 40, (h) 46, (i) 49, (j) 56, (k) 60, and (l) 66.

and Xiang and Wang [59] (water column) employed configurations with comparable Mach numbers to ours.

In the initial stages, the wave patterns observed in our near-critical case (our Figs. 3 and 9) resembled those reported by Feng *et al.* [57] under subcritical conditions (their Figs. 4 and 7). This suggests similar shock interactions (Mach stem, transmitted shock, shock focusing, etc.).
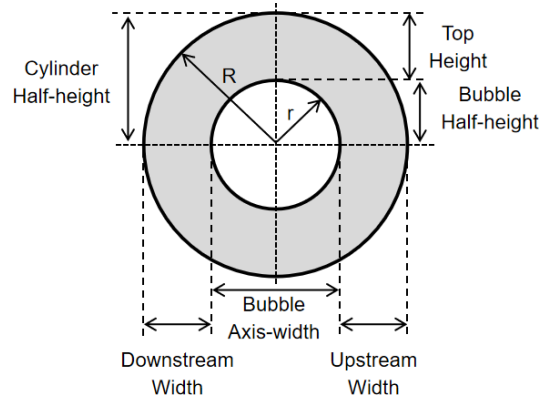
FIG. 11. The diagram of the measured parameters (sketch map).

However, the deformation behavior of our near-critical cylinder diverged significantly from the SF_6 gas cylinder response under subcritical conditions [57].

Interestingly, our near-critical wave patterns (our Figs. 3 and 9) differed from those observed by Xiang and Wang [59] for a subcritical water column without a cavity (their Fig. 5). However, the two-phase structures observed in their study with a cavity (their Figs. 14 and 16) exhibited a strong resemblance to the deformation behavior of our near-critical cylinder (our Fig. 10).

These comparisons lead to the following conclusions:

(i) Early-stage wave patterns in our near-critical cylinder case are similar to subcritical SF_6 gas cylinder cases [57].

(ii) The deformation behavior of our near-critical cylinder deviates significantly from the classical subcritical SF_6 gas cylinder behavior shown in Ref. [57].

(iii) While the wave patterns in our case differ from subcritical water columns, the deformation behavior of our near-critical cylinder closely resembles that of a subcritical water column in air as investigated by Xiang and Wang [59].

3. Quantitative analysis of shock-cylinder ring interaction

Figures 11 and 12 present a quantitative analysis of the shock-cylinder ring interaction, focusing on the evolution of key parameters. These parameters include the top height of the cylinder ring, the half-height of the internal bubble, the width of the inner bubble, the upstream width of the cylinder ring, and the downstream width of the cylinder ring. This analysis allows for a detailed understanding of the complex interactions taking place.

Top height of the cylinder ring (green line). After T1, the IS induces Richtmyer-Meshkov instabilities (RMIs), leading to the development of concave-convex structures in the two-phase interface. These instability structures grow and rotate forward, resulting in variations in the top height of the cylinder ring.

Half-height of the internal bubble (purple line). Following T2, this parameter initially remains relatively flat. However, as transmitted shock 1 (TS1) passes the semicircle of the internal bubble, it begins to decrease due to the converging TS1. Subsequently, the internal bubble takes on a kidney shape and the height gradually increases.

Half-height of the cylinder ring (dark yellow line). This parameter is the sum of the top height of the cylinder ring and the half-height of the internal bubble, which reflects the behavior of the top height of the cylinder ring and closely follows the same trends.

Upstream width of the cylinder ring (black line). The width decreases shortly after T1. Subsequently, as TS1 interacts with the USB, the width tends to increase, mainly due to the formation of the kidney-shaped internal bubble.

Width of the internal bubble (blue line). The width of the internal bubble begins to decrease after T2.
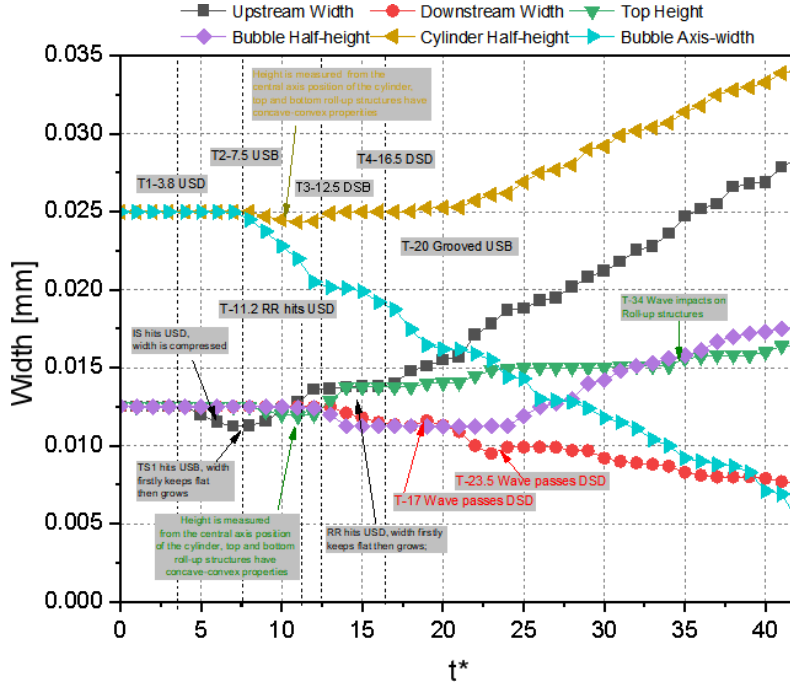
FIG. 12. The evolution histories of the measured parameters of the cylinder ring. T1–T4 separately represent four important times: IS reaches the USC, TS1 reaches the USB, TS2 reaches the DSB, and TS3 reaches the DSC. The dimensionless time used here is calculated from the beginning and is normalized by 8.68×10^{-6} s. The heights are measured at the line $x = 50$ mm.

Downstream width of the cylinder ring (red line). After TS2 passes the DSB, the downstream width of the cylinder ring decreases. It slightly increases after TS3 passes the DSC, but then continues to decrease. Another TS wave passing the DSC induces a small increase. Subsequently, the cylinder ring appears to stretch in the normal direction, and the width between DSC and DSB decreases. A decreased jet formation near the DSC is also observed, which differs from the behavior in shock interaction with a pure cylinder.

B. Quantitative comparison between pure cylinder and cylinder ring

1. Quantitative analysis of vorticity dynamics

Baroclinic vorticity production arises from unbalanced gradients between density and pressure, particularly when the IS or TS passes the two-phase interface. This phenomenon plays a crucial role in RMI and the induction of turbulent mixing. Figure 13 shows the process of vortex generation by baroclinic production in the shock-cylinder ring interaction. The vorticity transport equation is represented by $D\omega/Dt = 1/\rho^2 \nabla \rho \times \nabla p$. The angle between the pressure gradient and density gradient is most significant near the top and bottom vertices of the cylinder, as depicted in Fig. 14(a). The vortex pairs develop near the pits and bumps (peaks and valleys) of the outer cylinder, gradually increasing in intensity. Notably, in both cases with and without a cavity, vortex growth and rotation are observed near the top and bottom vertices of the cylinder, ultimately forming prominent wake roll-up structures [Figs. 13(a) and 13(b)]. Positive and negative vortices predominantly form on the upper and lower surfaces of the outer cylinder, respectively.

In the pure cylinder case (without a cavity), a jet is evident near the DSC, with the vertex of the jet being particularly noticeable in the equator region. In contrast, in the case with a cavity, the outer jet is suppressed [Fig. 13(c)], but baroclinic effects caused by shock interaction with the internal light bubble within the heavy cylinder environment lead to additional vorticity generation. The newly formed internal mushroom jet is associated with a pair of vortices characterized by opposite spin

(a) t^*=5, 10, 15, 20 (from left to right).

(b) t^*=25, 30, 35, 40 (from left to right).

(c) t^*=45, 50, 55, 60 (from left to right).
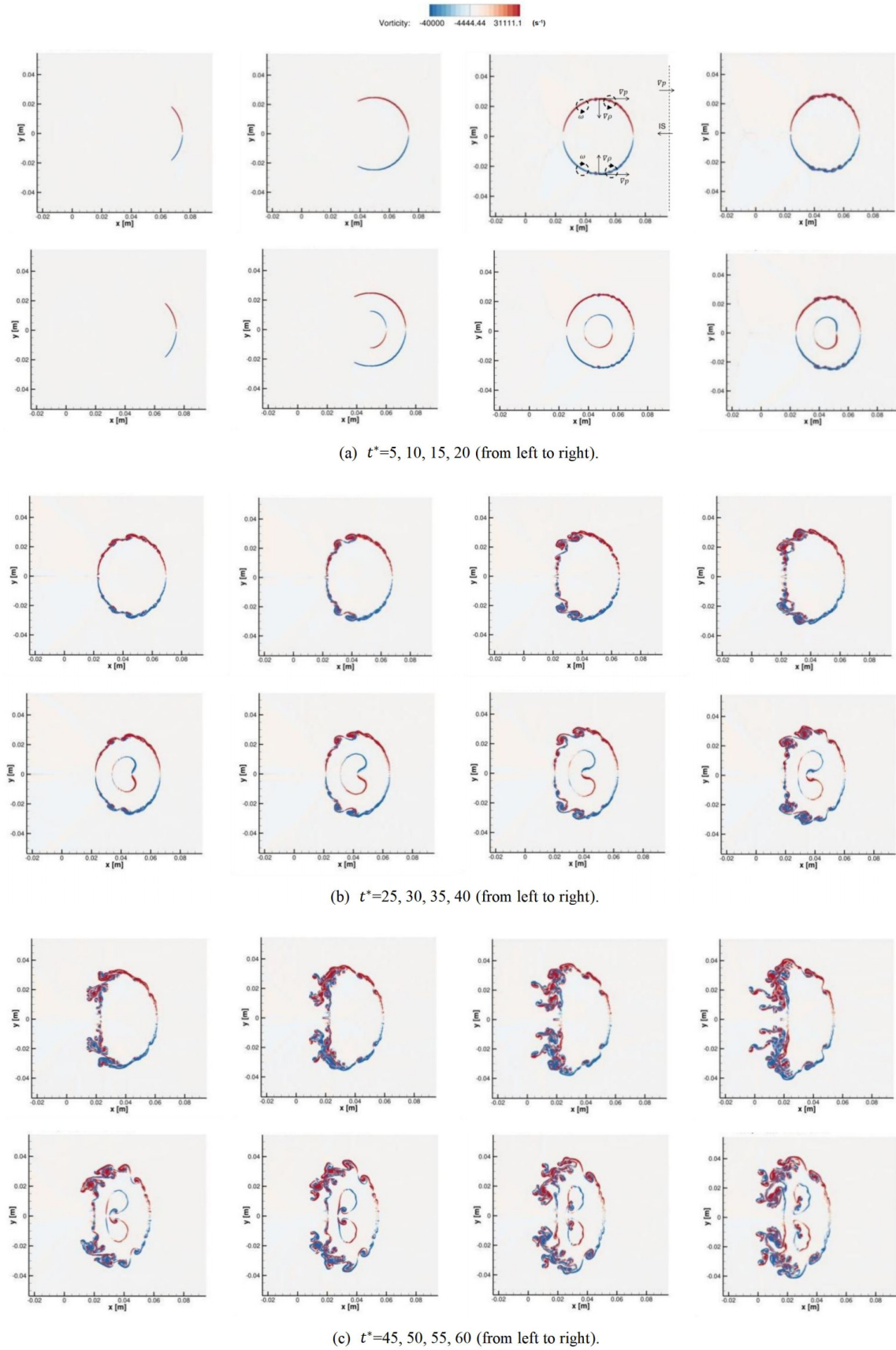
FIG. 13. Schematic diagram of vorticity generation in the shock-cylinder ring interaction (vorticity restricted to the same range of values). For t*, (a) 5, 10, 15, 20, (b) 25, 30, 35, 40, (c) 45, 50, 55, 60, (d) 65, 70, 75, 80.
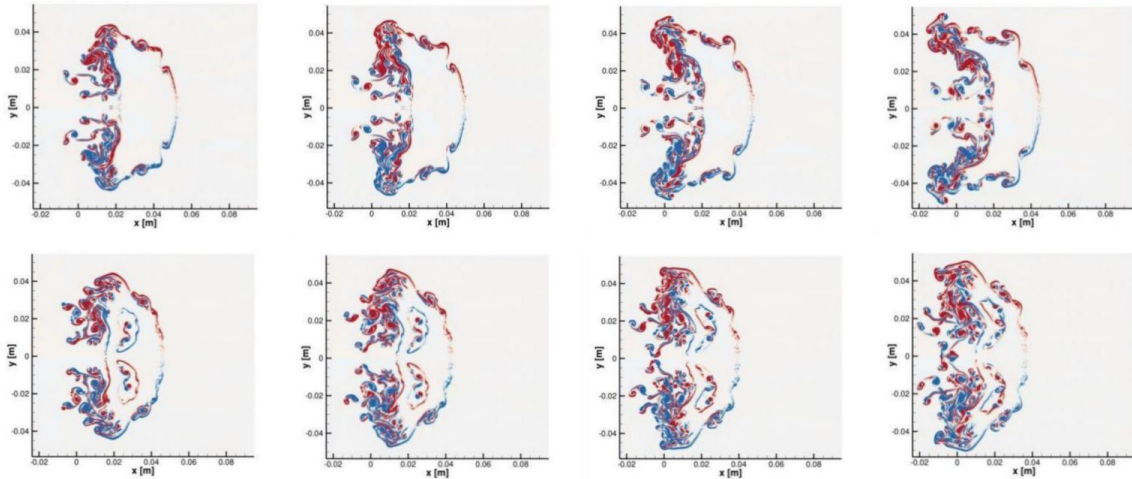
(d) t^*=65, 70, 75, 80 (from left to right).

FIG. 13. (*Continued*).

directions [Fig. 13(c)]. This jet carries roll-up vortex structures. Vortex patterns of negative and positive vorticity primarily form on the upper and lower surfaces of the inner bubble, respectively, which is the opposite pattern to that observed on the outer cylinder.

In Fig. 14, we examine the impact of an internal gas cavity on the time evolution of enstrophy in the shock wave–cylinder interaction at near-critical conditions. Enstrophy, which accounts for compressibility, is presented in a mass-averaged form as $(\int \rho\omega^2 dxdy)/(\int \rho dxdy)$. For both cases, with and without a cavity, the enstrophy values are initially zero before the shock wave reaches the USC. Subsequently, they increase almost linearly. In the early stage ($t^* < 36$), enstrophy in both cases is similar, primarily due to the negligible enstrophy of the internal bubble. However, once the internal bubble forms a jet, the enstrophy of the cylinder ring case becomes greater than that of the pure cylinder case. During a narrow time interval ($63 < t^* < 69$), the enstrophy of the pure cylinder case surpasses that of the cylinder ring case. This shift could be attributed to the formation of a jet
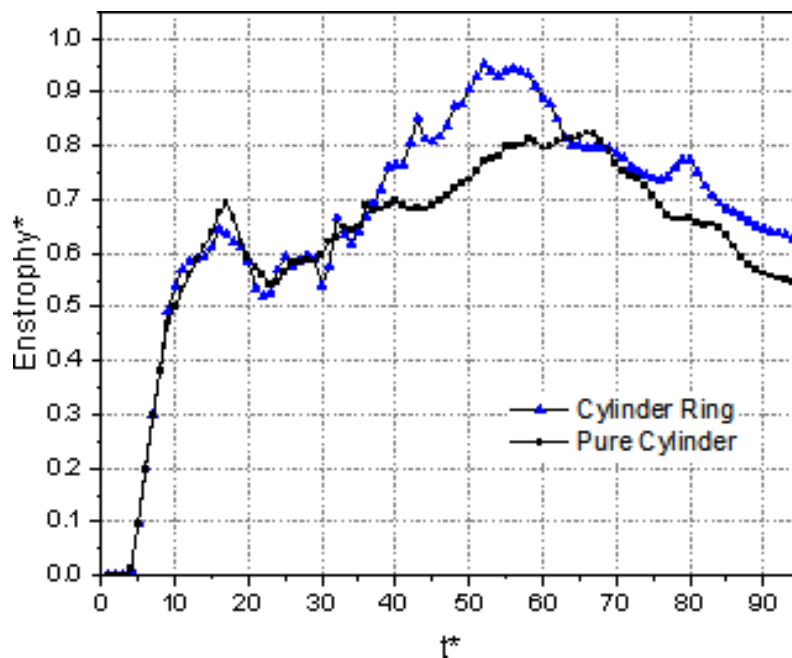
FIG. 14. The evolution of the enstrophy integrated in the domain (normalized by 1×10^8 s^{-2}).
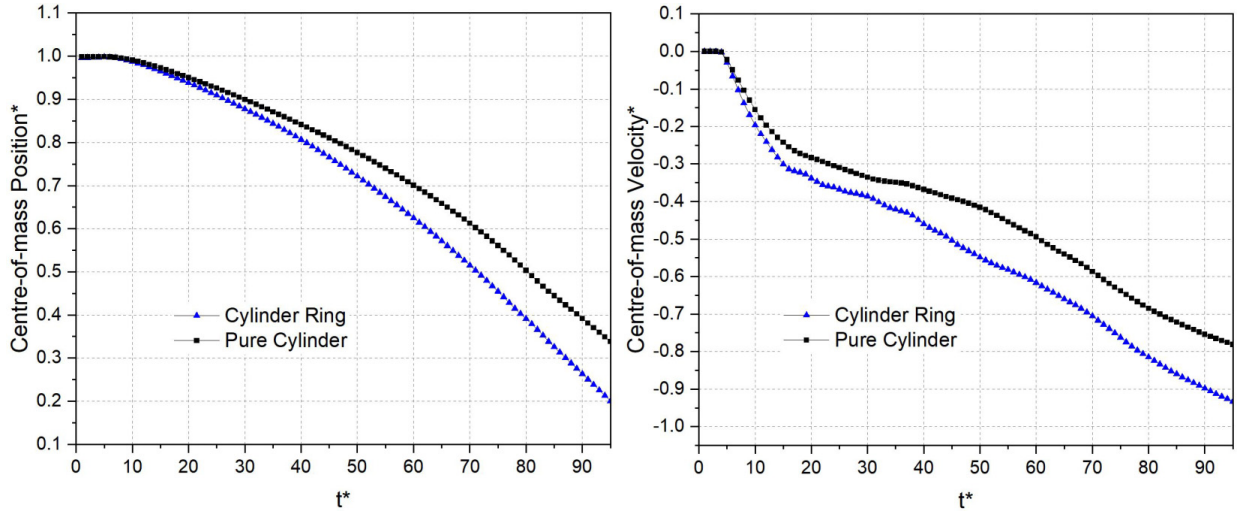
FIG. 15. The drift of the center-of-mass position and velocity (dimensionless by 0.05 m and 100 m/s).

near the downstream surface of the pure cylinder and the role of the internal bubble in accelerating the vorticity consumption process.

As the internal bubble forms additional mushroom structures, which contain more enstrophy, and with the presence of more complex structures near the downstream surface, the trend is reversed, and the enstrophy of the cavity case exceeds that of the pure cylinder case ($t^* > 69$). Overall, the generation of baroclinic vorticity significantly increases enstrophy during the early and intermediate stages of shock wave interaction with the two-phase interface. This enhanced vorticity promotes the mixing of internal and external ambient gases with the fuel cylinder (or ring) and facilitates vorticity energy transfer and consumption, ultimately leading to a reduction in enstrophy strength.

This analysis illustrates how the internal gas cavity influences the enstrophy dynamics in the shock-cylinder ring interaction, particularly in the context of enstrophy generation, transfer, and consumption throughout the interaction process.

2. Drift of the center-of-mass position and velocity

The center-of-mass properties of both the deforming cylinder and the cylinder ring are essential for diagnostics [33] and can be quantitatively analyzed through simulations. Drift analysis involves calculating the center-of-mass position and velocity of these objects as indicated by the following equations:

$$x_c = \frac{\int (1 - \xi_{\text{Gas}})\rho \boldsymbol{x} dx dy}{\int (1 - \xi_{\text{Gas}})\rho dx dy}, \tag{13}$$

$$u_c = \frac{\int (1 - \xi_{\text{Gas}})\rho \boldsymbol{u} \, dx dy}{\int (1 - \xi_{\text{Gas}})\rho \, dx dy}. \tag{14}$$

The integration region refers to the entire computational domain.

Figure 15 provides a comparison of the center-of-mass location and velocity between the pure cylinder and the cylinder with an embedded gas cavity. Generally, the center-of-mass location and velocity of the ring are similar to those of the pure cylinder. However, the presence of the gas cavity results in the entire ring moving at a higher velocity compared to the pure cylinder, which can have implications for enhancing the mixing process.

C. Three-dimensional simulation of shock interaction with droplet with and without cavity

In this section, we will conduct three-dimensional simulations of shock interaction with a droplet, under the same conditions as described in Sec. III A. The setup involves using a quarter of the
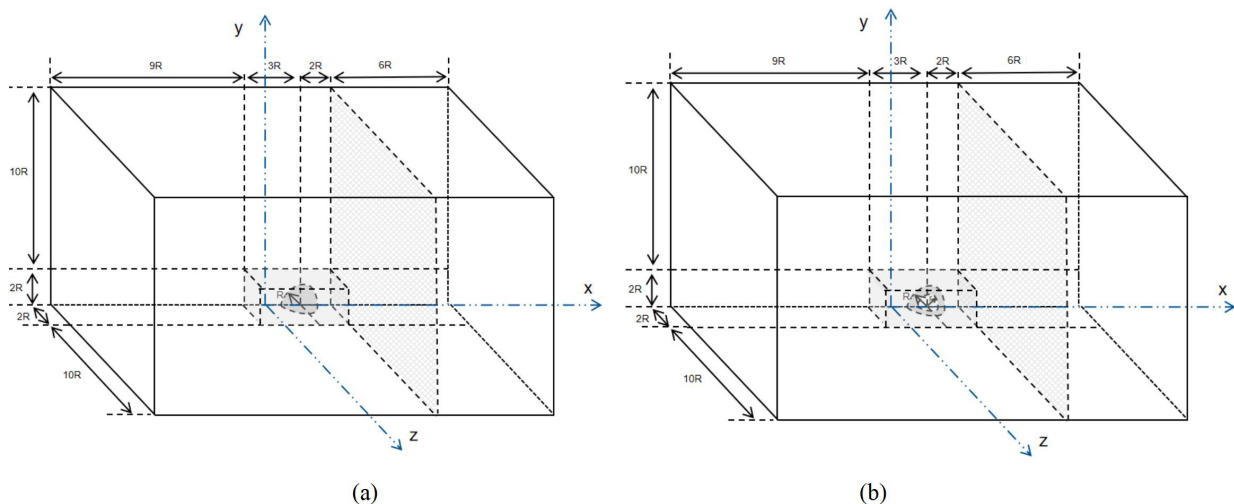
FIG. 16. Schematic of the computational domain for shock interaction with (a) a droplet or (b) a droplet shell.

spherical droplet and a quarter of the droplet shell, as depicted separately in Figs. 16(a) and 16(b), with a diameter ratio of $r/R = 0.5$.

Building upon the insights gained from the two-dimensional results, we will observe the evolution of the shock-droplet interaction. To capture the intricate details of the spherical droplet, a uniform mesh will be employed in the region adjacent to the droplet, while a coarser mesh will be used in regions farther away from the droplet. Specifically, a uniform mesh resolution of 0.115 mm will be applied within the shadowed cuboid box region, which matches the parameters used in the two-dimensional case. This resolution corresponds to approximately 434 cells to effectively capture the characteristics of the spherical droplet. This region will contain about 2.1×10^8 mesh cells to comprehensively cover the typical development area of the droplet shell.

Beyond this region, the mesh resolution will become progressively coarser at a ratio of 1.1. All other conditions will be consistent with those used in the two-dimensional simulations, with the adoption of symmetry boundary conditions for two surfaces connected to the droplet.

It is worth noting that the computational configuration used in this study surpasses that of previous simulations involving water droplets, such as the work by Meng and Colonius [33], where they used WENO3 and a grid resolution equivalent to 100 cells per original droplet diameter. In the following section, we will delve into the deformation of the two-phase interfaces and the development of vortices, considering the three-dimensional characteristics of the interaction.

1. Evolution of surface deformation

Simulating two-phase interfaces often results in a smeared interface spanning several grid cells, as observed in our study and others [33]. This is because the chosen method inherently averages properties across a small region. The accuracy of the interface visualization can be further affected by the specific value chosen for the isosurface or isopleth (which represent surfaces or lines of constant value).

In our postprocessing, we distinguish between liquid and gas phases using the mass fraction of the gas phase and employ isosurfaces ranging from 0.01 to 0.99 to represent the two-phase interface. These isosurfaces account for the inherent uncertainty in the postprocessing stage due to the smeared interface characteristics [refer to Figs. 17(f)–17(h) and the Supplemental Material [95] for examples]. As noted in Ref. [33], the choice of gas mass fraction value can influence the observed interface structures.
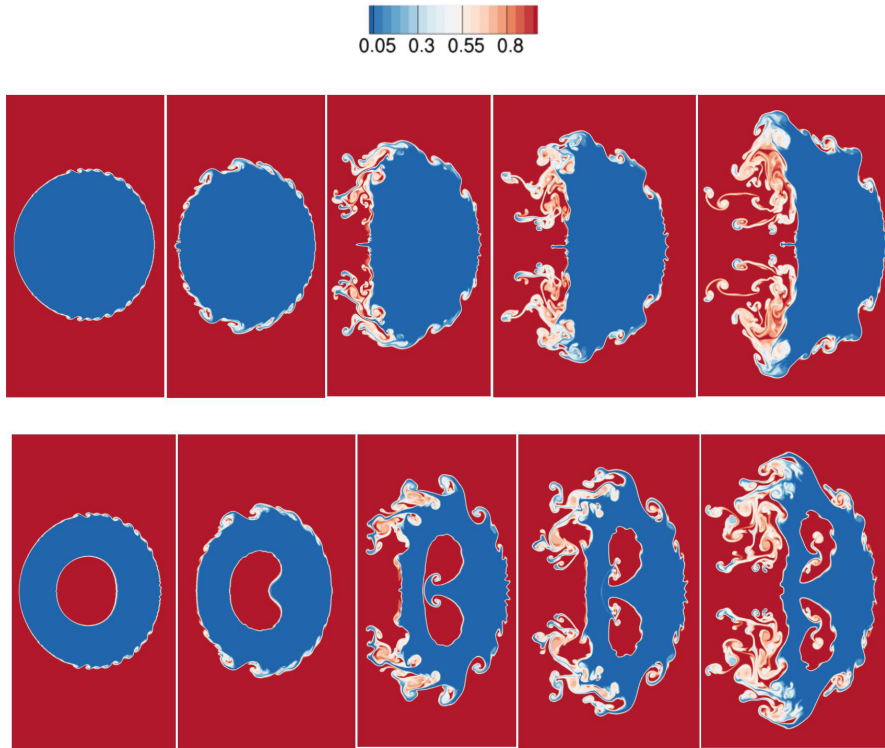
(a) Pure cylinder: upper; the cylinder embedded with a cavity: lower.
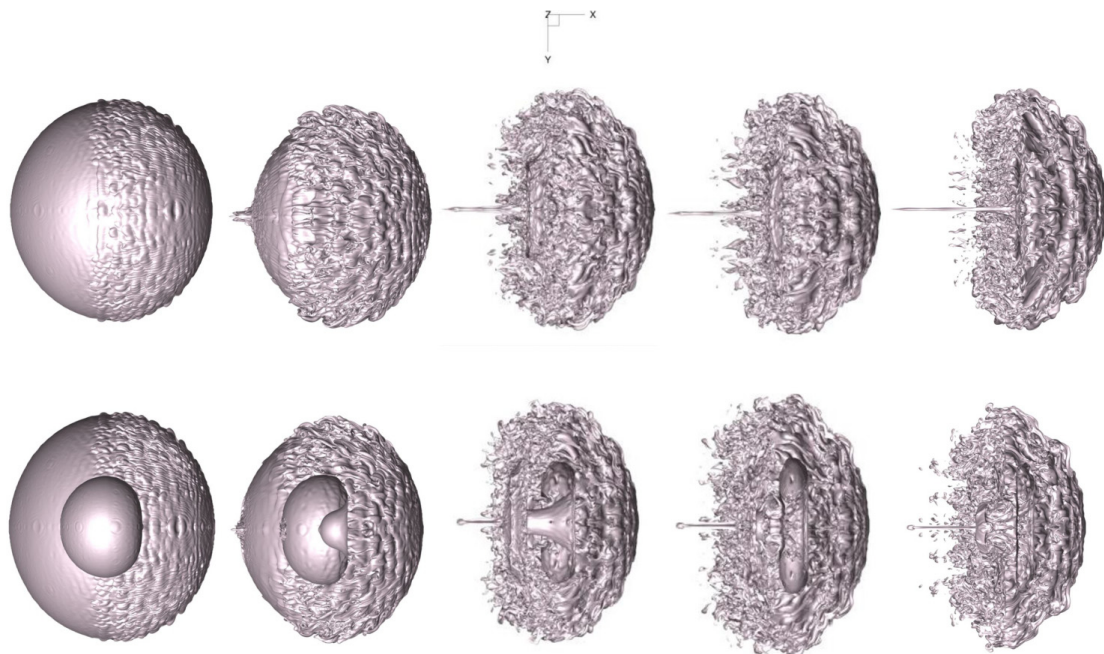
(b) Pure droplet: upper; droplet shell: lower.

FIG. 17. (a) Gas mass fraction contour of the cylinder case at $t^* = 15, 27, 49, 56$, and 66 (from left to right). [(b)–(e)] Isosurface of the gas mass fraction 0.5 of the droplet case at $t^* = 15, 27, 49, 56$, and 66 (from left to right). (f) Isosurfaces of the gas mass fraction, 0.01, 0.05, 0.25, 0.5, 0.75, 0.95, and 0.99 (from left to right) at $t^* = 27$. (g) Isosurfaces of the gas mass fraction, 0.01, 0.05, 0.25, 0.5, 0.75, 0.95, and 0.99 (from left to right) at $t^* = 49$. (h) Isosurfaces of the gas mass fraction, 0.01, 0.05, 0.25, 0.5, 0.75, 0.95, and 0.99 (from left to right) at $t^* = 56$.
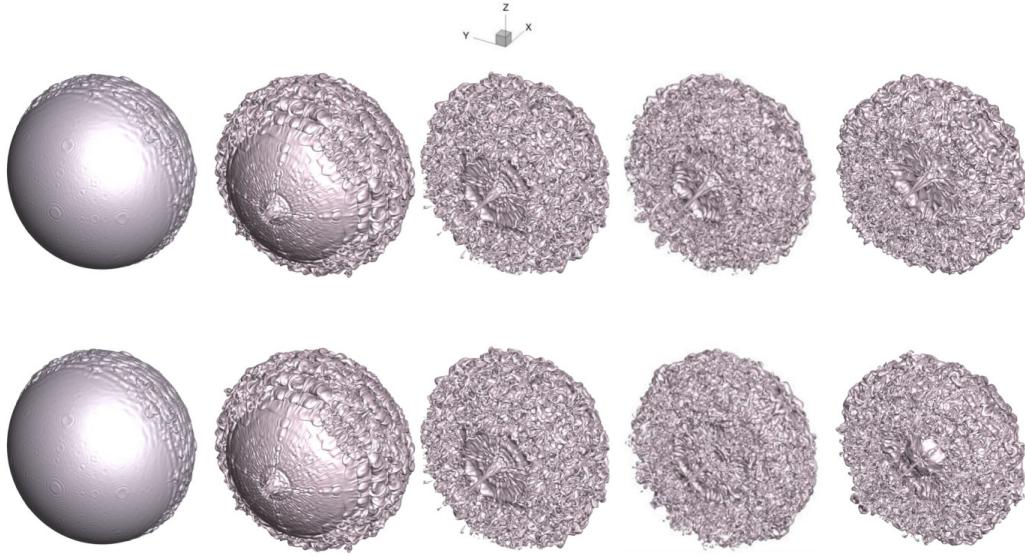
(c) Pure droplet: upper; droplet shell: lower.
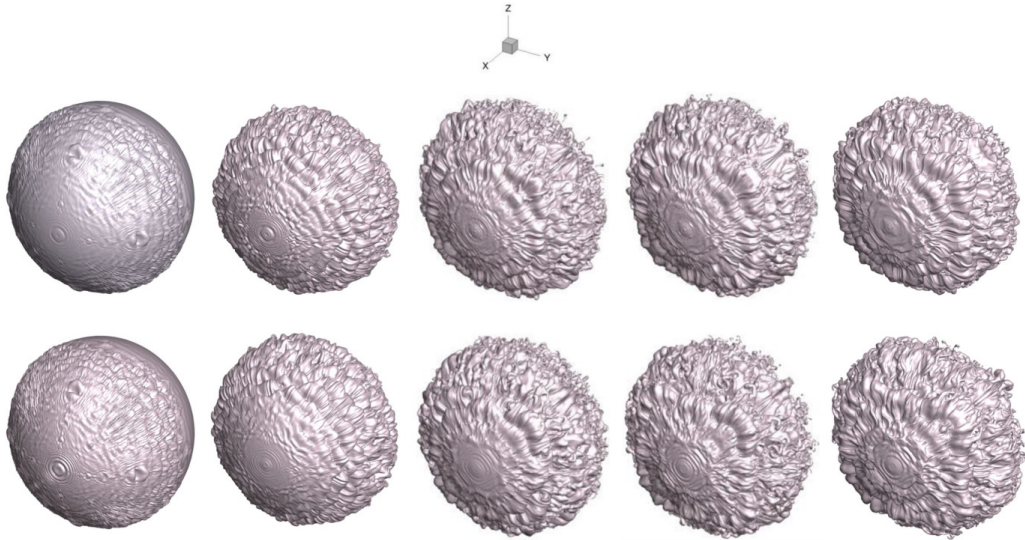
(d) Pure droplet: upper; droplet shell: lower.
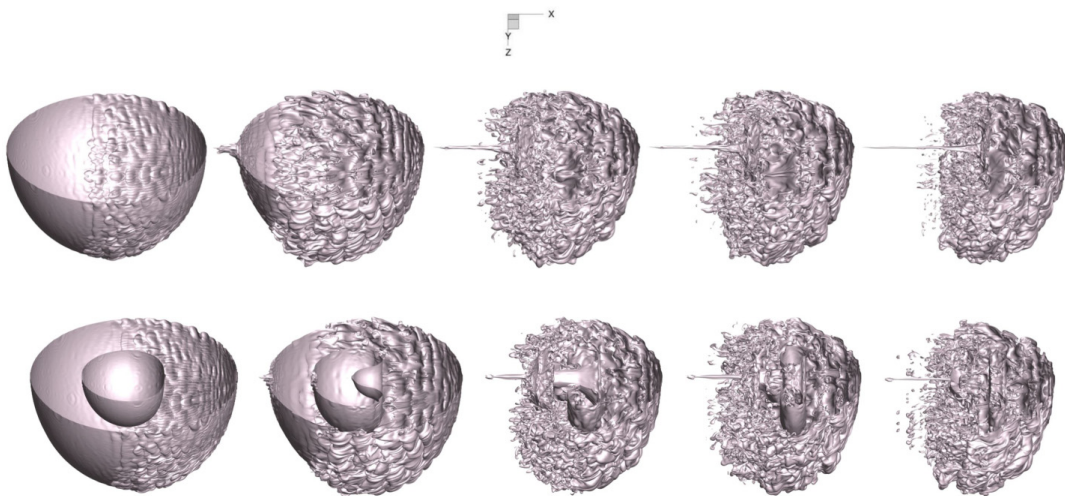
(e) Pure droplet: upper; droplet shell: lower.
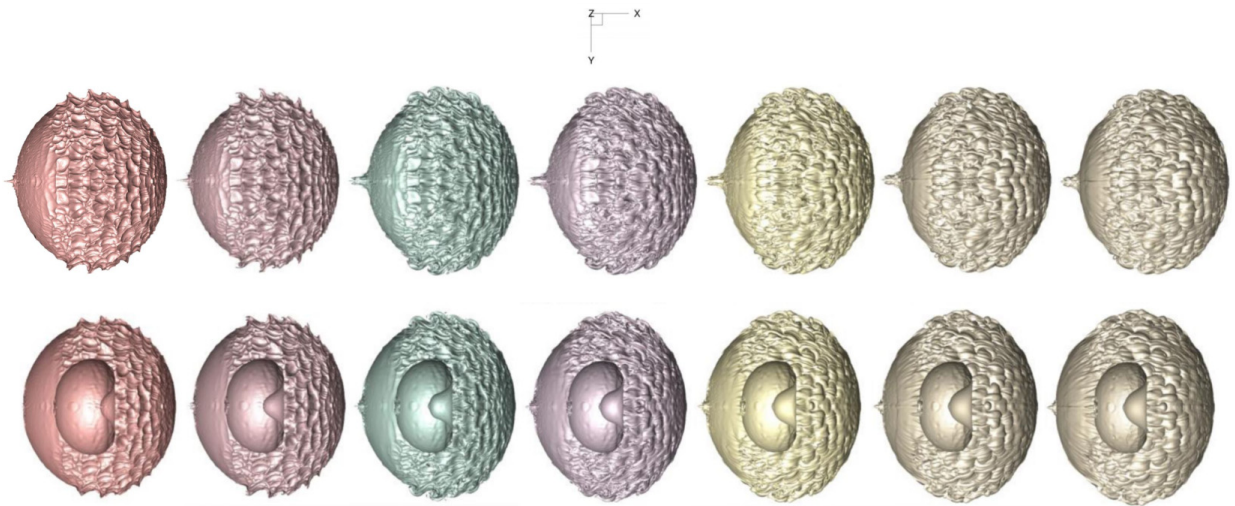
FIG. 17. (*Continued*).

(f) Pure droplet: upper; droplet shell: lower.
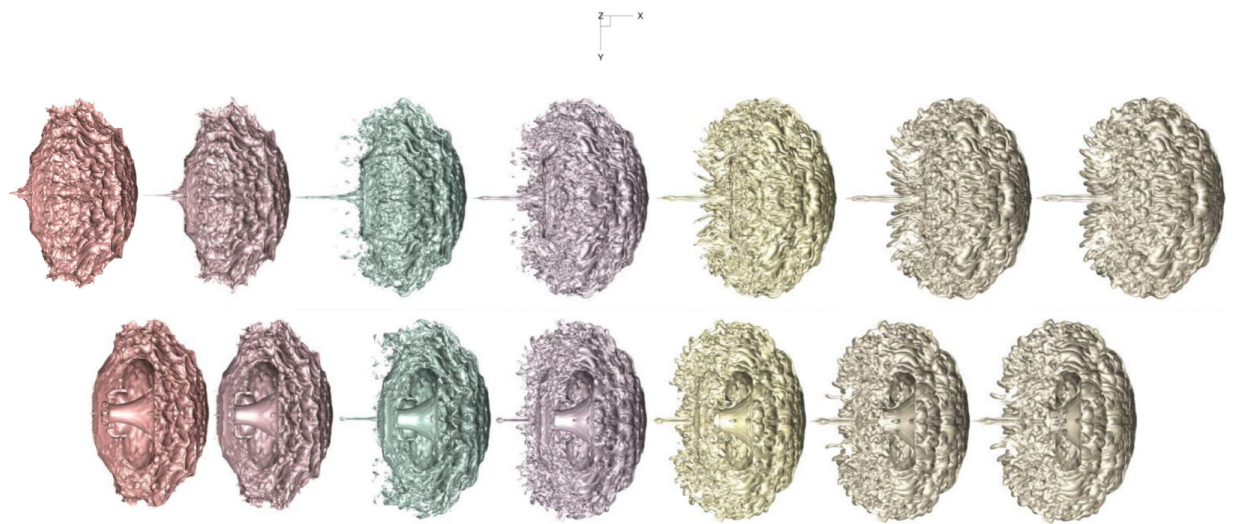
(g) Pure droplet: upper; droplet shell: lower.
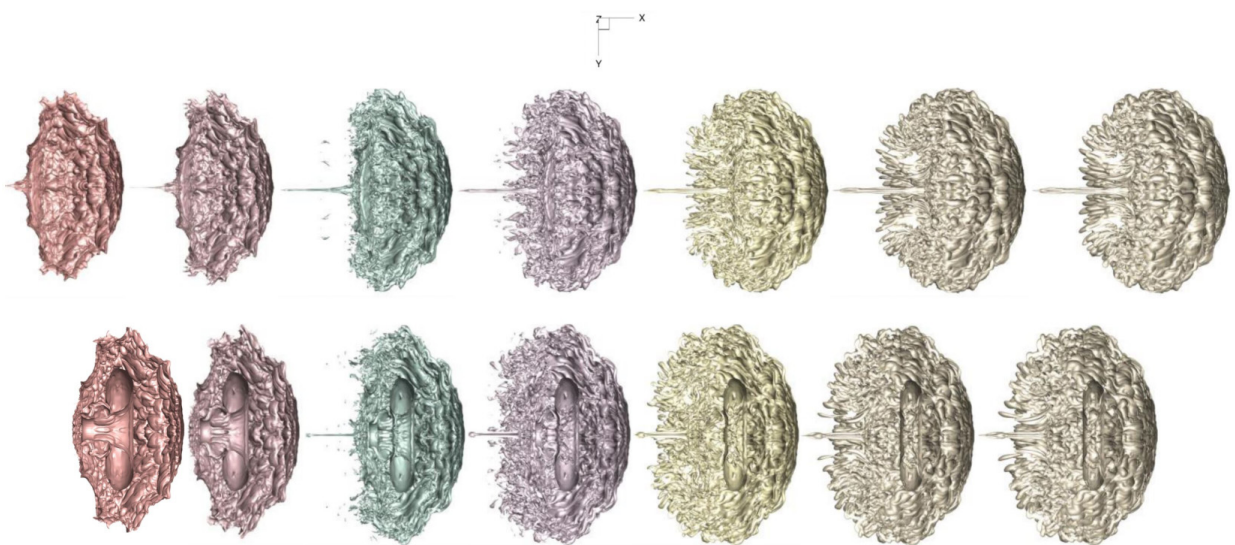
(h) Pure droplet: upper; droplet shell: lower.

FIG. 17. (*Continued*).

It is important to remember that these three-dimensional structures are only visualized for a specific isosurface value (e.g., 0.5 for gas mass fraction). This approach aligns with the postprocessing technique used in Ref. [33], where varying gas fraction values for isosurfaces resulted in the visualization of different droplet breakup structures. Unfortunately, there is no perfect choice for the isosurface value, as the numerical method itself introduces uncertainty that cannot be entirely eliminated. In essence, the chosen value (mass or volume fraction) to define the interface affects the shapes and structures captured by the isosurfaces.

Similar to the work in Ref. [33], we acknowledge the presence of smeared or diffuse features in our visualization, even with our resolution of 434 cells per initial diameter to represent the droplet. Nevertheless, based on our grid convergence study and the chosen numerical scheme, we are confident that the dominant structures and key features are accurately captured. While the numerical scheme might lead to the appearance of smaller breakups, these phenomena cannot be validated against experimental data and are likely artifacts of the simulation. It is important to emphasize that the overall conclusions are not affected by the isosurface value selection, as we consistently apply the same analytical and quantitative methods throughout all cases. Considering the numerical methods employed and the achieved mesh independence with 434 grids per diameter, the results provide a reasonable representation of the physical phenomena, with the understanding that the smeared region incorporates the effects of numerical viscosity.

The results depicted in Fig. 17 illustrate the progression of deformed two-phase contact structures for both the cylinder case and the three-dimensional droplet case simulations. A threshold value of 0.5 is employed for the isosurface to delineate the gas phase for the three-dimensional droplet case. Various distinctive deformation scenarios that capture the dynamics of the droplet structure have been chosen for analysis. The qualitative descriptions provided in two-dimensional simulations, as discussed in Secs. III A 1 and III A 2, are equally applicable to the three-dimensional simulations, with the primary distinction being the added dimension. In comparison to the two-dimensional findings, the deformation processes remain quite analogous, yet the inclusion of the third dimension allows for a more comprehensive representation of the dynamics. The structures observed in these simulations, including sheets, petal-shaped structures or lobes, and ligaments, exhibit pronounced three-dimensional characteristics that were not discernible in the two-dimensional simulations.

Combining the insights from Secs. III A 2 and III B 1, we can draw the following conclusions: The droplet effectively behaves like a solid block, contributing to the formation of a plume shape characterized by a flattened disk or a cupcakelike structure. Within the recirculation region, counter-rotating vortices develop near the leeward side of the droplet, playing a crucial role in shaping this distinctive form and drawing liquid sheets from both the droplet's equator and its flattened rear [33]. The presence of an enclosed cavity attached to the downstream side of the deforming droplet is associated with the development of a recirculation region that entrains fluid and redirects it upstream to impact the leeward side of the droplet. The continual deformation of the droplet in the normal direction increases its projected area for aerodynamic effects, further promoting the flattening of the liquid droplet and assisting in its breakup [49]. Additionally, as shown in Fig. 17(e), the internal cavity serves to reduce jet formation. Notably, the internal spherical cavity undergoes deformation, transforming into a kidney-shaped structure before breaking into a toroidal shape.

Surface tension is typically disregarded in transcritical flows [10,51,52,71–76] because the surface tension coefficient significantly diminishes in the vicinity of the critical point. In references related to simulation at near-critical conditions [51,52], the Weber number is defined as $We = \rho_{post} u_{post}^2 D_0 / \sigma$, which is adopted to assess the type of deformation. For the current case with a Mach number of 1.2, with $T_{ref} = 650$ K, $p_{ref} = 6$ MPa, $u_{post} = -160.3$ m/s, $D_0 = 50$ mm, and $\rho_{post} = 40.38$ kg/m^3, assuming that $\sigma = 0.001$ N/m [51], then the approximate Weber number is about 5×10^7. It is therefore reasonable to assume that, during the initial phase of development, there should be no discernible difference between the flow simulated with or without surface tension. Consequently, it is anticipated that these cases with a very large Weber number [96] will fall into the regime of shear-induced entrainment (SIE) breakup. However, neglecting surface tension in
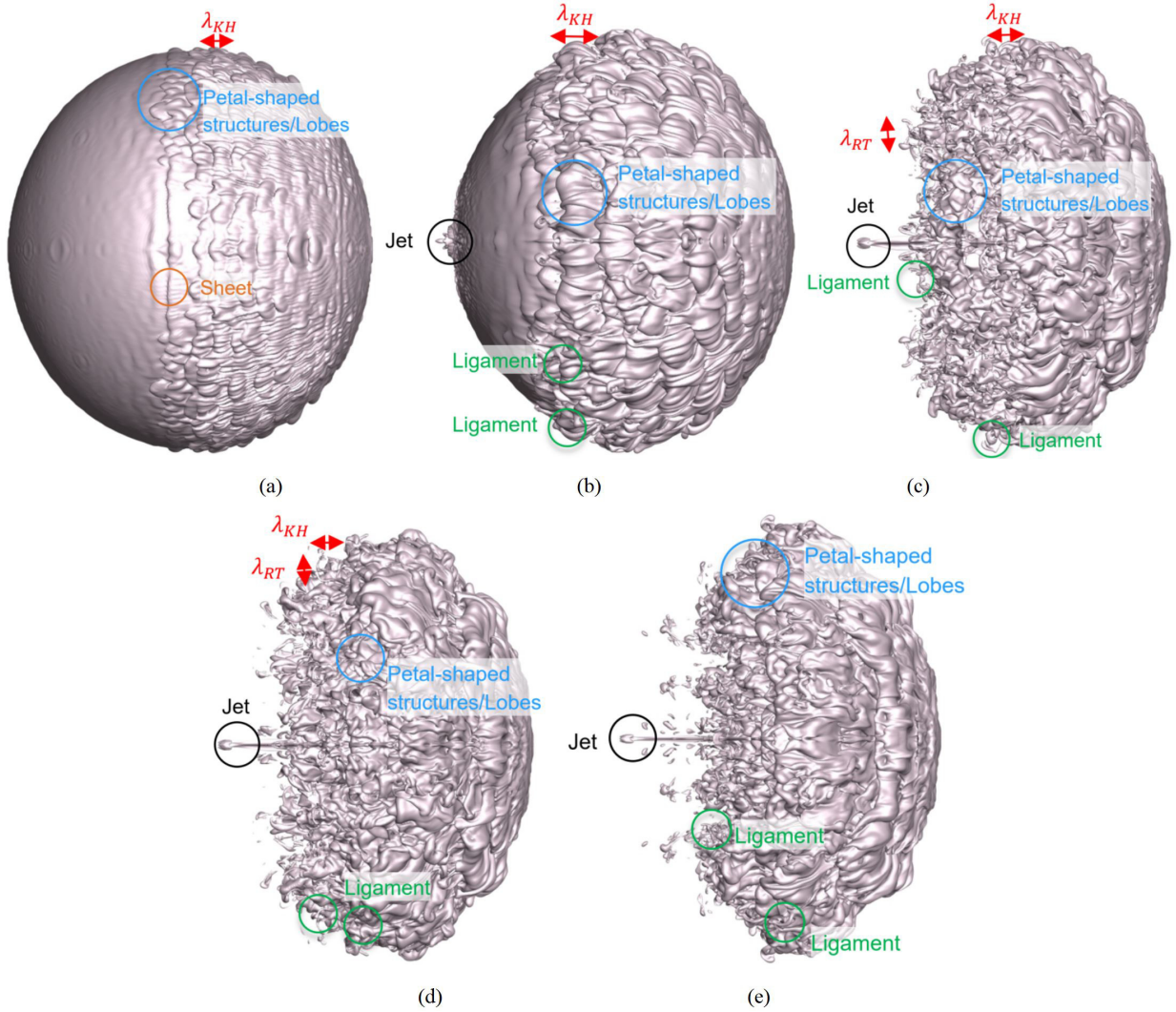
FIG. 18. Isosurface of the gas mass fraction 0.5 of the droplet with gas cavity at $t^* =$ (a) 15, (b) 27, (c) 49, (d) 56, and (e) 66.

the model simplifies the problem by replacing the actual phase interface with a contact region. While both fluids are initially separated in this region, they can mix during the deformation process. Strictly speaking, neglecting surface tension means simulating contact region deformation rather than interface breakup, although the established terminology in the field seems to differ.

In the initial stages, spanning from $t^* = 0$ to $t^* = 27$, the RMI induces morphological deformations of the two-phase structures, causing lobes to stretch and ligaments to form. In the later stages, occurring between $t^* = 49$ and $t^* = 66$, the deformation of ligaments becomes apparent, especially when visualized using an isosurface value of a mass fraction of 0.5.

The numerical results capture the key characteristics of inertia-driven mechanisms, although neglecting surface tension inherently leads to a loss of sharp interfaces. Despite satisfying the SIE breakup condition and capturing the expected phenomena, the results are limited by their numerical nature and dependence on a specific isosurface value selection. These limitations (surface tension neglect and finite resolution) confine the interpretation of the simulated structures as analogies, albeit reasonable ones based on the dominant forces.

In Fig. 18, we observe the formation of internal jets, deformation of the internal bubble, and its eventual transformation into a toroidal shape. Notably, the emergence of external jets on the downstream side of droplet (DSD) is suppressed in cases involving a gas cavity.

Our analyses are based on analogies and further confirmation will require experimental data. It should be noted that numerous mechanisms contribute to the disintegration process, an area explored in prior studies [49,97–103] yet still evolving. SIE breakup involves the formation of sheets, petal-shaped structures or lobes, and ligaments. This process is closely linked to the development of Kelvin-Helmholtz (KH) waves and flow entrainment, particularly on the windward side of the droplet, as well as liquid transport [49] due to droplet deformation, especially on the leeward side.

KH waves primarily form on the droplet's surface between the front to the peak (FTP) and the equator, where shear effects are predominant [97]. These waves can induce droplet stripping, resulting in KH-based liquid transport mechanisms [49,97,98] [see Fig. 18(a)]. As observed in Figs. 18(a)–18(c) and Sec. III A 2, KH waves gradually increase in amplitude and then deflect in the streamwise direction when becoming entrained by the external airflow. The entrainment of the flow causes the surface waves to move downstream [49], leading to the accumulation of liquid as sheets, petal-like structures, or lobes. The development of these surface structures is influenced by the entrainment force induced by the external airflow and by the driving force of the internal flow due to the KH wave. Additionally, shock-induced internal flow with vortices can contribute to the rupture of surface structures [99].

Moreover, petal-like structures or lobes undergo a cascade process [49] during the formation of ligaments, including the stretching of the structures, corrugation stretching, and the perforation of holes that lead to bridge breakup [100,101]. The formation of holes can result in the rupture of sheet and petal-like structures, ultimately yielding cylindrical ligaments. These holes can increase in size over time. In cases where surface tension dominates, these formed ligaments can undergo further secondary atomization into smaller droplets via Rayleigh-Plateau instability (RPI). However, for fluids at near-critical conditions with a relatively higher gas-liquid density ratio and high kinetic energy, surface tension effects are negligible [52] for relatively large ligaments. It should be noted that our simulation's resolution cannot capture the minuscule effects of surface tension, particularly given the chosen method's limitations in representing infinitely sharp boundaries.

Furthermore, Liang *et al.* [58] conducted an experiment on the interaction between a planar shock wave and a water droplet containing a vapor cavity under subcritical conditions. In our cases, under near-critical conditions (our Fig. 17), the ringlike structures, the transverse jets are similar to their experimental data under subcritical conditions (their Fig. 2). In this way, the deformation of our near-critical droplet behaves similarly to a water droplet in air under subcritical conditions [58].

We also analyze the drift of the center-of-mass velocity for these selected times. The results from the two-dimensional simulation are used for comparison, as shown in Fig. 19. When comparing the results between two-dimensional and three-dimensional simulations, it becomes evident that there are significant differences, highlighting the importance of three-dimensional simulations for more realistic and quantitatively accurate descriptions. The presence of a gas cavity enhances the drift velocity in both cases. While two-dimensional studies offer qualitative insights into the effects of a cavity on the droplet evolution process, three-dimensional studies provide more detailed information on deformation and interactions.

2. Vorticity evolution and vortical structures

Figure 20 shows the contour of Z vorticity of the plane $Z = 0$, and Y vorticity of the plane $Y = 0$. Figures 21 and 22 show the isosurface of $\Omega = 0.52$. $\Omega = ||B||^2/(||B||^2 + ||A||^2 + \varepsilon)$, where, ε is a minor value to prevent division by zero, $||B|| = 0.5((\partial u/\partial y - \partial v/\partial x)^2 + (\partial u/\partial z - \partial w/\partial x)^2 + (\partial v/\partial z - \partial w/\partial y)^2)$, and $||A|| = (\partial u/\partial x)^2 + (\partial v/\partial y)^2 + (\partial w/\partial z)^2 + 0.5(\partial u/\partial y + \partial v/\partial x)^2 + 0.5(\partial u/\partial z + \partial w/\partial x)^2 + 0.5(\partial v/\partial z + \partial w/\partial y)^2$.

The results presented in Figs. 20–22 demonstrate the gradual development of vortex structures after the shock interacts with the two-phase interface. The following key observations can be made:

Early vorticity induction. In the initial stages, vorticity is induced on the outer surface of the droplet due to baroclinic effects (baroclinic vorticity). Near the upstream surface of the droplet (USD), most vortices are oriented perpendicular to the flow direction [Figs. 21(a) and 22(a)].
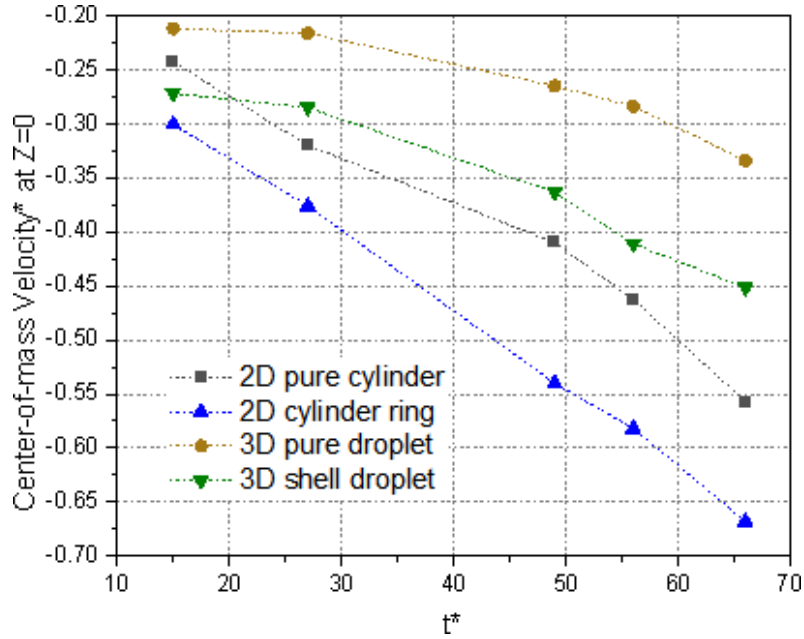
FIG. 19. The drift of the center-of-mass position and velocity (dimensionless at 100 m/s).

Streamwise-type vortices. As the simulation progresses, additional vortices are generated near the USD. Notably, most of the newly formed vortex filaments near the downstream surface of the droplet (DSD) are parallel to the flow direction [Fig. 21(b)]. These streamwise-type vortices exhibit elongated hairpinlike structures in the azimuthal direction of the vortex core [Figs. 21(c)–21(e) and 22(c)–22(e)].

Vortex stretching and mixing. Fine filaments of vorticity serve as indicators of areas with intense vortex stretching. Much like the discussion in Sec. III B 1, the heightened vorticity fosters the mixing of fluids and amplifies the process of transferring and dissipating vortex energy. In the later stages, the progression of Richtmyer-Meshkov instability (RMI), Rayleigh-Taylor instability (RTI), and Kelvin-Helmholtz instability (KHI) further contributes to the deformation of the shocked droplet and augments its mixing properties, as illustrated in Figs. 21(e) and 22(e).

Azimuthal instability. The azimuthal instability of the axisymmetric KH waves can be caused by baroclinic effects (associated with RMI or RTI) and the generation of streamwise vortices [49]. This leads to the formation of petal-like structures or lobes.

Baroclinic effects and vortex strain. At low gas-liquid density ratios, the baroclinic effects are significant due to the high-density gradient across the interface. As the density ratio increases, vortex-strain interactions (due to the vortex tilting and stretching mechanism) become more important in azimuthal modulation on KH waves due to higher gas inertia [100–103]. This results in a higher vortex strain near the liquid interface, and the contribution of the baroclinic effect to the generation of streamwise vorticity is reduced.

Roll-up vortex structures. When we combine the findings from Fig. 17, which pertains to the region near ligament formation and deformation, with the insights from Fig. 18, we observe a profusion of roll-up vortex structures, particularly streamwise vortices, as depicted in Fig. 21. These streamwise vortices exhibit a pair of positive and negative values, as shown in Fig. 20, and play a pivotal role in influencing the dynamic behavior of the system.

Such vortex structures and behavior of the droplet with a cavity represent an observation at near-critical conditions. The complex interplay of various vorticity mechanisms, baroclinic effects, and instabilities contributes to the intricate dynamics observed in the simulations.
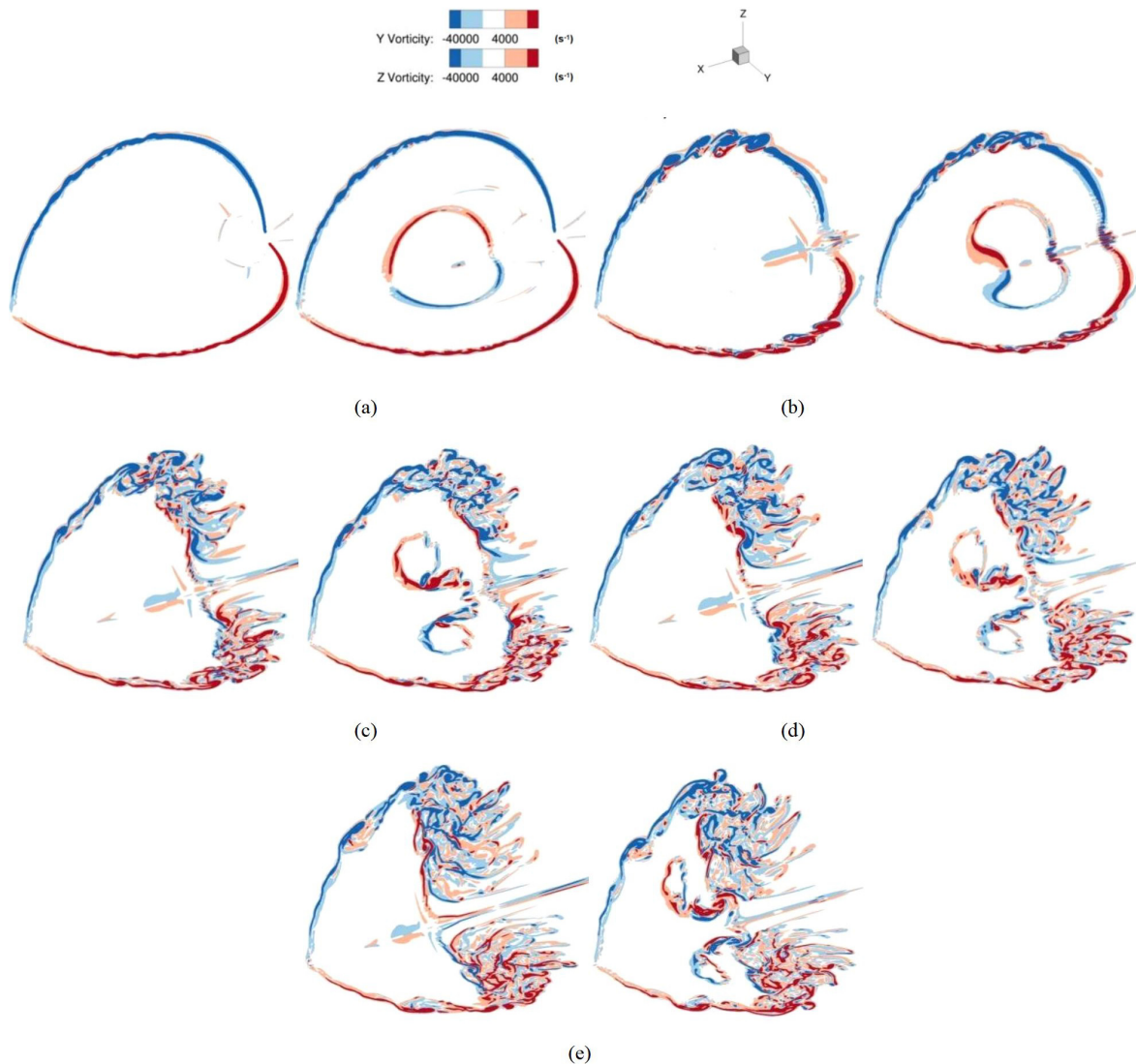
FIG. 20. The contour of Z vorticity of the plane $Z = 0$, and Y vorticity of the plane $Y = 0$ at $t^* = $ (a) 15, (b) 27, (c) 49, (d) 56, and (e) 66.

IV. CONCLUSIONS

This study examines the intricate interactions of shock waves with a cylinder or droplet containing an embedded gas cavity, particularly under near-critical thermodynamic conditions. The gas-cavity presence significantly impacts various properties of the cylinder or droplet, encompassing flow wave patterns, morphological changes, vortex formation, enstrophy, and three-dimensional developmental characteristics. For processes at a near-critical conditions, we come to the following observations.

(1) Distinct wave patterns and morphology changes: The presence of an internal gas cavity significantly alters the observed wave patterns and interactions. A detailed analysis of various parameters, including cylinder and internal bubble morphological changes, provides valuable insights into shock-induced deformation and wave interactions. We examined the interaction in detail, focusing on the early and late stages such as shock impingement, wave evolution, and morphological deformation. The internal structures observed resemble those reported in numerical and experimental studies of shocked light bubbles. Interestingly, while the wave patterns at near-critical conditions are similar to those obtained in the case with the cylinder consisting of SF_6 in air at subcritical
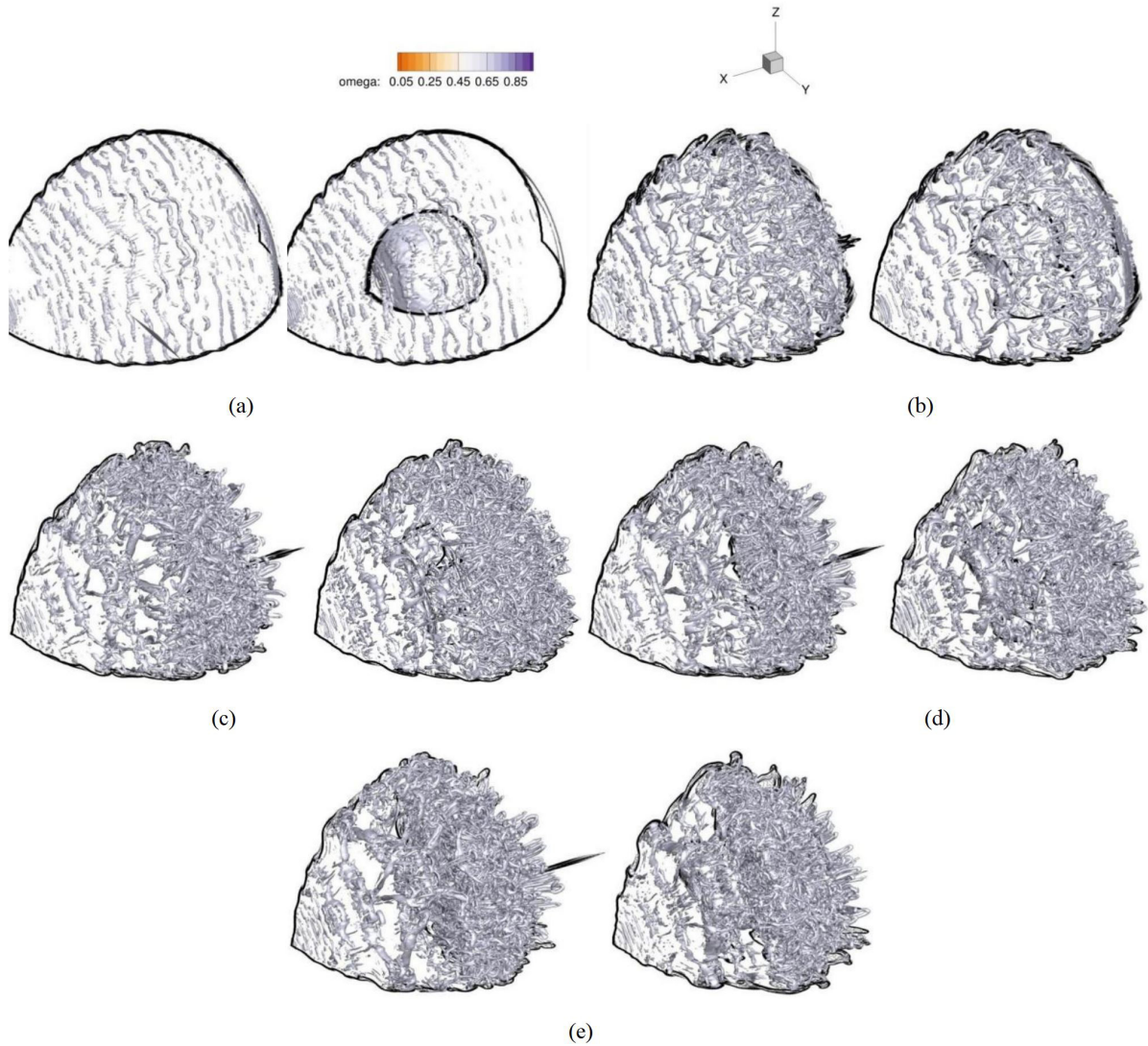
FIG. 21. Isosurface of $\Omega = 0.65$ at $t^* =$ (a) 15, (b) 27, (c) 49, (d) 56, and (e) 66.

conditions, the deformation behavior of the current cylinder under near-critical conditions is more akin to that of a water column in air under subcritical conditions.

(2) Vortex formation and baroclinic effects: The simulations demonstrate the emergence of vortices and the deposition of vorticity on the surfaces of the cylinder or droplet. Vortices develop on the external surfaces, and the presence of the gas cavity has a notable impact on the creation of liquid mushroom jets, vortex structures, and the rupture of the cavity bubble, all of which contribute to the deformation of the interface.

(3) Enstrophy and mixing: Enstrophy, reflecting the mixing process, evolves over time. The presence of the gas cavity results in increased enstrophy due to internal jet formation and distortion of the mushroom structure. The generation of baroclinic vorticity intensifies enstrophy, promoting liquid-gas mixing.

(4) Center-of-mass redistribution: The analysis includes the drift of the center-of-mass position and velocity. The presence of the gas cavity enhances the shift velocity in both cylinder and droplet cases.

(5) Three-dimensional interface deformation: Three-dimensional simulations are crucial for revealing complex, deformed structures near the two-phase interface, such as ligaments, lobes, petal
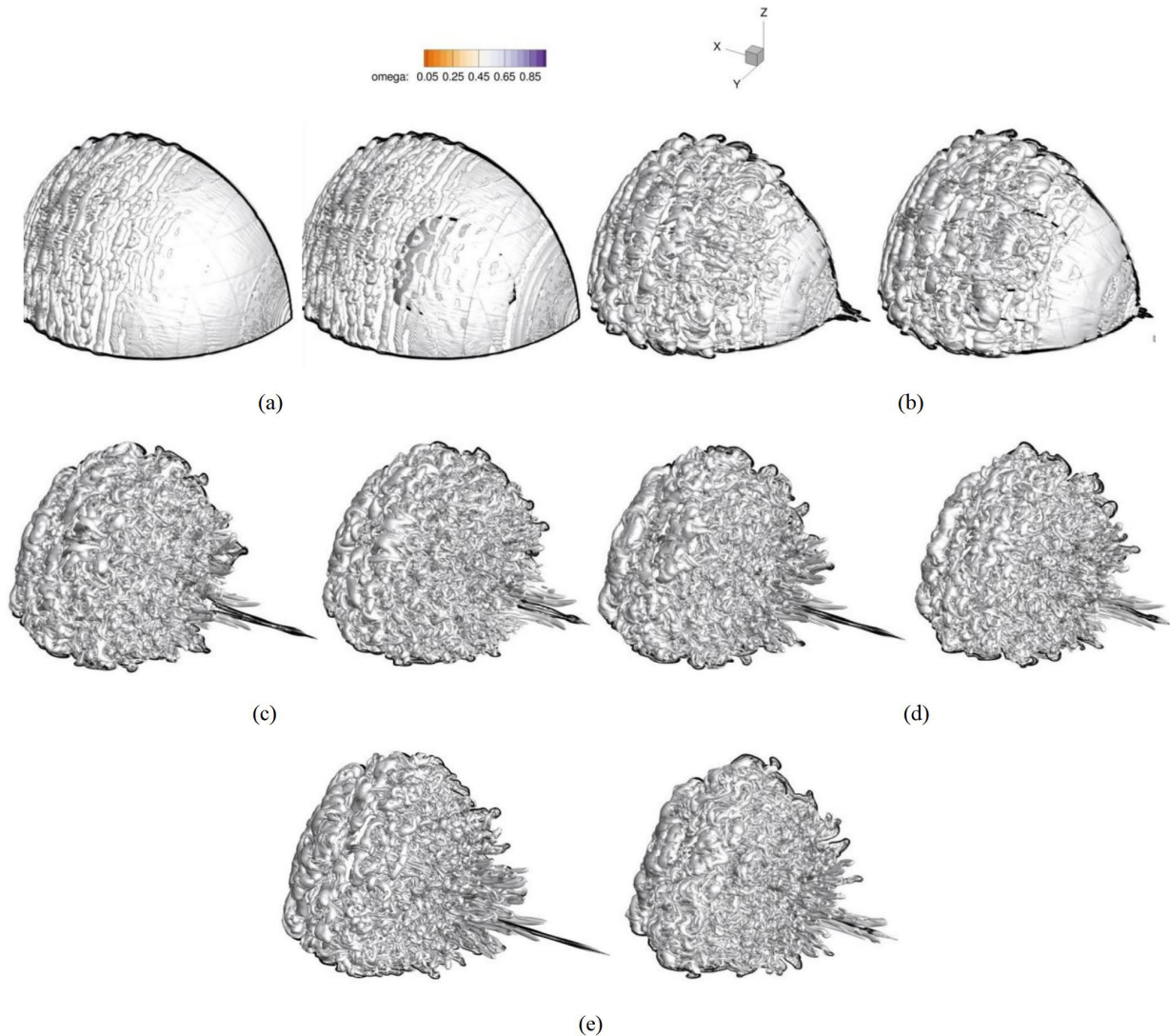
FIG. 22. Isosurface of $\Omega = 0.52$ at $t^* =$ (a) 15, (b) 27, (c) 49, (d) 56, and (e) 66.

shapes, and toroidal structures. These features, along with the three-dimensional vorticity distribution, cannot be captured by two-dimensional simulations. A comparative analysis is conducted to examine the similarities and differences between the cases involving droplets and the cylindrical column. Interestingly, the deformation of the droplet shell at near-critical conditions resembles that of a water droplet containing a cavity in air under subcritical conditions, exhibiting similar ringlike structures and the transverse jet. While our simulations are comparable to the characteristics of shear-induced entrainment for a chosen mass fraction, a complete understanding of the underlying physics requires further experimental validation.

Future work should encompass additional simulations with varying parameters alongside more extensive experimental research. This comprehensive approach will enable a deeper understanding of the complex mechanisms governing these interactions and disintegration processes.

APPENDIX A: DETAILS OF THE PENG-ROBINSON EOS

Here

$$p = \frac{RT}{v-b} - \frac{a}{v^2 + 2bv - b^2},$$ (A1)

where T is the temperature, R is the universal gas constant, v is the molar volume, $v = M/\rho$, and M is the molar mass. Coefficients are $a = \sum_{\alpha=1}^{N} \sum_{\beta=1}^{N} X_\alpha X_\beta a_{\alpha\beta}$ and $b = \sum_{\alpha=1}^{N} X_\alpha b_\alpha$.

Specifically, X_α is the mole fraction of species α and in-total species number is N; coefficients $a_{\alpha\beta} = 0.457236(RT_{c,\alpha\beta})^2/p_{c,\alpha\beta}(1 + c_{\alpha\beta}(1 - \sqrt{T}/T_{c,\alpha\beta}))^2$ and $b_\alpha = 0.077796RT_{c,\alpha}/p_{c,\alpha}$ are obtained according to the mixing rules [104]. $p_{c,\alpha\beta}$ is the critical mixture pressure and $p_{c,\alpha\beta} = Z_{c,\alpha\beta}RT_{c,\alpha\beta}/v_{c,\alpha\beta}$, $c_{\alpha\beta} = 0.37464 + 1.5422\omega_{\alpha\beta} - 0.26992\omega_{\alpha\beta}^2$, $T_{c,\alpha\beta}$ is the critical mixture temperature, and $T_{c,\alpha\beta} = \sqrt{T_{c,\alpha}T_{c,\beta}}(1 - k_{\alpha\beta})$. $T_{c,\alpha}$ and $T_{c,\beta}$ are critical temperatures for species α and β, and $k_{\alpha\beta}$ is the binary interaction parameter.

The critical mixture molar volume $v_{c,\alpha\beta}$, the critical mixture compressibility $Z_{c,\alpha\beta}$, and the acentric factor $\omega_{\alpha\beta}$ are denoted as $v_{c,\alpha\beta} = (1/8)(v_{c,\alpha}^{1/3} + v_{c,\beta}^{1/3})^3$, $Z_{c,\alpha\beta} = (1/2)(Z_{c,\alpha} + Z_{c,\beta})$, and $\omega_{\alpha\beta} = (1/2)(\omega_\alpha + \omega_\beta)$, where $v_{c,\alpha}^{1/3}$ and $v_{c,\beta}^{1/3}$ are critical molar volumes for species α and β, $Z_{c,\alpha}$ and $Z_{c,\beta}$ are critical compressibility factors for species α and β, and ω_α and ω_β are acentric factors for species α and β. Further details can be found in Refs. [17,104].

APPENDIX B: SOLUTION OF THE CUBIC EQUATION

When solving cubic equations of state (EOS), such as the PR-EOS, it is important to recognize that there may be three roots. However, it is essential to disregard nonphysical roots, which include negative values and complex values, and focus on identifying the real, positive roots [105–107]. The process of solving the cubic equation is outlined as follows:

$$x^3 + Ax^2 + Bx + C = 0,$$ (B1)

where A, B, and C are known coefficients obtained directly from the cubic EOS. The discriminant is $\Delta = D^2 + E^2$ and $D = (A/3)^3 - AB/6 + C/2$, $E = B/3 - (A/3)^2$.

For $\Delta = 0$, there are at least two equal roots, which are given by

$$x_1 = 2\sqrt[3]{-D} - \frac{A}{3}, \quad x_2 = x_3 = -\sqrt[3]{-D} - \frac{A}{3}.$$ (B2)

$\Delta > 0$, there are two nonphysical conjugate roots and one real root, $F = \sqrt[3]{-D + \sqrt{\Delta}}$, $G = \sqrt[3]{-D - \sqrt{\Delta}}$

$$x_1 = F + G - \frac{A}{3}, \quad x_2 = -\left[\frac{1}{2}(F+G) + \frac{A}{3}\right] + \frac{\sqrt{3}}{2}(F-G)i,$$

$$x_3 = -\left[\frac{1}{2}(F+G) + \frac{A}{3}\right] - \frac{\sqrt{3}}{2}(F-G)i.$$ (B3)

$\Delta < 0$, there are three real and unequal roots, $\theta(\mathrm{rad}) = \arccos(-D/\sqrt{-E^3})$,

$$x_1 = 2\sqrt{-E}\cos\left(\frac{\theta}{3}\right) - \frac{A}{3},$$

$$x_2 = 2\sqrt{-E}\cos\left(\frac{\theta}{3} + \frac{2}{3}\pi\right) - \frac{A}{3},$$

$$x_3 = 2\sqrt{-E}\cos\left(\frac{\theta}{3} + \frac{4}{3}\pi\right) - \frac{A}{3}.$$ (B4)

APPENDIX C: MODIFIED PR-EOS

The modified PR-EOS is designed to represent the saturation line in a straightforward manner. Within the vapor dome region, an approximate saturation pressure for the mixture is utilized. The algorithm for determining the pressure, which yields the temperature, density, and mass fraction, is as follows:

Step 1. Calculate the pressure from the PR-EOS giving the temperature and density, as well as the mass fraction. If nonpositive pressure ($p^* \leqslant 0$) is obtained from the relation $p^* = p_{\text{PR}-\text{EOS}}(T, \rho, \xi_i)$, a small arbitrarily positive value such as 1 would be adopted to replace this nonpositive value ($p^* = 1\,\text{Pa}$).

Step 2. Calculate the density from PR-EOS given the PR-EOS pressure p^*, temperature, and mass fraction, and check how many roots are obtained in the process $\rho^* = p_{\text{PR}-\text{EOS}}(p^*, T, \xi_i)$.

Step 3.1. If there is only one real value for ρ^*, then the PR-EOS pressure p^* is chosen as the corrected pressure.

Step 3.2. If there is more than one root for (ρ^*), then the saturation pressure (p_{sat}) is given by calculating the root, $\partial p/\partial \rho = 0$, via PR-EOS. Generally, the one at the lower density value (ρ_{min}) would be selected from the two resulting roots. The saturation pressure (p_{sat}) is then defined as the pressure corresponding to this root (ρ_{min}).

Step 4. If the density that is given by the PR-EOS (lowest density root, $\rho^* = p_{\text{PR}-\text{EOS}}(p^*, T, \xi_i)$) is very similar to the density provided (ρ), like ($\rho^* - \rho)/\rho < 10^{-4}$, then return the PR-EOS pressure p^*; otherwise, return the saturation pressure (p_{sat}).

In the case of DF methods or hybrid numerical schemes with a modified PR-EOS, it is crucial to calculate the temperature (T) for a given set of pressure (p), density (ρ), and mass fraction (ξ_i) using the modified PR-EOS ($T = p_{\text{modified}-\text{PR}-\text{EOS}}(p, \rho, \xi_i)$). This can be expressed as follows:

Step 1. Initial guess (T_{guess}) temperature according to the initial condition and the temperature from the last time step.

Step 2. This T_{guess} is used to calculate the pressure, using modified PR-EOS $p_{\text{guess}} = p_{\text{modified}-\text{PR}-\text{EOS}}(T_{\text{guess}}, \rho, \xi_i)$, where the state inside the vapor dome has already been corrected.

Step 3. If the pressure given by the modified PR-EOS ($p_{\text{guess}} = p_{\text{modified}-\text{PR}-\text{EOS}}(T_{\text{guess}}, \rho, \xi_i)$) is very similar to the pressure given by the modified PR-EOS (p^*), e.g., ($p_{\text{guess}} - p^*)/p^* < 10^{-6}$, then the temperature T_{guess} is selected as the correct temperature, $T = T_{\text{guess}}$.

Step 4. Otherwise, the guess temperature is updated according to the secant method or gradient descent or Newton method, and the criteria are $p^* = p_{\text{modified}-\text{PR}-\text{EOS}}(T_{\text{guess}}, \rho, \xi_i)$ and ($p^* - p)/p < 10^{-6}$.

Step 5. The modified PR-EOS [71] also limits the speed of sound to a minimum value—the minimum speed of sound value used in this paper is 1 m/s [71]. Three subcritical isotherms of varying composition are depicted in Fig. 30 of Ref. [51] to showcase the modified PR-EOS.

APPENDIX D: EFFECTS OF COMPUTATIONAL DOMAIN AND BOUNDARY CONDITIONS ON NEAR-CRITICAL SHOCK-CYLINDER INTERACTIONS

Additional validations are presented in this section. These cases, when compared to previous validation cases, serve to elucidate the influence of the computational domain and boundary conditions on shock-cylinder interactions. As depicted in Fig. 23, reflective boundary conditions are employed within a constrained computational domain. The purpose of this comparison is to highlight the advancements offered by OWENO3 in contrast to the results obtained by the classical WENO3 method.

Due to its lower dissipation characteristics in comparison to the WENO3 scheme, the results obtained using the WENO3 scheme (Fig. 24) are outperformed by those of the OWENO3 scheme (Fig. 25) when employing the same mesh resolution. Irrespective of the mesh resolution chosen, the OWENO3 consistently delivers favorable results, whereas the performance of the WENO3
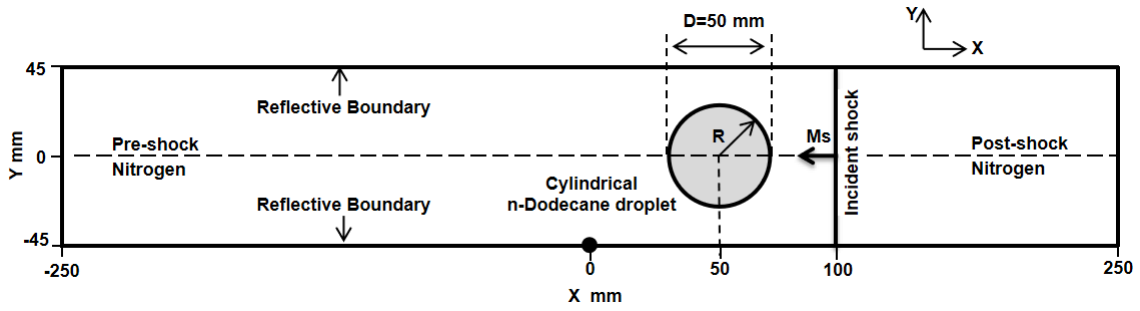
FIG. 23. The restricted computational domain of the shock-cylinder interaction at near-critical conditions (sketch map).
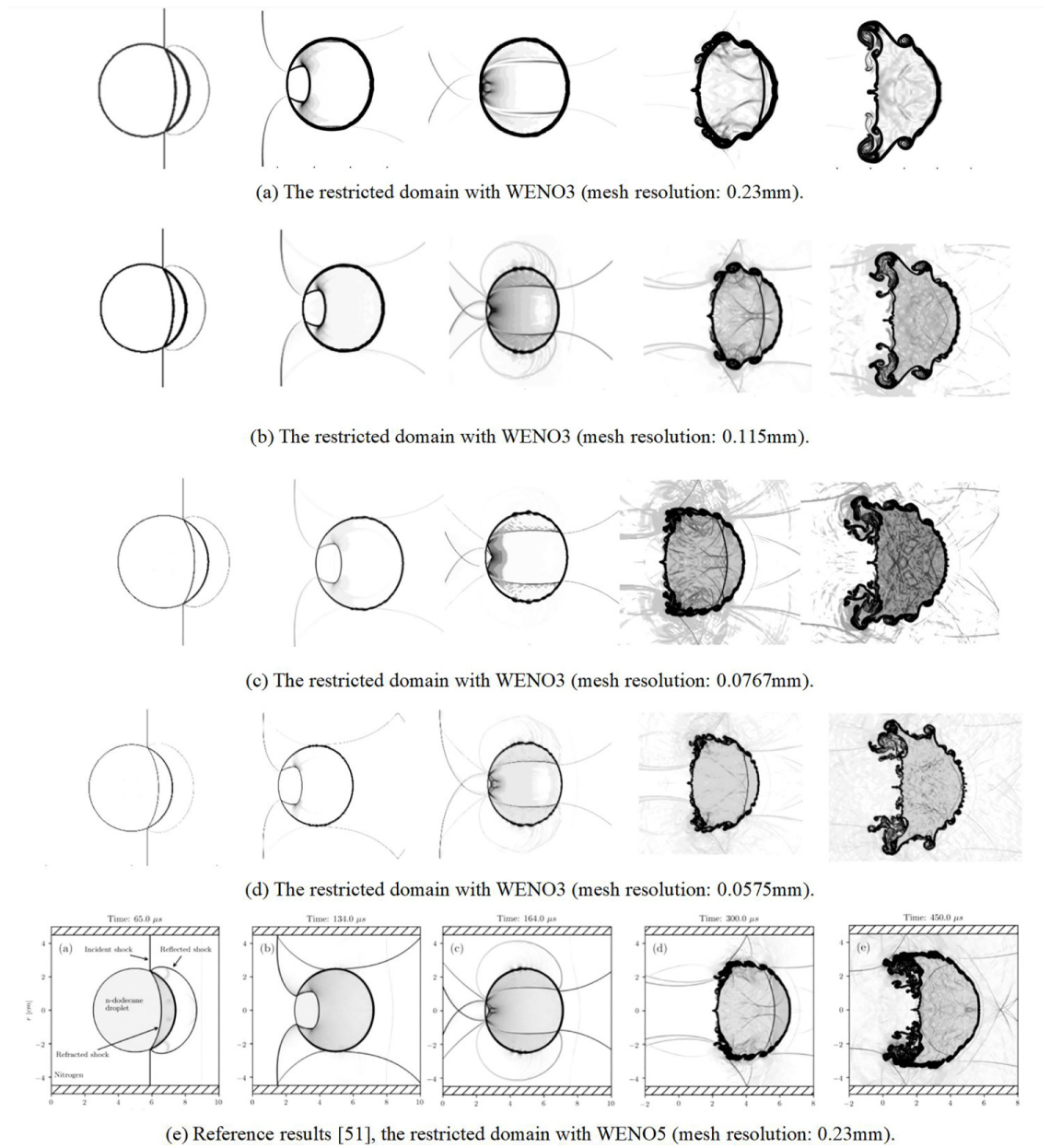

(a) The restricted domain with WENO3 (mesh resolution: 0.23mm).

(b) The restricted domain with WENO3 (mesh resolution: 0.115mm).

(c) The restricted domain with WENO3 (mesh resolution: 0.0767mm).

(d) The restricted domain with WENO3 (mesh resolution: 0.0575mm).

(e) Reference results [51], the restricted domain with WENO5 (mesh resolution: 0.23mm).

FIG. 24. The shock cylinder interaction within the restricted domain at times 65, 134, 164, 300, and 450 µs (from left to right). WENO3 with a mesh resolution of (a) 0.23 mm, (b) 0.115 mm, (c) 0.0767 mm, (d) 0.0575 mm. WENO5 with a mesh resolution of (e) 0.23 mm [51]. Reproduced from Ref. [51].

(a) The restricted domain with OWENO3 (mesh resolution: 0.23 mm).

(b) The restricted domain with OWENO3 (mesh resolution: 0.115 mm).

(c) The restricted domain with OWENO3 (mesh resolution: 0.0767 mm).

(d) The restricted domain with OWENO3 (mesh resolution: 0.0575 mm).
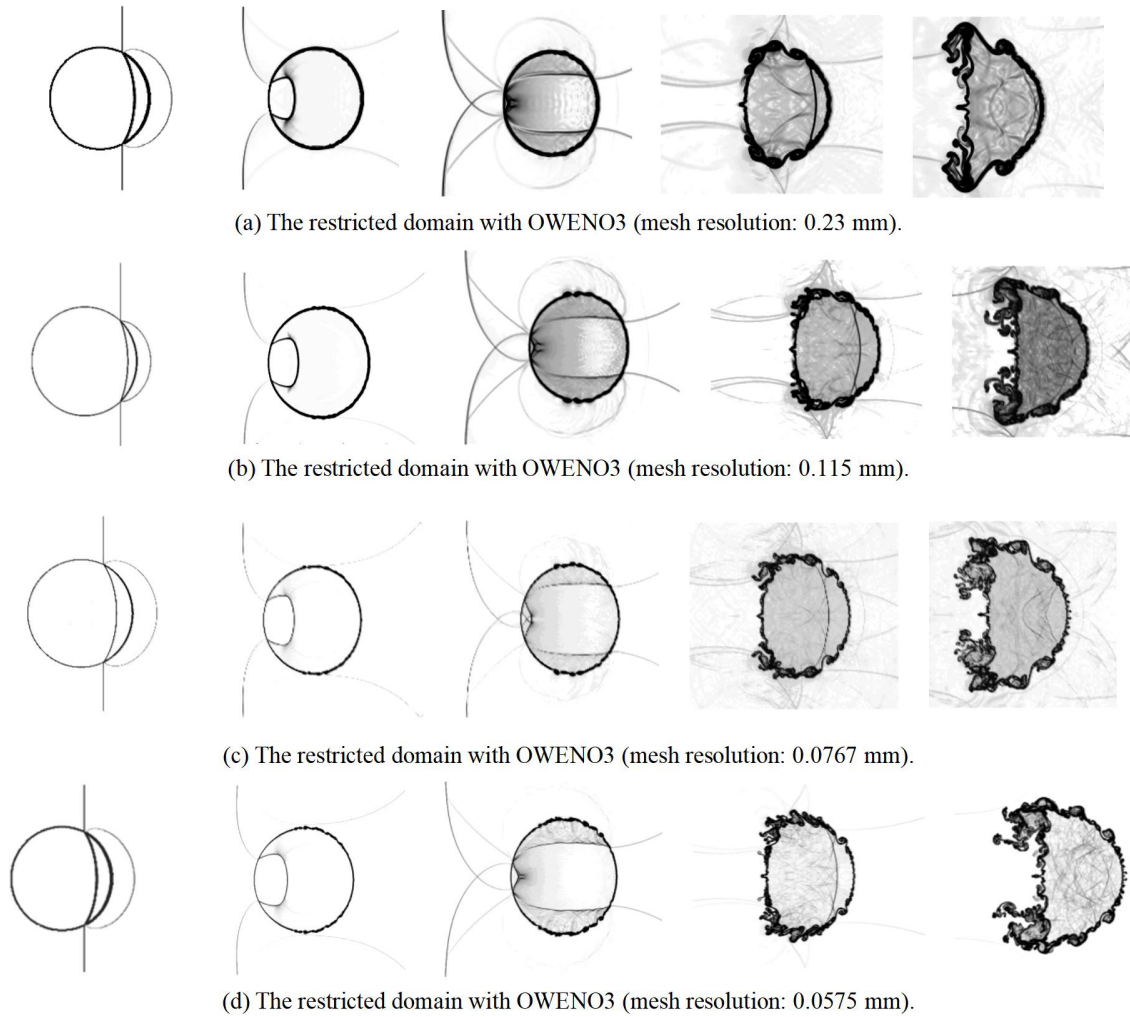
FIG. 25. The shock n-dodecane cylinder interaction within the restricted domain at times 65, 134, 164, 300, and 450 µs. OWENO3 with a mesh resolution of (a) 0.23 mm, (b) 0.115 mm, (c) 0.0767 mm, (d) 0.0575 mm.

scheme diminishes during later evolution times ($t = 450$ µs) when using mesh resolutions of 0.23 or 0.115 mm.

Upon comparing results obtained from coarser mesh resolutions to finer ones across different numerical schemes, it can be deduced that the OWENO3 method, combined with a mesh resolution of 0.115 mm, can yield results comparable to those of the WENO5 scheme from Ref. [52], all while maintaining computational efficiency and accuracy.
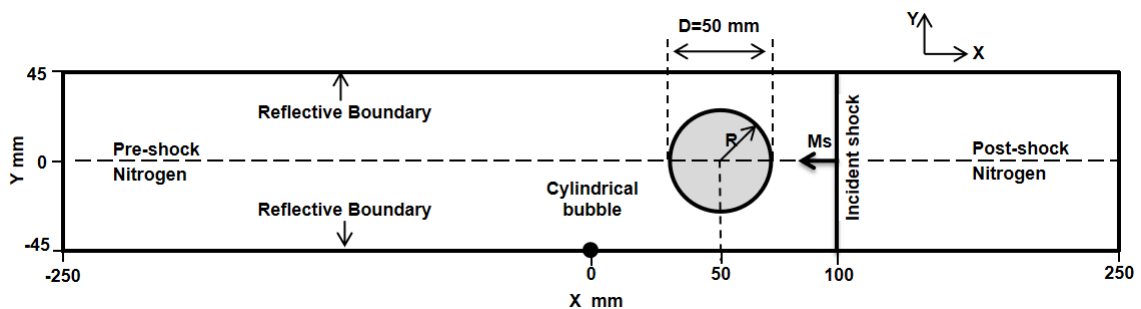
FIG. 26. Schematic of the shock-bubble interaction computational domain.

TABLE II. Initial conditions for the shock-bubble interaction.

Stage	p (Pa)	u (m/s)	v (m/s)	ρ (kg/m^3)	Non-dimension [108] (p, u, v, ρ)
Preshocked air	101325	0	0	1.225	(1,0,0,1)
Postshocked air	159059	113.5	0	1.686	(1.5698, −0.394, 0,1.3764)
Helium	101325	0	0	0.169	(1,0,0,0.138)

APPENDIX E: SHOCK INTERACTION WITH HELIUM BUBBLE

We have validated the current numerical scheme using the shock–helium bubble case as discussed in Refs. [22,108]. The computational domain is depicted in Fig. 26. The initial conditions are given in Table II.

We have employed a Cartesian mesh with a uniform resolution of 0.115 mm. The parameters for the NASA polynomials can be found in Ref. [78].

As depicted in Fig. 27, the results for the helium-air case exhibit excellent agreement with the findings presented by Quirk and Karni [22]. This alignment in results has also been observed by Haas and Sturtevant [21] and other researchers [109]. The methodology employed in this study effectively captures the underlying physical phenomena while ensuring robust performance. The selection of evolution time steps closely approximates the reference time, making minor deviations acceptable.

(a)

(b)

(c)

(d)

(e)
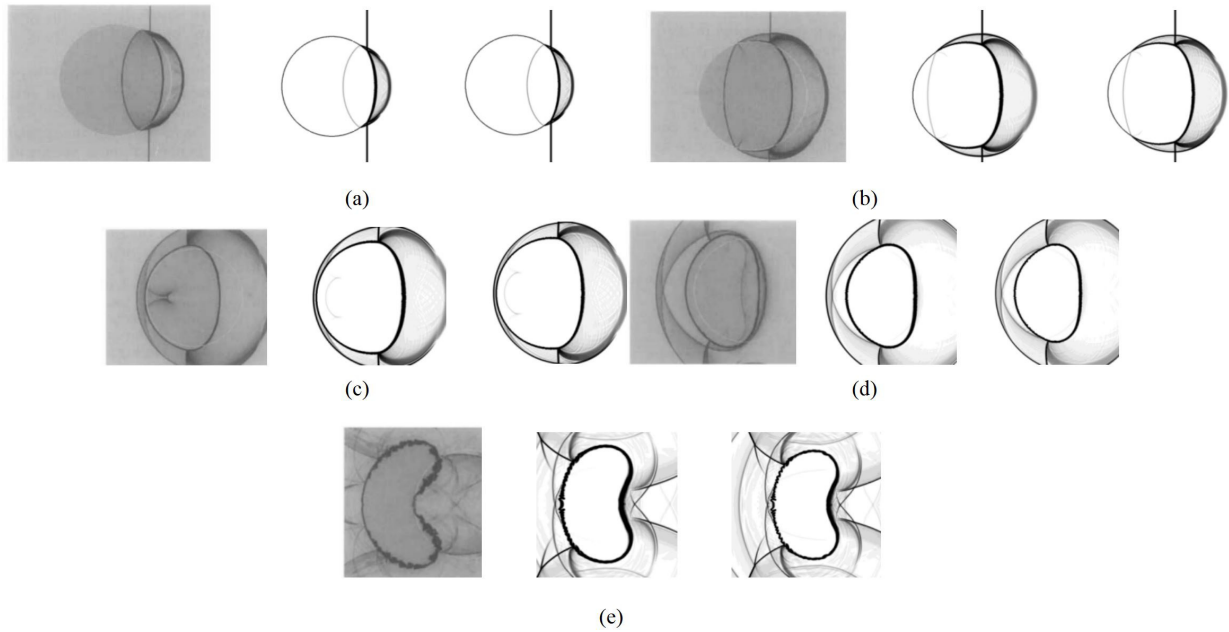
FIG. 27. Numerical schlieren images for the evolution of the shocked air-helium interaction at time (a) 32 μs, (b) 52 μs, (c) 72 μs, (d) 102 μs, and (e) 245 μs. The first column shows the current numerical results, while the others show the results from Ref. [22]. From left to right: numerical scheme (mesh resolution), reference scheme (0.056 mm), WENO3 (0.23 mm), and OWENO3 (0.23 mm). Reproduced from Ref. [22].

[1] Y. Zhou, Rayleigh-Taylor and Richtmyer-Meshkov instability induced flow, turbulence, and mixing. I, Phys. Rep. **720–722**, 1 (2017).

[2] Y. Zhou, Rayleigh-Taylor and Richtmyer-Meshkov instability induced flow, turbulence, and mixing. II, Phys. Rep. **723–725**, 1 (2017).

[3] M. Brouillette, The Richtmyer-Meshkov instability, Annu. Rev. Fluid Mech. **34**, 445 (2002).

[4] V. K. Tritschler, B. J. Olson, S. K. Lele, S. Hickel, X. Y. Hu, and N. A. Adams, On the Richtmyer-Meshkov instability evolving from a deterministic multimode planar interface, J. Fluid Mech. **755**, 429 (2014).

[5] R. D. Richtmyer, Taylor instability in shock acceleration of compressible fluids, Commun. Pure Appl. Math. **13**, 297 (1960).

[6] E. E. Meshkov, Instability of the interface of two gases accelerated by a shock wave, Fluid Dyn. **4**, 101 (1972).

[7] Z. Falgout, M. Rahm, D. Sedarsky, and M. Linne, Gas/fuel jet interfaces under high pressures and temperatures, Fuel **168**, 14 (2016).

[8] R. N. Dahms, J. Manin, L. M. Pickett, and J. C. Oefelein, Understanding high-pressure gas-liquid interface phenomena in diesel engines, Proc. Combust. Inst. **34**, 1667 (2013).

[9] R. N. Dahms, Understanding the breakdown of classic two-phase theory and spray atomization at enginerelevant conditions, Phys. Fluids **28**, 042108 (2016).

[10] J. Oefelein, G. Lacaze, R. Dahms, A. Ruiz, and A. Misdariis, Effects of real-fluid thermodynamics on high-pressure fuel injection processes, SAE Int. J. Engines **7**, 1125 (2014).

[11] P. C. Ma, Y. Lv, and M. Ihme, An entropy-stable hybrid scheme for simulations of transcritical real-fluid flows, J. Comput. Phys. **340**, 330 (2017).

[12] D. T. Banuti, M. Raju, and M. Ihme, *Supercritical pseudoboiling for general fluids and its application to injection*, Annual Research Briefs (2016), pp. 211–221.

[13] M. Oschwald, J. Smith, R. Branam, J. Hussong, A. Schik, B. Chehroudi, and D. Talley, Injection of fluids into supercritical environments, Combust. Sci. Technol. **178**, 49 (2006).

[14] W. O. H. Mayer, A. H. A. Schik, B. Vielle, C. Chauveau, I. Gokalp, D. G. Talley, and R. D. Woodward, Atomization and breakup of cryogenic propellants under high-pressure subcritical and supercritical conditions, J. Propul. Power **14**, 835 (1998).

[15] J. W. Chae, H. S. Yang, and W. S. Yoon, Supercritical droplet dynamics and emission in low speed cross-flows, J. Mech. Sci. Technol. **22**, 1586 (2008).

[16] V. Yang, Modeling of supercritical vaporization, mixing, and combustion processes in liquid-fueled propulsion systems, Proc. Combust. Inst. **28**, 925 (2000).

[17] V. Yang, N. Natan, and J.-S. Shuen, Vaporization of liquid oxygen (LOX) droplets in supercritical hydrogen environments, Combust. Sci. Technol. **97**, 247 (1994).

[18] V. Yang, G. C. Hsiao, J. S. Shuen, and K. C. Hsieh, Droplet behavior at supercritical conditions, Recent Adv. Spray Combust. **1**, 413 (1996).

[19] C. Crua, J. Manin, and L. M. Pickett, On the transcritical mixing of fuels at diesel engine conditions, Fuel **208**, 535 (2017).

[20] H. Meng, G. C. Hsiao, V. Yang, and J. S. Shuen, Transport and dynamics of liquid oxygen droplets in supercritical hydrogen streams, J. Fluid Mech. **527**, 115 (2005).

[21] J. F. Haas and B. Sturtevant, Interaction of weak shock waves with cylindrical and spherical gas inhomogeneities, J. Fluid Mech. **181**, 41 (1987).

[22] J. J. Quirk and S. Karni, On the dynamics of a shock-bubble interaction, J. Fluid Mech. **318**, 129 (1996).

[23] S. Kumar, G. Orlicz, C. Tomkins, C. Goodenough, K. Prestridge, P. Vorobieff, and R. Benjamin, Stretching of material lines in shock-accelerated gaseous flows, Phys. Fluids **17**, 082107 (2005).

[24] G. Layes, G. Jourdan, and L. Houas, Distortion of a spherical gaseous interface accelerated by a plane shock wave, Phys. Rev. Lett. **91**, 174502 (2003).

[25] G. Layes, G. Jourdan, and L. Houas, Experimental investigation of the shock wave interaction with a spherical gas inhomogeneity, Phys. Fluids **17**, 028103 (2005).

[26] G. Layes, G. Jourdan, and L. Houas, Experimental study on a plane shock wave accelerating a gas bubble, Phys. Fluids **21**, 074102 (2009).

[27] A. F. Nowakowski, A. Ballil, and F. C. G. A. Nicolleau, Passage of a shock wave through inhomogeneous media and its impact on gas-bubble deformation, Phys. Rev. E **92**, 023028 (2015).

[28] D. Ranjan, J. Oakley, and R. Bonazza, Shock-bubble interactions, Annu. Rev. Fluid Mech. **43**, 117 (2011).

[29] C. Tomkins, S. Kumar, G. Orlicz, and K. Prestridge, An experimental investigation of mixing mechanisms in shock accelerated flow, J. Fluid Mech. **611**, 131 (2008).

[30] C. Tomkins, K. Prestridge, P. Rightley, M. Marr-Lyon, P. Vorobieff, and R. Benjamin, A quantitative study of the interaction of two Richtmyer-Meshkov-unstable gas cylinders, Phys. Fluids **15**, 986 (2003).

[31] Y. Zhu, L. Yu, J. Pan, Z. Pan, and P. Zhang, Jet formation of SF_6 bubble induced by incident and reflected shock waves, Phys. Fluids **29**, 126105 (2017).

[32] N. Hoppe, J. M. Winter, S. Adami, and N. A. Adams, ALPACA-a level-set based sharp-interface multiresolution solver for conservation laws, Comput. Phys. Commun. **272**, 108246 (2022).

[33] J. C. Meng and T. Colonius, Numerical simulation of the aerobreakup of a water droplet, J. Fluid Mech. **835**, 1108 (2018).

[34] P. Das and H. S. Udaykumar, A sharp-interface method for the simulation of shock-induced vaporization of droplets, J. Comput. Phys. **405**, 109005 (2020).

[35] H. J. Q. Wan, R. Deiterding, and V. Eliasson, Numerical and experimental investigation of oblique shock wave reflection off a water wedge, J. Fluid Mech. **826**, 732 (2017).

[36] K. Schmidmayer and L. Biasiori-Poulanges, Geometry effects on the droplet shock-induced cavitation, Phys. Fluids **35**, 063315 (2023).

[37] B. Dorschner, L. Biasiori-Poulanges, K. Schmidmayer, H. El-Rabii, and T. Colonius, On the formation and recurrent shedding of ligaments in droplet aerobreakup, J. Fluid Mech. **904**, A20 (2020).

[38] R. W. Forehand, K. C. Nguyen, C. J. Anderson, R. Shannon, S. M. Grace, and M. P. Kinzel, A numerical assessment of shock–droplet interaction modeling including cavitation, Phys. Fluids **35**, 023315 (2023).

[39] B. Guan, Y. Liu, C. Y. Wen, and H. Shen, Numerical study on liquid droplet internal flow under shock impact, AIAA J. **56**, 3382 (2018).

[40] Z. Wang, T. Hopfes, M. Giglmaier, and N. A. Adams, Effect of Mach number on droplet aerobreakup in shear stripping regime, Exp. Fluids **61**, 193 (2020).

[41] R. Abgrall, How to prevent pressure oscillations in multicomponent flow calculations: A quasi conservative approach, J. Comput. Phys. **125**, 150 (1996).

[42] D. Banuti, M. Raju, P. C. Ma, M. Ihme, and J.-P. Hickey, Seven questions about supercritical fluids towards a new fluid state diagram, in *Proceedings of the 55th AIAA Aerospace Sciences Meeting* (AIAA, Reston, VA, 2017), p. 1106.

[43] M. Raju, D. T. Banuti, P. C. Ma, and M. Ihme, Widom lines in binary mixtures of supercritical fluids, Sci. Rep. **7**, 3027 (2017).

[44] C. F. Delale, *Bubble Dynamics and Shock Waves* (Springer, Berlin, 2013).

[45] T. Theofanous, Aerobreakup of Newtonian and viscoelastic liquids, Annu. Rev. Fluid Mech. **43**, 661 (2011).

[46] N. J. Zabusky, Vortex paradigm for accelerated inhomogeneous flows: Visiometrics for the Rayleigh-Taylor and Richtmyer-Meshkov environments, Annu. Rev. Fluid Mech. **31**, 495 (1999).

[47] V. Duke-Walker, W. C. Maxon, S. R. Almuhna, and J. A. McFarland, Evaporation and breakup effects in the shock-driven multiphase instability, J. Fluid Mech. **908**, A13 (2021).

[48] J. W. J. Kaiser, J. M. Winter, S. Adami, and N. A. Adams, Investigation of interface deformation dynamics during high-Weber number cylindrical droplet breakup, Int. J. Multiphase Flow **132**, 103409 (2020).

[49] S. Sharma, A. P. Singh, S. S. Rao, A. Kumar, and S. Basu, Shock induced aerobreakup of a droplet, J. Fluid Mech. **929**, A27 (2021).

[50] P. Tudisco and S. Menon, Numerical investigations of phase-separation during multi-component mixing at super-critical conditions, Flow Turbul. Combust. **104**, 693 (2020).

[51] B. Boyd and D. Jarrahbashi, A diffuse-interface method for reducing spurious pressure oscillations in multicomponent transcritical flow simulations, Comput. Fluids **222**, 104924 (2021).

[52] B. Boyd and D. Jarrahbashi, Numerical study of the transcritical shock-droplet interaction, Phys. Rev. Fluids **6**, 113601 (2021).

[53] S. Wang, Z. Jiao, X. Huang, C. Yang, and N. Nguyen, Acoustically induced bubbles in a microfluidic channel for mixing enhancement, Microfluid. Nanofluid. **6**, 847 (2009).

[54] O. Shpak, M. Verweij, N. de Jong, and M. Versluis, Droplets, bubbles and ultrasound interactions, Ther. Ultrasound **880**, 157 (2016).

[55] L. Ming, N. Zhi, and S. Chunhua, Numerical simulation of cavitation bubble collapse within a droplet, Comput. Fluids **152**, 157 (2017).

[56] G. Wang, Y. Wang, D. Li, and B. Guan, Numerical study on shock-accelerated gas rings, Phys. Fluids **32**, 026102 (2020).

[57] L. Feng, J. Xu, Z. Zhai, and X. Luo, Evolution of shock-accelerated double-layer gas cylinder, Phys. Fluids **33**, 086105 (2021).

[58] Y. Liang, Y. Jiang, C. Wen, and Y. Liu, Interaction of a planar shock wave and a water droplet embedded with a vapour cavity, J. Fluid Mech. **885**, R6 (2020).

[59] G. Xiang and B. Wang, Numerical study of a planar shock interacting with a cylindrical water column embedded with an air cavity, J. Fluid Mech. **825** 825 (2017).

[60] K. Yang and T. Aoki, Weakly compressible Navier-Stokes solver based on evolving pressure projection method for two-phase flow simulations, J. Comput. Phys. **431**, 110113 (2021).

[61] T. Schmitt, L. Selle, A. Ruiz, and B. Cuenot, Large-eddy simulation of supercritical-pressure round jets, AIAA J. **48**, 2133 (2010).

[62] H. Terashima and M. Koshi, Approach for simulating gas-liquid-like flows under supercritical pressures using a high-order central differencing scheme, J. Comput. Phys. **231**, 6907 (2012).

[63] G. Lacaze, T. Schmitt, A. Ruiz, and J. C. Oefelein, Comparison of energy-, pressure- and enthalpy-based approaches for modeling supercritical flows, Comput. Fluids **181**, 35 (2019).

[64] K. Kitamura and E. Shima, Pressure-equation-based SLAU2 for oscillation-free, supercritical flow simulations, Comput. Fluids **163**, 86 (2018).

[65] H. Terashima and M. Koshi, Strategy for simulating supercritical cryogenic jets using high-order schemes, Comput. Fluids **85**, 39 (2013).

[66] R. Abgrall and S. Karni, Computations of compressible multifluids, J. Comput. Phys. **169**, 594 (2001).

[67] C. P. Egerer, S. J. Schmidt, S. Hickel, and N. A. Adams, Efficient implicit LES method for the simulation of turbulent cavitating flows, J. Comput. Phys. **316**, 453 (2016).

[68] S. J. Schmidt, A low Mach number consistent compressible approach for simulation of cavitating flow, Ph.D. thesis, Technical University of Munich, 2015.

[69] Y. Jiao, S. J. Schmidt, and N. A. Adams, An all-Mach consistent numerical scheme for simulation of compressible multi-component fluids including surface tension, cavitation, turbulence modeling and interface sharpening on compact stencils, Comput. Fluids **274**, 106186 (2024).

[70] T. Trummler, S. J. Schmidt, and N. A. Adams, Investigation of condensation shocks and re-entrant jet dynamics in a cavitating nozzle flow by Large-Eddy Simulation, Int. J. Multiphase Flow **125**, 103215 (2020).

[71] E. Knudsen, E. M. Doran, V. Mittal, J. Meng, and W. Spurlock, Compressible Eulerian needle-to-target large eddy simulations of a diesel fuel injector, Proc. Combust. Inst. **36**, 2459 (2017).

[72] J. Matheis and S. Hickel, Multi-component vapor-liquid equilibrium model for LES of high-pressure fuel injection and application to ECN Spray A, Int. J. Multiphase Flow **99**, 294 (2018).

[73] A. M. Ruiz, G. Lacaze, J. C. Oefelein, R. Mari, B. Cuenot, L. Selle, and T. Poinsot, Numerical benchmark for high-Reynolds-number supercritical flows with large density gradients, AIAA J. **54**, 1445 (2016).

[74] H. Müller, C. A. Niedermeier, J. Matheis, M. Pfitzner, and S. Hickel, Large-eddy simulation of nitrogen injection at trans- and supercritical conditions, Phys. Fluids **28**, 015102 (2016).

[75] W. Wei, H. Liu, M. Xie, M. Jia, and M. Yue, Large eddy simulation and proper orthogonal decomposition analysis of fuel injection under trans/supercritical conditions, Comput. Fluids **179**, 150 (2019).

[76] N. Okong'o and J. Bellan, Perturbation and initial Reynolds number effects on transition attainment of supercritical, binary, temporal mixing layers, Comput. Fluids **33**, 1023 (2004).

[77] D.-Y. Peng and D. B. Robinson, A new two-constant equation of state, Ind. Eng. Chem. Fundam. **15**, 59 (1976).

[78] B. J. McBride, *Coefficients for Calculating Thermodynamic and Transport Properties of Individual Species* (NASA, Office of Management, Scientific and Technical Information Program, Washington, DC, 1993), Vol. 4513.

[79] G. Billet and R. Abgrall, An adaptive shock-capturing algorithm for solving unsteady reactive flows, Comput. Fluids **32**, 1473 (2003).

[80] G. Billet and J. Ryan, A Runge-Kutta discontinuous Galerkin approach to solve reactive flows: The hyperbolic operator, J. Comput. Phys. **230**, 1064 (2011).

[81] Y. Lv and M. Ihme, Discontinuous Galerkin method for multi-component chemically reacting flows and combustion, J. Comput. Phys. **270**, 105 (2014).

[82] P. C. Ma, H. Wu, D. T. Banuti, and M. Ihme, On the numerical behavior of diffuse-interface methods for transcritical real-fluids simulations, Int. J. Multiphase Flow **113**, 231 (2019).

[83] S. Kawai, H. Terashima, and H. Negishi, A robust and accurate numerical method for transcritical turbulent flows at supercritical pressure with an arbitrary equation of state, J. Comput. Phys. **300**, 116 (2015).

[84] P. C. Ma, H. Wu, T. Jaravel, L. Bravo, and M. Ihme, Large-eddy simulations of transcritical injection and auto-ignition using diffuse-interface method and finite-rate chemistry, Proc. Combust. Inst. **37**, 3303 (2019).

[85] C. Traxinger, M. Pfitzner, S. Baab, G. Lamanna, and B. Weigand, Experimental and numerical investigation of phase separation due to multicomponent mixing at high-pressure conditions, Phys. Rev. Fluids **4**, 074303 (2019).

[86] D. T. Banuti, P. C. Ma, and M. Ihme, Phase separation analysis in supercritical injection using large-eddy-simulation and vapor-liquid-equilibrium, in *Proceedings of the 53rd AIAA/SAE/ASEE Joint Propulsion Conference* (AIAA, Reston, VA, 2017), p. 4764.

[87] A. Baeza, R. Bürger, P. Mulet, and D. Zorío, An efficient third-order WENO scheme with unconditionally optimal accuracy, SIAM J. Sci. Comput. **42**, A1028 (2020).

[88] E. F. Toro, *Riemann Solvers and Numerical Methods for Fluid Dynamics: A Practical Introduction*, 3rd ed., (Springer, Dordrecht, 2009).

[89] J. W. Jacobs, The dynamics of shock accelerated light and heavy gas cylinders, Phys. Fluids A **5**, 2239 (1993).

[90] Z. Zhai, T. Si, L. Zou, and X. Luo, Jet formation in shock-heavy gas bubble interaction, Acta Mech. Sin. **29**, 24 (2013).

[91] L. Zou, Z. Zhai, J. Liu, Y. Wang, and C. Liu, Energy convergence effect and jet phenomenon of shock-heavy spherical bubble interaction, Sci. China: Phys., Mech. Astron. **58**, 014711 (2015).

[92] E. Fan, B. Guan, C.-Y. Wen, and H. Shen, Numerical study on the jet formation of simple-geometry heavy gas inhomogeneities, Phys. Fluids **31**, 026103 (2019).

[93] B. Guan, H. Yang, H. Yang, and G. Wang, On the irregular jet formation of shock-accelerated spherical heavy gas bubbles, Phys. Fluids **34**, 126111 (2022).

[94] A. M. Abd-el Fattah and L. F. Henderson, Shock waves at a slow-fast gas interface, J. Fluid Mech. **89**, 79 (1978).

[95] See Supplemental Material at http://link.aps.org/supplemental/10.1103/PhysRevFluids.9.074002 for the evolution of surface deformation with different isosurface values.

[96] T. G. Theofanous and G. J. Li, On the physics of aerobreakup, Phys. Fluids **20**, 052103 (2008).

[97] N. Liu, Z. Wang, M. Sun, H. Wang, and B. Wang, Numerical simulation of liquid droplet breakup in supersonic flows, Acta Astronaut. **145**, 116 (2018).

[98] T. G. Theofanous, V. V. Mitkin, C. L. Ng, C. H. Chang, X. Deng, and S. Sushchikh, The physics of aerobreakup. II, Viscous liquids, Phys. Fluids **24**, 022104 (2012).

[99] S. Sharma, A. P. Singh, and S. Basu, On the dynamics of vortex-droplet co-axial interaction: Insights into droplet and vortex dynamics, J. Fluid Mech. **918**, A37 (2021).

[100] A. Zandian, W. A. Sirignano, and F. Hussain, Planar liquid jet: Early deformation and atomization cascades, Phys. Fluids **29**, 062109 (2017).

[101] A. Zandian, W. A. Sirignano, and F. Hussain, Vorticity dynamics in a spatially developing liquid jet inside a co-flowing gas, J. Fluid Mech. **877**, 429 (2019).

[102] D. Jarrahbashi, W. A. Sirignano, P. P. Popov, and F. Hussain, Early spray development at high gas density: Hole, ligament and bridge formations, J. Fluid Mech. **792**, 186 (2016).

[103] A. Zandian, W. A. Sirignano, and F. Hussain, Length-scale cascade and spread rate of atomizing planar liquid jets, Int. J. Multiphase Flow **113**, 117 (2019).

[104] K. G. Harstad, R. S. Miller, and J. Bellan, Efficient high-pressure state equations, AlChE J. **43**, 1605 (1997).

[105] J. H. Perry, *Chemical Engineers' Handbook* (ACS Publications, Washington, DC, 1950).

[106] G. Wilczek-Vera and J. H. Vera, Understanding cubic equations of state: A search for the hidden clues of their success, AlChE J. **61**, 2824 (2015).

[107] P. Yi, S. Yang, C. Habchi, and R. Lugo, A multicomponent real-fluid fully compressible four-equation model for two-phase flow with phase change, Phys. Fluids **31**, 026102 (2019).

[108] R. P. Fedkiw, T. Aslam, B. Merriman, and S. Osher, A non-oscillatory Eulerian approach to interfaces in multimaterial flows (the ghost fluid method), J. Comput. Phys. **152**, 457 (1999).

[109] A. Bagabir and D. Drikakis, Mach number effects on shock-bubble interaction, Shock Waves **11**, 209 (2001).

Supplementary materials

Evolution of surface deformation with different isosurface values
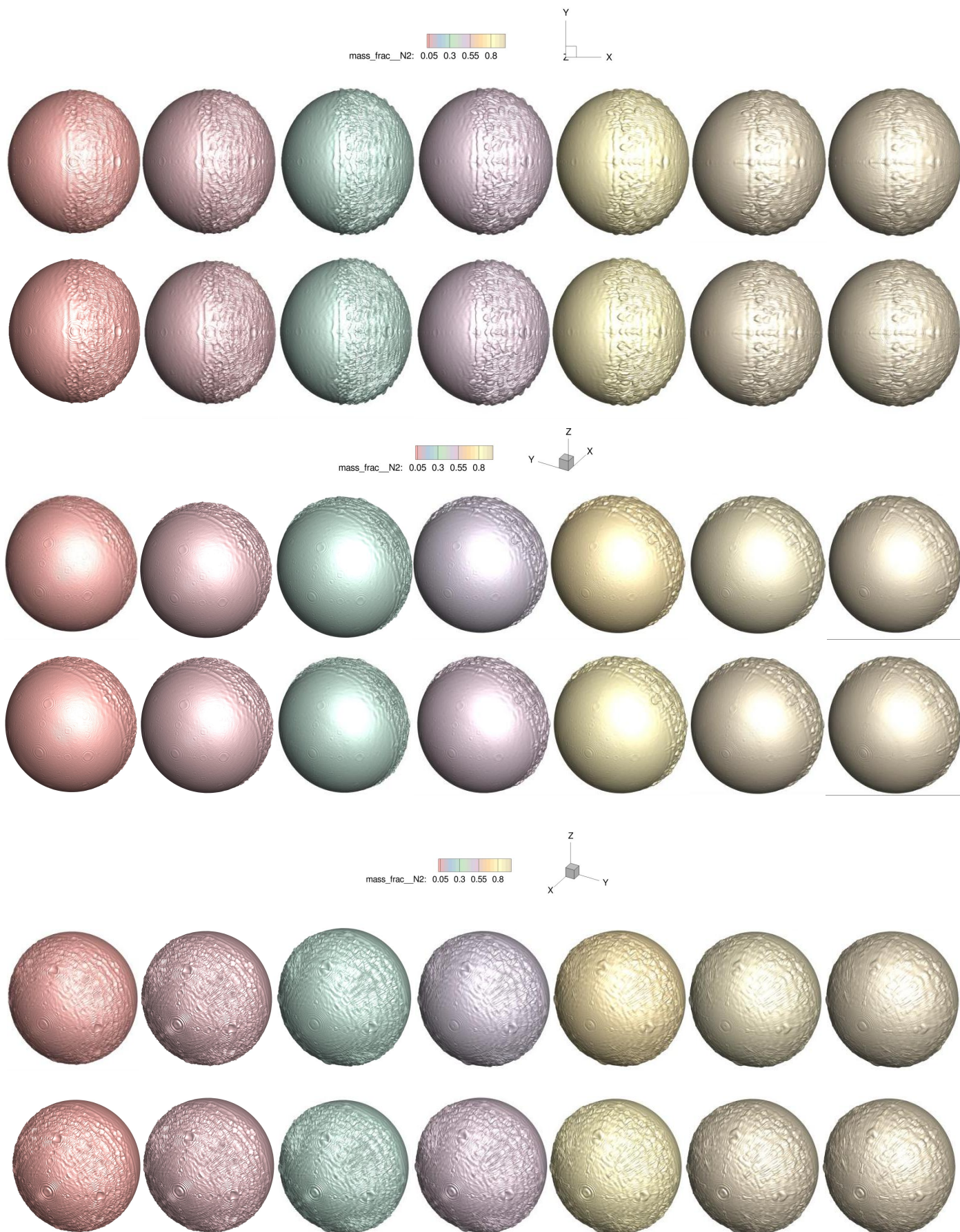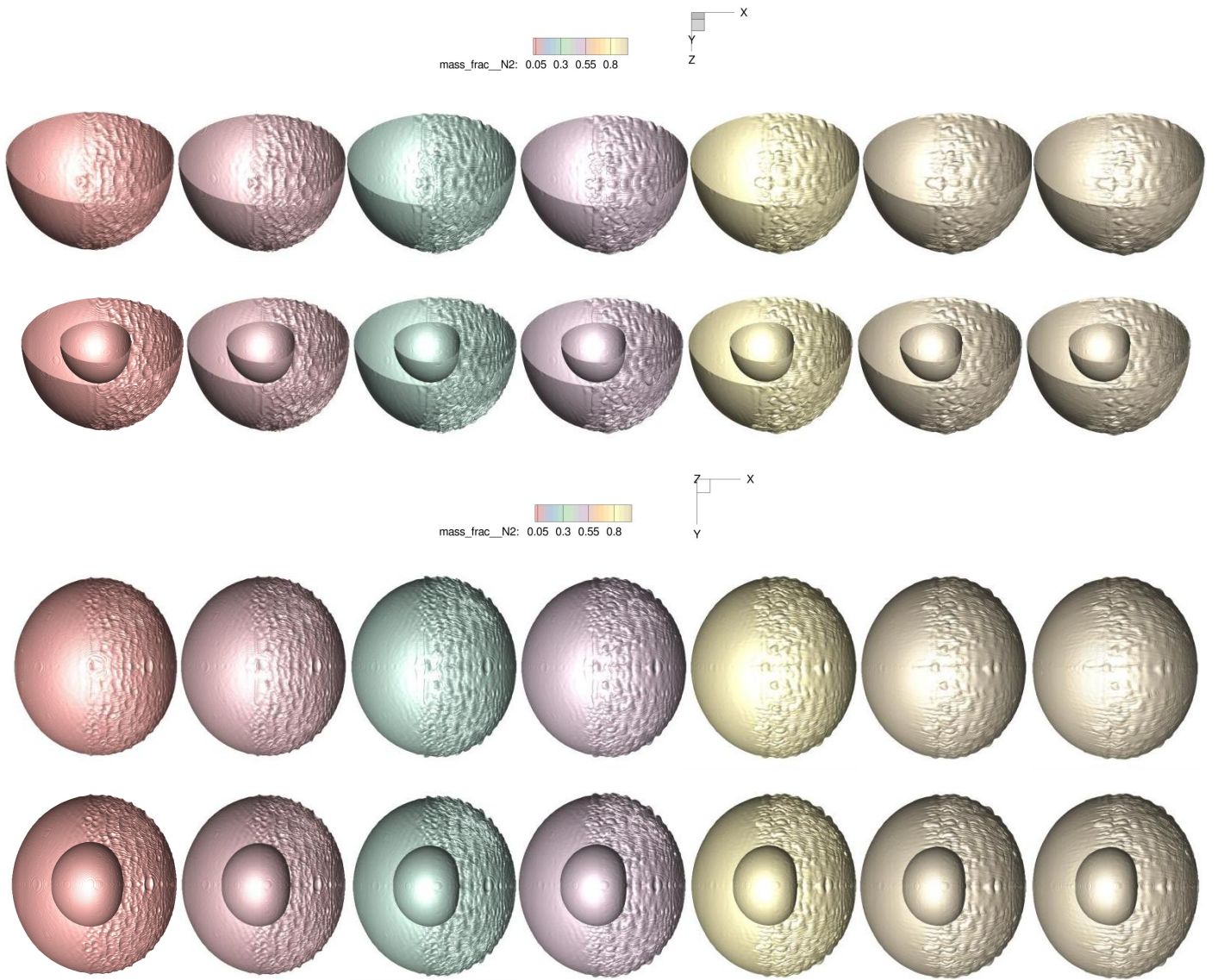
(a) Pure droplet: upper; droplet shell: lower. $t^*=15$.
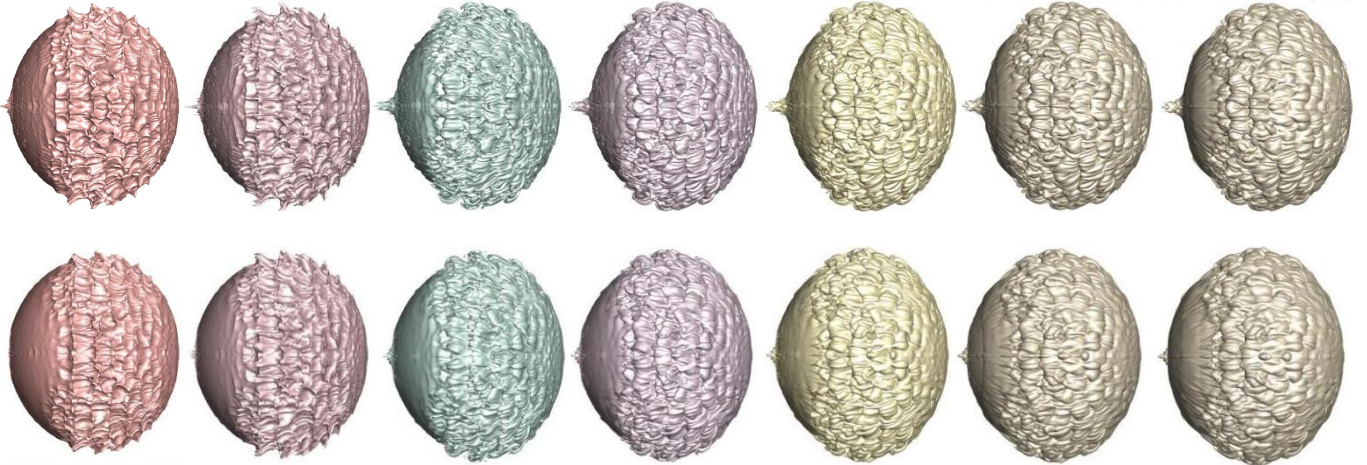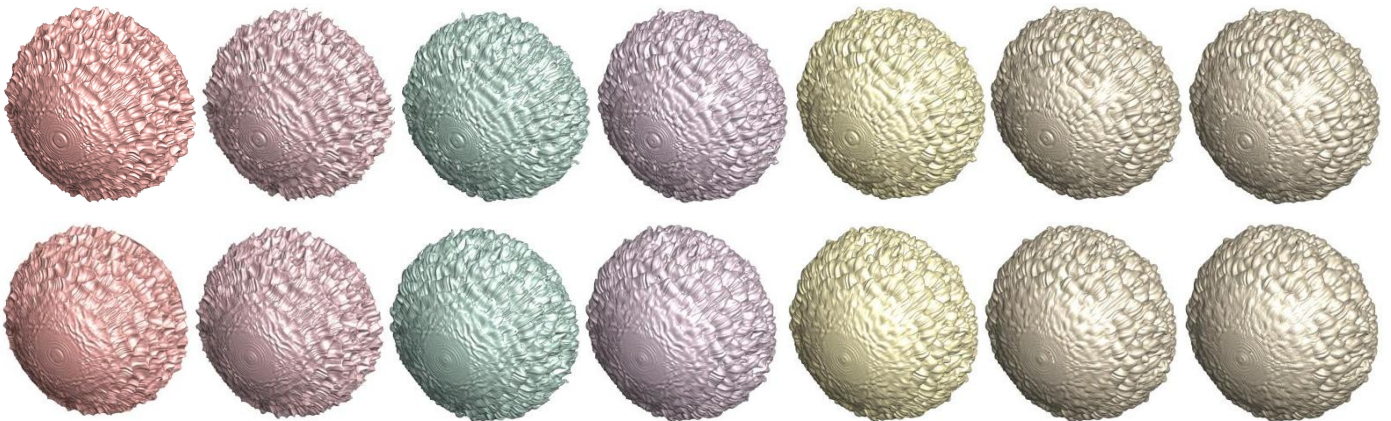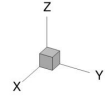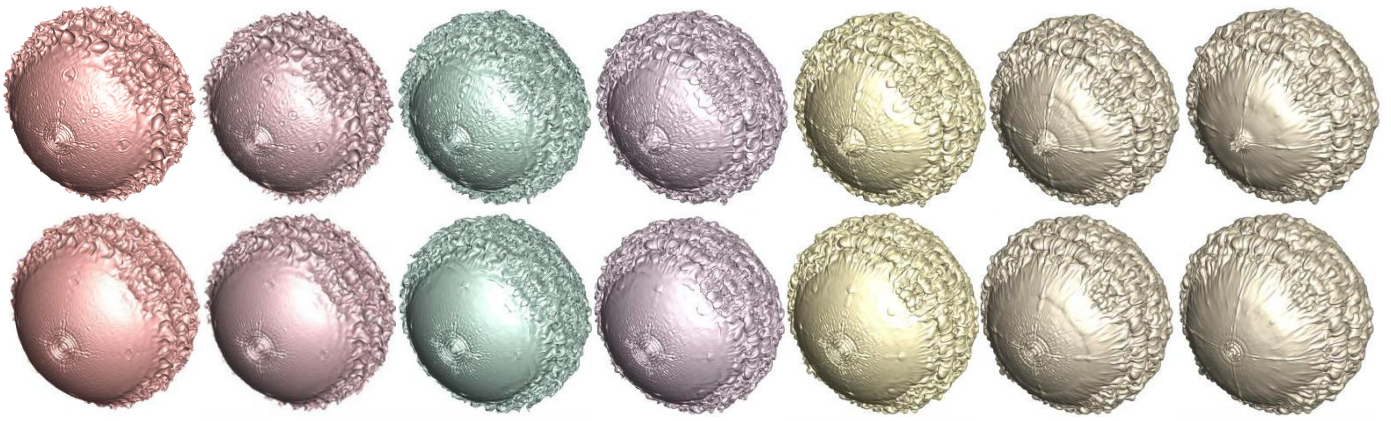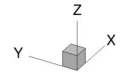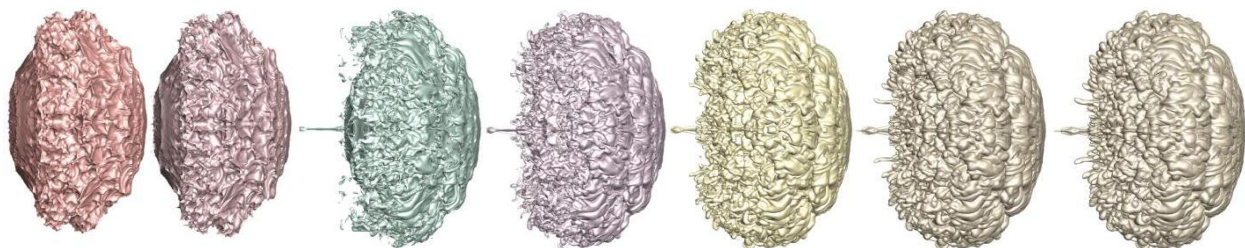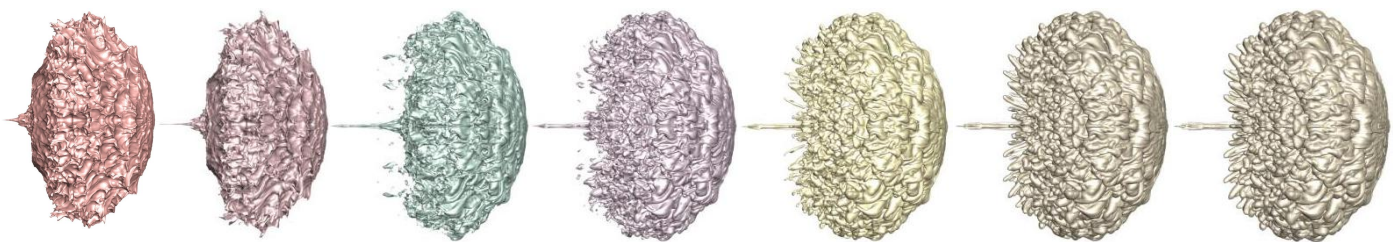
(b) Pure droplet: upper; droplet shell: lower. $t^*=27$.
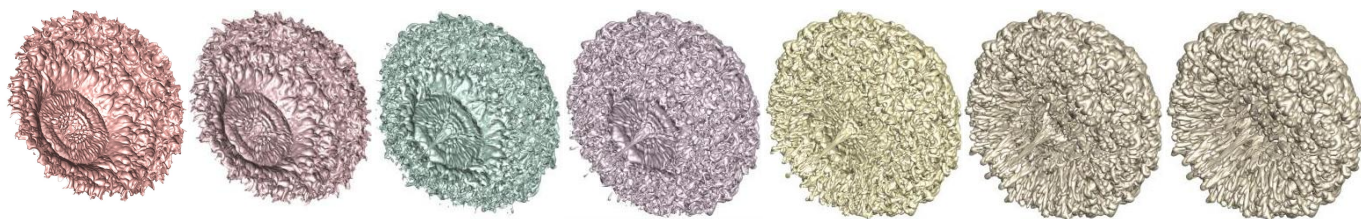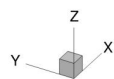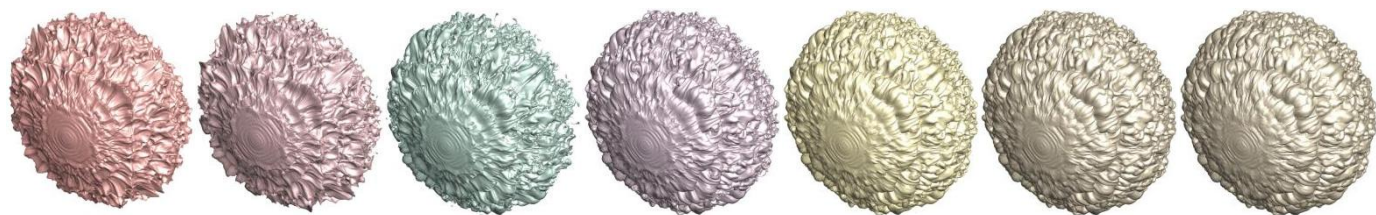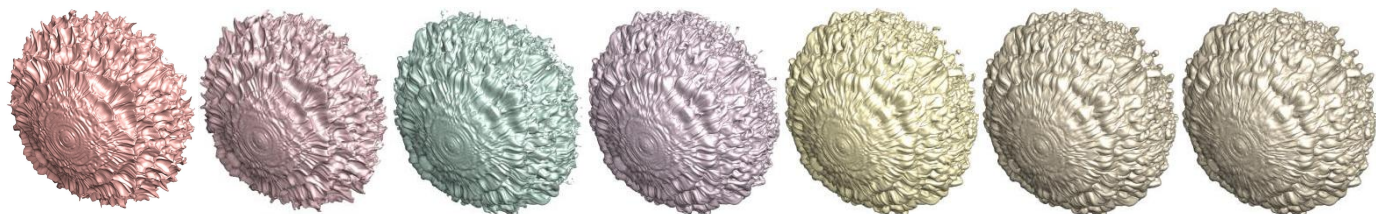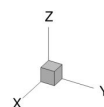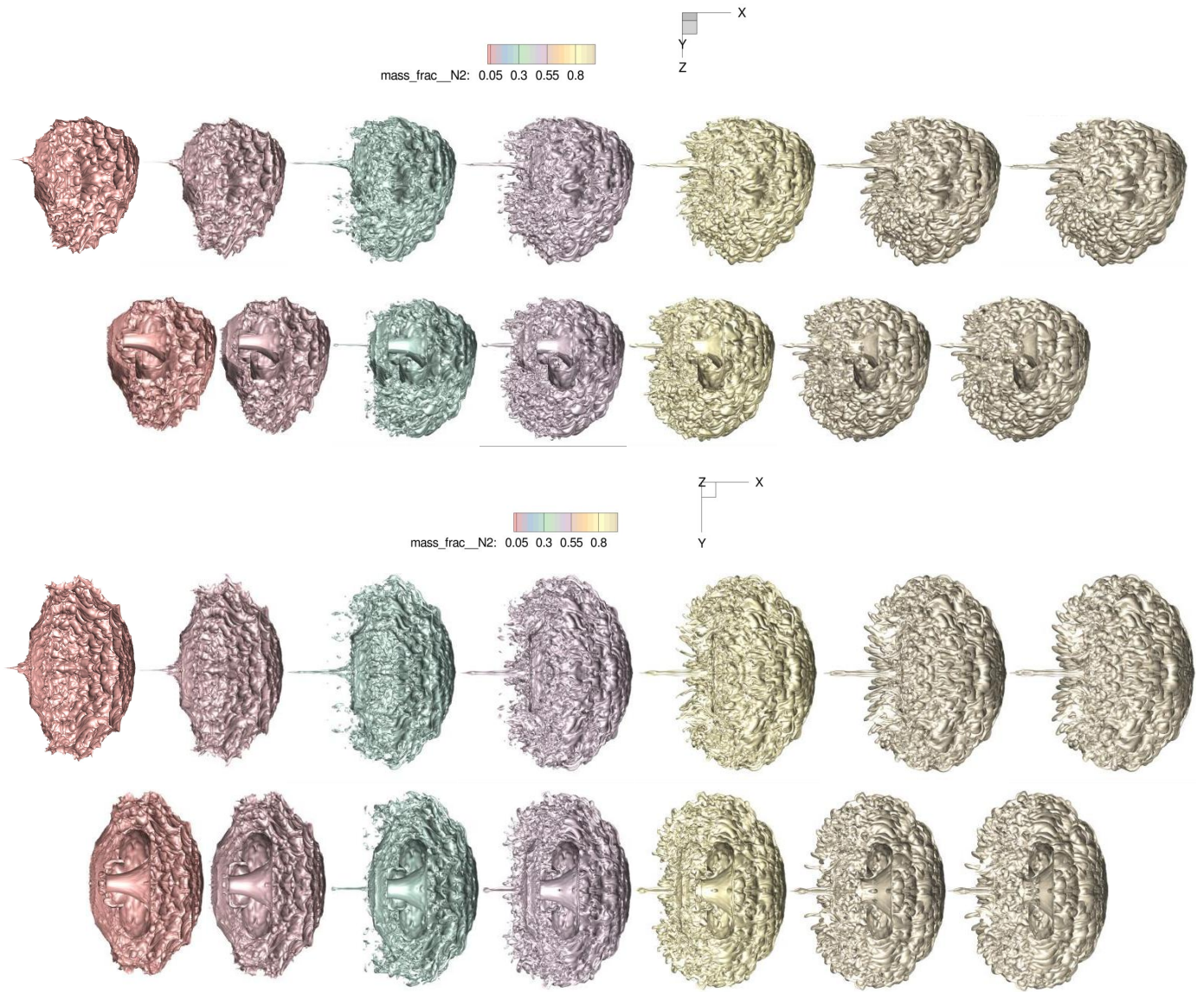
(c) Pure droplet: upper; droplet shell: lower. t^*=49.
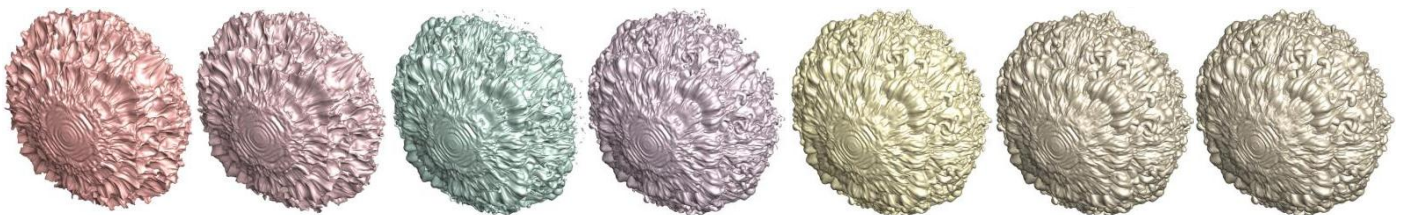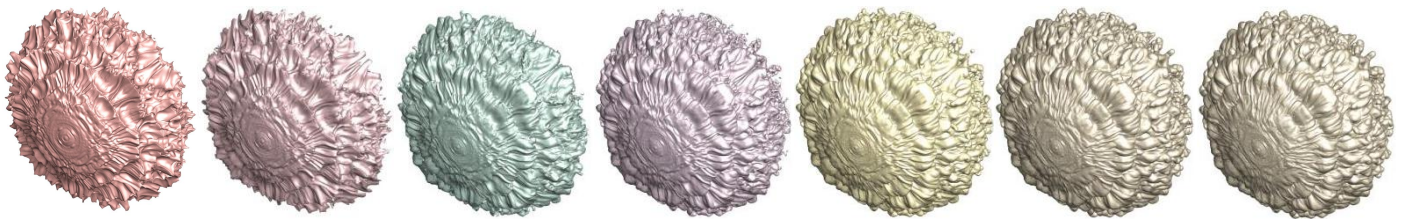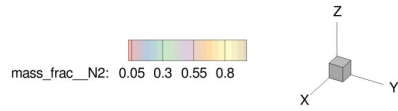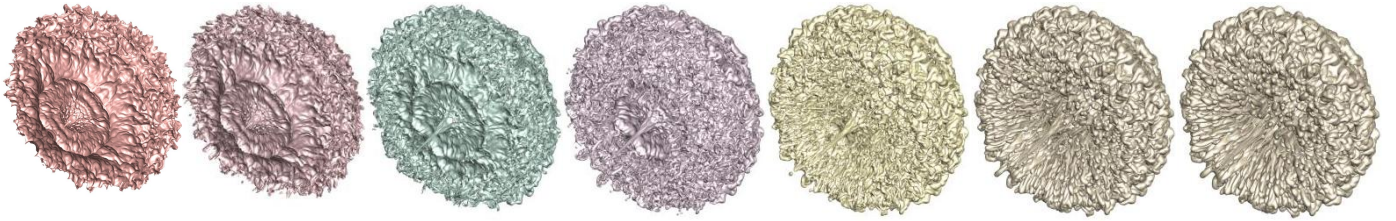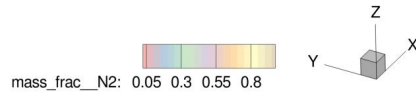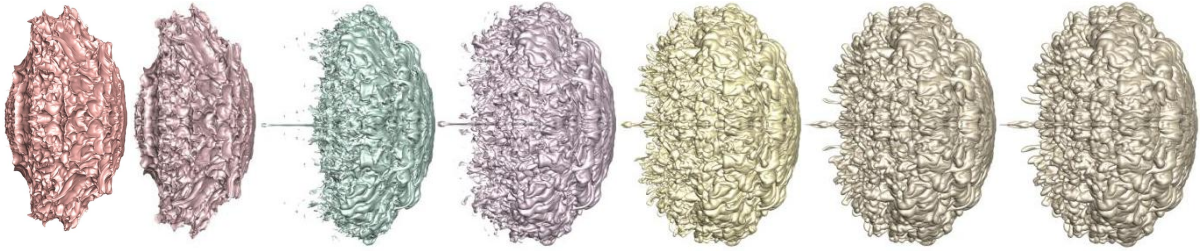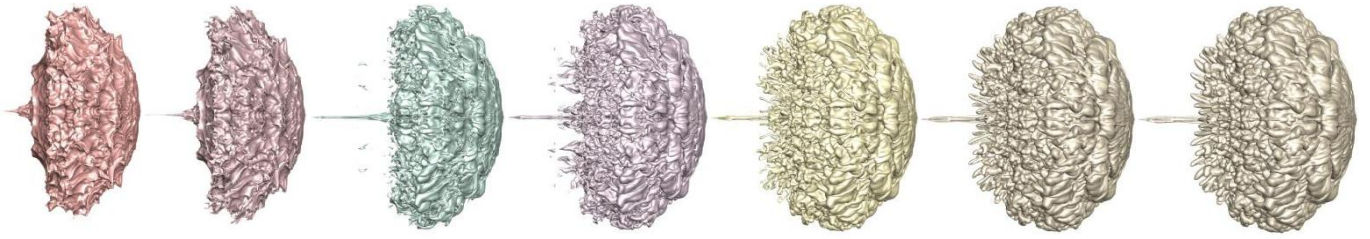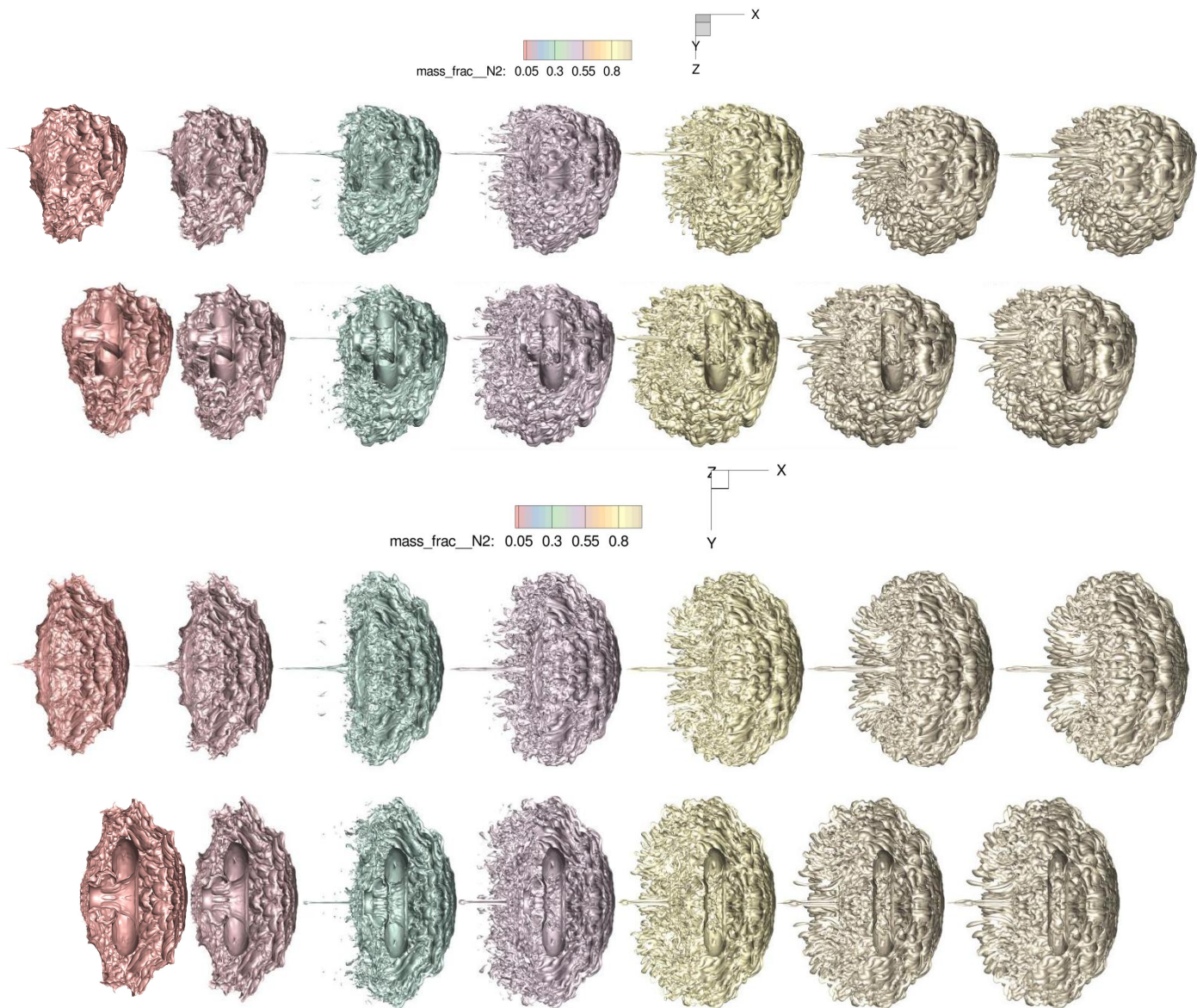
(d) Pure droplet: upper; droplet shell: lower. t^*=56.
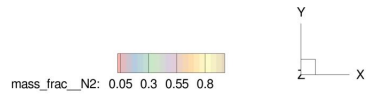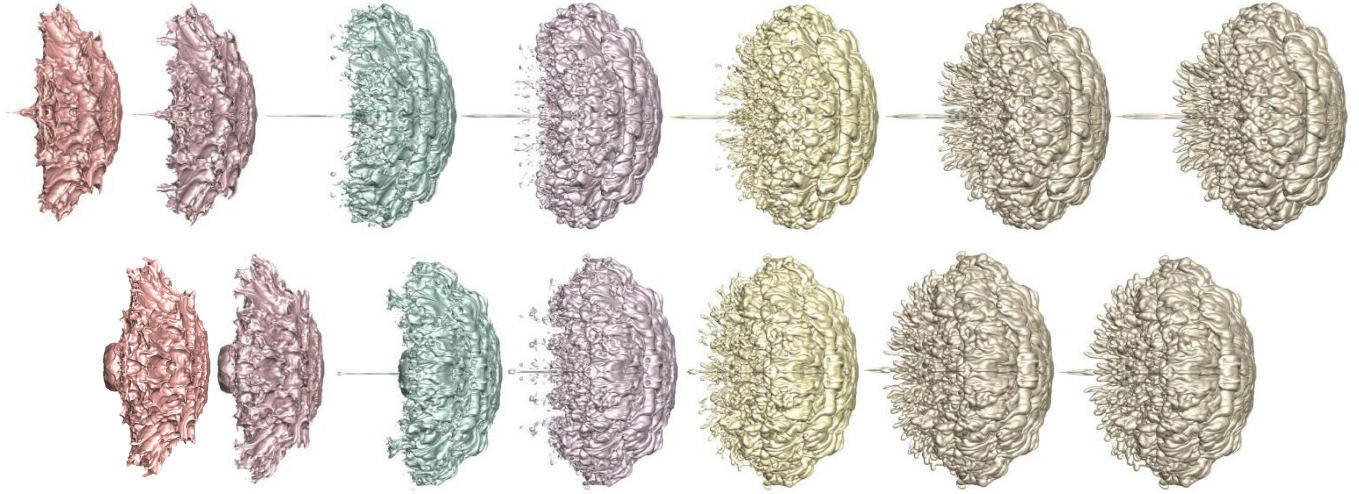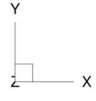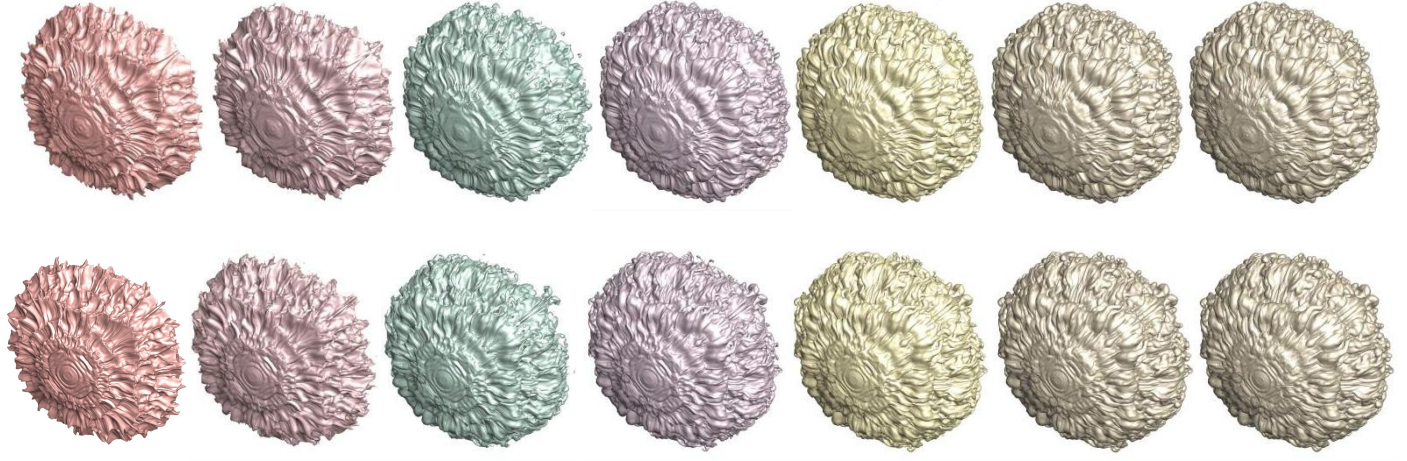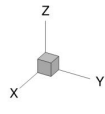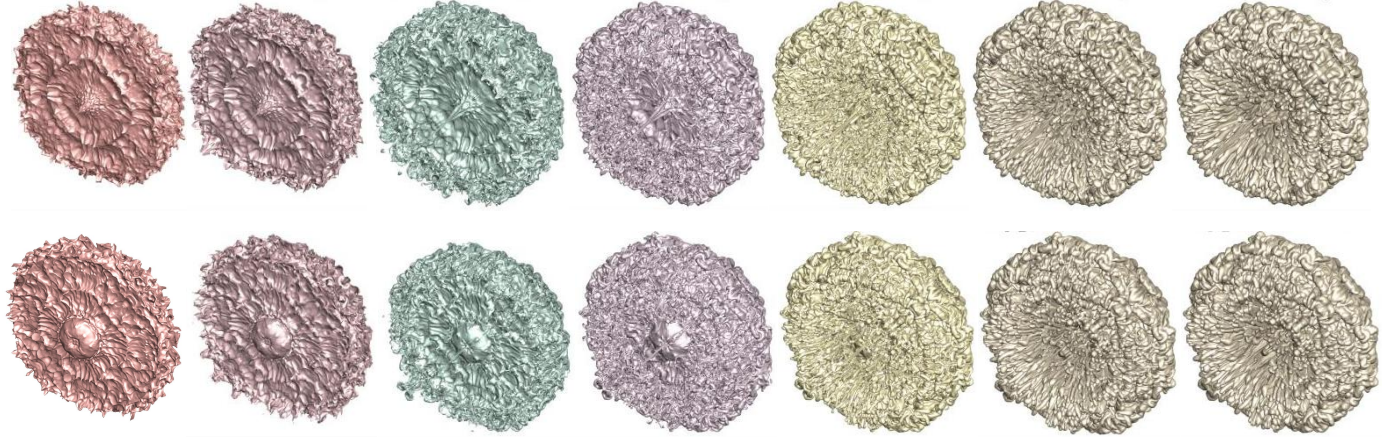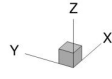
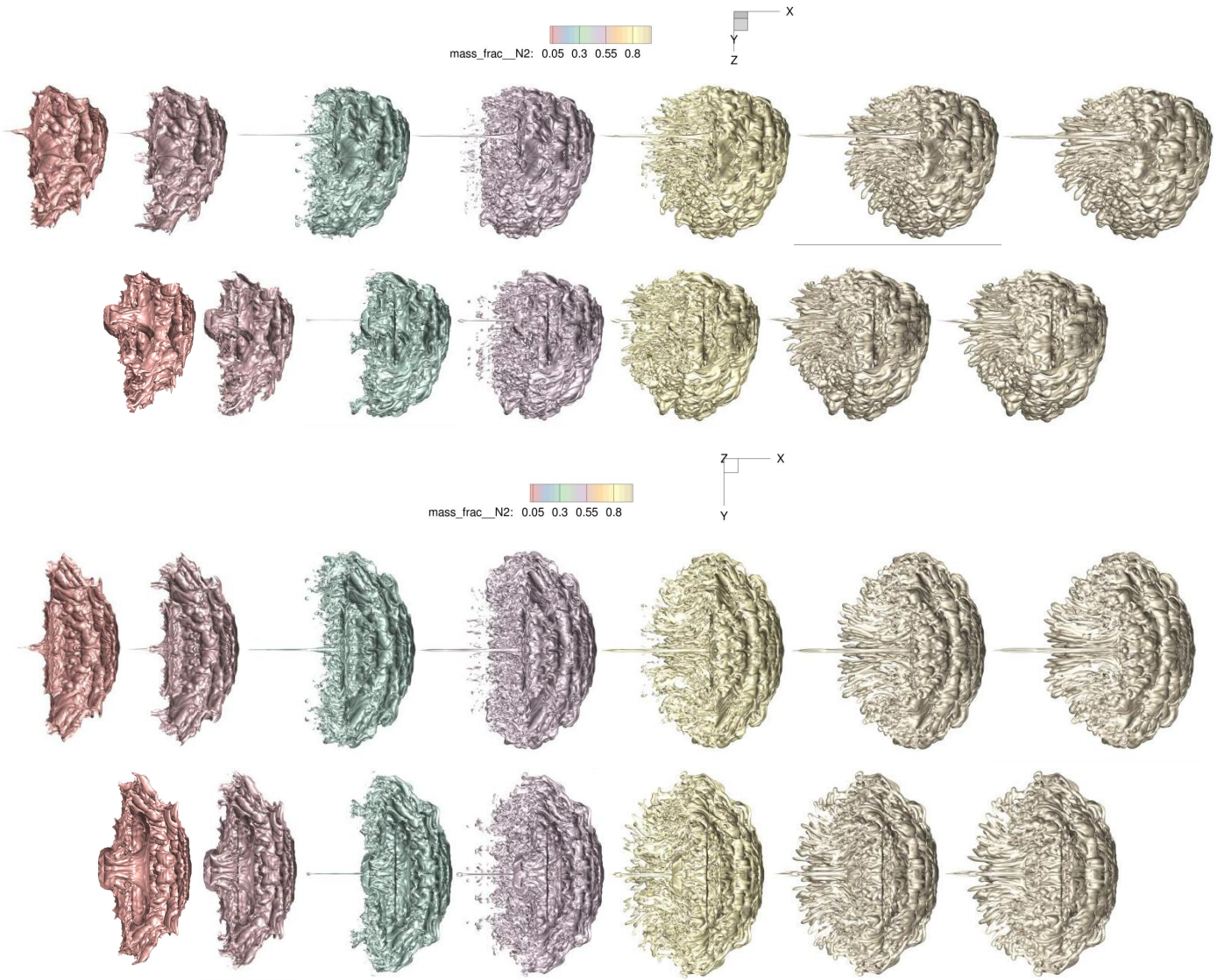mass_frac__N2: 0.05 0.3 0.55 0.8

mass_frac__N2: 0.05 0.3 0.55 0.8

mass_frac__N2: 0.05 0.3 0.55 0.8

(e) Pure droplet: upper; droplet shell: lower. t^*=66.

FIG. 28. Isosurfaces of the gas mass fraction, 0.01, 0.05, 0.25, 0.5, 0.75, 0.95, 0.99 (from left to right) at t^* (a) 15, (b) 27, (c) 49, (d) 56, (e) 66.

Figure 28 shows the evolution process of deformed two-phase interface structures, with isosurfaces of the gas mass fraction varying from 0.01 to 0.99. Detailed observations of the evolutionary process are made from different viewing angles.

A.3   Paper III

Effect of gas cavity size and eccentricity on shock interaction with a cylinder at near-critical conditions
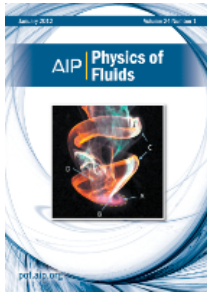
Yu Jiao, Steffen J. Schmidt, Nikolaus A. Adams

Contribution: My contribution to this research paper was to propose the concept and idea of the paper, complete the programming codes and numerical methods, perform the validations, analyse the results, and write the manuscript.

CCC

RightsLink

? 🔗

Effect of gas cavity size and eccentricity on shock interaction with a cylinder at near-critical conditions

Author: Jiao, Yu; Schmidt, Steffen J.

Publication: Physics of Fluids

Publisher: AIP Publishing

Date: Sep 5, 2024

Rights managed by AIP Publishing.

Creative Commons

Effect of gas cavity size and eccentricity on shock interaction with a cylinder at near-critical conditions

Yu Jiao ✉ ⓘ ; Steffen J. Schmidt ⓘ ; Nikolaus A. Adams ⓘ

Check for updates

View Online

Export Citation

Physics of Fluids

Special Topic:

Flow and Lipid Nanoparticles

Guest Editors: Richard Braatz and Mona Kanso

Submit Today!

AIP Publishing

AIP Publishing

Effect of gas cavity size and eccentricity on shock interaction with a cylinder at near-critical conditions

View Online   Export Citation   CrossMark

Yu Jiao,[1,a] [ID] Steffen J. Schmidt,[1] [ID] and Nikolaus A. Adams[1,2] [ID]

AFFILIATIONS

[1]Chair of Aerodynamics and Fluid Mechanics, TUM School of Engineering and Design, Technical University of Munich, 85748 Garching bei München, Germany
[2]Munich Institute of Integrated Materials, Energy and Process Engineering (MEP), Technical University of Munich, 85748 Garching bei München, Germany

[a]Author to whom correspondence should be addressed: yu.jiao@tum.de
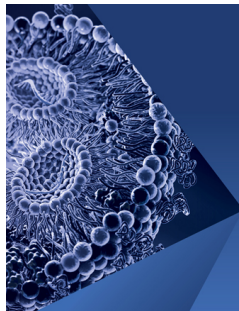
ABSTRACT

In this study, we investigate the impact of gas cavity size and eccentricity on the interaction of shockwaves with a cavity-embedded fuel-liquid cylinder under near-critical conditions. We analyze a range of scenarios involving both eccentric and concentric cavities, varying cavity radii ($0-0.875R$), eccentricity angles ($0°-180°$), and distances ($0R-0.45R$). Our methodology entails modeling the evolution of the fuel cylinder and surrounding gas flow using compressible multi-component equations, employing a finite-volume-based hybrid numerical framework capable of accurately capturing shocks and interfaces. Additionally, real-fluid thermodynamic relationships are employed, validated against reference data, showing excellent agreement. Mesh independence studies are provided. We analyze the shock impingement characteristics, deformation of the cylinder and cavity, and the formation of vortices. Various phenomena at different evolution stages are explored, including wave pattern evolution, jet formation, cavity breakup, baroclinic vorticity distribution, and circulation histories. Size and eccentricity of the cavity determine time intervals between wave contact with the cylinder and with the cavity, thereby influencing the evolution of wave patterns and interface deformation. We propose an analytical model for deposited circulation, obtained by appropriately combining the Yang, Kubota, and Zukoski (YKZ) and the Zhang and Zou (ZZ) models, which agrees well with numerical findings for cases involving smaller cavities. However, for larger cavities, as the cavity gradually reaches the cylinder surface, induced coupling effects invalidate the model. Furthermore, we introduce four predictive fits for the center-of-mass position of the shocked cylinder under near-critical conditions. These fits—the Time-Size Polynomial Prediction Fit, the Time-Eccentricity Polynomial Prediction Fit, the Time-Eccentricity Distance Polynomial Prediction Fit, and the Connecting Rod Prediction Fit—are tailored for cases involving cavities of varying sizes, eccentricity angles, and distances. Demonstrating good predictive performance, these fits offer valuable insights into the mixing behavior of liquid fuel sprays in a diverse range of near-critical environments and high-speed propulsion systems.

I. INTRODUCTION

The Richtmyer–Meshkov instability (RMI) arises when an interface between fluids of different densities experiences impulsive forces, such as shock waves, with an initial perturbation. This instability undergoes a linear growth phase followed by nonlinear development, resulting in the generation of numerous small-scale structures near the interface, ultimately leading to turbulent mixing.[1–4] This phenomenon has been studied both theoretically by Richtmyer[5] and experimentally by Meshkov,[6] making fundamental contributions to understanding shock-induced instabilities.

The significance of RMI spans various fields including high-speed propulsion, inertial confinement fusion, and astrophysics. In high-speed propulsion, enhancing the interaction between shock waves and the fuel-oxidizer interface is crucial for improving mixing, reducing combustion distances, and engine volumes. Shock interactions with fuel–gas interfaces are particularly relevant in high-speed propulsion systems,[7,8] such as ramjets and scramjets, especially during processes like startup, mixing, and combustion of high-speed liquid fuel injection. When a high-speed fuel jet enters a combustion chamber with pressure near the critical pressure of the fuel, it can induce

05 September 2024 13:17:46

shock waves that interact with the fuel. Investigating such interactions provides valuable insights for improving fuel mixing in propulsion systems.

Near the critical point, it is essential to consider "transcritical" properties, where the pressure in the combustion chamber approaches the critical pressure of the fuel. Under these conditions, higher temperatures can cause a transition from a liquid-like state to gas-like behavior. At transcritical conditions, both supercritical (diffusion-controlled) behavior and subcritical (two-phase) properties can occur.[9,10] For example, the critical properties of n-dodecane are defined by a critical pressure (p_c) of 1.82 MPa and a critical temperature (T_c) of 658.1 K. If n-dodecane fuel is injected into a combustion chamber at the supercritical pressure ($p/p_c > 1$) and at a temperature below the critical temperature ($T/T_c < 1$), it mixes with hot ambient air/Nitrogen, causing the fuel to undergo a transformation from a liquid-like fluid to a gas-like supercritical fluid by crossing the Nishikawa–Widom line. This scenario,[11–13] known as "pseudo-boiling," occurs at higher supercritical temperatures and pressures, where fuel fluids exhibit ideal gas behavior when their compressibility factor equals one, and the transition from liquid-like to gas-like behavior occurs.[14,15]

While there have been numerous studies of transcritical fluids in low-speed convective environments, where fluid evaporation is significantly influenced by viscous effects and heat conduction,[16–22] research on the interaction of transcritical fuel cylinders with shock waves or high-speed flows is limited. In these high-speed flows, viscous diffusion, thermal diffusion, and surface tension forces are expected to have negligible effects.

Shock–cylinder interactions (SCIs) are valuable studies as the liquid/gas cylinder spans a wide range of angles between pressure and density gradient, supporting various degrees of baroclinic productions. SCIs have been widely reported and studied for many years,[23–31] both numerically and experimentally. However, these studies have predominantly explored subcritical and supercritical conditions, with limited investigation into transcritical conditions. In earlier research, Haas and Sturtevant[23] presented intricate phenomena that occur during shock interaction with helium and R22 refrigerant gas cylinders through experimentation. The wave patterns both inside and outside the shocked cylinder were analyzed. Jacobs[24,25] studied shock interaction with a membraneless light/heavy gas cylinder. Wang et al.[26] experimentally generated a two-dimensional, discontinuous SF6-gas cylinder with a controllable shape. Additionally, planar shock interaction with three-dimensional discontinuous gas cylinders has been discussed by Ding et al.[27,28] Numerical simulations[29–31] have also been utilized to investigate the development of circular or elliptical gas cylinders. These SCIs have been carried out at atmospheric pressure and temperature. Moreover, it should be noted that SCIs are more accessible to be studied experimentally than shock–droplet or shock–bubble interactions. However, obtaining detailed experimental data on multiphase shock-driven instabilities, particularly at high pressures and temperatures, remains challenging. Thus, numerical experiments have become vital for studying the impact of shock waves on fuel cylinders at near-critical conditions.

The interaction between shock waves and cylinders containing gas cavities is rarely explored for transcritical cases. Conducting numerical experiments under these demanding conditions is challenging, requiring robust numerical methods. Previous investigations in this field have mainly focused on scenarios with low temperatures and pressures at ambient conditions.[32–39] Only a few studies have examined the impact of cavity size or position on shock–cylinder interaction. Feng et al.[32] experimentally investigated the interaction of shock with an SF6 ring and analyzed the impact of the internal gas cylinder on the evolution of the SF6 ring with different radius ratios. Xu et al.[33] analyzed the interaction between a shock and a circular air cylinder embedded in an elliptical SF6 cylinder. These cylinders with different radius ratios were formed by the soap film technique in a room environment.[32,33] Wang et al.[34] conducted a numerical study on a shock-accelerated gas ring with an inner circle radius of r/R = 0.25–0.9375. The initial stag mentions that stagnation air temperature was 288 K, and the pressure was 0.101 MPa. The study provides insights into the evolution of the gas ring and proposes a straightforward method for predicting its circulation. Xiang and Wang[35] analyzed the interaction of shock waves with a water column (0.101 MPa) containing an air cavity (below 0.665 MPa) of varying sizes at high Weber numbers. In the current study, the pre-shock pressure of Nitrogen is 6 MPa, and the temperature is 650 K, significantly deviating from the previously mentioned cases. A few studies have explored shock interactions with the droplet[40] and the shock interaction of a droplet above the critical pressure at varying temperatures.[41] These studies have provided insights into the early deformation behavior and mixing efficiency of high-pressure fuel injection but have not addressed the effects of the cavity.

To date, the interaction of a shock wave with a liquid cylinder embedded with a gas cavity at near-critical conditions has been investigated in Ref. 42. However, only a scenario with a concentric cavity was conducted. There is still a significant gap in understanding the interaction between shock waves and cavity-embedded cylinders with varying parameters. The present study employs numerical experiments to investigate the interaction of a planar shock wave with a fuel cylinder, involving eccentric and concentric cavities with varying radius, at transcritical conditions. This research is the first to investigate the effects of varying cavities on a fuel cylinder at transcritical conditions using a hybrid scheme with a real-fluid model. The findings provide valuable insights for practical applications in a variety of transcritical environments and high-speed propulsion systems.

II. PHYSICAL MODEL

The physical model used in this work is the same as that used in our previous work.[42] To solve the flow under near-critical conditions, we employ a model capable of switching between a fully conservative (FC) scheme and a quasi-conservative (QC) scheme under specific conditions.[42] This model is coupled with a modified Peng–Robinson equation of state (PR-EOS) and has recently been integrated into the CATUM (CAvitation Technical University of Munich) framework.[42–46] Notably, this hybrid approach demonstrates robust performance in mitigating pressure oscillations, maintaining positivity,[47] and minimizing energy conservation losses during shock wave interactions with interfaces, such as those between Nitrogen and n-dodecane.[40]

For the FC scheme, the vector of conserved quantities $\mathbf{q} = [\rho, \rho\mathbf{u}, \rho E, \rho\xi]^T$ is computed from the compressible Euler equations, $\partial\mathbf{q}/\partial t + \nabla \cdot \mathbf{F}(\mathbf{q}) = 0$, where ρ is the density, the flux vector $\mathbf{F}(\mathbf{q}) = \mathbf{u}[\rho, \rho\mathbf{u}, \rho E + p, \rho\xi]^T + [0, p\mathbf{I}, 0, 0]^T$, $\mathbf{u}$ is the velocity vector, $\rho E = \rho(e + |\mathbf{u}|^2/2)$ is the total energy and e is the internal energy, and ξ refers to the mass fraction of the gas component. In longer-duration interactions or low-speed cases, gravity, heat transfer

(thermal conduction), and viscous effects may play significant roles. However, for the current problem of interest, these factors, along with surface tension and chemical reactions, are deemed negligible[41] due to the very short time in the shock–cylinder interaction. Moreover, surface tension can be neglected in transcritical flows[10,48–54] as the surface tension coefficient diminishes significantly at the critical point.

Quasi-conservative (QC) schemes commonly employ methodologies such as the double flux (DF) method[11,55–57] and the pressure evolution (PE) method.[58,59] The DF model was initially introduced by Abgrall and Karni[56] for multi-component ideal-gas flows, later extended by Billet and Abgrall[57] for ideal-gas reacting flow systems. Subsequently, high-order schemes based on the DF method have been proposed.[11,60,61] In this study, we adopt the DF-based model proposed by Ma *et al.*[11,62] to handle transcritical flows, as detailed in our previous publication.[42]

The Peng–Robinson equation of state (PR-EOS)[63] is employed for both liquid and gas components. McBride *et al.*[64] provides the parameters for NASA polynomials used to derive internal energy, enthalpy, and entropy, with additional details available in Appendix A. While the PR-EOS is suitable for conditions outside the vapor dome, modifications are necessary for its application within this domain. In certain scenarios, negative pressures may arise at specific density values and relatively low temperatures, potentially leading to complex-valued speed of sound (SoS) within the vapor dome.[65] It is important to acknowledge that within the vapor dome, the thermodynamic state described by the classical Peng–Robinson equation may be metastable or unstable/non-convex.

To address these challenges, a modified PR-EOS[42] is introduced to approximate fluid states within the vapor dome region, ensuring that the speed of sound remains positive to enhance the numerical robustness. It is pertinent to mention that phase separation is not anticipated,[66,67] and the numerical procedure outlined in Ref. 48 adequately resolves pressure oscillations in transcritical flows, with further details available in Appendix B.

III. NUMERICAL METHODS

Observations from Refs. 40 and 41 indicate that the WENO3-type schemes suppress pressure oscillations, particularly in near-critical or transcritical scenarios. Boyd and Jarrahbashi[41] specifically recommends the use of the WENO3-type schemes for simulating higher-strength shock–droplet interactions. In instances of a Mach 2 shock, they even employ a minmod flux limiter based on the gradient of the mass fraction. Moreover, Boyd and Jarrahbashi[40] demonstrates that reducing the reconstruction order from WENO5 to WENO3 leads to a notable reduction in pressure fluctuation amplitudes, from 8 to 3.2 MPa, attributed to the increased numerical diffusion provided by WENO3. However, while compact reconstruction stencils can decrease computational effort, they also yield results of reduced accuracy compared to the same mesh resolution using WENO5. To mitigate this accuracy limitation of WENO3, an increase in mesh resolution and computational resources is necessary. At higher resolutions, results can be made comparable to those obtained with WENO5.

Taking these findings into account, the present study opts to replace WENO5 with a WENO3-type scheme to bolster numerical stability in complex cases, ensuring the preservation of key characteristics from the reference scheme. Specifically, an improved WENO3 scheme, OWENO3,[68] is adopted for reconstructing pressure, density, velocity, internal energy, and mass fraction to maintain numerical consistency.

OWENO3 retains the advantages of JS-WENO3 with reduced dissipation. It incorporates an additional fourth node in the weight calculation for measuring smoothness, based on a WENO approach with the unconditional third-order optimal accuracy on smooth data, without relying on any tuning parameters. The reconstruction domain remains limited to a maximum of four points, consistent with classical WENO3 schemes. Interface diffusion is controlled through the local adjustment of smoothness indicators and ENO stencil weights. OWENO3 has been meticulously validated to handle near-critical shock interactions with n-dodecane, with detailed validation cases presented and compared with previous results obtained using the WENO5-type scheme.[42]

On the compact four-stencil scheme, using reconstruction of mass fraction ξ as an example,

$$\xi^* = w_0 \xi^L + w_1 \xi^R, \tag{3.1}$$

the left and right side interpolation polynomials at the cell interface are $\xi^L = -(1/2)f_{-1} + (3/2)f_0$, $\xi^R = (1/2)f_0 + (1/2)f_1$. The OWENO3 stencil weights are defined as follows:

$$w_0 = \frac{1}{3}w + (1-w)\widetilde{w_0}, \quad w_1 = \frac{2}{3}w + (1-w)\widetilde{w_1}, \tag{3.2}$$

where $\widetilde{w_0} = (I_1 + \varepsilon)/(I_0 + I_1 + 2\varepsilon)$ and $\widetilde{w_1} = (I_0 + \varepsilon)/(I_0 + I_1 + 2\varepsilon) = 1 - \widetilde{w_0}$, with ε being a small value ($\varepsilon = 1 \times 10^{-6}$), and a corrector weight defined as $w = J/(J + \tau + \varepsilon)$, where $J = I_0(I_1 + I_2) + (I_0 + I_1)I_2$ and $0 \leq w \leq 1$. τ represents the product of the square of the undivided difference associated with the extended stencil (four stencils) and the sum of the smoothness indicators, $\tau = dI$, where $d = (-f_{-1} + 3f_0 - 3f_1 + f_2)^2$ and $I = I_0 + I_1 + I_2$. An additional smoothness indicator I_2 using the additional node is employed, leading to $I_0 = (f_0 - f_{-1})^2$, $I_1 = (f_1 - f_0)^2$ and $I_2 = (f_2 - f_1)^2$. f_i indicates the variable at cell i.

Moreover, an HLLC Riemann solver is applied, and additional details can be found in Refs. 69 and 70. Time integration is performed by an explicit, low-storage four-step Runge–Kutta method with an enhanced stability region, which is represented in CATUM.[42–46] The CFL value is generally 0.5 unless otherwise stated.

IV. VERIFICATION AND MESH INDEPENDENCE STUDY

Table I and Fig. 1 present the initial conditions, encompassing thermodynamic parameters, cylinder and cavity position, diameter, boundary conditions, and the computational domain with the shaded fine-mesh region. These illustrate the interaction between a shock wave and a cylinder composed of n-dodecane in a Nitrogen

TABLE I. Initial conditions for the shock interaction with cavity-embedded cylinder at near-critical conditions.

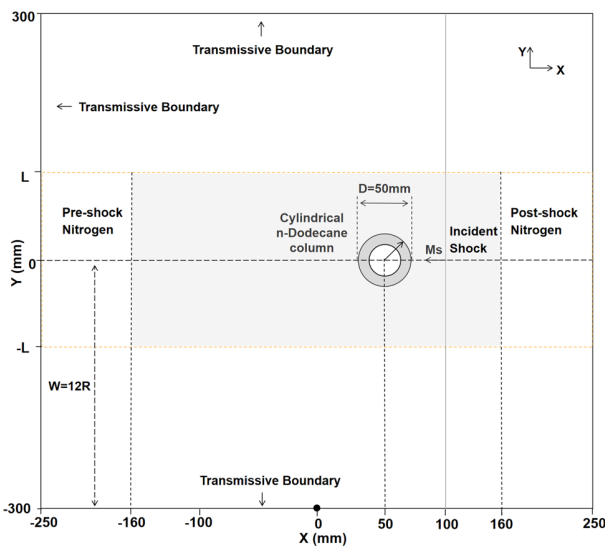| Stage	p(MPa)	u(m/s)	v(m/s)	ρ(kg/m³)	T(K)
Pre-shocked nitrogen	6.0	0	0	30.46	650.0
Cavity nitrogen	6.0	0	0	30.46	650.0
POST-shocked nitrogen	9.096	−160.3	0	40.38	736.2
n-Dodecane	6.0	0	0	419.9	650.0

FIG. 1. Computational domain of the shock interaction with the cavity-embedded cylinder at near-critical conditions (sketch map).

environment. Moreover, a cavity filled with Nitrogen gas is situated within the n-dodecane cylinder. The thermodynamic parameters (pressure, velocity, density, temperature, etc.) and the thermodynamic relationship of the internal gas cavity remain consistent with those of the pre-shock Nitrogen. McBride et al.[64] provide the NASA polynomial parameters.

This interaction occurs at a supercritical pressure and subcritical temperature, placing the n-dodecane in a liquid-like supercritical state. The critical properties of n-dodecane are defined by a critical pressure (p_c) of 1.82 MPa and a critical temperature (T_c) of 658.1 K. As a result, the n-dodecane cylinder is first supercritically pressurized at the subcritical temperature. Nitrogen's critical properties are characterized by a critical pressure (p_c) of 3.369 MPa and a critical temperature (T_c) of 126.2 K. Thus, for Nitrogen, the temperature exceeds the critical temperature and the pressure is above the critical pressure. The shock wave in this environment maintains a Mach number of 1.2. The dimensionless time t^* corresponds to the simulated physical time t, divided by a chosen reference time of 8.68×10^{-6}s.

In our previous work,[42] we qualitatively and quantitatively analyzed the morphology of the shock interaction with a cylinder under the same conditions, considering the effects of mesh resolution, computational domain, boundary conditions, and numerical scheme. Our results were comparable to the work of Boyd and Jarrahbashi.[41] The study concluded that the numerical scheme used was accurate in handling the shock interaction with an n-dodecane cylinder at near-critical conditions. A mesh resolution of 0.115 mm was found to be sufficient to achieve mesh independence convergence and capture detailed features. The combination of high-order OWENO3 and a mesh resolution of 0.115 mm produced results comparable to the WENO5 results of Ref. 41 in terms of computational efficiency, robustness, stability, and accuracy, employing more than 434 computational cells per diameter (diameter = 50 mm).

Given the validated accuracy of the current scheme, Fig. 2 demonstrates the effect of mesh resolution on the shock interaction with the cavity-embedded cylinder at near-critical conditions. Figure 3 shows the density distribution, which completes the mesh independence studies. The density distributions directly display the contact positions of both fluids and converge to the purple line with the finest mesh resolution of 0.0575 mm, as shown in Figs. 3(b) and 3(c). There are slight differences between the results obtained using mesh resolutions of 0.115 and 0.0575 mm. A mesh resolution of 0.115 mm is a suitable choice, balancing accuracy and computational consumption. This resolution is half of the reference mesh resolution of 0.2300 mm and is consistent with our previous analysis.[42]

In summary, a mesh resolution of 0.115 mm offers comparable and accurate results with reasonable computational efforts, thus concluding the study of mesh convergence.

To generate numerical schlieren images, we utilize the following formula to define the pseudo-schlieren value:

$$\varnothing = \exp\left(-\mathrm{k}\frac{|\nabla\rho| + A}{B + A}\right). \tag{4.1}$$

The pseudo-schlieren value, denoted as $\varnothing$, is determined using the formula $|\nabla\rho| = \left[(\partial\rho/\partial\mathrm{x})^2 + (\partial\rho/\partial\mathrm{y})^2\right]^{1/2}$, where three adjustable parameters, A, B, and C, influence its calculation. Typically, A is set to 0, and B equals $|\nabla\rho|_{\max}$, gradually leading to $\varnothing = \exp(-\mathrm{k}|\nabla\rho|/|\nabla\rho|_{\max})$. The gray values displayed in the schlieren images are fine-tuned based on the approach recommended in Ref. 71. It is important to note that the constant "k" plays a role here, taking the value of 600
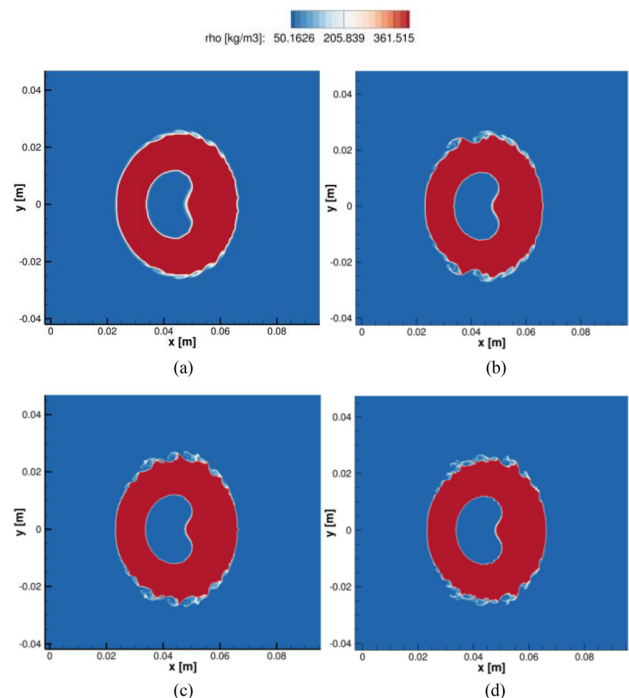

FIG. 2. Shock interaction with the cavity-embedded n-dodecane cylinders at different mesh resolutions: (a) 0.2300, (b) 0.1150, (c) 0.0767, and (d) 0.0575 mm.
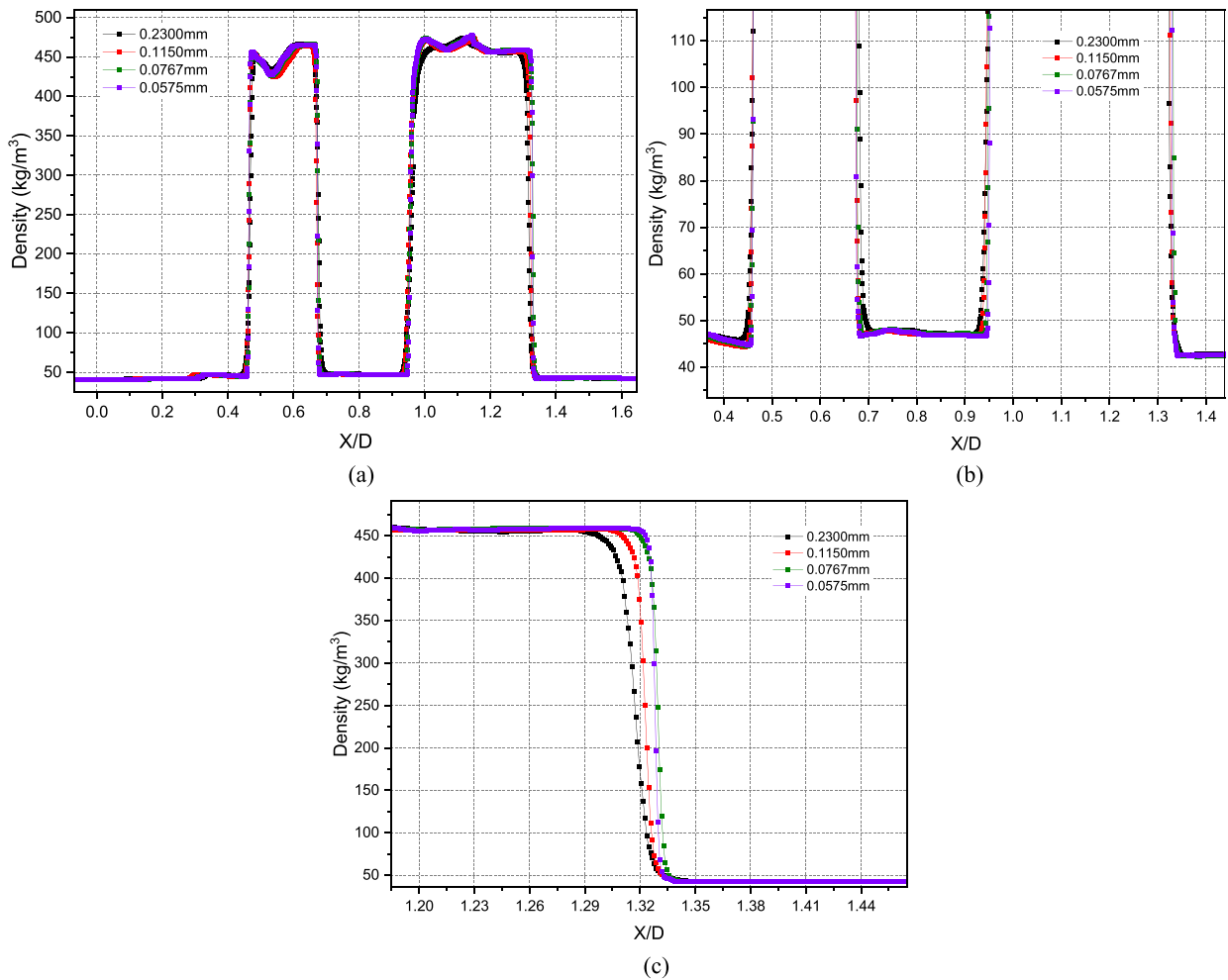
FIG. 3. Grid convergence test on shock interaction with the cavity-embedded cylinder by OWENO3: $t^* = 25$. (a)–(c) show the distribution at different positions.

for light fluids (such as helium) and 120 for heavy fluids (like R22). In the case of shock interaction with a cylindrical fuel column, k is set to 600 for the Nitrogen environment and 120 for the n-dodecane cylinder.

V. RESULTS AND DISCUSSION

A. Analysis of cavity size effects

This section investigates the impact of cavity size on the shock interaction with a cavity-embedded cylinder at near-critical conditions. As depicted in Fig. 4, the ratio of the radius of the gas cavity (r) to the liquid cylinder (R) varies from 0 (full cylinder) to 0.875 (the thinnest cylinder ring). The shaded area represents the "cylinder ring," with its characteristic diameter (width) calculated as the difference between the cylinder radius R and the cavity radius r. The diameter of the gas cavity determines the gas fraction within the cylinder. The thermodynamic parameters, such as pressure, velocity, density, and temperature, as well as the thermodynamic relationship of the internal gas cavity,

remain consistent with those of the pre-shock Nitrogen. The initial dimensionless time is $t^* = 0$.

In our terminology, USD stands for the "Upstream Surface of the cylinder," distinguishing it from USC (the "Upstream Surface of the Cavity"). Similarly, DSD denotes the "Downstream Surface of the cylinder," differentiating it from DSC (the "Downstream Surface of the
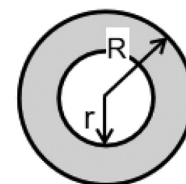

FIG. 4. Schematic of a cavity-embedded cylinder with different cavity radii r.

Cavity"). Additionally, the cases used for comparison with current near-critical studies generally operate under sub-critical conditions, unless otherwise specified, such as the shock-helium bubble interaction under sub-critical conditions. In Secs. V A 1 and V A 2, the early and late stages are defined in the same way as in previous work,[42] with the early stage focusing on the evolution of wave patterns and the late stage focusing on the evolution of cylinder deformation and cavity rupture. We do not focus on the very late stage, where even finer resolution is required.

1. Early wave pattern evolution

Figure 5 depicts the influence of gas cavity size on the shock–cylinder interaction process at near-critical conditions. In Fig. 5(a), the incident shock (IS) traverses over the upstream surface of the cylinder (USD), resulting in the generation of the reflected shock (RS) and the converging (refracted) transmitted shock (TS1). Concurrently, the cylinder undergoes deformation and initiates downstream movement (at $t^* = 5$ and $r/R = 0.250$).

Upon TS1 encountering the upstream surface of the cavity (USC), the angle between USC and TS1 begins to increase from 0. At this early stage, the second reflected rarefaction wave (RR) and the diverging (refracted) transmitted shock (TS2) form, both at relatively small angles (at $t^* = 10$ and $r/R = 0.250$). Meanwhile, the cavity moves and deforms downstream, resembling typical refraction processes. Additionally, the interaction process between the inner shock and cavity resembles shock interactions with lighter gas bubbles.

As TS1 progresses, the angle between USC and TS1 increases, resulting in a refraction process. TS2 inside the Nitrogen cavity moves faster than TS1 inside the n-dodecane cylinder due to the higher impedance of n-dodecane compared to Nitrogen. This generates a side shock (SS) and a new shock (NS1) (at $t^* = 11$ and $r/R = 0.500$). At this stage, TS1, SS, NS1, and reflected shock (RS2) converge at a point marked as "P4," resembling the free precursor refraction (FPR) phenomenon. RS2 and SS propagate in different directions, forming an angle between them. Consequently, P4 is replaced by two distinct intersection points (P2), and a Mach stem is formed (at $t^* = 13$ and $r/R = 0.375$), resembling the twin von Neumann refraction (TNR).[73] Key observations from Fig. 5(a) include the following:

(1) The wave structures (RS, TS1, IS) remain consistent across all cases before TS1 reaches the USC, with the RS located outside the cylinder toward the upstream unaffected by the cavity, as is the IS around the cylinder surface.
(2) The size of the cavity determines when TS1 touches the cavity, resulting in varying interaction durations between TS1 and the cavity, with TS1 touching the cavity of the case with the largest r/R first.
(3) For cases where $r/R = 0.625$, 0.750, and 0.875, the RR/RS2 touches the cylinder and is reflected from it.
(4) As the cavity size increases, the ring thickness decreases, leading to more reflection waves being generated within the ring for the same duration and to a faster occurrence of another TS within the cavity, making the wave pattern more complex.

Figure 5(b) shows that as TS2 reaches the downstream surface of the cavity (DSC), it gives rise to a transmitted shock (TS3) and a reflected shock (RS3), both traveling in opposite directions. The points of intersection for these three shock waves (P3) arise from the movement of TS1 (at $t^* = 15$ and $r/R = 0.500$). Afterward, both the transmitted wave (TS5) and the reflected wave (RS5) emerge near the upstream surface of the cavity (at $t^* = 16$ and $r/R = 0.500$). RS2 refracts from the downstream surface of the cylinder (DSD), forming a transmitted shock from RS2 (TRS2). Additionally, diffracted shock waves form a crossover point outside the DSD. Furthermore, TS3 passes through the DSD, creating a fourth transmitted shock (TS4) and a rarefaction wave heading toward the downstream surface of the cavity (at $t^* = 17$ and $r/R = 0.500$). The primary structures of the wave pattern outside the cylinder ring are the diffracted shock, TRS2, and TS4. Inside the cylinder ring, further evolution of NS1, TS1, the rarefaction wave of TS3, and other waves form a complicated pattern of waves.

Due to variations in the speed of sound (Sos) between liquid and gas phases, as well as differences in the distance between the cavity surface and cylinder surface, a number of discrepancies arise between cases, as illustrated in Fig. 5(b).

(1) For cases with a larger cavity, the transmitted shocks (TS1, TS3) reach the downstream pole of the outer cylinder surface before the DS does. Additionally, the formation of TS4 is accelerated.
(2) As the cavity size decreases, the RS3 reaches the upstream surface of the cavity at an earlier stage.
(3) When the cavity is larger, the TS5 and RS5 are generated earlier near the upstream surface of the cavity.

In addition, it can be observed from Fig. 5(c) that between $t^* = 19$ and $t^* = 23$, the following applies:

(1) The smaller the cavity, the earlier it begins to deform into kidney-shaped structures. Cases with a larger cavity exhibit a greater delay in deformation of the cavity.
(2) The pattern of waves inside the cavity is too intricate to identify, whereas the IS, DS, TS, and TRS outside the cylinder exhibit similarity across all instances.
(3) Following the discussion for Fig. 5(b), for cases with a larger cavity, the wave structures connected to TS4 move faster.

Figure 5(d) shows the upstream pole displacement of the cylinder. The dotted straight lines with the numbers 1, 2, 3 represent the moment when the reflections touch the upstream pole of the cylinder (UPD). For the cases where the ratio between the cavity and the cylinder is greater, the surfaces between the cavity and the cylinder are so close that the reflections are difficult to observe. It should be noted that the displacement measurement could have some measurement error, which could not be completely avoided. For cavity radii between 0.25 and 0.5, the times of the reflections occurring at the UPD are the same. The smaller the cavity, the larger the ring, the longer the time (t_{ring}) for the first reflection to occur at the UPD, which is clear since the time depends on the distance between the cylinder and the cavity ($W_{ring} = R_{cylinder} - R_{cavity}$) and the speed of sound (c_{ring}) inside the ring.
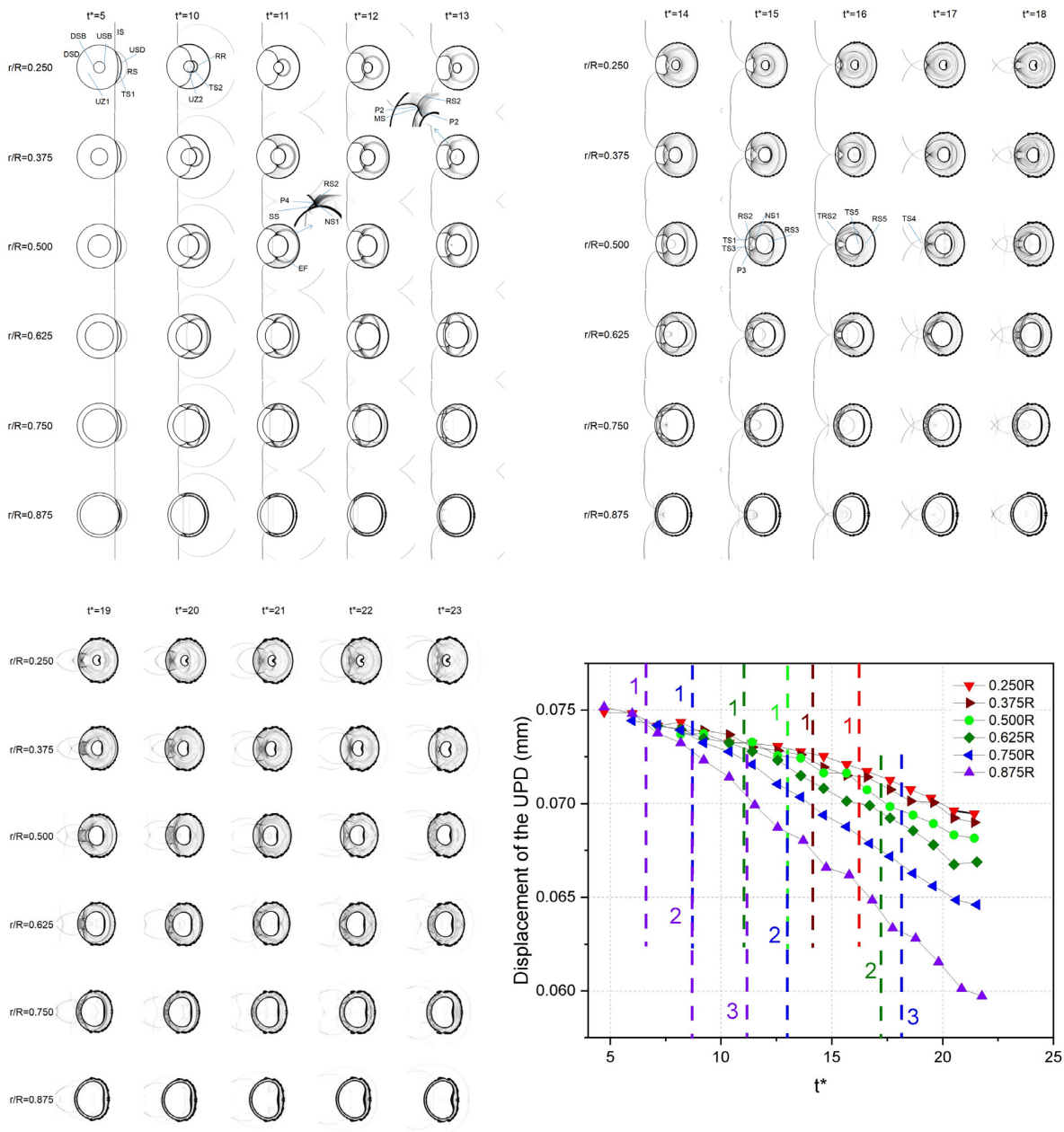
FIG. 5. Representative view of the flow morphology, wave pattern evolution, and displacements in a shock-accelerated cylinder ring at near-critical conditions. (a)–(c) IS, incident shock wave; TS1, converging (refracted) transmitted shock1; TS2, diverging (refracted) transmitted shock2; RS, reflected shock; RR, reflected rarefaction wave; UZ1, undisturbed zone1; UZ2, undisturbed zone2; DSD, downstream surface of the cylinder; DSC, downstream surface of the cavity; USD, upstream surface of the cylinder; USC, upstream surface of the cavity; JF, jet formation; RS2, reflected shock2; SS, side shock; NS1, new shock1; EF, expansion fan; P4, intersection point for four shock waves; MS, Mach stem; P2, intersection point for two shock waves; TS3, transmitted shock3; TS4, transmitted wave4; TS5, transmitted wave5; RS3, reflected shock3; RS5, reflected wave5; TRS2, transmitted shock of RS2; P3, intersection point for three shock waves; and (d) displacement of the upstream pole of the cylinder (UPD).

Overall, a comparison of the evolution of the outer cylinder for all cases in Figs. 5(a)–5(c) indicates similar patterns resembling the shock interaction with a heavy fluid in the sub-critical region. The timing of TS1 passing the upstream surface of the cavity is determined by the streamwise distance between the upstream pole of the cavity and the upstream pole of the cylinder. Over time, the upstream surface of the cavity presses into the center of the Nitrogen, taking on a kidney shape, reminiscent of shock-accelerated light bubbles. It is noteworthy

that the internal shock wave pattern bears resemblances to shock helium bubble interaction cases in the sub-critical region. However, in the current cylinder ring scenario, IS of shock-helium bubble cases is replaced by TS1, a reasonable substitution given the shared attributes of "heavy–light layer" cases.

2. Late development of cylinder deformation and cavity rupture

Differences in cavity rupture and cylinder deformation among cases are clearly observed along with the evolution.

(1) The internal kidney-shaped gas cavity continues to move downstream. For this cavity region, a jet forms and grows over time [as seen in Fig. 6(a)], displaying similarities to shock-helium bubble interaction in the sub-critical region.

(2) The smaller the cavity, the earlier the jet formation occurs. This structure containing a pair of vortices develops first in the downstream direction and then meets the downstream surface of the cavity [as seen in Figs. 6(a) and 6(b)].

(3) The cavity gradually splits into two small parts. The smaller the cavity, the earlier the cavity splits. Subsequently, two pairs of vortices move in opposite directions and separately into two Nitrogen cavities, forming several smaller jets.

(4) Another mushroom containing a pair of vortices forms in the cavity and tends to impact the upstream surface of the cavity. These processes introduce complex impacts and interactions that increase the mixing of gas and fuel fluids when compared to the case where there is no cavity in the cylinder.

(5) For a shocked cylinder, the region of high pressure created by the shock focusing inside the cylinder causes the development of an outward jet in the vicinity of the cylinder's downstream. In contrast, for cases with a larger cavity, the cavity disrupts the motion of the shock waves, reducing the tendency for jet formation.

(6) For instances where the cavity is larger (resulting in a thinner ring), there is an intersection between the structures found on the surface of the cavity and those on the cylinder surface.

3. Center-of-mass position and velocity evolution and associated prediction fit

From Fig. 6, it is evident that the center-of-mass location is changing. The details are analyzed in the following part.

Simulations can be used to quantitatively analyze the center-of-mass properties of the deforming cylinder ring, which are essential for diagnostics.[73] The center-of-mass position and velocity of these objects can be calculated through drift analysis, as indicated by the following equations:

$$x_c = \frac{\int (1 - \xi_{Gas})\rho x \, dx \, dy}{\int (1 - \xi_{Gas})\rho \, dx \, dy}, \quad u_c = \frac{dx_c}{dt} = \frac{\int (1 - \xi_{Gas})\rho u \, dx \, dy}{\int (1 - \xi_{Gas})\rho \, dx \, dy}. \quad (5.1)$$
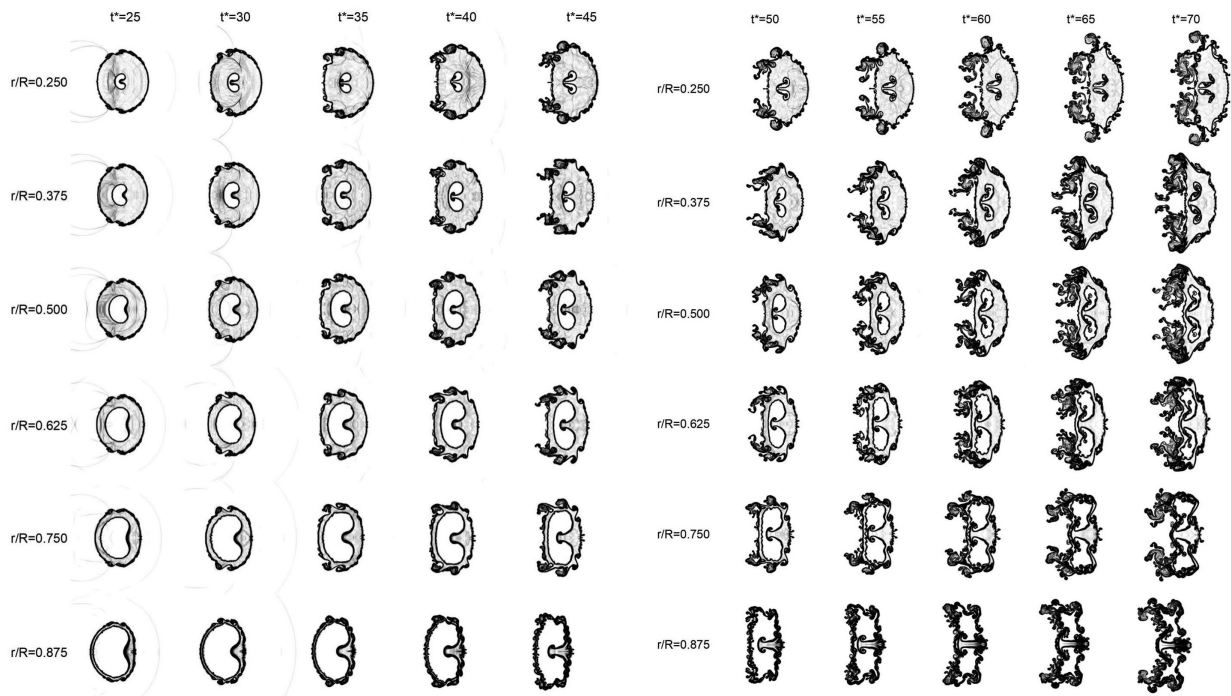
FIG. 6. Late development of cylinder deformation, jet formation, and cavity rupture at near-critical conditions.
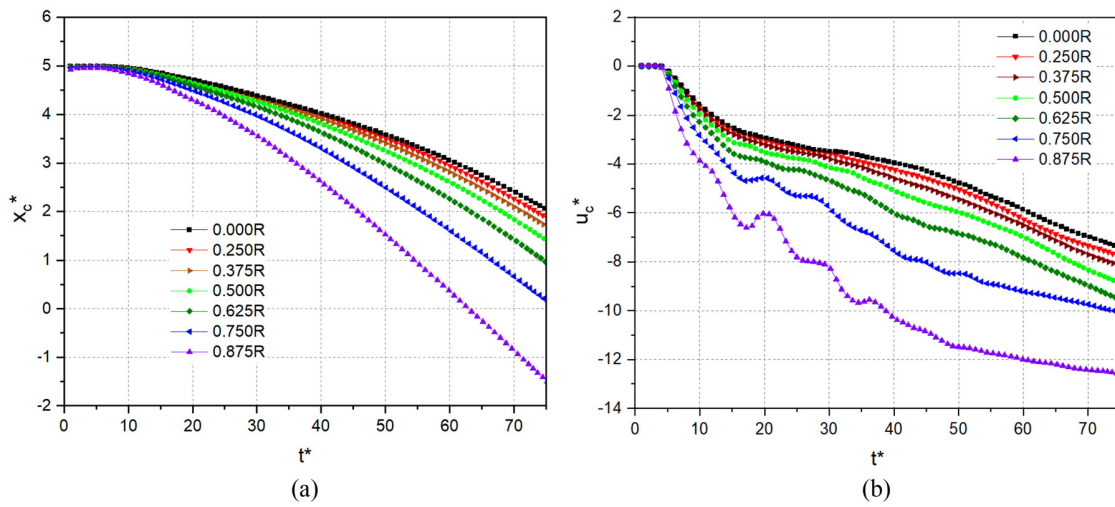
FIG. 7. The drift of the center-of-mass position (a) and velocity (b) (normalized by 0.01 and 10 m/s).

The integration region refers to the entire computational domain. These equations are validated if the liquid mass in the domain remains constant.

Figure 7 shows the center-of-mass position [Fig. 7(a)] and velocity [Fig. 7(b)] of the cases where the radius of the cavity varies from 0R (full cylinder) to 0.875R. Generally, the tendency for the center-of-mass position and velocity of the ring to evolve is similar to that of the full cylinder. Here are some observations.

(1) A significant discrepancy exists between the smaller cavity (e.g. the case with a cavity radius of 0.250R) and the larger cavity (e.g. the case with a cavity radius of 0.875R).

(2) The drift of the case with the larger cavity radius exhibits a greater tendency to decrease. For instance, the center-of-mass position and velocity of the case with a radius of 0.875R decrease at a faster rate compared to those of the case with a radius of 0.25R.

(3) As the cavity size increases, the center-of-mass position difference also increases for two adjacent cases with a radius difference of 0.125R. For example, at $t^* = 60$, the position difference between cases with 0.875R/0.750R is greater than that between cases with 0.375R/0.250R.

(4) This difference in the center-of-mass position between two cases increases over time. For instance, the disparity in the center-of-mass position between cases with 0.875R/0.750R at $t^* = 5$ is superior to that at $t^* = 30$. The difference between two adjacent cases is greatest at $t^* = 75$.

(5) For cases ranging between 0.000R and 0.625R, the velocity decays continuously.

(6) In situations where there is a small amount of gas (small gas cavity) in the cylinder, the movement of the liquid component is very important. Differences in the center-of-mass position and velocity for cases with smaller cavities compared to the full liquid cylinder are relatively small.

(7) Overall, the configuration of the cavity causes the ring cases to move at a greater speed than the full cylinder case. The greater the radius of the cavity, the quicker the cylinder ring moves, which can be useful in controlling the mixing process.

Furthermore, it is noted that there could be some relationships between time, cavity size, and the center-of-mass location. Based on the intuitive observation, except for using the data from the cavity case with 0.5R, a Time-Size Polynomial Predictive Fit (TS-PPF) is proposed, which may be used to predict the center-of-mass location as a function of time and cavity size in the same (initial) near-critical conditions. As shown in Table II, R^* refers to the ratio of cavity radius to the cylinder radius ($0 \leq R^* \leq 0.875$), t^* is the non-dimensional time ($10 \leq t^* \leq 65$).

Once again, we display the simulation data alongside the fit curves derived from the TS-PPF. As depicted in Fig. 8, the fit curves closely align with the simulation results, even for the case where the cavity radius is 0.5R, suggesting its applicability and potential extension to cases with varying cavity sizes.

4. Quantitative analysis of vorticity dynamics

This section provides a detailed discussion on the vorticity production, circulation deposition, and theoretical model for the upper-semi plane. Due to symmetry, the analysis applies to the lower semi-plane. Baroclinic vorticity production arises due to unbalanced gradients between density and pressure, particularly when the incident

TABLE II. Parameters and expressions of Time-Size Polynomial Predictive Fit (TS-PPF) for center-of-mass location considering cavity size.

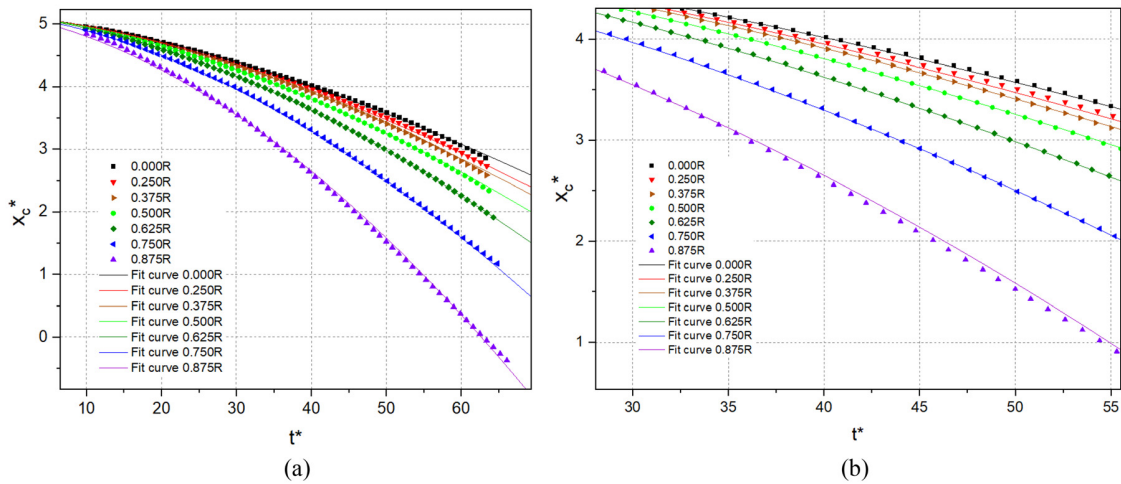| Parameters	Expressions
$f(t^*, R^*)$	$0.051\,42 + Bt^* + Ct^{*2} + 1.2873 \times 10^7 t^{*3}$
B	$-12.779\,28 - 17.304\,17\,R^* + 164.562\,91\,R^{*2}$
	$- 550.278\,43\,R^{*3} + 760.216\,44\,R^{*4} - 388.410\,07\,R^{*5}$
C	$-43\,659.262\,21 - 28\,122.375\,81\,R^* + 86\,092.406\,37\,R^{*2}$
	$- 146\,392.925\,39\,R^{*3}$

05 September 2024 13:17:46

FIG. 8. The drift of the center-of-mass position by Time-Size Polynomial Predictive Fit (TS-PPF) and simulations (normalized by 0.01 m). (b) is a magnified image of (a).

shock (IS) or transmitted shock (TS) passes through the two-phase interface. This phenomenon plays a pivotal role in the Richtmyer–Meshkov instability (RMI) and the induction of turbulent mixing.

Figure 9 illustrates the evolution of vortex generation through baroclinic production. Across all cases, vortex growth and rotation occur near the top and bottom vertices of the cylinder, ultimately forming distinct wake roll-up structures. Positive and negative vortices predominantly form on the upper and lower surfaces of the outer cylinder, respectively. Baroclinic productions resulting from shock interaction with the internal light cavity within the heavy fluid environment leads to additional vorticity generation. On the upper and lower surfaces of the inner cavity, vortex patterns of negative and positive vorticity primarily form, respectively, contrasting the pattern observed on the outer cylinder. Additionally, the emergence of the newly formed internal mushroom jet is associated with a pair of vortices characterized by opposite spin directions.

Furthermore, the time variations of negative circulation, positive circulation, total real circulation (TRC), and total absolute circulation (TAC) are obtained by integrating the vorticity in the upper-half of the calculation domain, as illustrated in Fig. 10.

Figure 10(a) shows the following:

(1) In all cases with a cavity, before the cavity is touched by the TS, the circulation history is the same as that of a full cylinder.
(2) As soon as the cavity is touched, the negative circulation increases almost linearly.
(3) The cases with the cavity are touched by the TS at different times. The thinner the ring, the sooner the TS touches the cavity and the earlier the growth phase begins.
(4) At the earlier stage, assuming negligible minimal influence of the cavity on the outer cylinder, the difference between the case with the full cylinder and the case with the cavity (at the same time) is due to the circulation within the cavity. A larger cavity leads to a bigger negative circulation of the cavity.
(5) After the initial linear phase, the negative circulations continue to increase, indicating an increase of mixing.

Figure 10(b) reveals the following:

(1) The positive circulation of all cases exhibits linear growth at early stages, preceding the linear growth phase of negative circulation depicted in Fig. 10(a). The reason is that the outer cylinder upon shock (IS) generates positive circulation in the upper half plane, followed by the interaction of the cavity with the transmitted shock (TS), resulting in negative circulation in the upper half plane.
(2) The larger the cavity, the earlier the linear growth phase is distorted. Multiple wave reflections, such as RR, between the cavity and the cylinder contribute to the deposition of opposite circulations at the interfaces. Particularly, cases with larger cavity experience an earlier influence of RR on the positive circulations of the outer cylinder. Additionally, when the cavity is larger (resulting in a thinner ring), the transmitted shock (TS) reaches the downstream pole of the outer cylinder before the DS [Fig. 5(b)], depositing negative circulation on the outer cylinder. This deposited negative circulation offsets the subsequently deposited positive circulation. Consequently, the final maximum positive circulations (around $t^* = 18$) of cases with a smaller cavity (a thicker ring) are notably larger than those with a bigger cavity (a thinner ring).
(3) The positive circulation for all cases with a cavity (indicated as Xt) encompasses the positive values of the cavity (indicated as Yt) and the positive values of the outer cylinder (indicated as Zt, which is equal to Xt-Yt). The positive circulation of the cylinder without cavity is denoted as Z0. Accordingly, Z0-Zt represents the effect of the cavity on the circulation of the outer cylinder. Initially, the cavity has minimal impact on the outer cylinder. Thus, the circulation variation between a case with the cavity (Xt) and one without a cavity (Z0), Z0-Xt, is smaller than the effect of the cavity on circulation of the external cylinder, Z0-Zt. This means that just looking at the disparity (Z0-Xt) between the circulation of the cylinder case (Z0) and the circulation of the cavity embedded case (Xt) shown in Fig. 10(b), the effect of the cavity on the circulation of the outer cylinder (Z0-Xt+Yt) is underestimated.
(4) Positive circulation continues to grow after the early stage. In the later stage (around $t^* = 70$), the results of cases with a cavity radius of around 0.500R (0.375R-0.625R) show bigger circulation characteristics than others.
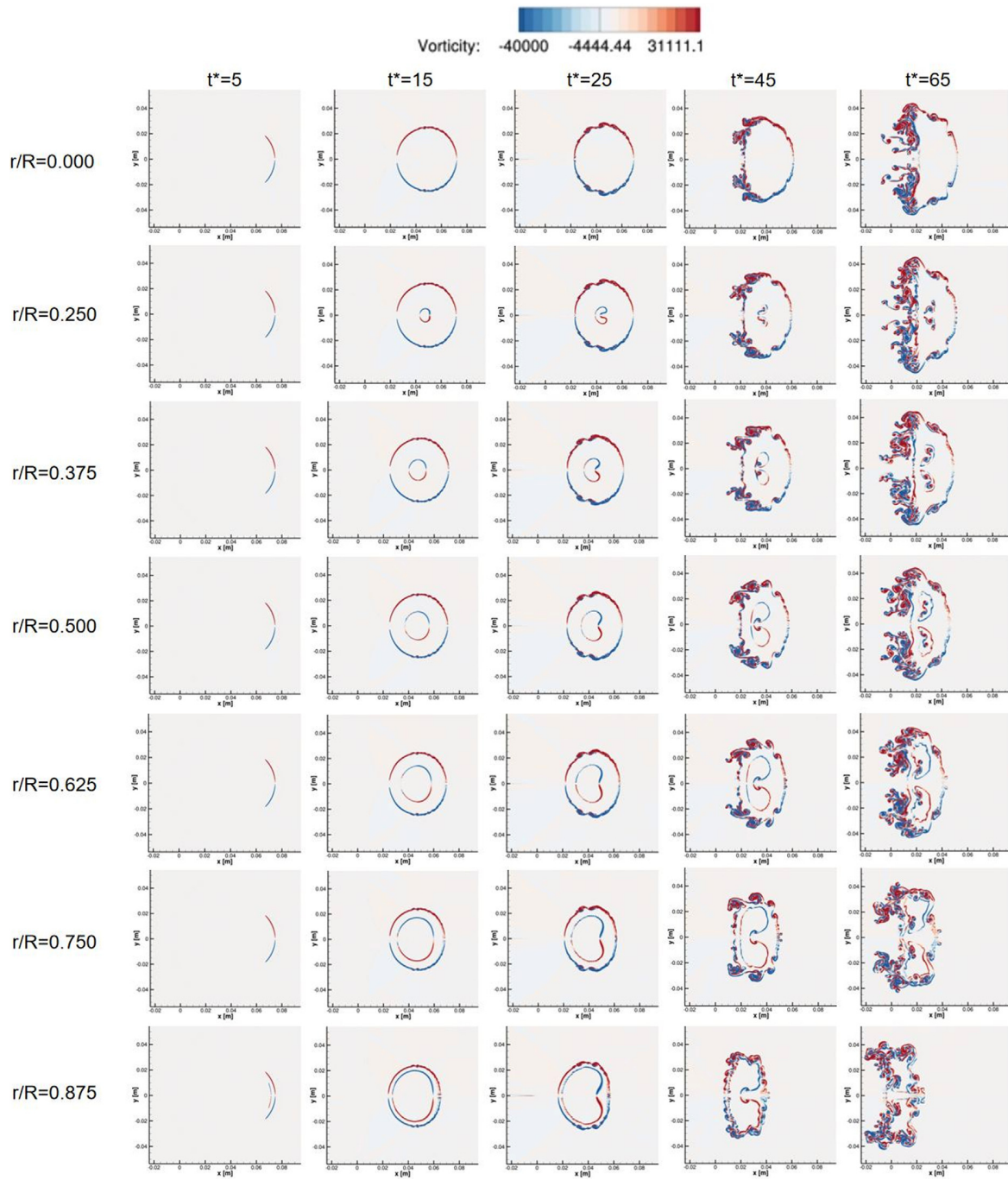
05 September 2024 13:17:46

FIG. 9. Schematic diagram of vorticity generation in the shock–cylinder ring interaction (vorticity restricted to the same range of values).

The Total Real Circulation (TRC) illustrated in Fig. 10(c) comprises the negative circulation [Fig. 10(a)] and the positive circulation [Fig. 10(b)]. For the cylinder without cavity, where r = 0, TRC is obtained at the outer surface of the cylinder. For cases featuring a cavity, both positive and negative circulation are generated at the cylinder and the cavity surfaces. Here are some observations:

The larger the cavity, the thinner the cylinder ring, the sooner the negative TRC of the cavity is produced and the larger the negative
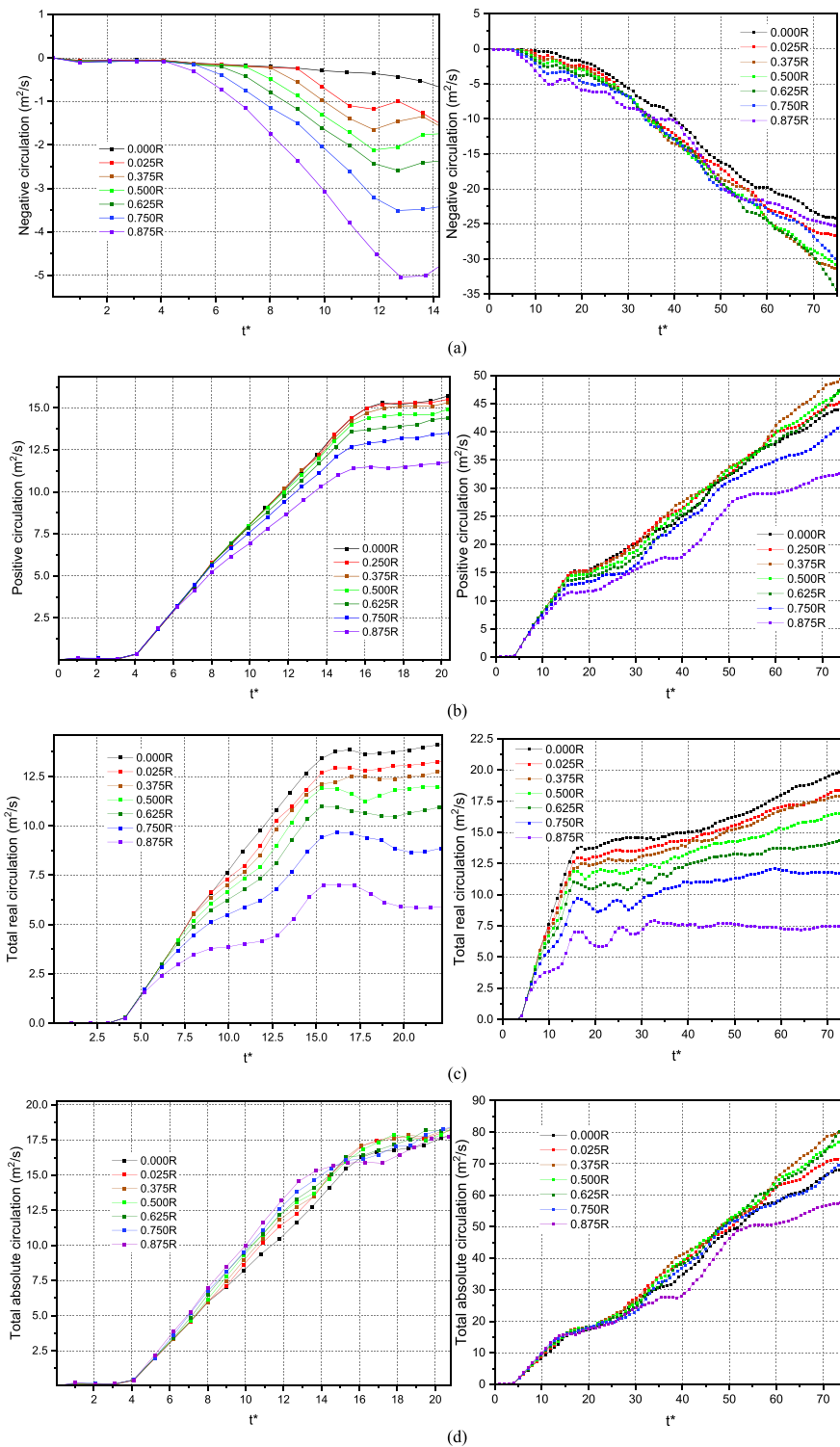
FIG. 10. Positive circulation (a), negative circulation (b), total real circulation (c) and total absolute circulation (d), and histories of the interaction between the shock wave and the full cylinder/cylinder ring.

TRC of the cavity. The difference in TRC between the cylinder with and without the cavity, or the TRC of the cavity, increases gradually during the initial stages.

Figure 10(d) shows the total absolute circulation (TAC), which is the sum of the absolute values of the positive and negative circulations for both the cavity (if present) and the outer cylinder. Here are some observations.

(1) It has been observed that, prior to $t^* < 15$, the cases with a cavity typically exhibit higher circulation values than without the cavity.

(2) At $35 < t^* < 55$, the circulation values of most of the cases with the cavity are higher than those of the cases with the full cylinder, with the exception of the largest cavity case, 0.875R. The reason is that the distance between the cavity and the outer cylinder is so short that the cavity and the outer cylinder interact with each other, affecting the development of the circulation [Fig. 6(a)].

(3) At the even later stages, $t^* > 60$, for the case with the second largest cavity ($r = 0.750R$), its circulation values are lower than those of the full cylinder [Fig. 6(b)]. This can also be attributed to the interplay between the cylinder and the cavity surface. It is concluded that the thinner the ring, the sooner the circulation values become lower than those of the full cylinder.

(4) Cases with a cavity radius of 0.375R to 0.625R show bigger circulation characteristics.

Furthermore, the vorticity deposition and circulation histories are the inspiration for proposing the theoretical model for circulation forecasting. As the evolution pattern exhibits similarities with cases presented in Refs. 33 and 34, it is assumed that the circulation can be calculated using the Yang, Kubota, and Zukoski (YKZ) model[33,34,74] for the current shock interaction with an internal Nitrogen cylinder in a heavy fluid (n-dodecane) environment,

$$\Gamma_O = \frac{4r}{V_i} \frac{p_1' - p_1}{\rho_1'} \left(\frac{\rho_1 - \rho_2}{\rho_1 + \rho_2} \right), \qquad (5.2)$$

where r is the radius of the cavity, V_i is the velocity of the shock waves, p_1' and ρ_1' are the pressure and density of the post-shocked ambient fluid, respectively, and p_1 is the pressure of the pre-shocked ambient fluid. It should be noted that the direction of the flow affects the sign but not the absolute values due to symmetry.

The circulation generated on the surface of the cylinder is considered to be that calculated by the ZZ model.[34,75] The ZZ model is suitable for predicting the circulation deposited on the cylinder when e (aspect ratio of the ellipse) is equal to 1

$$\Gamma^* = \frac{\pi r_0 c_0}{\gamma + 1} \left(1 - \eta^{-1/2} \right) \left(1 + M_I^{-1} + 2M_I^{-2} \right) (M_I - 1), \qquad (5.3)$$

where r_0 is the cylinder radius, c_0 is the pre-shock sound speed of the ambient Nitrogen, γ is the arithmetic average ratio of the effective specific heat ratio of the outer Nitrogen (γ_1^*) and internal n-dodeance (γ_2^*), $\gamma = (\gamma_1^* + \gamma_2^*)/2$; $\eta = \rho_2/\rho_1$ is the density ratio, ρ_2 and ρ_1 are the pre-shocked n-dodecane and Nitrogen densities, respectively, and M_I stands for the Mach number of the incident shock.

Wang et al.[34] proposed that for the interaction of a planar shock with two circular concentric cylinders, the deposited circulation can be obtained by superimposing the circulations generated on two separate cylinder surfaces. It is reasonable to assume that during the initial stages when coupling effects are insignificant, the interaction between the outer cylinder and cavity can be neglected. Thus, the total circulation can be obtained by summarizing the absolute circulation values of the two separate circulation values described above (for two separate surfaces, cavity surface and cylinder surface), $\Gamma_T = \Gamma_O + \Gamma^*$.

A comparison of the theoretical (Γ_T) and numerical results (Γ_{num}) is given in Table III. The calculations are obtained when the IS crosses the two concentric cylinders. Results are given for two instants close to this moment. The theoretical results are in good agreement with the numerical results for the case with the full cylinder and the case with the smaller cavity (thicker ring), especially when $r = 0.000R$-$0.625R$. In the cases with a bigger cavity (thinner ring), the cavity gradually comes into contact with the outer cylinder and the induced coupling effects (frequent shock reflections) distort the theoretical results.

B. Analysis of eccentricity angle effect

The gas cavity could occur in any position of the cylinder. In this section and Sec. V C, the cases with an eccentrically located gas cavity are presented to show the effects of eccentricity on the shock–cylinder interaction at near-critical conditions.

As shown in Fig. 11, a gas cavity with a diameter $r/R = 0.500$ and $L/R = 0.250$ is embedded in the eccentric part of the cylinder, where L is the distance between the center of the cavity and the center of the cylinder. The dimensionless eccentricity angles (θ^*) of 180, 135, 90, 45, 0 are adopted to separately represent the cases with the left eccentric cavity, the top-left eccentric cavity, the top eccentric cavity, the top-right eccentric cavity, and the right eccentric cavity. The cases with the

TABLE III. Comparison of circulations obtained from the theoretical (Γ_T) and mumerical (Γ_{num}) results of the full cylinder/cylinder rings impacted by the incident shock of Mach number 1.2.

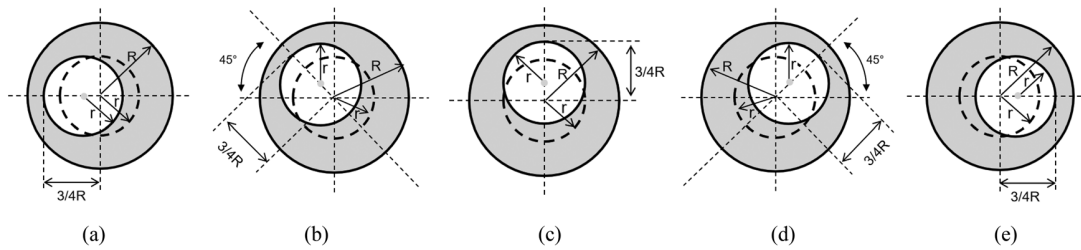| Cases		r = 0.000R	r = 0.250R	r = 0.375R	r = 0.500R	r = 0.625R	r = 0.750R	r = 0.875R
Γ_T(m/s)		15.309	16.465	17.043	17.621	18.199	18.777	19.355
$t^* = 15$	Γ_{num}(m²/s)	15.448	16.074	16.267	15.996	16.289	16.063	15.865
	Error (±%)	0.908	−2.375	−4.553	−9.222	−10.495	−14.454	−18.032
$t^* = 16$	Γ_{num}(m²/s)	16.268	17.055	17.107	16.834	16.405	16.135	15.919
	Error (±%)	6.264	3.583	0.376	−4.466	−9.858	−14.070	−17.753
Max [Error (±%)]		6.264	3.583	4.553	9.222	10.495	14.454	18.032

FIG. 11. The schematic of the eccentric located gas cavity with r/R = 0.500, L/R = 0.250. (a) Left eccentric, (b) Top-left eccentric, (c) Top eccentric, (d) Top-right eccentric, and (e) Right eccentric.

eccentric located cavity at the bottom/bottom-left/bottom-right are ignored due to symmetry.

1. Wave pattern evolution, development of cylinder deformation and cavity rupture

In Fig. 12(a), the shock wave patterns (IS, TS, RS) are identical for all cases at $t^* = 5$. However, when the cavity center is above the cylinder center (as in cases with the top-right/top/top-left eccentric cavity), the TS2/RR direction of movement forms an inclined angle with the cylinder equator.

The timing of TS passing the cavity upstream surface depends on the projected position of the cavity upstream pole onto the equator. The closer this position is to the cylinder upstream pole, the earlier TS2 forms. Consequently, earlier TS2 results in TS3 formation downstream of the cylinder. This accelerates RR contact with the cylinder upstream surface and the subsequent formation of RS5/TS5. Wave pattern outside the cylinder, such as IS/DS, remains unaffected during these initial stages.

As depicted in Fig. 12(b), a closer streamwise distance between the cavity upstream pole and the cylinder upstream pole leads to earlier RS3 formation and its passage over the cavity upstream surface. For cases with top-left/top/top-right eccentric cavities, the wave pattern within the cylinder and the structures related to TS4 tend to skew toward the streamwise direction.

Figure 12(c) demonstrates that cases featuring eccentric cavities at the top-left/top/top-right induce slight asymmetrical deformation in the cylinder. The upstream cylinder surface tends to curve, and a closer streamwise distance between the cavity upstream pole and the cylinder upstream pole enhances this asymmetry, prompting earlier transition of the cavity into kidney-shaped structures.

In Fig. 13, the late-stage development of cylinder deformation and cavity rupture is illustrated. In Fig. 13(a), kidney-shaped structures continue to deform, forming a mushroom-shaped jet within the cavity. Eccentric cavities at the top-left, top, or top-right redirect the jet's momentum toward the streamwise direction due to prior asymmetrical interactions. Vortex formations outside the cylinder remain similar across all cases, though those near the top are influenced by the cavity.

As shown in Fig. 13(b), eccentric cavities at the top-left, top, or top-right lead to asymmetrical fragmentation of the entire cavity, gradually splitting it into two parts of differing sizes, with the upper part larger than the lower one. Vortex structures near the top region outside the cylinder are affected by the cavity, particularly with an increase in the vertical distance between cavity and cylinder centers.

2. Center-of-mass position and velocity evolution and associated prediction fit

Figure 14 presents the center-of-mass position and velocity of the cylinder for various cases with a cavity located from left-eccentric to right-eccentric. The center-of-mass positions for center-located and top-located cavities are nearly identical, indicating minimal effects of the normal distance between the cavity and cylinder on this parameter. However, for cases with a cavity, a larger horizontal distance between the upstream poles of the cylinder and cavity results in a downstream shift in the center-of-mass position. Nonetheless, the curves for the center-of-mass position/velocity of cases with a cavity exhibit similar shapes.

Overall, the inclusion of the cavity configuration leads to an increased rate of movement due to the enhanced acceleration effect by the cavity, as noted in Sec. V A 3, compared to cases without a cavity.

Similar to Sec. V A 3, there may be relationships between time, cavity position, and the center-of-mass location. Utilizing data from the cases described in this part, except for the top-located cavity case, we establish a Time-Eccentricity Polynomial Predictive Fit (TE-PPF) to predict the center-of-mass location as a function of time and cavity eccentricity in the same initial near-critical conditions.

As shown in Table IV, t^* has been defined above ($10 \leq t^* \leq 65$); θ^* refers to the angle between the line connecting the cavity and cylinder centers and the cylinder equator ($0 \leq \theta^* \leq 180$). We represent the cases with cavities located in the left, top left, top, top right, and right positions, respectively, using dimensionless degrees θ^* of 180, 135, 90, 45, and 0.

Once again, we present the simulation data alongside fit curves obtained using TE-PPF. The results, illustrated in Fig. 15, show a robust agreement between the fit curves and simulation data, including cases with a top-located cavity. This suggests the method's potential applicability across various scenarios.

This concludes the fit for predicting the center-of-mass position of a full cylinder/cylinder ring at near-critical conditions, incorporating the eccentricity angle of the cavity.

3. Quantitative analysis of vorticity dynamics

The analysis of vortex distribution in various cases depicted in Fig. 16 demonstrates similarity to that in Sec. V A 4, along with certain asymmetrical occurrences, which have been elucidated in Sec. V B 1.

As depicted in Fig. 17(a), the results for cases with a cavity exhibit lower values compared to those of the full cylinder case, indicating the generation of negative circulation on the cavity surface. The timing of
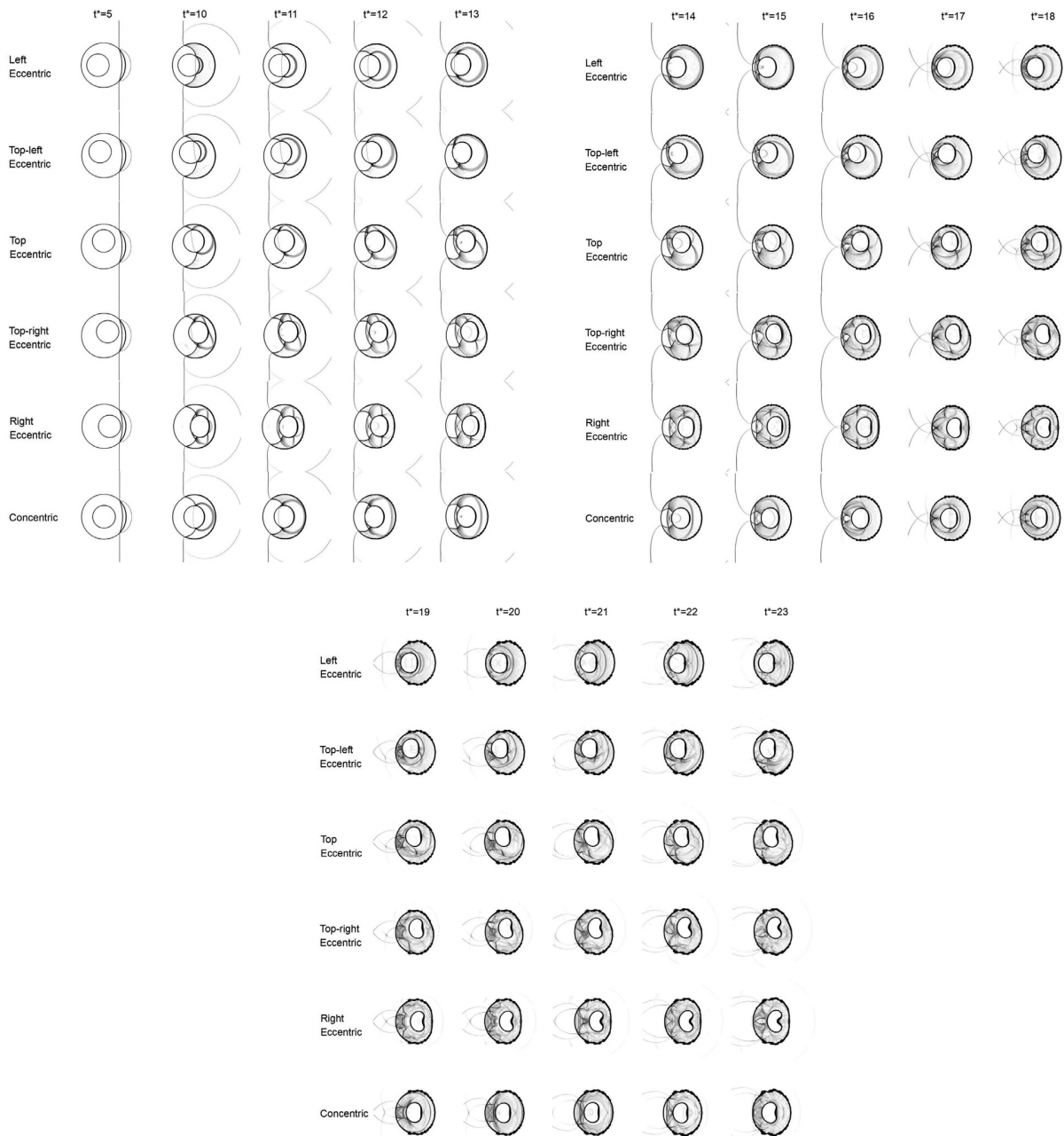
FIG. 12. Representative view of the flow and wave pattern evolution. (a)–(c) show the development at different times.

the upstream pole of the cavity's contact with the TS is determined by the streamwise distance between the upstream poles of the cavity and the cylinder. As this distance decreases, the cavity's upstream pole is struck by the TS earlier, resulting in the emergence of negative values on the cavity.

For scenarios where the cavity is concentrically located in the middle of the cylinder, the evolution of circulation follows a path largely similar to that of cases with the cavity embedded in the upper portion of the cylinder. The normal distance between the cavity and the cylinder has a negligible effect on circulation production in the early stages.
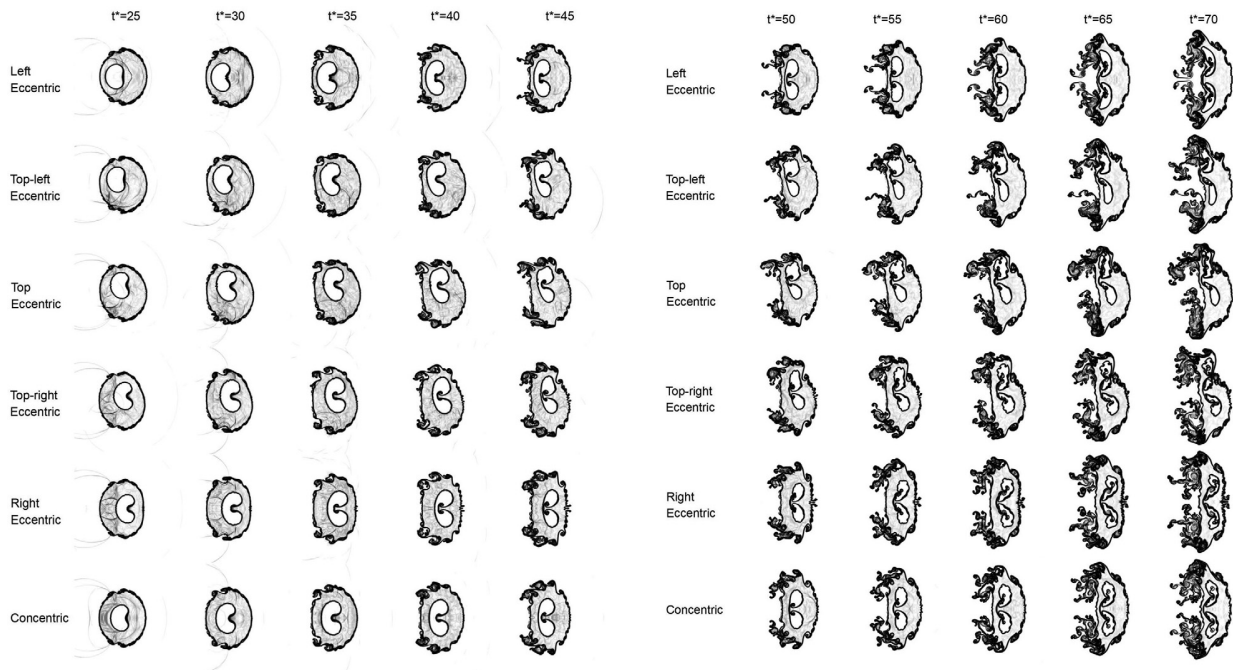
FIG. 13. Representative view of the flow and wave pattern evolution at near-critical conditions. (a)–(c) show the development at different times.

As shown in Fig. 17(b), a decrease in the streamwise distance between the upstream poles of the cavity and the cylinder leads to an earlier onset of positive circulation. Positive circulations exceed the absolute values of negative circulations [as shown in Fig. 17(a)], indicating the dominance of positive circulations in the upper-half plane of the computational region. In later periods, regardless of the cavity's location, the positive circulations of nearly all cases with a cavity exceed those of the full cylinder case, with the circulation induced in the deformed cavity contributing to these findings (Fig. 16).

As illustrated in Fig. 17(c), the TRC rises at an earlier stage for instances where there is a shorter streamwise distance between the upstream poles of the cavity and the cylinder. In the late evolution
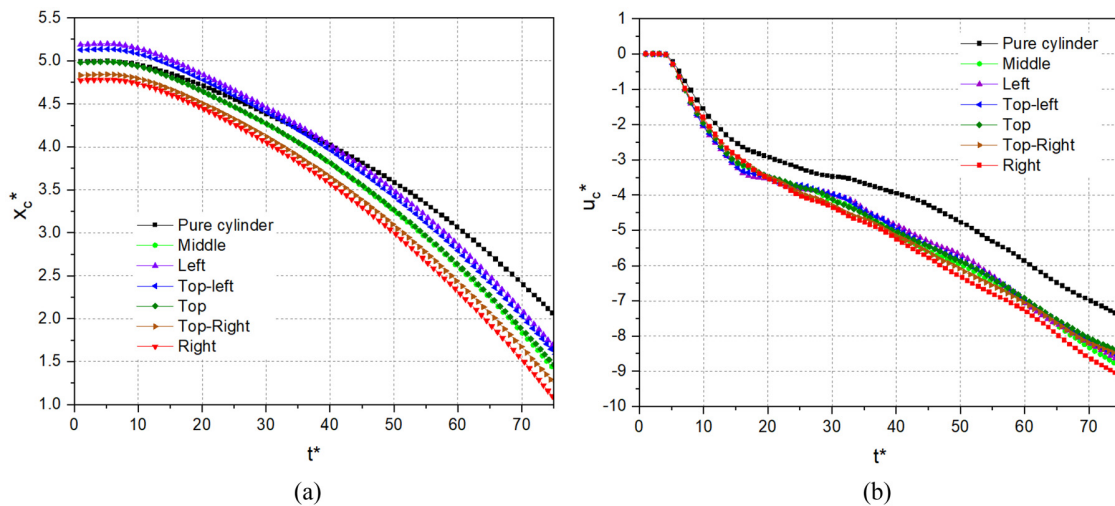

(a)

(b)

FIG. 14. The drift of the center-of-mass position (a) and velocity (b) (normalized by 0.01 and 10 m/s).

TABLE IV. Parameters and expressions of Time-Eccentricity Polynomial Predictive Fit (TE-PPF) for center-of-mass location considering cavity eccentricity.

Parameters	Expressions
$f(t^*, \theta^*)$	$A + Bt^* - 43\,597.706\,46\,t^{*2}$
A	$0.049\,88 - 7.7619 \times 10^{-6}\theta^* + 4.017\,64 \times 10^{-7}\theta^{*2}$
	$\quad - 1.426\,61 \times 10^{-9}\theta^{*3}$
B	$-18.122\,43 + 0.0025\,\theta^* + 8.026\,37 \times 10^{-4}\theta^{*2}$
	$\quad - 7.544\,69 * 10^{-6}\theta^{*3} + 1.983\,34 \times 10^{-8}\theta^{*4}$

period, it is observed that the presence of a cavity in all cases significantly impacts the TRC. Furthermore, as shown in Fig. 17(d), TAC increases in almost all cases with cavities during the late period regardless of their placement, with the cavity contributing to the results.

C. Analysis of eccentricity distance effect

The study examines the impact of the eccentricity distance between the cavity center and the cylinder center on the interaction between the shock wave and the fuel cylinder at near-critical conditions. As illustrated in Fig. 18, a gaseous cavity is situated in an off-center position of the cylinder. The cavity has a size of $r/R = 0.5$ and an eccentricity angle $\theta = 45°$. The cases with the eccentricity distance $L/R = 0, 0.25, 0.35,$ and 0.45 are considered. The findings pertaining to cases with an L/R ratio of 0 and 0.25 have been discussed separately in Secs. V A and V B. The remaining cases will be briefly examined in the ensuing parts since they are akin to the analysis discussed in Secs. V A and V B.

1. Wave pattern evolution, development of cylinder deformation, and cavity rupture

As shown in Fig. 19, the shock wave patterns (IS, TS, RS) outside of the cylinder at $t^* = 5$ are identical for all cases. The closer the
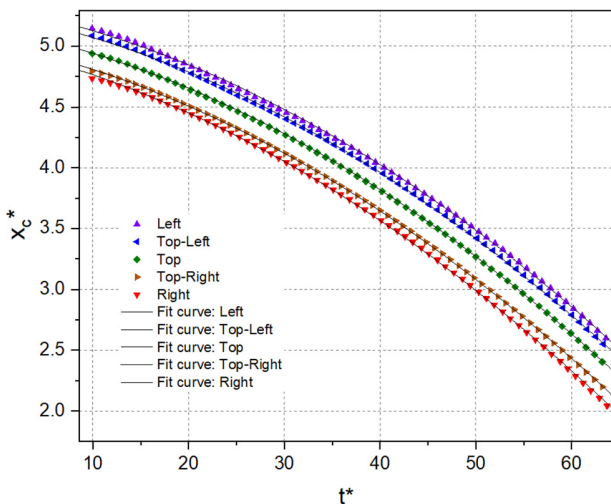

FIG. 15. The drift of the center-of-mass position by Time-Eccentricity Polynomial Predictive Fit (TE-PPF) and simulations (normalized by 0.01 m).

streamwise distance between the upstream pole of the cavity and the upstream pole of the cylinder, the earlier TS2 forms. With earlier TS2 passing downstream of the cylinder, TS3 then forms. Consequently, the earlier the RR contacts the upstream surface of the cylinder, and the earlier RS5/TS5 forms. For $t^* = 14$–18, the closer the streamwise distance between the upstream pole of the cavity and the upstream pole of the cylinder, the earlier the RS3 is formed and the earlier the RS3 passes the upstream surface of the cavity. For $t^* = 19$–23, the upstream surface of the cylinder is inclined to be curved. As the upstream pole of the cylinder and the upstream pole of the cavity draw nearer in the stream-wise direction, the resulting shape becomes increasingly asymmetric, and the cavity assumes kidney-shaped structures earlier.

As shown in Fig. 20, the kidney-shaped structures continue to deform and a mushroom-shaped jet is formed within the cavity. The whole cavity is broken up asymmetrically, and the cavity gradually splits into two parts of different sizes. The larger the vertical distance between the cavity center and the cylinder center, the greater the effect of the cavity on the vortex structures near the top of the cylinder surface. The process of evolution resembles the situation with the cavity in the upper right part of the cylinder, as shown in Sec. V B 1.

2. Center-of-mass position evolution and associated prediction fit

Similar to Secs. V A 3 and V B 2, there could be some relationships between time, eccentricity distance, and the center-of-mass location. Based on the intuitive observation in Fig. 21, by using the data with $L = 0.000R, 0.250R, 0.350R,$ and $0.450R$, we summarize a Time-Eccentric Distance Polynomial Predictive Fit (TED-PPF), which could be used to predict the center-of-mass location as a function of time and eccentricity distance in the same (initial) near-critical conditions. As shown in Table V, $L^* = 0.00, 0.25, 0.35,$ and 0.45.

Again, we present the simulation data and accompanying fit curves obtained through the use of TED-PPF. The results, as illustrated in Fig. 22, demonstrate a strong agreement between the fit curves and simulation data, even in a validation case with case with parameter $L = 0.177R$. As depicted in Fig. 22, when examining the prediction curve for $L = 0.177R$, the maximum relative error is 3.09%, which is acceptable. This suggests potential to adopt the method in other scenarios.

3. Quantitative analysis of vorticity dynamics

The findings pertaining to cases with an L/R ratio of 0 and 0.25 have been discussed separately in Secs. V A and V B. The analysis of vortex distribution in various cases depicted in Fig. 23 demonstrates similarity to that in Sec. V A 4, along with certain asymmetrical occurrences, which have been elucidated in Sec. V C 1.

The following discussions follow those in Sec. V B 3, and a succinct summary is provided here. As depicted in Fig. 24(a), as the streamwise distance between the upstream pole of the cavity and the upstream pole of the cylinder diminishes, the TS strikes the upstream pole of the cavity earlier, leading to the emergence of negative values on the cavity. In Fig. 24(b), it is evident that the values of positive circulations surpass the absolute values of negative circulations [as depicted in Fig. 24(a)], indicating the prevalence of positive circulations in the upper-half plane of the computational region. Furthermore, in Fig. 24(c), it can be observed that the TRC increases at
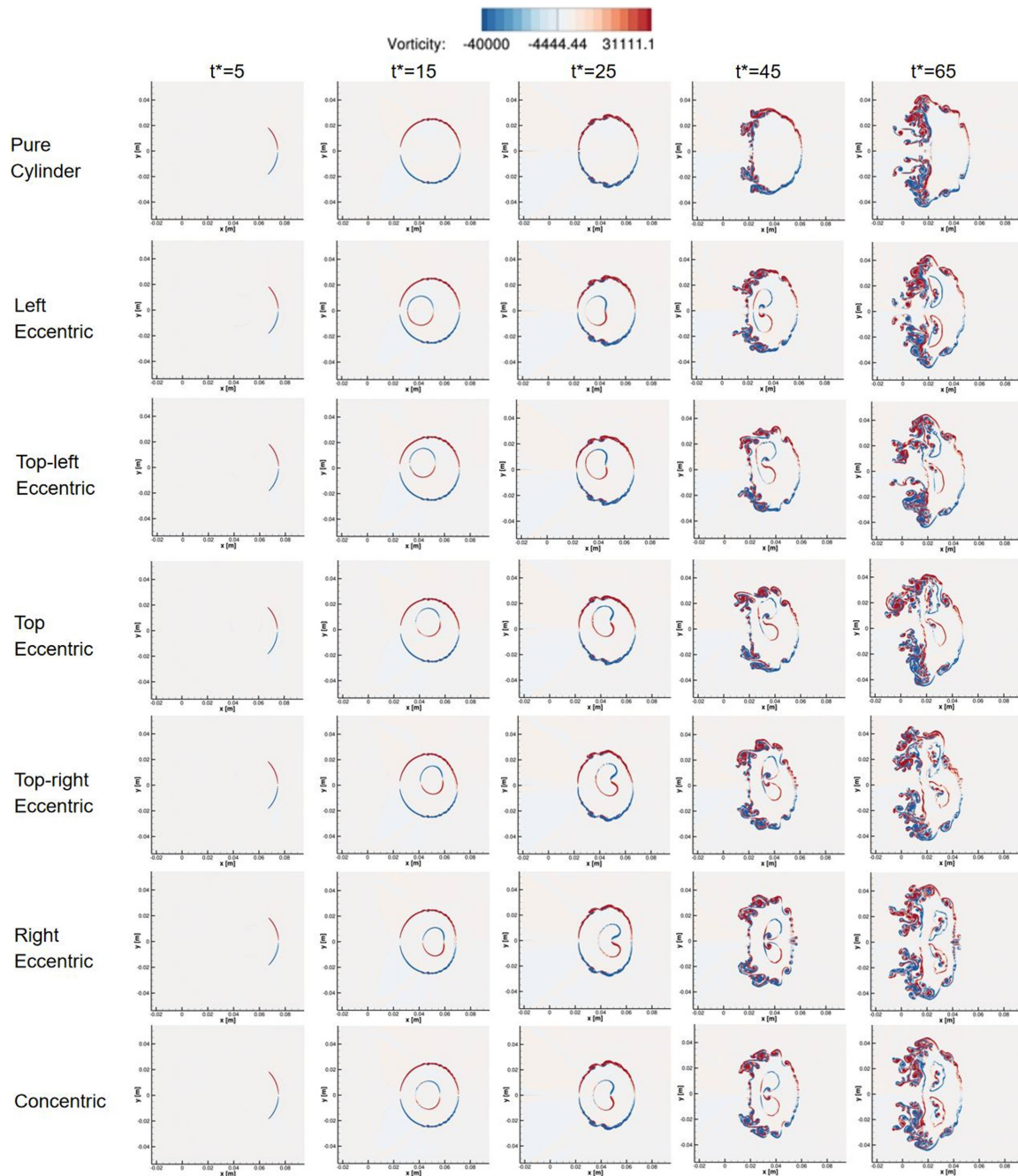
FIG. 16. Schematic diagram of vorticity generation for the shock–cylinder ring interaction (vorticity restricted to the same range of values).

an earlier stage for instances where the streamwise distance between the upstream pole of the cavity and the upstream pole of the cylinder is shorter. Finally, as demonstrated in Fig. 24(d), TAC increases in almost all cases with cavities during the late period regardless of their placement, with the cavity playing a contributing role in the results.

D. Connecting rod prediction fit for center-of-mass location considering cavity size and eccentricity

As depicted in Fig. 25, the shock–cylinder interaction is significantly influenced by three key parameters determining the position and shape of the cavity within the cylinder. Extensive discussions have
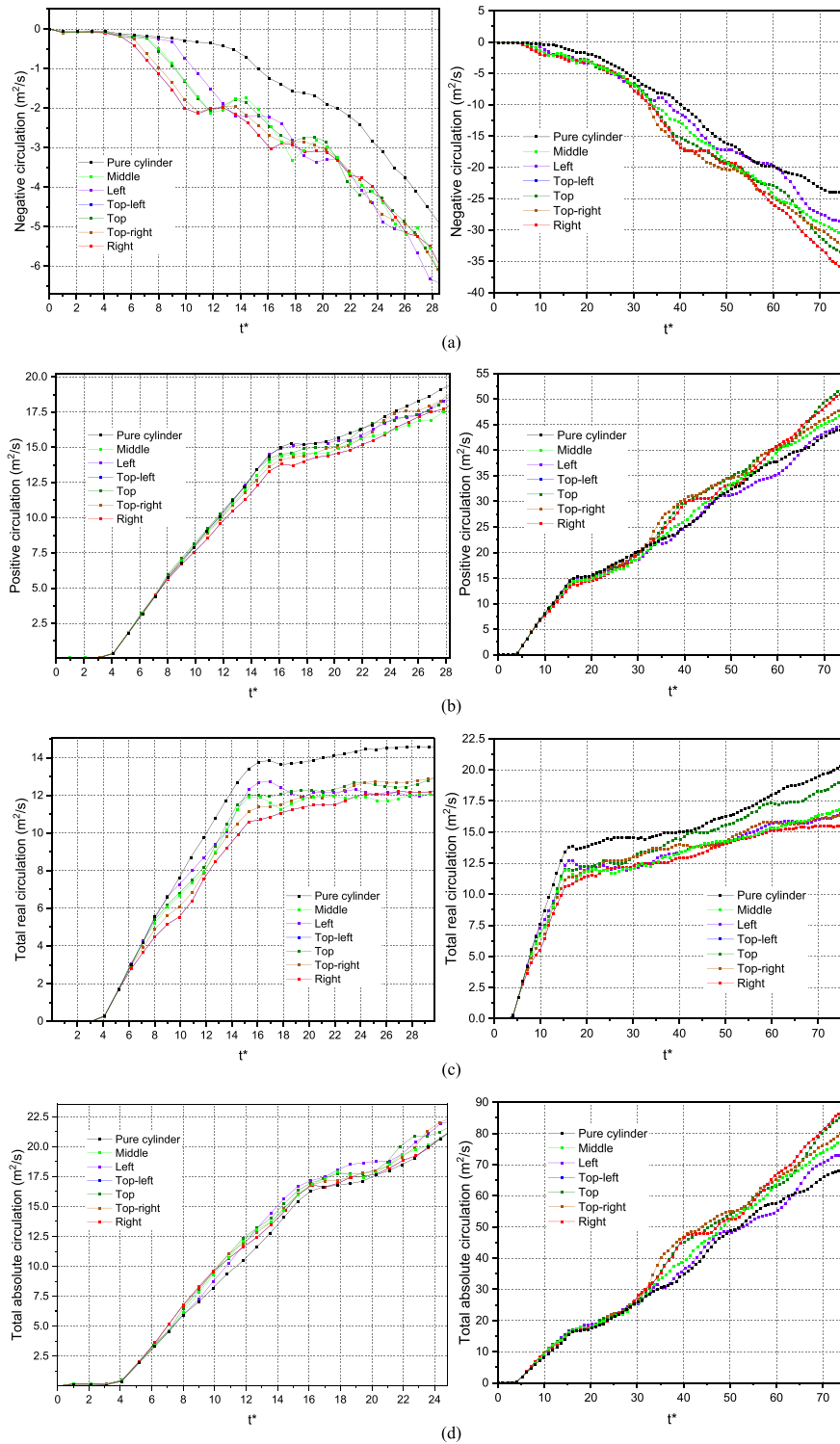
FIG. 17. Positive circulation (a), negative circulation (b), total real circulation (c) and total absolute circulation (d), and histories of the interaction between the shock wave and full cylinder/cylinder ring.
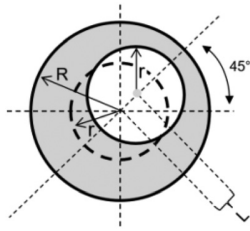
FIG. 18. The schematic diagram of an eccentrically located gas cavity with $r/R = 0.5$, $\theta = 45°$.

elucidated their effects. Building upon this analysis, a hybrid prediction fit, termed the Connecting Rod Prediction Fit (CRPF), is proposed. It is named by analogy because the relationship between the cavity and the cylinder resembles the connecting rod. The CRPF holds potential

for extension to explore the evolution of the center-of-mass position in various cylinder configurations featuring a cavity at near-critical conditions. This fit accounts for factors such as evolution time, cavity size, and eccentricity.

With the aid of the findings obtained from the case featuring a cavity located at the concentric position with a radius of 0.5R, the ensuing predictive fit was identified as follows:

$$f(t^*, \theta^*, r^*, L^*) = f(t^*, r^*) + \beta\big(f(t^*, \theta^*) - f(t^*, \theta^* = 90)\big) - \gamma\big(f(t^*, L^*) - f(t^*, L^* = 0)\big), \quad (5.4)$$

where as can be seen from Figs. 14 and 21, θ^* and L^* serve as a translation function that elucidates the components $f(t^*, \theta^*)$-$f(t^*, \theta^* = 90)$ and $f(t^*, L^*)$-$f(t^*, L^* = 0)$. According to Secs. V B 2 and V C 2, Table VI is obtained. β and γ could be adjustable and could be further modified to improve the prediction accuracy, here $\beta = 1$, $\gamma = 1$.
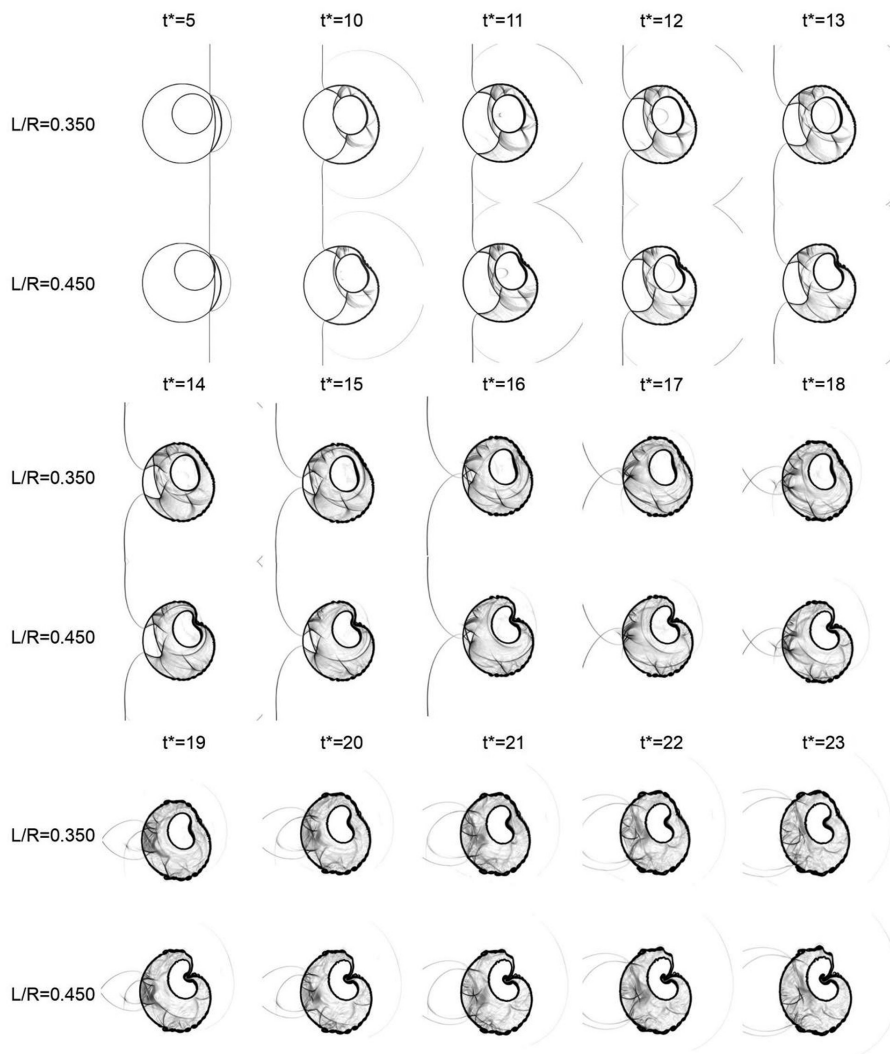

FIG. 19. Representative view of the flow morphology and wave pattern evolution at near-critical conditions.
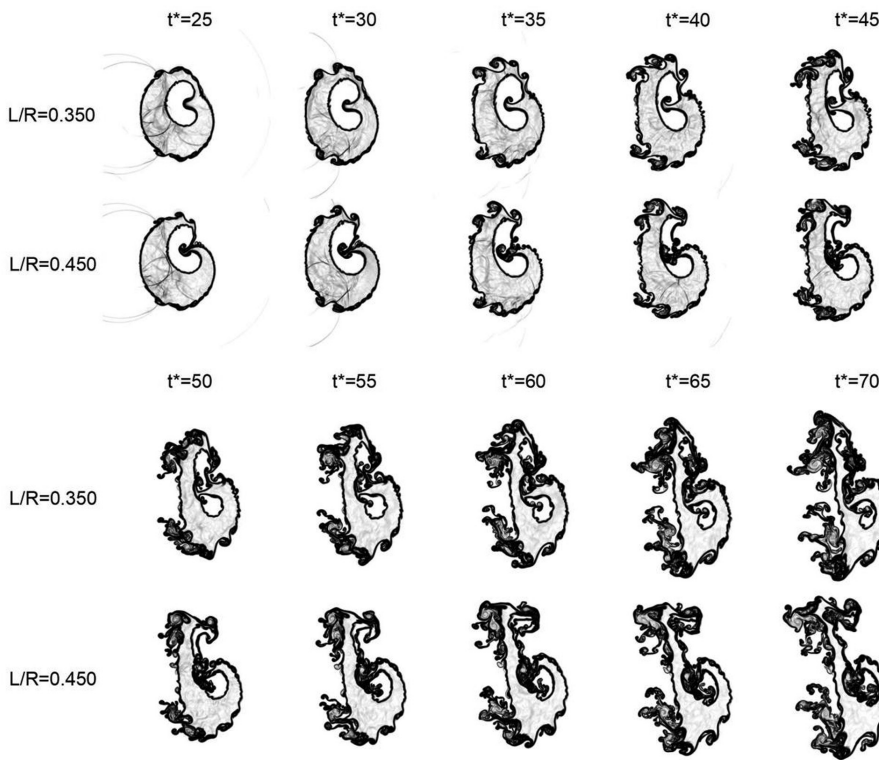
FIG. 20. Representative view of the flow morphology and wave pattern evolution at near-critical conditions.

To further validate the fit, we simulate a general case with $r^* = 0.31$, $\theta^* = 60$, $L = 0.58R$. The result, obtained by the CRPF, is used for comparison. As illustrated in Fig. 26, the results obtained by the hybrid prediction fit agree very well with those obtained by the simulation. The maximum relative error is approximately 3%, indicating the accuracy and generalizability of the present predictive fit. This fit could assist in predicting fuel mixing and adjusting mixing conditions.

VI. CONCLUSIONS

The effects of gas cavity size, eccentricity angle, and eccentricity distance on the shock–cylinder interaction with the intricate layered fluid/interfaces at near-critical conditions are elucidated through detailed simulations, each considering real-fluid effects. Specifically, various cases involving eccentric and concentric cavities with different

cavity radii (0-0.875R), eccentricity angles ($0°$–$180°$), and distances (0R-0.45R) are analyzed.

These factors significantly impact various properties of fuel cylinders at near-critical conditions, leading to the following observations:

TABLE V. Parameters and expressions of Time-Eccentric Distance Polynomial Predictive Fit (TED-PPF) for center-of-mass location considering eccentricity distance.

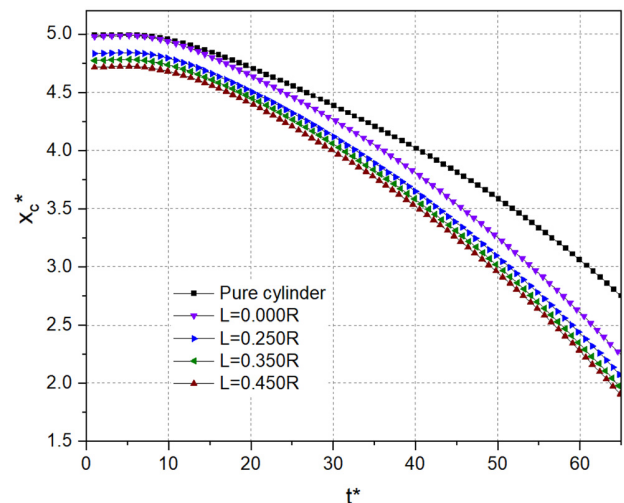| Parameters	Expressions
$f(t^*, L^*)$	$A + Bt^* - 43\,597.706\,46\,t^{*2}$
A	$0.051\,76 - 0.005\,24\,L^*$
B	$-17.063\,25 - 0.643\,64\,L^* - 13.7124\,L^{*2} + 20.980\,86\,L^{*3}$

FIG. 21. The drift of the center-of-mass position (normalized by 0.01 m).
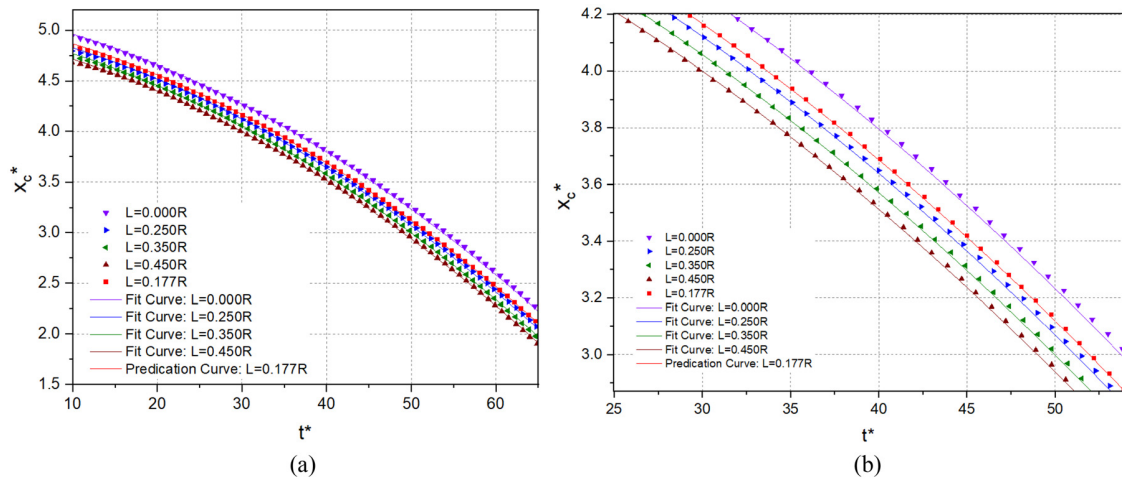
FIG. 22. The drift of the center-of-mass position by Time-Eccentric distance Polynomial Predictive Fit (TED-PPF) and simulations (normalized by 0.01 m). (b) is a zoomed figure of (a).
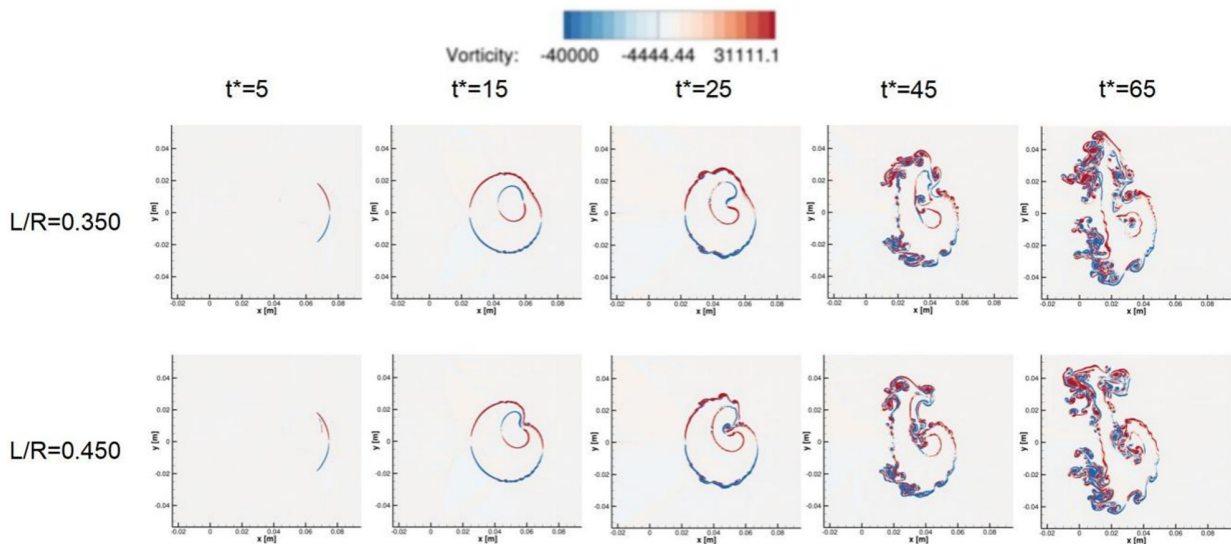

FIG. 23. Schematic diagram of vorticity generation in the shock–cylinder ring interaction (vorticity restricted to the same range of values).

(1) **Pronounced Wave Patterns and Morphological Changes:** Gas cavity size and eccentricity significantly alter wave patterns and shock-induced deformation. Detailed examinations cover the early and late stages of wave interaction, including shock impingement and evolution, along with morphological changes like jet formation and cavity breakup. The streamwise distance between the upstream pole of the cavity and the cylinder crucially affects wave pattern evolution. Asymmetric properties emerge when the cavity is not centered on the equator, leading to unequal cavity sizes. However, the wave pattern outside the cylinder remains largely unaffected by varying cavity sizes in the early stages. Comparisons with subcritical cases are drawn.

(2) **Vortex Generation and Baroclinic Effects:** Simulations reveal the emergence of vortices and the deposition of baroclinic vorticity on cylinder and cavity surfaces. Vortices form on external surfaces, and the presence of a gas cavity significantly impacts liquid mushroom jet creation, vortex structures, and cavity rupture, contributing to interface deformation. Vortices on cavity surfaces exhibit opposite characteristics to those on the cylinder. Additionally, cavities not centered on the cylinder's equator exhibit asymmetric vortex distributions along the axis.
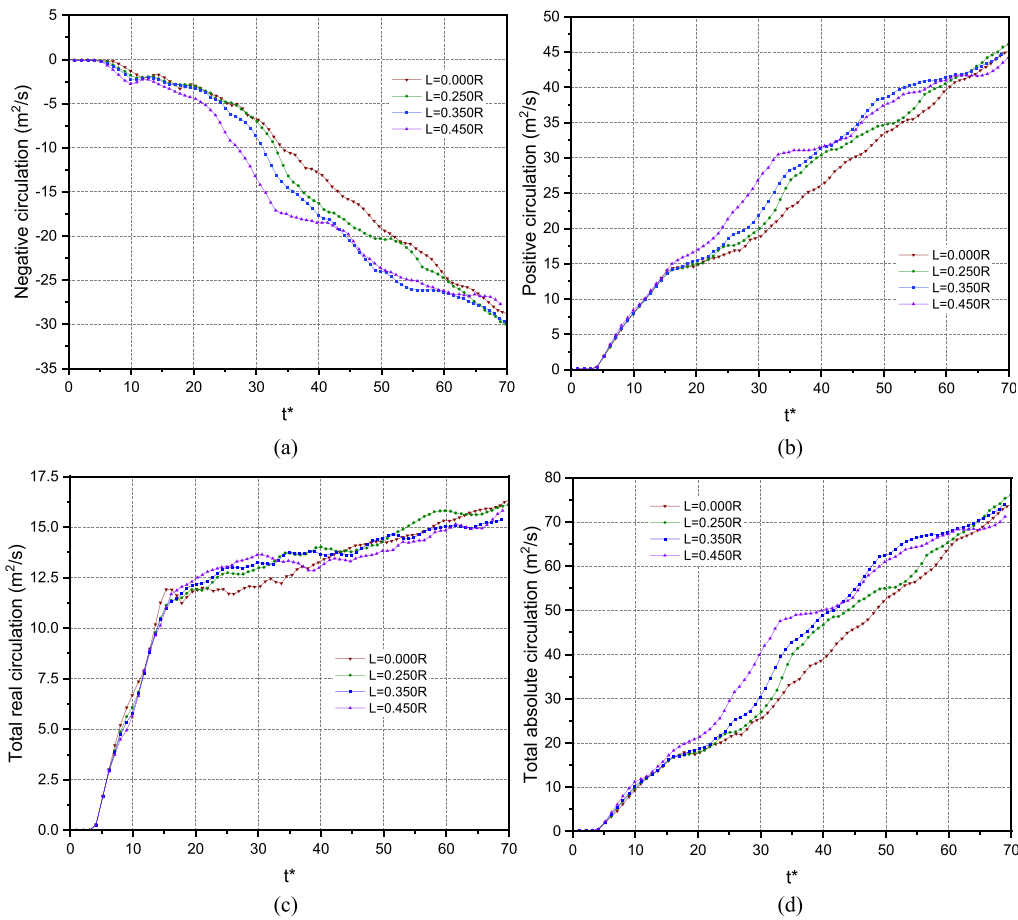
FIG. 24. Positive circulation (a), negative circulation (b), total real circulation (c) and total absolute circulation (d), and histories of the interaction between the shock wave and the full cylinder/cylinder ring.

(3) **Circulation Analysis:** Variations in negative circulation, positive circulation, total real circulation, and total absolute circulation (TAC) over time are thoroughly documented. Interaction between the cavity and cylinder surfaces affects circulation development, with reduced TAC observed when the gap between them is small. Thinner gaps lead to earlier reductions compared to full cylinder cases. Concentric cavity scenarios (especially for cavity radius of 0.375R to 0.625R) show potential for enhancing circulation performance, aiding the mixing process.

(4) **Theoretical Model for Deposited Circulation:** Successful prediction of deposited circulation for concentric scenarios at near-critical conditions is achieved. Theoretical results from properly combining YKZ and ZZ models align well with numerical results for smaller cavity cases (r = 0.000R-0.625R). However, for larger cavity cases, cavity–cylinder contact and induced coupling effects distort theoretical predictions. The normal distance between the cavity and the cylinder center has minimal effect on circulating production in early stages.

(5) **Prediction fit for center-of-mass displacement:** Four predictive fits for the center-of-mass position of shocked cylinders at near-critical conditions demonstrate excellent predictive performance. TS-PPF, TE-PPF, and TED-PPF are proposed for cases involving cavities of various sizes, eccentricity angles, and eccentricity distances. The hybrid fit (CRPF) incorporates evolution time, cavity size, and eccentricity, with minimal effect
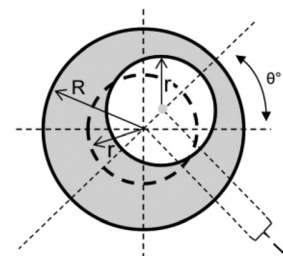

FIG. 25. The schematic of a cavity-embedded cylinder.

TABLE VI. Parameters and expressions of Connecting Rod Prediction Fit (CRPF) for center-of-mass location considering cavity size and eccentricity.

| Parameters	Expressions
$f(t^*, \theta^*, r^*, L^*)$	$0.051\,42 + B_2 t^* + C_2 t^{*2} + 1.2873 \times 10^7 t^{*3} + \beta(A_1 + B_1 t^* - 0.051\,395\,718\,71 + 15.594\,879\,936\,t^*) - \gamma(A_3 + B_3 t^*)$
B_2	$-12.779\,28 - 17.304\,17\,r^* + 164.562\,91\,r^{*2} - 550.278\,43\,r^{*3} + 760.216\,44\,r^{*4} - 388.410\,07\,r^{*5}$
C_2	$-43\,659.262\,21 - 28\,122.375\,81\,r^* + 86\,092.406\,37\,r^{*2} - 146\,392.925\,39\,r^{*3}$
A_1	$0.049\,88 - 7.7619 \times 10^{-6}\theta^* + 4.017\,64 \times 10^{-7}\theta^{*2} - 1.426\,61 \times 10^{-9}\theta^{*3}$
B_1	$-18.122\,43 + 0.002\,5\,\theta^* + 8.026\,37 \times 10^{-4}\theta^{*2} - 7.544\,69 \times 10^{-6}\theta^{*3} + 1.983\,34 \times 10^{-8}\theta^{*4}$
A_3	$-0.005\,24\,L^*$
B_3	$-0.643\,64\,L^* - 13.7124\,L^{*2} + 20.980\,86\,L^{*3}$
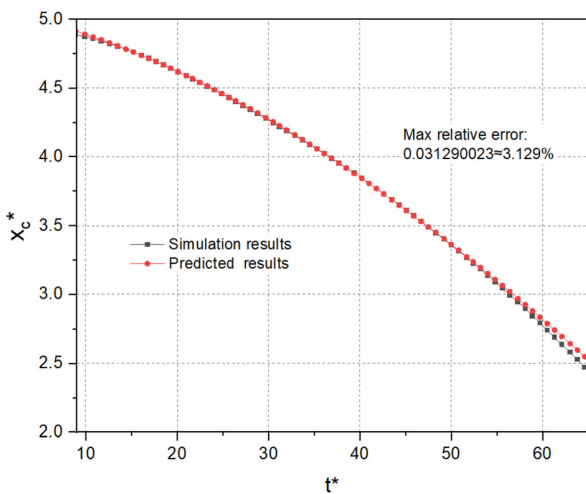
FIG. 26. The comparison and relative discrepancy between predicted results and simulation results.

from the normal distance between the cavity and the cylinder center.

This study offers insights into mixing processes at near-critical conditions, with potential engineering applications in high-speed propulsion systems utilizing liquid fuel sprays. Future research may involve more extensive experimental investigations to deepen the understanding of the underlying mechanisms and disintegration processes.

ACKNOWLEDGMENTS

AUTHOR DECLARATIONS
Conflict of Interest

The authors have no conflicts to disclose.

Author Contributions

Yu Jiao: Conceptualization (lead); Data curation (lead); Formal analysis (lead); Investigation (lead); Methodology (lead); Software (lead); Validation (lead); Visualization (lead); Writing – original draft (lead). **Steffen J. Schmidt:** Funding acquisition (equal); Project administration (equal); Supervision (equal); Writing – review & editing (equal). **Nikolaus A. Adams:** Funding acquisition (equal); Project administration (equal); Supervision (equal); Writing – review & editing (equal).

DATA AVAILABILITY

The data that support the findings of this study are available from the corresponding author upon reasonable request.

APPENDIX A: PENG–ROBINSON EQUATION OF STATE

For the liquid and gas components,

$$p = \frac{RT}{v - b} - \frac{a}{v^2 + 2bv - b^2}, \qquad (A1)$$

where T is the temperature; R is the universal gas constant, v is the molar volume, $v = M/\rho$, and M is the molar mass. Coefficients $a = \sum_{\alpha=1}^{N}\sum_{\beta=1}^{N} X_\alpha X_\beta a_{\alpha\beta}$ and $b = \sum_{\alpha=1}^{N} X_\alpha b_\alpha$.

Specifically, X_α is the mole fraction of species α and in-total species number is N; coefficients $a_{\alpha\beta} = 0.457\,236(RT_{c,\alpha\beta})^2 / p_{c,\alpha\beta}(1 + c_{\alpha\beta}(1 - \sqrt{T/T_{c,\alpha\beta}}))^2$ and $b_\alpha = 0.077\,796 RT_{c,\alpha}/p_{c,\alpha}$ are obtained according to the mixing rules.[76] $p_{c,\alpha\beta}$ is the critical mixture pressure and $p_{c,\alpha\beta} = Z_{c,\alpha\beta}RT_{c,\alpha\beta}/v_{c,\alpha\beta}$, $c_{\alpha\beta} = 0.374\,64 + 1.5422\omega_{\alpha\beta} - 0.269\,92\omega_{\alpha\beta}^2$, $T_{c,\alpha\beta}$ is the critical mixture temperature and $T_{c,\alpha\beta} = \sqrt{T_{c,\alpha}T_{c,\beta}}(1 - k_{\alpha\beta})$. $T_{c,\alpha}$ and $T_{c,\beta}$ are the critical temperature for species α and β, and $k_{\alpha\beta}$ is the binary interaction parameter.

The critical mixture molar volume $v_{c,\alpha\beta}$, the critical mixture compressibility $Z_{c,\alpha\beta}$, and the acentric factor $\omega_{\alpha\beta}$ are denoted as $v_{c,\alpha\beta} = (1/8)(v_{c,\alpha}^{1/3} + v_{c,\beta}^{1/3})^3$, $Z_{c,\alpha\beta} = (1/2)(Z_{c,\alpha} + Z_{c,\beta})$, $\omega_{\alpha\beta} = (1/2) \times (\omega_\alpha + \omega_\beta)$, respectively, where $v_{c,\alpha}^{1/3}$ and $v_{c,\beta}^{1/3}$ are the critical molar volume for species α and β, $Z_{c,\alpha}$ and $Z_{c,\beta}$ are the critical compressibility factor for species α and β, and ω_α and ω_β are the acentric factor for species α and β, respectively. Further details can be found in Refs. 11 and 76.

In solving this equation of state, it is essential to note that there may be three roots. However, it is necessary to ignore the nonphysical roots, which include negative and complex values, and to focus on identifying the real, positive roots.[77–79] The process of solving the cubic equation is outlined in Ref. 42.

APPENDIX B: MODIFIED PR-EOS

The modified PR-EoS is designed to represent the saturation line in a clear and concise manner. To determine the pressure within the vapor dome region, an approximate saturation pressure for the mixture is used. The algorithm for calculating the pressure, which in turn yields the temperature, density, and mass fraction, is as follows:

Step 1. Calculate the pressure from the PR-EoS giving the temperature and density, as well as the mass fraction. If non-positive pressure ($p^* \leq 0$) is obtained from the relation $p^* = p_{PR-EOS}(T, \rho, \xi)$, a small arbitrarily positive value such as 1 would be adopted to replace this non-positive value ($p^* = 1$ Pa).

Step 2. Calculate the density from PR-EoS given the PR-EoS pressure p^*, temperature, and mass fraction, and check how many roots are obtained in the process $\rho^* = p_{PR-EOS}(p^*, T, \xi)$.

Step 3.1. If there is only one real value for ρ^*, then the PR-EoS pressure p^* is chosen as the corrected pressure.

Step 3.2. If there is more than one root for (ρ^*), then the saturation pressure (p_{sat}) is given by calculating the root, $\partial p/\partial \rho = 0$ via PR-EOS ($p = RT/(v - b) - a/(v^2 + 2bv - b^2)$). Generally, the one at the lower density value (ρ_{min}) would be selected from the two resulting roots. The saturation pressure (p_{sat}) is then defined as the pressure corresponding to this root (ρ_{min}).

Step 4. If the density that is given by the PR-EOS (lowest density root, $\rho^* = p_{PR-EOS}(p^*, T, \xi)$ is very similar to the density provided (ρ), like ($\rho^* - \rho)/\rho < 10^{-4}$, then return the PR-EoS pressure p^*; otherwise, return the saturation pressure (p_{sat}).

In the case of DF methods or hybrid numerical schemes with a modified PR-EoS, it is crucial to calculate the temperature (T) for a given set of pressure (p), density (ρ), and mass fraction (ξ) using the modified PR-EOS [$T = p_{Modified-PR-EOS}(p, \rho, \xi)$]. This can be expressed as follows:

Step 1. Initial guess (T_{guess}) temperature according to the initial condition and the temperature from the last time-step.

Step 2. This T_{guess} is used to calculate the pressure, using the modified PR-EOS $p_{guess} = p_{Modified-PR-EOS}(T_{guess}, \rho, \xi)$; here, the state inside the vapor dome has already been corrected.

Step 3. If the pressure given by the modified PR-EOS [$p_{guess} = p_{Modified-PR-EOS}(T_{guess}, \rho, \xi)$] is very similar to the pressure given by the modified PR-EoS (p^*), e.g., ($p_{guess} - p^*)/p^* < 10^{-6}$, then the temperature T_{guess} is selected as the correct temperature $T = T_{guess}$.

Step 4. Otherwise, the guess temperature is updated according to the secant method/Gradient descent/Newtonian method, and the criteria are $p^* = p_{Modified-PR-EOS}(T_{guess}, \rho, \xi)$ and ($p^* - p)/p < 10^{-6}$.

Step 5. The modified PR-EoS[48] also limits the speed of sound to a minimum value—the minimum speed of sound value used in this paper is 1 m/s.[48] Three subcritical isotherms of varying compositions are depicted in Fig. 30 of Ref. 40 to showcase the modified PR-EoS.

REFERENCES

[1] Y. Zhou, "Rayleigh-Taylor and Richtmyer-Meshkov instability induced flow, turbulence, and mixing. I," Phys. Rep. **720–722**, 1–136 (2017).

[2] Y. Zhou, "Rayleigh-Taylor and Richtmyer-Meshkov instability induced flow, turbulence, and mixing. II," Phys. Rep. **723–725**, 1–160 (2017).

[3] M. Brouillette, "The Richtmyer-Meshkov instability," Annu. Rev. Fluid Mech. **34**, 445–468 (2002).

[4] V. K. Tritschler, B. J. Olson, S. K. Lele, S. Hickel, X. Y. Hu, and N. A. Adams, "On the Richtmyer-Meshkov instability evolving from a deterministic multi-mode planar interface," J. Fluid Mech. **755**, 429–431 (2014).

[5] R. D. Richtmyer, "Taylor instability in shock acceleration of compressible fluids," Commun. Pure Appl. Math. **13**, 297–319 (1960).

[6] E. E. Meshkov, "Instability of the interface of two gases accelerated by a shock wave," Fluid Dyn. **4**, 101–104 (1972).

[7] Z. Falgout, M. Rahm, D. Sedarsky, and M. Linne, "Gas/fuel jet interfaces under high pressures and temperatures," Fuel **168**, 14–21 (2016).

[8] R. N. Dahms, J. Manin, L. M. Pickett, and J. C. Oefelein, "Understanding high-pressure gas-liquid interface phenomena in diesel engines," Proc. Combust. Inst. **34**(1), 1667–1675 (2013).

[9] R. N. Dahms, "Understanding the breakdown of classic two-phase theory and spray atomization at engine-relevant conditions," Phys. Fluids **28**(4), 042108 (2016).

[10] J. Oefelein, G. Lacaze, R. Dahms, A. Ruiz, and A. Misdariis, "Effects of real-fluid thermodynamics on high-pressure fuel injection processes," SAE Int. J. Engines **7**(3), 1125–1136 (2014).

[11] P. C. Ma, Y. Lv, and M. Ihme, "An entropy-stable hybrid scheme for simulations of transcritical real-fluid flows," J. Comput. Phys. **340**, 330–357 (2017).

[12] D. T. Banuti, M. Raju, and M. Ihme, "Supercritical pseudoboiling for general fluids and its application to injection," in *Annual Research Briefs* (Center for Turbulence Research, Stanford University, 2016), pp. 3–16.

[13] M. Oschwald, J. Smith, R. Branam, J. Hussong, A. Schik, B. Chehroudi, and D. Talley, "Injection of fluids into supercritical environments," Combust. Sci. Technol. **178**(1–3), 49–100 (2006).

[14] D. Banuti, M. Raju, P. C. Ma, M. Ihme, and J.-P. Hickey, "Seven questions about supercritical fluids—Towards a new fluid state diagram," AIAA Paper No. 2017-1106, 2017.

[15] M. Raju, D. T. Banuti, P. C. Ma, and M. Ihme, "Widom lines in binary mixtures of supercritical fluids," Sci. Rep. **7**(1), 3027 (2017).

[16] W. O. H. Mayer, A. H. A. Schik, B. Vielle, C. Chauveau, I. Gokalp, D. G. Talley, and R. D. Woodward, "Atomization and breakup of cryogenic propellants under high-pressure subcritical and supercritical conditions," J. Propul. Power **14**(5), 835–842 (1998).

[17] J. W. Chae, H. S. Yang, and W. S. Yoon, "Supercritical droplet dynamics and emission in low speed cross-flows," J. Mech. Sci. Technol. **22**(11), 1586–2107 (2008).

[18] V. Yang, "Modeling of supercritical vaporization, mixing, and combustion processes in liquid-fueled propulsion systems," Proc. Combust. Inst. **28**(2), 925–942 (2000).

[19] V. Yang, N. Natan, and J.-S. Shuen, "Vaporization of liquid oxygen (LOX) droplets in supercritical hydrogen environments," Combust. Sci. Technol. **97**(4–6), 247–270 (1994).

[20] V. Yang, G. C. Hsiao, J. S. Shuen, and K. C. Hsieh, "Droplet behavior at supercritical conditions," in *Recent Advances Spray Combustion: Spray Atomization Drop Burning Phenomena* (American Institute of Aeronautics and Astronautics, Inc., 1996), Vol. 1, pp. 413–437.

[21] C. Crua, J. Manin, and L. M. Pickett, "On the transcritical mixing of fuels at diesel engine conditions," Fuel **208**, 535–839 (2017).

[22] H. Meng, G. C. Hsiao, V. Yang, and J. S. Shuen, "Transport and dynamics of liquid oxygen droplets in supercritical hydrogen streams," J. Fluid Mech. **527**, 115–139 (2005).

[23] J. F. Haas and B. Sturtevant, "Interaction of weak shock waves with cylindrical and spherical gas inhomogeneities," J. Fluid Mech. **181**, 41–76 (1987).

[24] J. Jacobs, "Shock-induced mixing of a light-gas cylinder," J. Fluid Mech. **234**, 629–649 (1992).

[25] J. Jacobs, "The dynamics of shock-accelerated light and heavy gas-cylinders," Phys. Fluids A **5**(9), 2239–2247 (1993).

[26] X. Wang, D. Yang, J. Wu, and X. Luo, "Interaction of a weak shock wave with a discontinuous heavy-gas cylinder," Phys. Fluids **27**(6), 064104 (2015).

[27] J. Ding, T. Si, M. Chen, Z. Zhai, X. Lu, and X. Luo, "On the interaction of a planar shock with a three-dimensional light gas cylinder," J. Fluid Mech. **828**, 289–317 (2017).

[28] J. Ding, Y. Liang, M. Chen, Z. Zhai, T. Si, and X. Luo, "Interaction of planar shock wave with three-dimensional heavy cylindrical bubble," Phys. Fluids **30**(10), 106109 (2018).

[29]Z. Wang, B. Yu, H. Chen, B. Zhang, and H. Liu, "Scaling vortex breakdown mechanism based on viscous effect in shock cylindrical bubble interaction," Phys. Fluids **30**, 126103 (2018).

[30]D. Li, G. Wang, and B. Guan, "On the circulation prediction of shock-accelerated elliptical heavy gas cylinders," Phys. Fluids **31**(5), 056104 (2019).

[31]S. Singh, M. Battiato, and R. Myong, "Impact of bulk viscosity on flow morphology of shock-accelerated cylindrical light bubble in diatomic and polyatomic gases," Phys. Fluids **33**(6), 066103 (2021).

[32]L. Feng, J. Xu, Z. Zhai, and X. Luo, "Evolution of shock-accelerated double-layer gas cylinder," Phys. Fluids **33**(8), 086105 (2021).

[33]J. Xu, H. Wang, L. Feng, Z. Zhai, and X. Luo, "Interaction of a shock with two concentric/eccentric cylinders," Exp. Fluids **62**(2), 211 (2021).

[34]G. Wang, Y. Wang, D. Li, and B. Guan, "Numerical study on shock-accelerated gas rings," Phys. Fluids **32**(2), 026102 (2020).

[35]G. Xiang and B. Wang, "Numerical study of a planar shock interacting with a cylindrical water column embedded with an air cavity," J. Fluid Mech. **825**, 825–852 (2017).

[36]S. Wang, Z. Jiao, X. Huang, C. Yang, and N.-T. Nguyen, "Acoustically induced bubbles in a microfluidic channel for mixing enhancement," Microfluid. Nanofluid. **6**(6), 847–852 (2009).

[37]O. Shpak, M. Verweij, N. de Jong, and M. Versluis, "Droplets, bubbles and ultrasound interactions," in *Bubble Dynamics and Shock Waves*, edited by M. Versluis, N. de Jong, and D. Lohse (Springer International Publishing, 2016), pp. 157–174.

[38]M. Lü, Z. Ning, and C. Sun, "Numerical simulation of cavitation bubble collapse within a droplet," Comput. Fluids **152**, 157–163 (2017).

[39]Y. Liang, Y. Jiang, C. Y. Wen, and Y. Liu, "Interaction of a planar shock wave and a water droplet embedded with a vapour cavity," J. Fluid Mech. **885**, R6 (2020).

[40]B. Boyd and D. Jarrahbashi, "A diffuse-interface method for reducing spurious pressure oscillations in multicomponent transcritical flow simulations," Comput. Fluids **222**, 104924 (2021).

[41]B. Boyd and D. Jarrahbashi, "Numerical study of the transcritical shock-droplet interaction," Phys. Rev. Fluids **6**(11), 113601 (2021).

[42]Y. Jiao, S. J. Schmidt, and N. A. Adams, "Simulating shock interaction with a cavity-embedded cylinder/droplet using a real-fluid hybrid scheme at near-critical conditions," Phys. Rev. Fluids **9**(7), 074002 (2024).

[43]Y. Jiao, S. J. Schmidt, and N. A. Adams, "An all-Mach consistent numerical scheme for simulation of compressible multi-component fluids including surface tension, cavitation, turbulence modeling and interface sharpening on compact stencils," Comput. Fluids **274**, 106186 (2024).

[44]C. P. Egerer, S. J. Schmidt, S. Hickel, and N. A. Adams, "Efficient implicit LES method for the simulation of turbulent cavitating flows," J. Comput. Phys. **316**, 453–469 (2016).

[45]F. Örley, T. Trummler, S. Hickel, M. S. Mihatsch, S. J. Schmidt, and N. A. Adams, "Large-eddy simulation of cavitating nozzle flow and primary jet break-up," Phys. Fluids **27**(8), 086101 (2015).

[46]T. Trummler, S. J. Schmidt, and N. A. Adams, "Investigation of condensation shocks and re-entrant jet dynamics in a cavitating nozzle flow by Large-Eddy Simulation," Int. J. Multiphase Flow **125**, 103215 (2020).

[47]R. Abgrall, "How to prevent pressure oscillations in multicomponent flow calculations: A quasi conservative approach," J. Comput. Phys. **125**(1), 150–160 (1996).

[48]E. Knudsen, H. Pitsch, and M. Ihme, "Compressible Eulerian needle-to-target large eddy simulations of a diesel fuel injector," Proc. Combust. Inst. **36**(2), 2459–2466 (2017).

[49]J. Matheis and S. Hickel, "Multi-component vapor-liquid equilibrium model for LES of high-pressure fuel injection and application to ECN Spray A," Int. J. Multiphase Flow **99**, 294–304 (2018).

[50]A. M. Ruiz, G. Lacaze, J. C. Oefelein, R. Mari, B. Cuenot, L. Selle, and T. Poinsot, "Numerical benchmark for high-Reynolds-number supercritical flows with large density gradients," AIAA J. **54**(5), 1445–1460 (2016).

[51]H. Müller, C. A. Niedermeier, J. Matheis, M. Pfitzner, and S. Hickel, "Large-eddy simulation of nitrogen injection at trans-and supercritical conditions," Phys. Fluids **28**(1), 015102 (2016).

[52]W. Wei, H. Liu, M. Xie, M. Jia, and Y. Yue, "Large eddy simulation and proper orthogonal decomposition analysis of fuel injection under trans/supercritical conditions," Comput. Fluids **179**, 150–160 (2019).

[53]N. Okong'o and J. Bellan, "Perturbation and initial Reynolds number effects on transition attainment of supercritical, binary, temporal mixing layers," Comput. Fluids **33**(8), 1023–1040 (2004).

[54]N. Okong'o and J. Bellan, "Small-scale dissipation in binary-species, thermodynamically supercritical, transitional mixing layers," Comput. Fluids **39**(8), 1112–1128 (2010).

[55]S. Yatsuyanagi, T. Furusawa, and S. Yamamoto, "Double-flux model for supercritical multicomponent flows at low Mach numbers with preconditioning method," J. Comput. Phys. **458**, 111091 (2022).

[56]R. Abgrall and S. Karni, "Computations of compressible multifluids," J. Comput. Phys. **169**(2), 594–623 (2001).

[57]G. Billet and R. Abgrall, "An adaptive shock-capturing algorithm for solving unsteady reactive flows," Comput. Fluids **32**(10), 1473–1495 (2003).

[58]H. Terashima and M. Koshi, "Approach for simulating gas–liquid-like flows under supercritical pressures using a high-order central differencing scheme," J. Comput. Phys. **231**(20), 6907–6923 (2012).

[59]S. Kawai, H. Terashima, and H. Negishi, "A robust and accurate numerical method for transcritical turbulent flows at supercritical pressure with an arbitrary equation of state," J. Comput. Phys. **300**, 116–135 (2015).

[60]G. Billet and J. Ryan, "A Runge–Kutta discontinuous Galerkin approach to solve reactive flows: The hyperbolic operator," J. Comput. Phys. **230**(4), 1064–1083 (2011).

[61]Y. Lv and M. Ihme, "Discontinuous Galerkin method for multi-component chemically reacting flows and combustion," J. Comput. Phys. **270**, 105–137 (2014).

[62]P. C. Ma, H. Wu, D. T. Banuti, and M. Ihme, "On the numerical behavior of diffuse-interface methods for transcritical real-fluids simulations," Int. J. Multiphase Flow **113**, 231–249 (2019).

[63]D.-Y. Peng and D. B. Robinson, "A new two-constant equation of state," Ind. Eng. Chem. Fundam. **15**(1), 59–64 (1976).

[64]B. J. McBride, S. Gordon, and M. A. Reno, "Coefficients for calculating thermodynamic and transport properties of individual species," NASA Technical Memorandum No. 4513 (NASA Langley Research Center, 1993).

[65]P. C. Ma, H. Wu, T. Jaravel, L. Bravo, and M. Ihme, "Large-eddy simulations of transcritical injection and auto-ignition using diffuse-interface method and finite-rate chemistry," Proc. Combust. Inst. **37**(3), 3303–3310 (2019).

[66]C. Traxinger, M. Pfitzner, S. Baab, G. Lamanna, and B. Weigand, "Experimental and numerical investigation of phase separation due to multicomponent mixing at high-pressure conditions," Phys. Rev. Fluids **4**(7), 074303 (2019).

[67]D. T. Banuti, P. C. Ma, and M. Ihme, "Phase separation analysis in supercritical injection using large-eddy-simulation and vapor-liquid-equilibrium," AIAA Paper No. 2017-4764, 2017.

[68]A. Baeza, R. Bürger, P. Mulet, and D. Zorío, "An efficient third-order WENO scheme with unconditionally optimal accuracy," SIAM J. Sci. Comput. **42**(2), A1028–A1051 (2020).

[69]E. F. Toro, *Riemann Solvers and Numerical Methods for Fluid Dynamics: A Practical Introduction*, 3rd ed. (Springer, 2009).

[70]E. F. Toro, "The HLLC Riemann solver," Shock Waves **29**(8), 1065–1082 (2019).

[71]J. Quirk and S. Karni, "On the dynamics of a shock–bubble interaction," J. Fluid Mech. **318**, 129–163 (1996).

[72]A. Abd-el Fattah and L. Henderson, "Shock waves at a slow-fast gas interface," J. Fluid Mech. **89**(1), 79–95 (1978).

[73]J. C. Meng and T. Colonius, "Numerical simulation of the aerobreakup of a water droplet," J. Fluid Mech. **835**, 1108–1135 (2018).

[74]J. Yang, T. Kubota, and E. E. Zukoski, "A model for characterization of a vortex pair formed by shock passage over a light-gas inhomogeneity," J. Fluid Mech. **258**, 217–244 (1994).

[75]W. Zhang, L. Zou, X. Zheng, and B. Wang, "Numerical study on the interaction of a weak shock wave with an elliptic gas cylinder," Shock Waves **29**(2), 273–284 (2019).

[76]K. G. Harstad, R. S. Miller, and J. Bellan, "Efficient high-pressure state equations," AIChE J. **43**(6), 1605–1610 (1997).

[77]J. H. Perry, *Chemical Engineers' Handbook* (ACS Publications, 1950).

[78]G. Wilczek-Vera and J. H. Vera, "Understanding cubic equations of state: A search for the hidden clues of their success," AIChE J. **61**(9), 2824–2831 (2015).

[79]P. Yi, S. Yang, C. Habchi, and R. Lugo, "A multicomponent real-fluid fully compressible four-equation model for two-phase flow with phase change," Phys. Fluids **31**(2), 26102 (2019).